The Stability of Viscoelastic Fluids in Complex Flows: The Role of Shear and Extensional Rheology

by

Jonathan P. Rothstein

M.S., Engineering Sciences
Harvard University, 1998

Submitted to the Department of Mechanical Engineering
in Partial Fulfillment of the Requirements for the Degree of
Doctor of Philosophy in Mechanical Engineering

at the
Massachusetts Institute of Technology
June 2001

BARKER

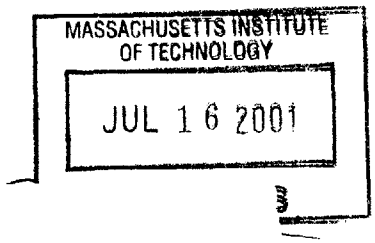

Signature of Author .....
Department of Mechanical Engineering
May 18, 2001

Certified by .....
Gareth H. McKinley
Professor of Mechanical Engineering
Thesis Supervisor

Accepted by .....
Ain A. Sonin
Chairman, Department Committee on Graduate Students

The Stability of Viscoelastic Fluids in Complex Flows: The Role of Shear and Extensional Rheology

by

Jonathan P. Rothstein

Submitted to the Department of Mechanical Engineering
on May 18, 2001 in partial fulfillment of the
requirements for the Degree of Doctor of Philosophy in
Mechanical Engineering

Abstract

Understanding the flow of polymeric fluids is important for optimizing commercial processes such as injection molding and fiber spinning. The combination of streamwise curvature and elastic normal stresses can lead to the onset of elastic flow instabilities, severely rate-limiting such processes. This thesis focuses on the stability of two complex non-Newtonian flows of dilute polystyrene solutions: the viscometric flow between a rotating cone-and-plate and the flow through an axisymmetric contraction-expansion.

Torsional shear flows of elastic fluids with closed streamlines can accumulate heat from viscous dissipation resulting in spatial nonuniformities in the temperature profile and viscometric properties. In this thesis, a detailed study of the effect of viscous heating on the steady shearing of elastic fluids between a rotating cone-and-plate is performed. The relative importance of viscous heating and elasticity can be quantified by a new dimensionless thermoelastic number. This parameter is a fluid material property which is a function of polymer molecular weight, geometry and temperature. As the thermoelastic number is increased, strong temperature gradients reduce the elasticity of the test fluid and delay the onset of the instability, eventually stabilizing the flow completely.

The flow of elastic fluids into an axisymmetric abrupt contraction-expansion is a complex flow containing regions of both shear and extension that tests the limits of current viscoelastic constitutive models. A large extra pressure drop above that measured for a similar Newtonian fluid is documented and found to correlate to the stress-conformation hysteresis observed in transient uniaxial extension measurements. Laser Doppler velocimetry, particle image velocimetry and flow induced birefringence are used to investigate the global kinematics upstream of contraction-expansions of various contraction ratios and degrees of re-entrant corner curvature. For a contraction ratio of $\beta=2$ a steady elastic lip vortex is observed whereas for $4<\beta<8$, no lip vortex is observed and instead a corner vortex is seen. At large Deborah numbers a time-dependent elastic flow instability is observed. Measurements of the transient extensional rheology show that the differing vortex growth pathways in viscoelastic fluids can be systematically understood in terms of a dimensionless ratio of the normal stress differences in shear and in extension.

Thesis Supervisor: Gareth H. McKinley
Title: Professor of Mechanical Engineering

Table of Contents

List of Figures

List of Tables

Acknowledgements

There are a great number of people I would like to thank for the professional, financial and personal support they have given me throughout the course of my graduate studies. Without a doubt, the person to whom I owe the largest debt of gratitude is my wife, Kara. If it were not for your constant support and love I could never have persevered. I thank you for always having faith in me and for tolerating these last five years of poverty so that I could fulfill this dream. I dedicate this thesis to you.

I want to thank my advisor, Gareth H. McKinley, for the opportunity to work in a fascinating research area. It was your unchecked enthusiasm and passion for science that convinced me to work for you at Harvard and I have never regretted my decision. I learned a great deal about research, academics and life from your instruction and example. I hope that I am as successful and influential in my career and with my students as you have been with yours.

I thank my parents for instilling in me the desire to learn and to the rest of my family and friends for always showing genuine interest in the sticky fluids I have spent the last five years studying.

I must acknowledge how lucky I have been to be a part of such a tight knit group of students and post-docs that have been a part of the Non-Newtonian Fluids Lab over the course of these last few years. Gavin, Steve and Mark, I would like to thank you for always finding time to answer my questions and for teaching me what it means to be an experimentalist. Shelley, I thank you for your advice and friendship, but most importantly, I thank you for always listening when I needed someone to talk to. Anubhav, it is hard to tell you just how much our friendship means to me. Everyone deserves to have a champion like you. I must also express my appreciation to the entire Fluid Mechanics Laboratory at MIT. Darryl, Jeremy, Pirouz and Ryan your friendship and our many conversations have been some of the best times I've had at MIT.

To my thesis committee, Doug Hart and Bob Armstrong, I would like to thank you for your advice, suggestions and questions. Finally, I thank the NASA Glenn Microgravity Research Program for financial support of my graduate studies.

CHAPTER 1 Introduction

"A fluid that's macromolecular
Is really quite weird – in particular
The big normal stresses
The fluid possesses
Give rise to effects quite spectacular"
[Bird *et al.* 1987]

Polymeric fluids are often called viscoelastic fluids because depending on the timescale with which one probes them, they may behave like an elastic Hookean solid or a viscous Newtonian fluid or a complex combination of the two. The extraordinary behavior of these fluids is imparted by the physical nature of the mobile polymer macromolecule. A macromolecule is a large molecule composed of several small chemical structural units, typically carbon based. The macromolecule and its physical properties are strongly influenced by the makeup of these structural units and their interconnectivity [Flory 1953]. In Table 1-1, the structural units for several well known synthetic polymers are listed.

Macromolecules are found abundantly in nature, from natural tree rubber to polypeptide chains that make up proteins to the DNA molecules that form the basis for life. The first man made polymer, Nylon 66, was developed by Wallace Carothers at Dupont in 1935 [Flory 1953]. Since that time the polymer industry has flourished, playing an ever increasing role in modern society. Polymers are light, durable and their material properties can be tailored to meet almost any need. They are an essential part of many major industries including aerospace, automotive, medicine and construction. According to the Committee on Polymer Science and Engineering (1994), in the United States alone, over 70 million pounds of polymers and plastics are produced, accounting for over $100 billion in annual revenues.

Polymers come in all shapes and sizes. Synthetic polymers, unlike polymers found in nature, are typically built up from a single structural repeat unit. The resulting polymers are referred to as homopolymers. The macromolecules can be linear (every internal structural unit is connected to precisely two other structural units) or the polymers can be branched (structural units are connected to three or more other structural units). The molecular weight of these macromolecules is variable, but typical values will span the range between $10^3 < M_w < 10^7$ g/mol. At these very large molecular weights, the macromolecule can grow large enough to be observed with an optical microscope [Perkins *et al.* 1994]. If the molecular weight distribution of a sample of polymer is very narrow, then the polymer is called monodisperse.

Alternatively, if there is a broad range of molecular weights in polymeric sample, then the polymer is classified as polydisperse. Through the course of the research presented in this thesis linear, high molecular weight, monodisperse, uncharged homopolymers will be used.

Polymer	Structural Unit
Polystyrene	$-CH_2-CH(C_6H_5)-$
Polyisobutylene	$-CH_2-C(CH_3)_2-$
Polyethylene	$-CH_2-$
Polyacrylamide	$-CH_2-CH(CONH_2)-$
Polydimethylsiloxane	$-Si(CH_3)_2-O-$
Polyisoprene (Natural Rubber)	$-CH_2-C(CH_3)=CH-CH_2-$
Polyhexamethylene adipamide (Nylon 66)	$-NH-(CH_2)_6-NH-C(O)-(CH_2)_4-C(O)-$

Table 1-1 Examples of the chemical structure of some common synthetic polymers [Bird *et al.* 1987].

Over the last half of the 20th century, our understanding of polymer science and polymer chemistry has progressed by leaps and bounds, although, it is interesting that one of the definitive references, Flory's Principles of Polymer Chemistry [Flory 1953], is nearly 50 years old. Even with all these advances, there still is a considerable amount of research to be done. In particular, the physical mechanisms governing the behavior of polymer chains under large straining motions in the molten state is still not well understood. For many polymer applications, the polymer must be first melted or dissolved into solution and then processed in the liquid state. To accurately predict the final physical characteristics and structural properties of an extrudate, mold or fiber one must first understand the response of these elastic fluids to different flow conditions.

The history of the study of fluid dynamics can be traced back to the beginning of human civilization. The modern study of fluid dynamics began with Sir Isaac Newton, who in 1687 proposed his law of viscosity which expressed in modern form can be written

$$\tau_{yx} = \mu \frac{\partial v_x}{\partial y} \tag{1-1}$$

i.e the shear stress, τ_{yx}, is the proportional to the velocity gradient, $\partial v_x/\partial y$, in a shear flow. The coefficient of proportionality is the viscosity, μ. Newton's law is an example of a constitutive equation which relates

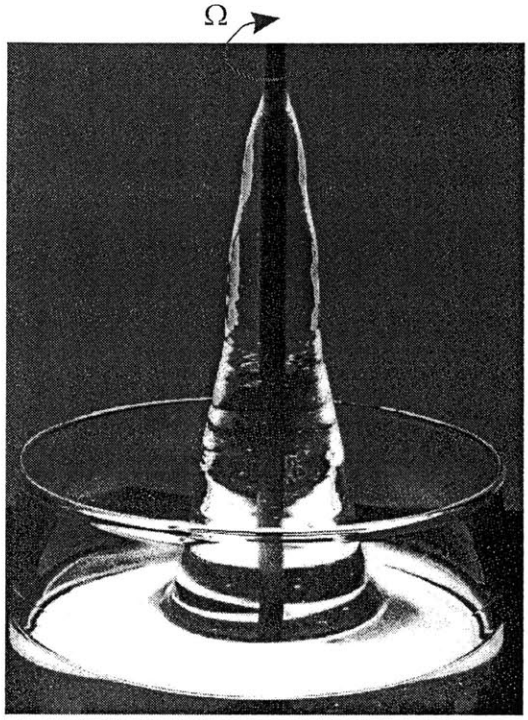

Figure 1-1 An example of rod climbing. The elastic hoop stresses generated by a rotating rod immersed in a viscoelastic fluid will cause the fluid to climb up the rod. Reproduced with permission from [Boger 1993] Copyright 1993 Elsevier.

the state of stress to the instantaneous deformation history of a fluid element. When used in conjunction with the equations for the conservation of mass, momentum and energy, Newton's law of viscosity describes quite well the flow of simple liquids and gasses with molecular weights less than $M_w \lesssim 1000$g/mol [Bird *et al.* 1987]. The addition of high molecular weight macromolecules to a fluid can significantly alter the response of a Newtonian fluid resulting in some very interesting and puzzling flow phenomenon. There are several excellent references on this topic including *Rheological Phenomenon in Focus* [Boger and Walters 1993] and *The Dynamics of Polymeric Liquids,* volumes 1 and 2 [Bird *et al.* 1987; Bird *et al.* 1987].

As a flexible polymer coil stretches within a flow field, it is deformed out of its equilibrium random walk configuration. An elastic restoring force results, driving the polymer coil back towards its entropically favorable equilibrium state [Flory 1953]. High molecular weight polymers can thus impart an entropic elasticity which allows a fluid to carry stress along the flow streamlines and can lead to the build up of normal stresses in simple shear flows. Examples of some interesting flow phenomenon resulting from these elastic stresses are rod climbing and the tubeless syphon, Figures 1-1 and 1-2 respectively. For these

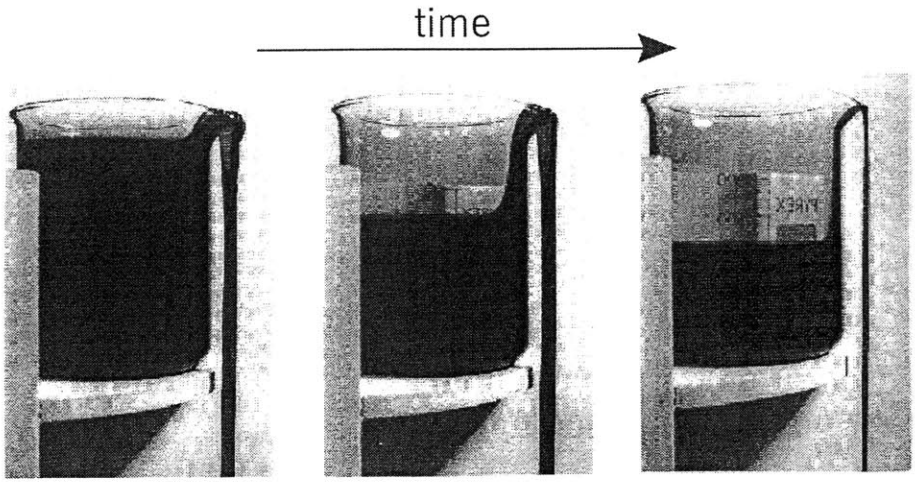

Figure 1-2 An example of the open syphon or Weissenberg effect. A viscoelastic fluid can be drawn out of the beaker without requiring a syphon to be in contact with the fluid. Reproduced with permission from [Boger 1993] Copyright 1993 Elsevier.

polymeric fluids, Newton's law of viscosity no longer holds. These fluids are therefore often described as *non-Newtonian*. One of the biggest challenges in this field is the derivation of constitutive models which can accurately describe the state of stress of the fluid. This is an ongoing, rich research area.

These non-Newtonian fluids have both the characteristics of an elastic Hookean solid for which the stress is proportional to the amount of strain

$$\tau_{ij} = G\varepsilon_{ij}, \tag{1-2}$$

where G is an elastic modulus and a viscous Newtonian fluid for which the stress components τ_{ij} is proportional to the strain rate, $\dot{\gamma}_{ij}$, see Equation 1-1. The combination of viscosity and elasticity leads to a characteristic fluid timescale known as the relaxation time which describes the time required for the polymer coil to relax from a deformed state back to its equilibrium configuration

$$\lambda \equiv \frac{G}{\mu}. \tag{1-3}$$

Thus the residence time of a fluid in a flow must also be considered to understand the response of a polymeric fluid. The relative importance of elasticity in a flow is often described by the Deborah number which is the ratio of the relaxation time of the fluid to a characteristic deformation timescale, t_{flow}, in the flow

$$De \equiv \frac{\lambda}{t_{flow}}. \tag{1-4}$$

If the deformation timescale is large in comparison to the relaxation time of the fluid, $De << 1$, then the polymer coils have ample time to relax back to equilibrium and the fluid will behave like a Newtonian fluid. If the relaxation time is much longer than the deformation timescale in the flow, $De >> 1$, then the fluid will react like an elastic Hookean solid. The behavior of the fluid between these two extremes is quite rich. For these fluids there is, therefore, the additional added complexity that the material properties of the polymeric fluids are not constant, but functions of the deformation rate.

To fully characterize a Newtonian fluid one only needs to measure its viscosity, the study of which is historically know as viscometry. The non-Newtonian analog of viscometry is known as rheometry and it involves the experimental measurement of one or more components of the stress tensor in several well defined flows, be it shear or extension. These experimental measurements are then used in theoretical studies to validate or motivate constitutive models. The simplest constitutive model for the state of stress in a non-Newtonian fluid must be a function of strain, strain rate and time

$$\tau = f\left(\varepsilon, \dot{\gamma}, t\right). \tag{1-5}$$

A great deal of research has focused on the development of constitutive models from kinetic theory. Two excellent references are *Dynamics of Polymeric Liquids* [Bird *et al.* 1987; Bird *et al.* 1987] and *Constitutive Equations for Polymer Melts and Solutions* [Larson 1988]. More recent developments can be found in Bird and Weist [1995]. In this thesis, three constitutive models are used in particular. A Rouse-Zimm model is used to help us understand the response of the fluid to small amplitude deformations over a spectrum of different timescales [Bird *et al.* 1987; Zimm 1956]. The Rouse-Zimm model architecture describes the polymer chain as a series of beads and springs with a variable degree of hydrodynamic interaction. The beads account for all the mass and the viscous drag while the springs impart elasticity to the fluid. Although, the Zimm model is very successful for describing the linear viscoelasticity of a fluid, it does not do a good job describing the behavior of these fluids in large amplitude straining motions. To understand the behavior of these polymer solutions in more realistic flows with larger deformations, the FENE-P and Bird-DeAguiar models will be used [Bird *et al.* 1987; Bird and DeAguiar 1983]. In these models, the polymer coil is described by two beads connected by a single spring. In the FENE-P model, the spring is given a finite extensibility, while in the Bird-DeAguiar model an anisotropy in the Brownian forces and the hydrodynamic interaction is also included. These models will be discussed in greater detail in Chapters 2 and 3.

The importance of non-Newtonian fluid dynamics research can be demonstrated by considering the following industrial-relevant polymer processing operations: injection molding, fiber spinning, coating flows, adhesion, and flow through porous media. Injection molding is one of the cornerstones of the plastics and elastomer industry. Many geometrically complicated parts are fabricated through this technique. Injection molding and extrusion processes in general are not limited to the polymer industry. Many foods, such as dough are processed in much the same way. Fiber spinning is again employed industrially to produce polymeric fibers such as Nylon or Kevlar, but is also common in nature. The spinerettes of silk worms and spiders operate under similar principles. Many fibers once formed require protective or reflective coatings made from polymeric fluids. Coating flows such as these are often dominated by the non-Newtonian response of the coating fluid. The study of adhesion and de-adhesion is also extremely important to manufacturers of all forms of tapes and epoxies. Lastly, in oil recovery, polymeric fluids as well as surfactant solutions and associative polymers are often used to drive oil out of reservoirs which are complex porous media.

These examples from industry are just a short list of important applications of elastic fluids. They were chosen because they all have two things in common; each of these polymer fluid applications is rate limited by the onset of elastic instabilities and each is dominated to some extent by a strong extensional component to the flow. In Research Trends in Fluid Dynamics, Mort Denn highlighted some of the key research needs in the fields of non-Newtonian fluid mechanics and rheology as

> "Identification of mechanisms for flow instabilities at low Reynolds numbers in rotational, converging and interfacial flows [and] reliable experimental techniques for the measurement of extensional stresses in mobile liquids, like polymer solutions." [Denn 1993]

In this thesis, I will address both of these important topics through a detailed experimental investigation into the stability of two prototypical flows of viscoelastic fluids. The first is a set of viscometric, simple shear flows between a rotating cone-and-plate and plate-and-plate geometry. The complexity is derived from the coupled interplay between flow geometry, fluid elasticity and viscous dissipation. The second is a prototypical complex flow containing regions of both strong shear and extension; the axisymmetric abrupt contraction-expansion. The combination of streamwise curvature and elastic normal stresses can lead to flow destabilization [McKinley *et al.* 1996]. These elastic flow transitions have been demonstrated by both experimental measurements and linear stability analyses of many curvilinear flows of viscoelastic fluids [Larson 1992; Shaqfeh 1996]. Each of these flows described above exhibits

streamline curvature and each is therefore prone to flow instabilities as the flow rate is increased and the elastic normal stresses grow.

Torsional shear flows of highly elastic fluids with closed streamlines have the added complexity that they accumulate heat from viscous dissipation. The thermal conductivity of the these polymer solutions is very poor; even if the temperature boundary conditions are isothermal, a nonuniformity in the temperature profile within the flow and nonlinearity in the viscometric properties of the fluid can result from internal viscous heating. It has recently been shown by Al-Mubaiyedh et al. [Al-Mubaiyedh *et al.* 1999] that the inclusion of energetic considerations in the linear stability analysis of viscoelastic Taylor-Couette flow can change the dominant mode of the purely elastic instability from a nonaxisymmetric and time-dependent secondary flow to an axisymmetric stationary Taylor-type toroidal vortex that more closely agrees with the stability characteristics observed experimentally. Elastic effects in the flow are characterized by the Deborah Number, *De*, while the magnitude of the viscous heating is characterized by the Nahme-Griffiths number, *Na*. In Chapter 2, the relative importance of these two competing effects is quantified by a new dimensionless thermoelastic parameter, $\Theta = Na^{1/2}/De$, which is a material property of a given viscoelastic fluid independent of the rate of deformation. The thermoelastic number is a function of the molecular weight of the polymer, the flow geometry and the temperature of the test fluid. By systematically varying any of these parameters, the thermoelastic number can be adjusted over a wide range. In the research presented in Chapter 2, the effect of viscous heating on the torsional steady shearing of several dilute polymer solutions between a rotating cone-and-plate and between two rotating coaxial parallel-plates is investigated experimentally. A better understanding of the effect of nonisothermal temperature fields on the flow and stability of polymeric fluids is critically important to the polymer processing industry.

The dynamical response of polymeric fluids in extension, especially mobile dilute polymer solutions, is quite different than in simple shear. As Denn writes, extensional rheology is a topic of great interest and importance to the polymer community as a whole [Denn 1993; McKinley and Sridhar 2002]. The flow of a viscoelastic fluid through an axisymmetric contraction-expansion is a prototypical complex flow containing regions of strong shearing near the walls, nonhomogeneous uniaxial extension along the centerline upstream of the contraction plane and nonhomogeneous biaxial expansion downstream of the expansion. The contraction flow is a long-standing numerical benchmark for computation of non-Newtonian fluids [Caswell 1996; Hassager 1988] and is the subject of several excellent review articles [Boger 1987; White *et al.* 1987]. To generate physically consistent constitutive models capable of predicting the behavior of these elastic liquids in complex flows, one must first understand the behavior of these elastic fluids in pure extension. With the emergence of the filament stretching rheometer, accurate, repeatable measurements of a fluid's

response to an imposed homogeneous uniaxial extensional flow field are now possible [Anna *et al.* 2001]. The work presented in Chapters 3-6, is intended to constitute a comprehensive set of quantitative experimental measurements to which theory and numerical simulations can be rigorously compared. To meet this goal, an ideal monodisperse, dilute polystyrene Boger fluid is first thoroughly characterized in both shear and extension. This ideal elastic fluid is then used to investigate the kinematics of the flow through several axisymmetric contraction-expansions of different contraction ratios and varying lip curvatures over a wide range of Deborah numbers. The experimental measurements include global pressure drop and local velocity measurements, streak images, and flow induced birefringence measurements of the elastically-enhanced upstream vortex structures.

Previous pressure drop measurements across a 16.4:1:16.4 contraction-expansion using a HPAM solution, show a large extra pressure drop that increases monotonically with Deborah number above the value observed for a similar Newtonian fluid at the same flow rate [Cartalos and Piau 1992]. This enhancement in the pressure drop is not predicted by existing steady-state or transient numerical computations with simple dumbbell models [Szabo 1997]. This extra pressure drop may be the result of an additional dissipative contribution to the polymeric stress arising from a *stress-conformation hysteresis* in the strong non-homogeneous extensional flow near the contraction plane. Such a hysteresis has been independently measured and computed in recent studies of homogeneous transient uniaxial stretching of PS/PS Boger fluids [Doyle *et al.* 1998], however, it is not quantitatively predicted by any current constitutive model. One question this thesis will address is whether quantitative agreement between experimental measurements of both local and global flow field variables and numerical simulations in complex viscoelastic flows can be achieved using an existing bead-spring model. If current constitutive models cannot adequately describe complex viscoelastic flow behavior, then new classes of constitutive equations retaining more detailed microscopic information may be required.

In Chapter 3, the flow of both a Newtonian oligomeric polystyrene and the polystyrene Boger fluid through a 4:1:4 contraction-expansion is experimentally investigated. The kinematics of the flow field are measured through laser Doppler velocimetry, particle image velocimetry and streak images. The stability and flow transitions are characterized using these techniques in conjunction with pressure drop measurements across the different contraction-expansions. In Chapter 4, the effect of contraction ratio on the extra pressure drop and the vortex growth dynamics is investigated. The elastic normal stresses generated in pure shear and transient extensional rheology are employed to rationalize the dependence of the growth of elastic 'lip' and corner vortices on contraction ratio and test fluid. In Chapter 5, the effects of systematic changes in curvature of the re-entrant corner are investigated. Understanding the role of lip curvature is extremely

important because the singular stress fields near a sharp re-entrant corner are a major difficulty for numerical simulations of the flow of a viscoelastic fluid through a contraction-expansion [Caswell 1996]. A simple geometric argument is used to collapse the data from several lip curvatures onto a single master curve. The axisymmetric flow induced birefringence upstream and downstream of the contraction-expansion is presented in Chapter 6. These measurements provide detailed information about the local orientation and deformation of the polymer coil *in situ*. In Chapter 7 non-homogenous transient uniaxial measurements are presented for the polystyrene Boger fluid. The strain rate profile of these measurements performed in the filament stretching rheometer is designed to mimic the strain rate history experienced by a fluid element traveling along the centerline of the axisymmetric contraction-expansion. Stress and birefringence measurements are coupled to investigate the hysteresis generated over a range of Deborah numbers and contraction ratios. This hysteresis, which corresponds to an internal energy dissipation of the polymer coils, is correlated to the extra pressure drop measurements experimentally observed in the flow of viscoelastic fluids through axisymmetric contraction-expansions.

Finally, in Chapter 8 the contributions of this thesis to the understanding of the physical mechanisms governing the flows of elastic liquids are summarized and comments are made on potential future research directions.

CHAPTER 2 Non-Isothermal Modification of Purely Elastic Flow Instabilities in Torsional Flows of Polymeric Fluids

2.1 Introduction

The torsional motion of a fluid between a rotating cone-and-plate and between two rotating coaxial parallel-plates is used extensively in rheometry to measure the material properties that characterize non-Newtonian fluids. For highly elastic fluids, the combination of streamline curvature and large normal stresses in a torsional shear flow results in a streamwise tension which can destabilize the flow [Larson *et al.* 1990; McKinley *et al.* 1996]. Beyond a critical rotation rate, experimental observations and linear stability analyses show that the steady, two-dimensional, torsional shearing motion becomes unstable to a three-dimensional, time-dependent flow of spiral plan-form [Avagliano and Phan-Thien 1996; McKinley *et al.* 1991; Olagunju 1994; Olagunju 1995]. The occurrence of instabilities in the processing of polymer melts and solutions has been understood for many years and has been well documented in reviews by Petrie and Denn [Petrie and Denn 1976] and Larson [Larson 1992] while a detailed review of purely elastic flow instabilities in viscometric flows can be found in Shaqfeh [Shaqfeh 1996]. The present study will focus on the latter class of viscometric motion with closed streamlines in which inertial effects are vanishingly small and the purely elastic instability is strictly a result of the interaction between the viscoelasticity of the fluid and the curvature of the flow streamlines.

In any shear flow with closed streamlines, the test fluid can be exposed to high shear rates over an extended period of time. As a result of the poor thermal conductivity of typical polymeric materials, the accumulating heat from viscous dissipation can have a significant effect on the temperature profile and, hence, on the measured viscometric properties of the fluid. For a fluid undergoing a steady shearing deformation the Nahme number quantifies the relative importance of viscous heating [Bird *et al.* 1987] and is given by

$$Na = \frac{\eta_0 \beta H^2 \dot{\gamma}^2}{kT} , \tag{2-1}$$

where η_0 is the viscosity in the limit of zero shear rate, $H\dot{\gamma} = U$ is the characteristic velocity, k is the thermal conductivity, T is the absolute temperature and β is the thermal sensitivity of the fluid viscosity defined as

$$\beta = \frac{T}{\eta_0}\left(\left|\frac{\mathrm{d}\eta}{\mathrm{d}T}\right|_T\right) . \qquad (2\text{-}2)$$

Recognizing the onset of viscous heating is important in the study of polymer solutions and melts because the thermal sensitivity of the fluid tends to increase monotonically as the molecular weight and the viscosity of the fluid are increased [Winter 1977]. Polymer melts are typically very viscous and in highly elastic dilute polymer solutions, the solvent is often chosen to have a very large viscosity (denoted η_s) in order to increase the relaxation time of the polymer and reduce inertial effects [Boger 1977/78] Therefore, it is to be expected that viscous heating in polymeric fluids may significantly affect the stability of viscoelastic flows. In fact, some of these effects have already been observed. Non-permanent reductions in the measured first normal stress difference after long periods of continuous shearing between a rotating cone-and-plate and parallel-plate under unstable conditions were reported by both MacDonald and Muller [MacDonald and Muller 1997] and Magda and Larson [Magda and Larson 1988]. This long time stabilization of the flow is indicative of the accumulation of energy as a direct result of viscous dissipation, despite careful control of the thermal boundary conditions. Non-isothermal effects on the stability conditions of more complex viscoelastic flows have also been investigated [Yesilata *et al.* 2000] and the possibility of using thermal modulation for optimal control of viscoelastic flow has recently been considered [Kunisch and Marduel 2000]

A number of theoretical studies have investigated the effect of viscous heating on the stability of shear flows. In the linear stability analyses of Newtonian planar Couette flow, viscous stratification induced by temperature gradients resulting from viscous heating was found to destabilize the flow at finite values of the Reynolds number [Ho *et al.* 1977; Yueh and Weng 1996]. However, at zero Reynolds number, the Newtonian plane shear flow was shown to be stable [Yueh and Weng 1996]. The addition of viscoelasticity does not destabilize the inertialess flow because of the poor coupling between the (stable) energy modes and the (stable) eigenmodes of the viscoelastic isothermal shear flow [Becker and McKinley 2000]. Isothermal viscoelastic Taylor-Couette flow, however, is unstable [Larson *et al.* 1990] even at zero Reynolds number because of the addition of streamline curvature. Detailed experimental investigations using a highly viscous polymer solutions have reported the appearance of steady axisymmetric toroidal vortices following the loss of flow stability [Baumert and Muller 1997]. These observations directly contradict the nonaxisymmetric and time-dependent form of the secondary flow predicted by isothermal linear stability analysis [Larson *et*

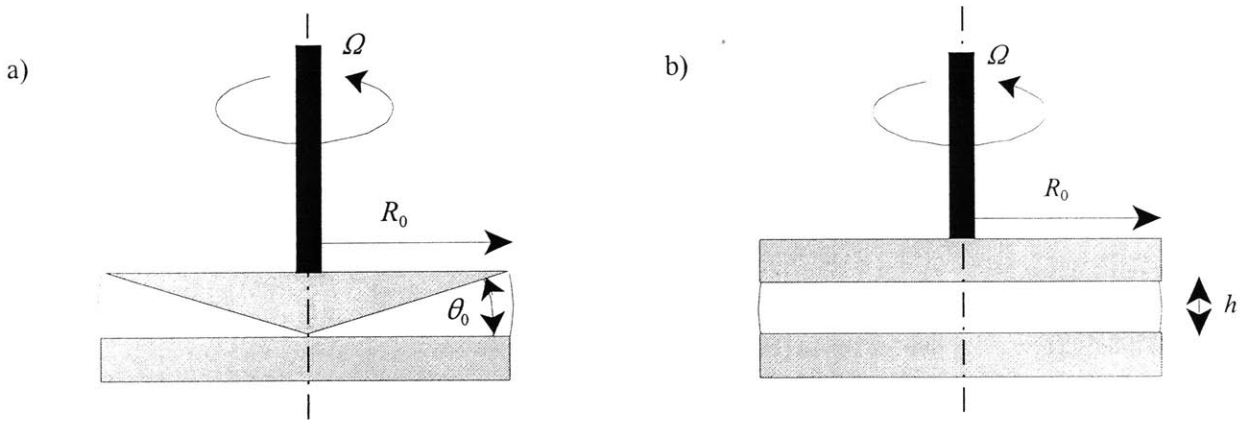

Figure 2-1 Schematic diagram of the cone-and-plate and the parallel-plate geometries.

al. 1990; Shaqfeh 1996]. Furthermore, the critical conditions for the onset of instability can differ by more than an order of magnitude from those observed experimentally [MacDonald and Muller 1997]. Recent work by Al-Mubaiyedh et al. has demonstrated that the form of the secondary flow observed experimentally can be predicted theoretically through inclusion of viscous heating terms in the linear stability analysis of the viscoelastic Taylor-Couette flow [Al-Mubaiyedh *et al.* 1999]. The resulting critical conditions are also much closer to the experimental observations. The effect of viscous heating on the stability boundaries of other torsional shear flows such as the flow between a rotating cone-and-plate and rotating coaxial parallel-plates remain to be investigated. The current work addresses these issues.

Schematic diagrams of the cone-and-plate and parallel-plate geometries are shown in Figure 2-1. In these devices it is possible to alter the flow geometry by varying the radius, R_0, cone angle, θ_0, and gap height separating the test fixtures, h. The corresponding dimensionless parameter characterizing the flow geometry can be written as $\alpha^{pp} = h/R_0$ for the parallel-plate and as $\alpha^{cp} = \theta_0$ for the cone-and-plate configuration. For small $\alpha << 1$, the base flow for each geometry is steady, two-dimensional and leads to measured values of torque, T, and normal thrust, N, which in turn can be used to compute the deformation-rate dependent viscosity, $\eta(\dot{\gamma})$, and the first normal stress coefficient, $\Psi_1(\dot{\gamma})$. As the differential angular velocity, Ω, between the upper and lower plates is increased, experiments have shown that the flow can become unstable. The critical flow conditions for the onset of this instability are typically reported in terms of a critical Deborah number

$$De_{crit} = \lambda \Omega_{crit} , \tag{2-3}$$

where λ is the characteristic relaxation time of the fluid and the characteristic residence time in the flow is equal to the inverse of the angular velocity, Ω. Alternatively, the critical conditions can be reported in terms of a critical Weissenberg number

$$Wi_{crit} = \lambda \dot{\gamma}_{crit} , \tag{2-4}$$

where $\dot{\gamma}_{crit}$ is the critical deformation rate at which the flow becomes unstable. For both test geometries, $\dot{\gamma} = \Omega/\alpha$.

The stability of inertialess viscoelastic flows in cone-and-plate and parallel-plate geometries was first investigated analytically by Phan-Thien [Phan-Thien 1983; Phan-Thien 1985]. Using the von Karmon similarity form for long wavelength disturbances in an Oldroyd-B fluid, Phan-Thien was able to calculate critical Deborah numbers that were, for both cases, dependent only on the ratio of solvent to total viscosity, $S = \eta_s / \eta_0$, although the precise form of the dependence on S for the cone-and-plate geometry was later corrected by Olagunju [Olagunju and Cook 1993]. Soon after, Magda and Larson [Magda and Larson 1988] made the first quantitative experimental investigation of an elastic torsional flow instability. They observed the onset of a time-dependent increase in viscosity and first normal stress difference in tests run in both a cone-and-plate and a parallel-plate rheometer when the shear rate was increased above a critical value. Visual observations of the induced secondary flow by McKinley et al. [McKinley *et al.* 1991] indicated that the flow transition was nonaxisymmetric, over-stable in time and subcritical in shear rate. These observations contradicted the theoretical analysis of Phan-Thien. This discrepancy was later resolved by Olagunju [Olagunju 1995; Olagunju 1997] who showed that the most unstable disturbance is not the long wavelength solution of Phan-Thien, but a short wavelength mode of dimensionless wave number $O(\alpha)$. He went on to show that the critical Deborah number is not simply a function of S, but scales with $\alpha^{1/2}$. A weakly nonlinear stability analysis for the small cone-angle limit of the viscoelastic flow between a cone-and-plate was also performed by Olagunju [Olagunju 1997]. The rheology of the test fluid was found to have a strong influence on the temporal form of the instability. For $S > 0.02$, the flow transition was found to be a subcritical Hopf bifurcation in shear rate whereas in the small solvent viscosity limit, $S \leq 0.02$, the flow transition was found to be supercritical. The results of these analyses are in good agreement with the work of McKinley et al. [McKinley *et al.* 1991; McKinley *et al.* 1995] for the cone-and-plate geometry, but do not agree with the radially localized flow structure experimentally observed in the parallel plate geometry because the analysis fails to include the influence of the free surface and the effect of shear thinning in the

non-homogeneous shearing flow [Byars *et al.* 1994]. The presence of a free surface at the edge of the parallel-plate geometry and the weak secondary flow that it induces were later included by Avagliano and Phan-Thien [Avagliano and Phan-Thien 1996]. The analysis of Avagliano and Phan-Thien improved agreement between theory and experiment and showed that when edge effects were considered the critical Deborah number scaled linearly with the geometric parameter α^{PP}. Using an analytical model equation developed by Olagunju [Olagunju 1997] that is valid in the limit of small gaps, Renardy and Renardy [Renardy and Renardy 1998] were able to closely approximate the two-dimensional numerical results of Avagliano and Phan-Thien [Olagunju 1997; Renardy and Renardy 1998]. The effect of a free surface on the instability in cone-and-plate flow has yet to be investigated. A summary of the predicted forms of the critical conditions given by the theoretical and numerical isothermal linear stability analyses discussed above can be found in Table 2-1.

Contributor	Description of work	Parallel-Plate Result	Cone-and-Plate Result
Phan-Thien (1983; 85)	• Oldroyd-B/ UCM • Similarity solution	$De_{crit} = \frac{\pi}{\sqrt{(1-S)(1-2S)}}$	$De_{crit} = \pi\sqrt{\frac{2}{(1-S)(1-2S)}}$
Olagunju (1994; 95)	• Oldroyd-B/ UCM • Short wavelength solution	$De_{crit} = 4.604\, f(S)\, \alpha^{1/2}$ $f(S) \sim S^{-1/2}$ for $S \to 1$	$De_{crit} = 4.604\, f(S)\, \theta_0^{1/2}$ $f(S) \sim S^{-1/2}$ for $S \to 1$
Avagliano & Phan-Thien (1996) Renardy & Renardy (1998)	• Oldroyd-B/ UCM • Short wavelength solution • Finite edge effects	$De_{crit} = K_1 + \alpha K_2$ $K_1 \approx 0 \to 2$ $K \approx 5 \to 10$	?

Table 2-1 Summary of analytical and numerical solutions to the isothermal cone-and-plate and parallel-plate linear stability problem. Note that $Wi = De / \alpha$ with $\alpha^{PP} = h / R_0$ and $\alpha^{CP} = \theta_0$.

The primary objective of the present experimental work will be to systematically characterize the effect of viscous heating and the resulting non-isothermal fluid temperature profiles on the onset conditions of purely elastic torsional flow instabilities. We have chosen the cone-and-plate and parallel-plate geometries because they allow for precise temperature control of the boundary, sensitive shear stress and first normal stress difference measurements and the flexibility to easily make significant changes in the

dimensionless geometric parameter α.

The isothermal stability analyses presented in Table 2-1 suggest that the stability boundary can be represented on a two-dimensional plot of the Deborah number against the dimensionless geometric parameter. Such diagrams have been presented in previous publications [McKinley *et al.* 1991; McKinley *et al.* 1995; McKinley *et al.* 1996; Shaqfeh 1996]. Incorporating the effects of viscous heating leads to the study of the stability boundary off of this plane. However, the proper dimensionless group to represent this third dimension is unclear. We explore possible three-dimensional representations of the stability diagram in Section 2.2.1 and introduce a dimensionless thermoelastic parameter, Θ, characterizing viscous heating in a polymeric fluid. In Section 2.2.2 we briefly summarize the rheological characteristics of our test fluids and the actual values of the thermoelastic parameter for the dilute polystyrene solutions used in these experiments. In Section 2.3 we first compare our experimental results for flow within a cone-and-plate and parallel-plate rheometer to isothermal linear stability analyses. The effect of viscous heating on the purely elastic flow instability is then demonstrated through experiments performed over a wide range of temperatures. Finally, in Section 2.4 we present our conclusions.

2.2 Experimental

2.2.1 *Stability Diagrams for Non-Isothermal Viscoelastic Flows*

By non-dimensionalizing the governing partial differential equations for momentum and energy, one can identify the timescales that characterize non-isothermal polymeric flows. These values are tabulated in Table 2-2 and include the timescales for thermal and viscous diffusion, the polymeric timescale for stress relaxation and the timescale for viscous heating. These timescales can be used to construct two types of dimensionless groups; (i) dynamical ratios which use the convective time as the characteristic scale and thus have values that depend on the shear rate and (ii) intrinsic or material ratios which are independent of kinematics. This table suggests that a self consistent set of dimensionless groups to use when considering the stability of viscoelastic flows are the Weissenberg number, which is a direct measure of the flow strength, in conjunction with the elasticity number, E, and thermoelastic number, Θ, which measure the intrinsic importance of the additional non-linearities arising from inertia and/or viscous heating. Baumert and Muller [Baumert and Muller 1997] have reported extensively on the effect of varying the elasticity number on the stability boundaries of viscoelastic Taylor-Couette flow by preparing a set of fluids with differing solvent viscosities. Al-Mubaiyedh et al [Al-Mubaiyedh *et al.* 1999] report their results in terms of a Péclet number (which will always be very large since $Pr >> 1$ for all polymer melts and organic solutions) and a Brinkman

number $Br = Na/\beta$ (which is always very small because $\beta >> 1$). To our knowledge no one has yet experimentally investigated the importance of the thermoelastic number, which may be of O(1) for elastic fluids undergoing a rapid shearing deformation. Systematic investigation of thermoelastic effects can be performed by preparing a set of viscoelastic fluids of different viscosities and/or relaxation times (by varying the molecular weight of the polymer or the viscosity of the solvent) and then conducting tests while varying the flow geometry and ambient temperature.

Timescale	**Dimensionless Group (Scaled with $t_{conv} = \dot{\gamma}^{-1}$)**		**Typical Value (Melts / Boger Fluids)**
① $t_{thermal} = \dfrac{\rho C_p H^2}{k}$	Péclet number	$Pé = \dfrac{\rho C_p H^2 \dot{\gamma}}{k}$	>> 1
② $t_{diffusion} = \dfrac{\rho H^2}{\eta_0}$	Reynolds number	$e = \dfrac{\rho H^2 \dot{\gamma}}{\eta_0}$	<< 1
③ $t_{polymer} = \lambda$	Weissenberg number	$Wi = \lambda\dot{\gamma}$	~ O(1)
④ $t_{heat} = \sqrt{\dfrac{\eta_0 H^2 \beta}{}}$	Nahme number	$Na = \dfrac{\eta_0 H^2 \beta \dot{\gamma}^2}{kT}$	~ O(1)
Natural Ratios (Material functions independent of kinematics)			
$\dfrac{①}{②} = \dfrac{t_{thermal}}{t_{diffusion}} =$ Prandtl number, $Pr = \dfrac{\eta_0 C_p}{k} >> 1$			
$\dfrac{③}{②} = \dfrac{t_{polymer}}{t_{diffusion}} =$ elasticity number, $E = \dfrac{\lambda \eta_0}{\rho H^2} >> 1$			
$\dfrac{④}{③} = \dfrac{t_{heat}}{t_{polymer}\alpha} =$ thermoelastic number, $\Theta = \dfrac{H}{\lambda\alpha}\sqrt{\dfrac{\eta_0 \beta}{kT}} \sim$ O(1)			

Table 2-2 Governing timescales of non-isothermal polymeric flows. Note that the characteristic length scale $H = h$ for parallel-plate geometries and $H = \theta_0 R$ for cone-and-plate geometries. The timescale for viscoelastic stress relaxation is indicated generically by λ; however in reality a polymeric fluid is characterized by a spectrum of time scales. A number of different average measures may therefore be used (see text and Equations 2-11 to 2-16 for details).

The combined effect of these variations on the thermoelastic number on the stability boundary for a typical elastic flow instability is shown graphically in Figure 2-2. Here we select the Deborah number as a measure of the elastic effects and the Nahme number as a measure of the importance of viscous heating. When flow stability experiments are performed with a given fluid in a fixed flow geometry by slowly incrementing the deformation rate, $\dot{\gamma}$, the slope of the trajectory in this three-dimensional space is given by the thermoelastic parameter

$$\Theta = \frac{\sqrt{Na}}{De} = \frac{R_0}{\lambda(T,M_w)} \sqrt{\frac{\eta_0(T,M_w)\beta(T)}{kT}} \quad . \tag{2-5}$$

For very low values of the thermoelastic parameter, $\Theta << 1$, (corresponding ideally to fluids of low viscosity and high relaxation time) the stability boundary is expected to collapse to the form given in Table 2-1.

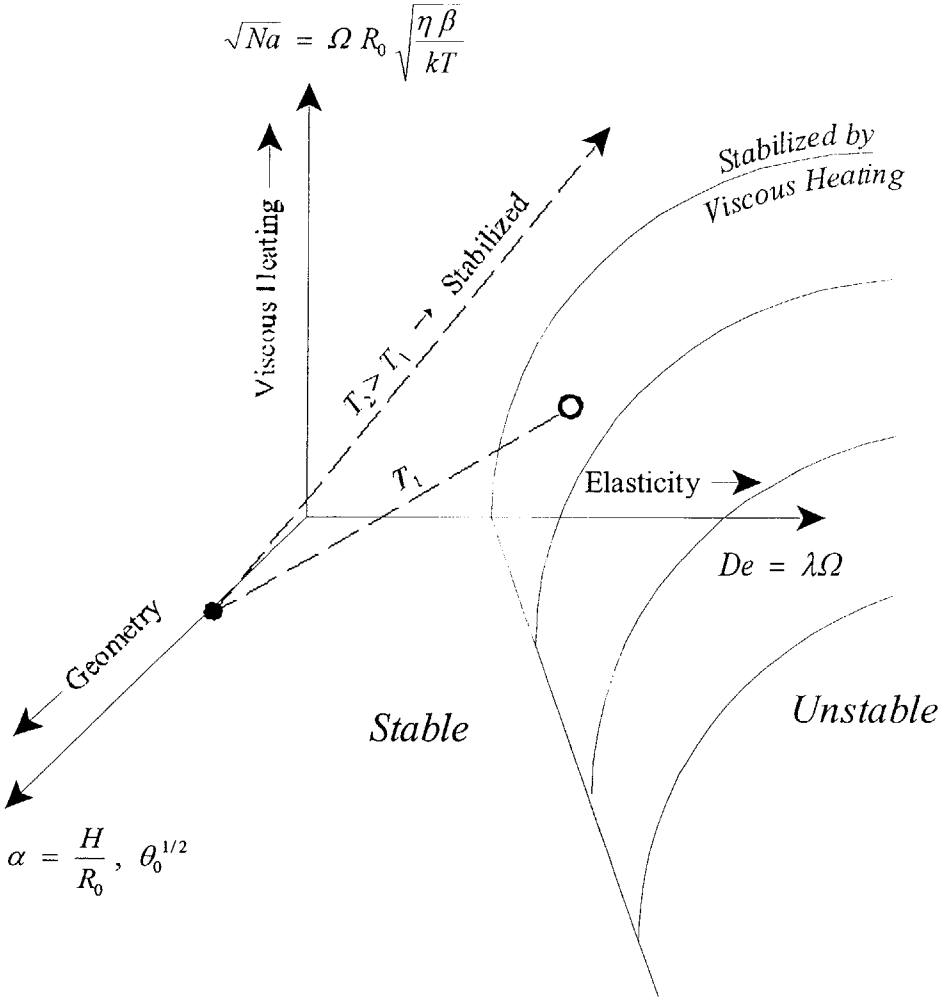

Figure 2-2 Three-dimensional schematic stability diagram for a typical viscoelastic fluid.

However, quite generally, we expect that when the two timescales are of comparable magnitude, viscous heating will affect the critical conditions for onset of the elastic instability.

For dilute polymer solutions, the Rouse-Zimm kinetic theory model predicts that the viscosity and the relaxation time are differing functions of the molecular weight [Bird *et al.* 1987; Gupta *et al.* 2000]. For example, in the non-free draining limit the Zimm model predicts that the polymeric contribution to the viscosity scales as $\eta_p \propto c\eta_s M_w^{1/2}/k_B T$ and $\lambda \propto M_w$ where c is the concentration, M_w is the molecular weight of the chain and k_B is Boltzmann's constant. Thus, decreasing the molecular weight of the polymer will increase the relative importance of viscous heating. The geometry can also be adjusted to alter the extent of viscous heating at a given Deborah number, but the flexibility for geometric variation is quite limited for standard test fixtures because the analytical form of the base flow assumes $\alpha << 1$.

Another alternative, and the avenue down which we have proceeded, is to vary the experimental test temperature, T. As the temperature is increased, the thermoelastic number increases and the critical Deborah number for the onset of the purely elastic instability occurs at progressively larger Nahme numbers. At these large Nahme numbers viscous heating will delay or even completely suppress the onset of the instability. This is indicated schematically in Figure 2-2, but it may not be clear from a cursory inspection of Equation 2-5. For amorphous viscoelastic materials, Time-Temperature Superposition (TTS) can be used to characterize the temperature dependence of the material properties of the fluid [Bird *et al.* 1987; Ferry 1980]. The viscosity and relaxation time can be explicitly determined at a temperature, T, in terms of a time-temperature shift factor and the known material properties at a reference temperature, T_0, by

$$a_T(T,T_0) = \frac{\eta_0(T)}{\eta_0(T_0)} = \frac{\lambda(T)\,T}{\lambda(T_0)\,T_0} \,. \tag{2-6}$$

A common functional form for the shift factor is given by the Arrhenius relationship

$$a_T = \exp\left[\frac{\Delta H}{\bar{R}}\left(\frac{1}{T} - \frac{1}{T_0}\right)\right], \tag{2-7}$$

where ΔH is known as the "activation energy for flow" [Bird *et al.* 1987], $\bar{R}$ is the universal gas constant and T_0 is the reference temperature. For this form, the thermal sensitivity β of the material given in Equation 2-2 is given by

$$\beta = \frac{\Delta H}{\bar{R} T} . \tag{2-8}$$

Substituting back into Equation 2-5, the thermoelastic number becomes

$$\Theta = \frac{R_0}{\lambda(T_0) T_0} \sqrt{\frac{\Delta H}{k\bar{R}} \frac{1}{a_T}} \sim \sqrt{\frac{1}{a_T}} . \tag{2-9}$$

Since the shift factor $a_T < 1$ for temperatures $T > T_0$, there is a monotonic increase in the thermoelastic number with increasing temperature. This can be seen clearly by taking the ratio of the value of the thermoelastic numbers for a given fluid and test geometry at any two temperatures:

$$\frac{\Theta(T_{test})}{\Theta(T_0)} = \sqrt{\frac{a_{T_0}}{a_{T_{test}}}} = \exp\left[\frac{\Delta H}{2\bar{R}} \left(\frac{1}{T_0} - \frac{1}{T_{test}} \right) \right] . \tag{2-10}$$

As the test temperature is decreased from the reference temperature, the thermoelastic number will decrease and the relative importance of viscous heating compared to elastic effects in the fluid will diminish.

2.2.2 *Fluid Rheology*

Two different test fluids are used in these experiments in order to investigate the effects of fluid rheology and thermophysical properties on the elastic flow instability. These viscoelastic fluids consist of a 0.05 wt% solution of monodisperse polystyrene (PS) (Scientific Polymer Products, Inc.) with a polydispersities of 1.03 and 1.2 and mass-average molecular weights of 6.5×10^6 g/mol (SM2) and 2.0×10^7 g/mol (SM3) respectively. In each case, the polystyrene is dissolved in oligomeric styrene (Hercules Piccolastic) with a molecular weight of $M_w \sim 500$g/mol. The resulting solutions fall into a class of fluids first described in detail by Boger and coworkers [Boger 1977/78] which are highly elastic with an almost constant viscosity. The large viscosities and long relaxation times of these fluids eliminate inertial effects and permit the study of viscoelastic flows at high Deborah numbers.

These two test fluids were initially prepared by Professor Susan J. Muller as part of an interlaboratory comparison of filament stretching rheometers. Detailed analysis of the steady and transient

shear and extensional rheology is presented elsewhere [Anna *et al.* 2001]. The rheological properties of importance to the present study of elastic flow instabilities will be briefly summarized here and are tabulated in Table 2-3.

Figure 2-3 shows a master curve of the rheological properties for fluid SM2 at $T_0 = 25\,^{\circ}\mathrm{C}$, measured with a controlled stress device (TA Instruments, Model AR1000N). A similar master curve can be generated

	Notation	Description	Parameter Value	
			SM2	SM3
Known:	c	Concentration of High Molecular Weight Polystyrene	0.05%	0.05%
	M_w/M_n	Polydispersity	1.03	1.2
	M_w	Molecular Weight [g/mol]	6.5×10^6	2.0×10^7
	$b = L^2$	Extensibility Parameter	25000	76700
	T_0	Reference Temperature [K]	298	298
Fitted:	η_0	Zero Shear Rate Viscosity [Pa·s]	46.1	55.5
	η_s	Solvent Viscosity [Pa·s]	34.0	34.0
	λ_{ps}	Solvent Relaxation Time [s]	2.7×10^{-4}	2.7×10^{-4}
	h^*	Hydrodynamic Interaction Parameter	0.15	0.18
	σ_{BD}	Extent of Anisotropy in Stokes' Law	0.59	0.79
	β_{BD}	Extent of Anisotropy in Brownian Motion Forces	1.0	1.0
Calculated:	λ_z	Zimm (Longest) Relaxation Time [s]	32.1	155
	$\overline{\lambda}$	Oldroyd Relaxation Time [s]	17.7	81.7
	Ψ_{10}	First Normal Stress Coefficient [Pa·s^2]	428	3510

Table 2-3 Parameters characterizing the viscometric properties of the dilute polystyrene solutions denoted SM2 and SM3.

for fluid SM3. The viscoelastic properties of the fluid are characterized in small amplitude oscillatory shear flow by the dynamic viscosity $\eta'(\omega)$ and the dynamic rigidity $2\eta''(\omega)/\omega \equiv 2G'(\omega)/\omega^2$ which are both functions of the frequency of oscillation. The linear viscoelastic properties are well described by the Rouse-Zimm bead-spring kinetic theory for dilute solutions [Zimm 1956] as indicated by the solid lines in Figure 2-3. Over an intermediate range of frequencies, $1/\lambda_z << \omega << 1/\lambda_{ps}$ the slope of the dynamic rigidity allows an approximate determination of the hydrodynamic interaction parameter [Larson 1988], h^*, which plays a large role in determining the spectrum of relaxation times [Bird *et al.* 1987] given by

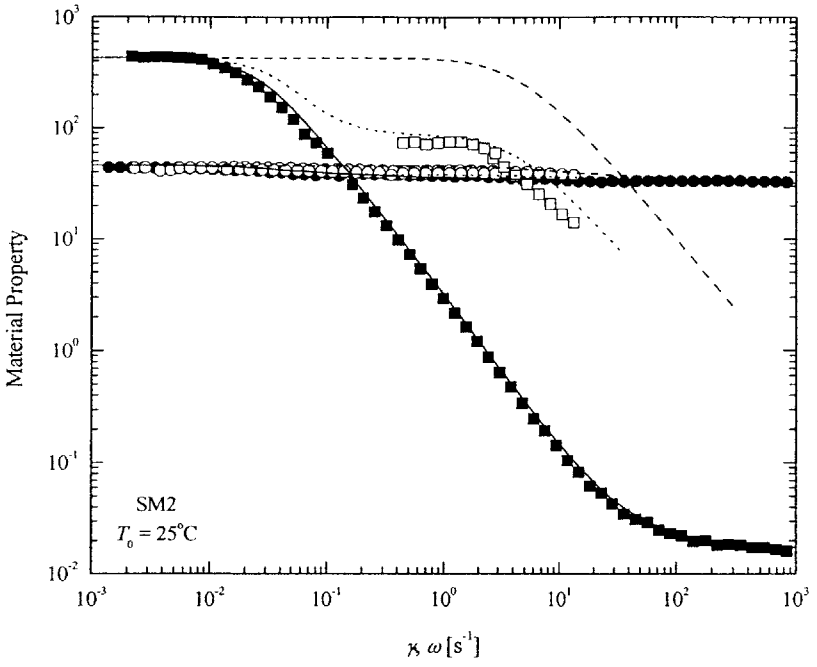

Figure 2-3 Rheological material functions of the SM2 fluid. The data includes: '○', steady shear viscosity $\eta(\gamma)$ [Pa·s]; '●', dynamic viscosity $\eta'(\omega)$ [Pa·s]; '■', dynamic rigidity $2\eta''(\omega)/\omega$ [Pa·s^2]; '□', first normal stress coefficient $\Psi_1(\gamma)$ [Pa·s^2]; and the corresponding Bird-Deaguiar, FENE-P and Rouse-Zimm model fits plotted as dotted lines '- - -', dashed lines '– –' and solid lines '—' respectively.

$$\lambda_j = \lambda_z j^{-(2+\sigma)} , \tag{2-11}$$

where $\sigma \approx -1.40\ (h^*)^{0.78}$. The linear viscoelastic modulii can then be conveniently expressed in the following compact form

$$\begin{aligned} G' &= \frac{c\bar{R}T}{M_w} \sum_{j=1}^{N_m} \frac{(\lambda_z\omega)^2}{j^{2(2+\sigma)} + (\lambda_z\omega)^2} + \frac{\eta_s}{\lambda_{ps}} \frac{(\lambda_{ps}\omega)^2}{1 + (\lambda_{ps}\omega)^2} , \\ G'' &= \frac{c\bar{R}T}{M_w} \sum_{j=1}^{N_m} \frac{\lambda_z\omega\, j^{2+\sigma}}{j^{2(2+\sigma)} + (\lambda_z\omega)^2} + \frac{\eta_s\omega}{1 + (\lambda_{ps}\omega)^2} , \end{aligned} \tag{2-12}$$

where N_m is the number of modes used to fit the linear viscoelastic data. In the limit $h^* = 0$, the free-draining Rouse model incorporates no hydrodynamic interaction and $2\eta''/\omega \sim \omega^{-3/2}$, whereas in the Zimm (non-free-

draining) limit $h^* \approx 0.25$ and $2\eta''/\omega \sim \omega^{-4/3}$. At low frequencies ($\omega \leq 0.01$ rad/s), the fluid is essentially Newtonian with a constant viscosity $\eta_0 = \sum j^{-(2+\sigma)} c \bar{R} T \lambda_z / M_w + \eta_s$. However, at high frequencies ($\omega \geq 1000$ rad/s), the predictions of the Zimm model deviate from the experimental measurements due to the small but finite elasticity of the oligomeric solvent. This additional elasticity can be modeled by an extra Maxwell element for the solvent (the final term in Equations 12 and 13) with a relaxation time $\lambda_{ps} \approx 2.7 \times 10^{-4}$ s which is in good agreement with the range of values reported by Mackay and Boger [Mackay and Boger 1987]. Table 2-3 lists the parameters used to compute the material properties for both fluids.

In steady shear flow, the viscometric properties of the fluids are characterized by the first normal stress coefficient $\Psi_1(\dot{\gamma}) = (\tau_{11}(\dot{\gamma}) - \tau_{22}(\dot{\gamma}))/\dot{\gamma}^2$ and viscosity $\eta(\dot{\gamma})$, each of which are functions of the shear rate. As shown in Figure 2-3, the viscosity of the solution is approximately constant over several decades of shear rate. The fluid is strongly elastic and the first normal stress coefficient shear-thins monotonically throughout the entire range over which data can be obtained. By contrast, the Rouse-Zimm bead-spring model predicts a constant value of the first normal stress coefficient as a consequence of the pre-averaging of hydrodynamic interactions [Ottinger 1987]. The dashed lines in Figure 2-3 represent the predictions of a single-mode FENE-P model for the steady shear data. The value of the extensibility parameter, L^2, is derived from molecular quantities for both fluids and can be found in Table 2-3. This value is consistent with measurements of the transient extensional viscosity [Anna *et al.* 2001], but clearly leads to an overprediction of the steady shear properties. An improved description requires a more detailed treatment of hydrodynamic interactions between segments of a polymer chain undergoing a steady shearing deformation. One such model that accounts for the anisotropy in the hydrodynamic drag forces in approximate form is the encapsulated dumbbell model of Bird and DeAguiar [Bird and DeAguiar 1983]. The dotted lines in Figure 2-3 represent the predictions of a single mode Bird-DeAguiar model fit and are in good agreement with both the viscosity and first normal stress difference measurements of the SM2 fluid. The Bird-DeAguiar model contains two parameters, σ_{BD} and β_{BD}, which specify the extent of anisotropy in the viscous drag on the beads and in the velocity distribution arising from anisotropic Brownian motion, respectively. When $\sigma_{BD} = \beta_{BD} = 1$, the FENE-P model is recovered. Our exploratory calculations suggest that to quantitatively describe the viscometric properties of dilute polymer solutions in viscous solvents, the anisotropy in the viscous drag is the primary effect of importance. The Brownian motion of the beads can thus be assumed to be isotropic with $\beta = 1$. To determine the proper values of σ_{BD}, the Bird-DeAguiar model was fit to the viscometric properties of the two fluids by minimizes the mean square error between the predicted and computed values of both $\eta(\dot{\gamma})$ and $\Psi_1(\dot{\gamma})$. The results of these fits can be found in Table 2-3.

When defining a Deborah number for reporting the experimental measurements of the critical rotation rate for the onset of the purely elastic instability, a representative measure of the spectrum of relaxation times of the fluid must be chosen. The simplest choice for this fluid time scale is the longest or Zimm relaxation time, λ_z, determined from the linear viscoelastic measurements and tabulated in Table 2-3. An alternative measure commonly used is the 'average' or Oldroyd relaxation time which is a viscosity weighted average of the relaxation spectrum

$$\bar{\lambda} = \frac{\Psi_{10}}{2\eta_{p,0}} = \frac{\sum_{j=1}^{N_m} \eta_j \lambda_j}{\sum_{j=1}^{N_m} \lambda_j} . \tag{2-14}$$

For the Rouse-Zimm spectrum in which the time constant and viscosity of each relaxation mode is related to the longest mode by a simple recursion relation this becomes

$$\bar{\lambda} = \frac{\sum_{j=1}^{N_m} j^{-2(2+\sigma)}}{\sum_{j=1}^{N_m} j^{-(2+\sigma)}} \lambda_z . \tag{2-15}$$

Theoretical stability analyses [Al-Mubaiyedh *et al.* 2000; Larson *et al.* 1994] and scaling arguments show that both the longest and the average value of the relaxation spectrum are important in determining the critical conditions for flow stability

Even though the shear viscosities of these dilute solutions do not have a strong rate dependence, Figure 2-3 demonstrates that, at the shear rates investigated in this research, the first normal stress coefficient shear thins quite heavily. This initial onset of shear thinning is primarily the result of hydrodynamic interaction while more drastic shear thinning at higher shear rates can be attributed to, amongst other effects, the finite extensibility of the polymer chain. The true relaxation time of the fluid, which can be calculated from the viscometric properties of the fluid previously determined, is thus a strong function of shear rate [McKinley *et al.* 1991]

$$\lambda(\dot{\gamma}) \equiv \frac{\Psi_1(\dot{\gamma})}{2\eta_p(\dot{\gamma})} . \tag{2-16}$$

It has been found in a number of studies of viscoelastic flow instabilities that to achieve quantitative

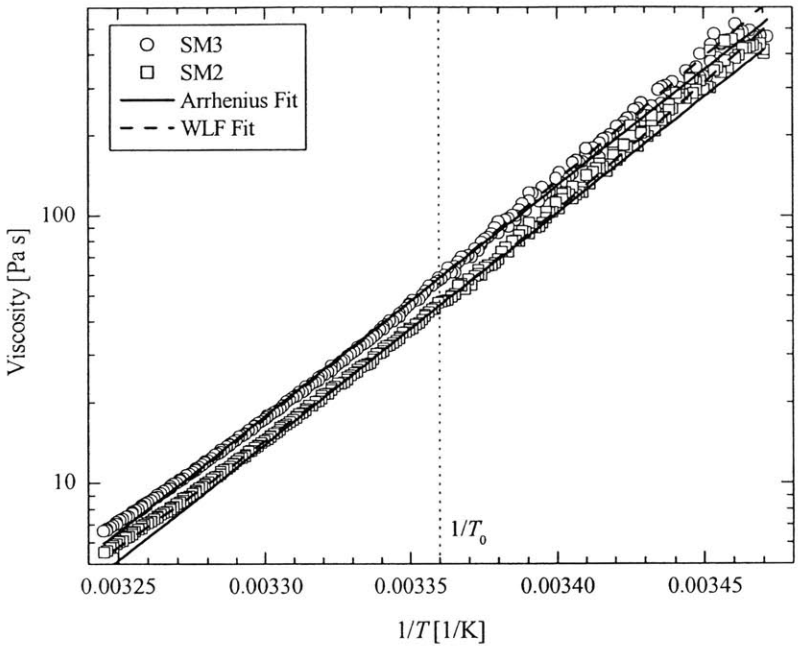

Figure 2-4 Steady shear viscosity $\eta(\dot{\gamma})$ as a function of fluid temperature. The data includes: '○', SM3 test fluid; '□', SM2 test fluid; and the corresponding WLF and Arrhenius model fits plotted as dashed lines '– –' and solid lines '—' respectively.

agreement with theoretical predictions it is necessary to use this shear-rate-dependent relaxation time when calculating the effective value of the critical Deborah number for the onset of elastic instabilities [Avagliano and Phan-Thien 1996; Larson *et al.* 1994; McKinley *et al.* 1996; Oztekin and Brown 1993]. The disadvantage of this approach is that the precise functional form of Equation 2-16 becomes model-dependent. Therefore, for convenience and clarity the average relaxation time evaluated in the limit of zero shear rate, $\bar{\lambda}$, will be used for reporting critical Deborah numbers unless explicitly indicated otherwise.

The viscoelastic properties of the test fluids will also change as the temperature of the experiments is varied. In order to compare tests performed at different temperatures, it is necessary to adjust the relaxation time, normal stress difference and viscosity to their values at a reference temperature of $T_0 = 25\,^{\circ}\mathrm{C}$. This is accomplished by employing time-temperature superposition with a shift factor $a_T(T, T_0)$ defined in Equation 2-6. In this paper we will use the Williams-Landel-Ferry (WLF) equation to specify the functional form of $a_T(T, T_0)$ as it has been found to accurately describe the thermorheological behavior of a wide variety of polymer solutions and melts [Ferry 1980]. However, we will also present results for the Arrhenius

formulation of $a_T(T, T_0)$ because of its simplicity and widespread use in previous analyses of flow stability [Al-Mubaiyedh, 1999 #143; Yueh, 1996 #154; Becker, 2000 #155]. The WLF equation has the form [Bird *et al.* 1987]

$$\log a_T = \frac{-c_1(T - T_0)}{c_2 + (T - T_0)}, \tag{2-17}$$

where c_1 and c_2 are constants to be determined. Figure 2-4 demonstrates how the viscosity of the SM2 and SM3 test fluids changes as the temperature is raised from 15 °C to 40 °C. Over the span of 25 °C the zero shear rate viscosity decreases by a factor of one hundred. Superimposed on these data are fits of the Arrhenius and WLF models for each fluid. The values of the constants used to fit the temperature dependence of the fluid viscosity of both SM2 and SM3 can be found in Table 2-4. When represented on a semilogarithmic scales of viscosity as a function of 1/T, the Arrhenius equation (Equation 2-7) predicts a linear relationship that accurately describes the experimental measurements close to the reference temperature T_0. However, the data in Figure 2-4 show clear nonlinear trends for large values of $|T - T_0|$ which are better described by the WLF model. For temperatures close to T_0, linearizing the WLF equation (Equation 2-17) suggests $\beta(T_0) = \Delta H/\overline{R}\,T_0 \approx c_1 T_0/c_2$. Both the WLF and Arrhenius models predict a thermal sensitivity of $\beta \approx 68$ for both SM2 and SM3. By contrast, the thermal sensitivity is $\beta \approx 20$ for a typical PIB Boger fluid [Arigo 1999].

Notation	Description of Parameter	Value of Parameter	
		SM2	SM3
c_1	WLF Constant	20.1	36.9
c_2	WLF Constant [K]	90.4	160
$\Delta H/$	Arrhenius Constant [K]	20200	19900

Table 2-4 Parameters used to describe temperature dependence of SM2 and SM3 polystyrene solutions with a reference temperature $T_0 = 298$K.

The density, thermal conductivity and heat capacity of fluid SM2 and SM3 can be found in Table 2-5 and are assumed to be identical to the thermophysical properties of the oligomeric solvent. Additionally, the properties of both fluids are assumed to be constant over the range of temperatures at which they are tested in this study.

Notation	Description of Parameter	Value of Parameter	
		SM2	SM3
ρ	Density [kg/m^3]	997	997
k	Thermal Conductivity [W/m·K]	0.11	0.11
C_p	Heat Capacity [J/kg·K]	2.04×10^3	2.04×10^3
α	Thermal Diffusivity [m^2/s]	5.4×10^{-8}	5.4×10^{-8}

Table 2-5 Thermophysical properties of SM2 and SM3 polystyrene solutions.

2.3 Experimental Results

Our goal is to construct an experimental stability diagram such as the one shown in Figure 2-2. We first investigate the horizontal (α, *De*) plane by using the SM3 fluid to perform essentially isothermal experiments all of which have a thermoelastic number smaller than $\Theta \leq 10^{-2}$.

2.3.1 *Comparison with Isothermal Theory*

The experiments were performed using a controlled stress rheometer (TA Instruments, AR1000N) capable of torque and normal force measurement as well as precise temperature control of the bottom plate using a Peltier device. Each measurement was performed using a fresh sample of Boger fluid. After carefully loading the rheometer, the fluid was allowed to reach thermal and structural equilibrium at a test temperature T before the testing commenced. A constant torque, T, was then applied to the upper fixture. The shear stress acting on the fluid is given by $\tau^{CP} = 3T/2\pi R_0^3$ for the homogeneous shear flow in the cone-and-plate geometry. For the non-homogeneous torsional flow in the parallel-plate geometry we report results in terms of the rim shear rate $\dot{\gamma}^{PP}(r = R_0) = \Omega R_0/h$ and the shear stress at the rim $\tau^{PP}(r = R_0) = T/\pi R_0^3$. The resulting experimentally measured shear rate was averaged over the course of one relaxation time, λ_2, and then compared with subsequent averages until the values were within a ±1 percent tolerance for two consecutive averages. The fluid was allowed to equilibrate over a maximum period of ten relaxation times at which point the applied torque was incremented and the fluid was again allowed to reach equilibrium. This protocol was established to insure that at each test point the fluid microstructure had reached equilibrium. By using a controlled stress device, it is possible to follow the complete flow curve corresponding to the steady two-dimensional base flow and the three-dimensional, time-dependent flow which bifurcates subcritically in the shear rate [Magda and Larson 1988; McKinley *et al.* 1991; Olagunju 1995]. The shear rate is a single valued function of stress and with careful experimentation it is possible to accurately determine the linear neutral stability condition by identifying the shear rate at which the slope,

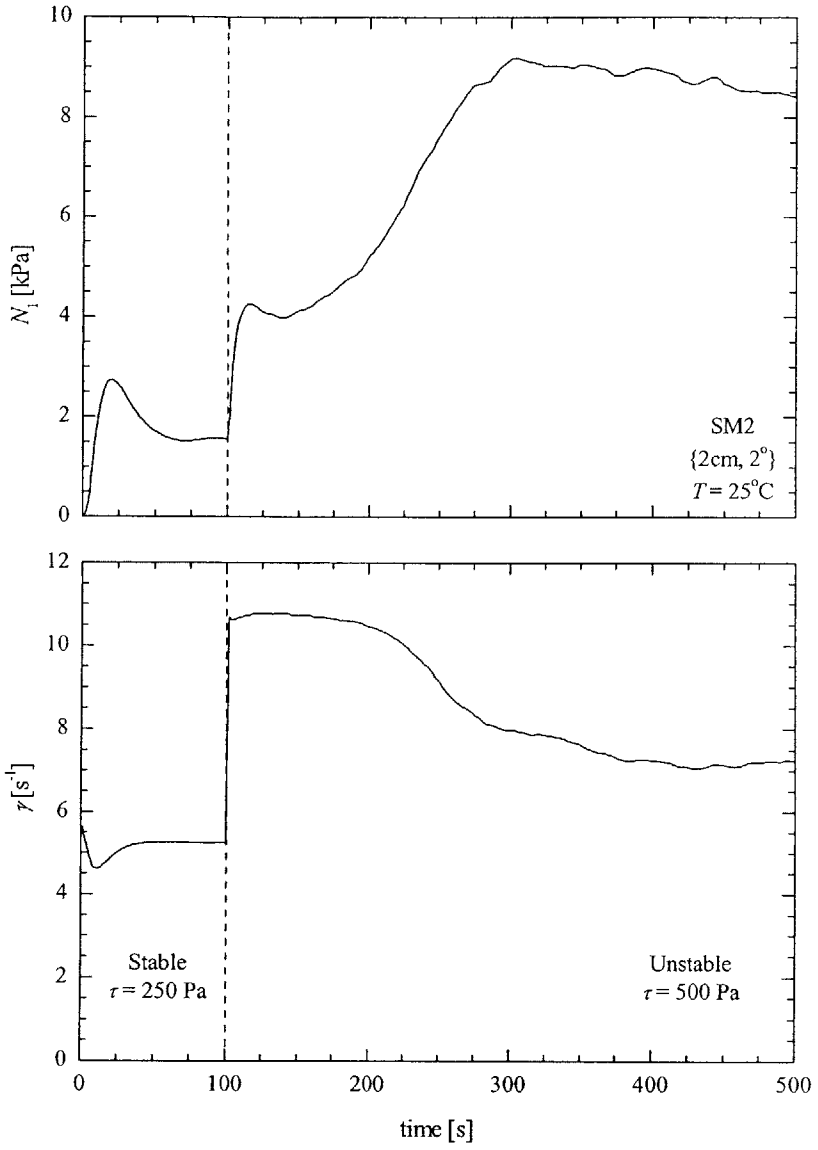

Figure 2-5 Transient first normal stress difference and shear rate measurements of the flow between a rotating {2cm, 2°}cone-and-plate geometry with the SM2 fluid at 25°C taken at constant applied shear stresses of 250Pa and 500Pa.

$d\dot{\gamma}/d\tau$, changes sign.

The time dependent nature of the purely elastic flow instability is demonstrated in Figure 2-5. A constant shear stress is applied to the SM2 test fluid between a rotating cone-and-plate with $\{R_0, \theta_0\}$ = {2cm, 2°} at a temperature of T = 25°C and the resulting shear rate, $\dot{\gamma}$, and first normal stress

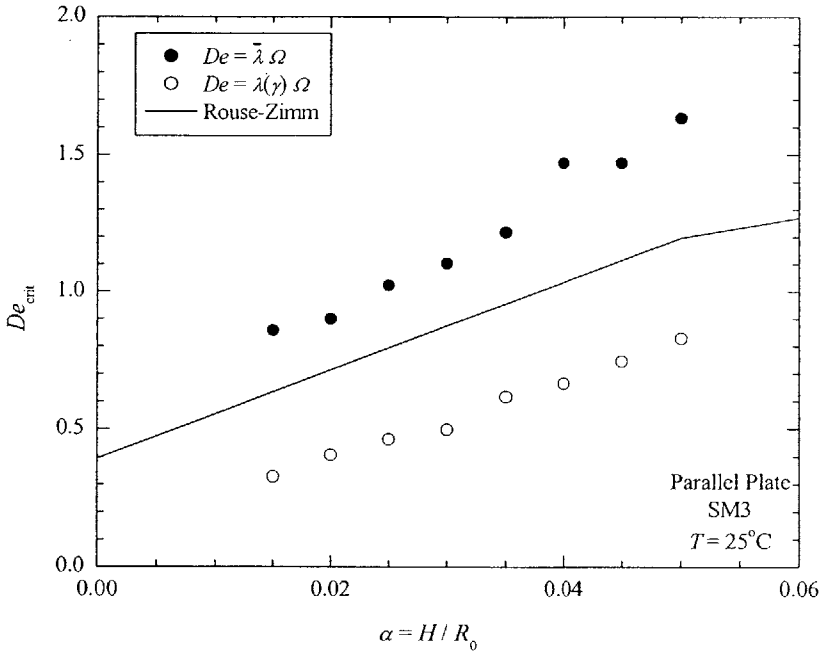

Figure 2-6 Effect of aspect ratio on the critical Deborah number for the onset of the purely elastic flow instability between a rotating parallel-plate for the SM3 test fluid at 25 °C.

difference, N_1, are observed over time. At a shear stress of τ = 250 Pa (t < 100s), the flow is stable, exhibiting an initial overshoot and then becoming steady in time. After 100 seconds, the shear stress is increased to a value of τ = 500 Pa. Subsequent measurements of normal stress and shear rate deviate sharply from the expected equilibrium values and do not reach a steady state, but instead demonstrate the time-dependent behavior and apparent antithixotropy seen in previous studies [Magda and Larson 1988; McKinley *et al.* 1991]. The duration of this experiment was chosen to be much larger than both the polymer relaxation time ($\lambda_z \cong$32s) and the timescale for thermal diffusion is ($t_{thermal} \cong$9s) to insure that kinematic and thermal equilibrium were achieved. A more detailed discussion of the importance of test protocol can be found in Section 2.3.3.

In Figure 2-6, the experimental results for the SM3 Boger fluids at very low Nahme number, $Na \leq 10^{-3}$, are compared with the multimode isothermal linear stability analysis of Avagliano and Phan-Thien [Avagliano and Phan-Thien 1999]. The experimentally observed critical Deborah number is presented both as the product of the angular frequency and the average relaxation time, $\bar{\lambda}$, evaluated in the limit of zero shear rate and as the product of the angular rotation rate and the shear-rate-dependent relaxation time, $\lambda(\dot{\gamma})$.

As noted in Table 2-1, when the free surface effects in the parallel-plate geometry are considered at small aspect ratios, the linear stability theory predicts that the critical Deborah number for the onset of the elastic instability should have a linear dependence on aspect ratio [Avagliano and Phan-Thien 1996; Avagliano and Phan-Thien 1999]. Through very careful experimental techniques, McKinley et al. [McKinley *et al.* 1991] were able to very closely approach the linear neutral stability condition and minimize the amplitude of the disturbance, which for a subcritical Hopf bifurcation must be finite. In fact, both Öztekin et al. [Oztekin *et al.* 1994] and Avagliano and Phan-Thien [Avagliano and Phan-Thien 1999] were able to quantitatively match their linear stability analysis predictions to the experimental neutral stability data of McKinley et al. [McKinley *et al.* 1991]. The solid line in Figure 2-6 is the linear stability analysis provided by Dr. Avagliano for the multimode Rouse-Zimm spectrum of fluid SM3. Although, neither value of the critical Deborah number quantitatively matches the theory over the entire range of aspect ratios tested, both measures demonstrate the predicted linear dependence on aspect ratio. The stability locus for the multimode model was calculated using the approximation proposed by McKinley et al. [McKinley *et al.* 1996]

$$\left(\frac{De_{\text{multimode}}}{De_{\text{single mode}}} \right)_{\text{crit}} \approx \left[\frac{\sum_{j=1}^{n} \frac{\lambda_j U}{R_c} \frac{\tau_{11j}}{\eta_0 \dot{\gamma}}}{\frac{\lambda_s U}{R_c} \frac{\tau_{11}}{\eta_0 \dot{\gamma}}} \right]^{1/2}, \tag{2-18}$$

where U is the local velocity along a streamline of curvature radius R_c. The tensile stress along the streamline for each mode is τ_{11j} and the local shear rate is $\dot{\gamma}$. Calculations show that this equation allows one to estimate the results for the analysis of any multimode spectrum from the results of a single mode analysis to within ten percent of the true value [Avagliano and Phan-Thien 1999]. For torsional flows in the parallel plate geometry, Equation 2-18 can be simplified by substituting $U = r\Omega$, $R_c = r$, $\tau_{11j} = 2c\,\bar{R}\,T\lambda_j^2\dot{\gamma}_j^2 / M_w$ and $\dot{\gamma} = \Omega/\alpha$ to yield

$$\left(\frac{De_{\text{multimode}}}{De_{\text{single mode}}} \right)_{\text{crit}} \approx \frac{\lambda_{\text{rms}}}{\bar{\lambda}}, \tag{2-19}$$

where

$$\lambda_{\text{rms}} = \left(\frac{\sum_{j=1}^{N_m} \eta_j \lambda_j^2}{\sum_{j=1}^{N_m} \eta_j} \right)^{1/2} . \qquad (2\text{-}20)$$

The predictions of the isothermal linear stability analysis for flow in a rotating cone-and-plate have also been compared against experimentally-determined critical conditions for both the SM2 and SM3 fluids in other geometries with $\{R_0, \theta_0\} = \{3\text{cm}, 1°\}$, $\{2\text{cm}, 2°\}$and $\{1\text{cm}, 4°\}$. These tests were performed at low temperatures and vanishingly small Nahme numbers, $Na \leq 10^{-3}$. The results of these tests can be found in Figure 2-7. The experimental and theoretical critical Deborah numbers are presented as the product of the critical angular frequency and the average or Oldroyd relaxation time evaluated in the limit of zero shear rate, $De = \bar{\lambda}\Omega$. The predictions of the FENE-PM and the Bird-DeAguiar models, computed using the scaling approach discussed by McKinley et al., [McKinley *et al.* 1996]. are presented along with the Rouse-Zimm multimode analysis. Recalling the results of the linear stability theory of Olagunju [Olagunju 1997] presented in Table 2-1, one expects the critical Deborah number for the onset of the elastic instability to scale with the square root of the cone angle and to appear as a straight line in Figure 2-7. As one quickly observes, this is only true for the shear-rate-independent Rouse-Zimm model. The modifications to the multimode FENE-PM curve, the Bird-DeAguiar curve and the experimental data at small cone angles are the result of the shear-rate-dependence of the viscometric properties caused by the polymer's finite extensibility [McKinley *et al.* 1991] and hydrodynamic interactions [Bird and DeAguiar 1983]. For very small cone angles, the shear rate at the onset of instability is very high and the true relaxation time of the fluid is much smaller than the Oldroyd relaxation time used in formulation of the Deborah number. For example, choosing a moderately large cone angle of $\theta_0^{1/2} = 0.5$ ($\cong 14°$), which for the SM2 fluid and the Rouse-Zimm model corresponds to a critical Deborah number of $De_{\text{crit}} = 2.08$, results in critical shear rate of $\dot{\gamma}_{crit} = De_{crit} / (\theta_0 \lambda_{SM2}) = 0.47\,\text{s}^{-1}$. It is clear from Figure 2-3 that an appreciable decrease in the fluid elasticity has already occurred at this shear rate. A quantitative agreement can only be achieved when evaluating the critical Deborah number with the (constant) average relaxation time, $\bar{\lambda}$, provided the constitutive model accurately represents the viscometric properties of the fluid. This requirement can be

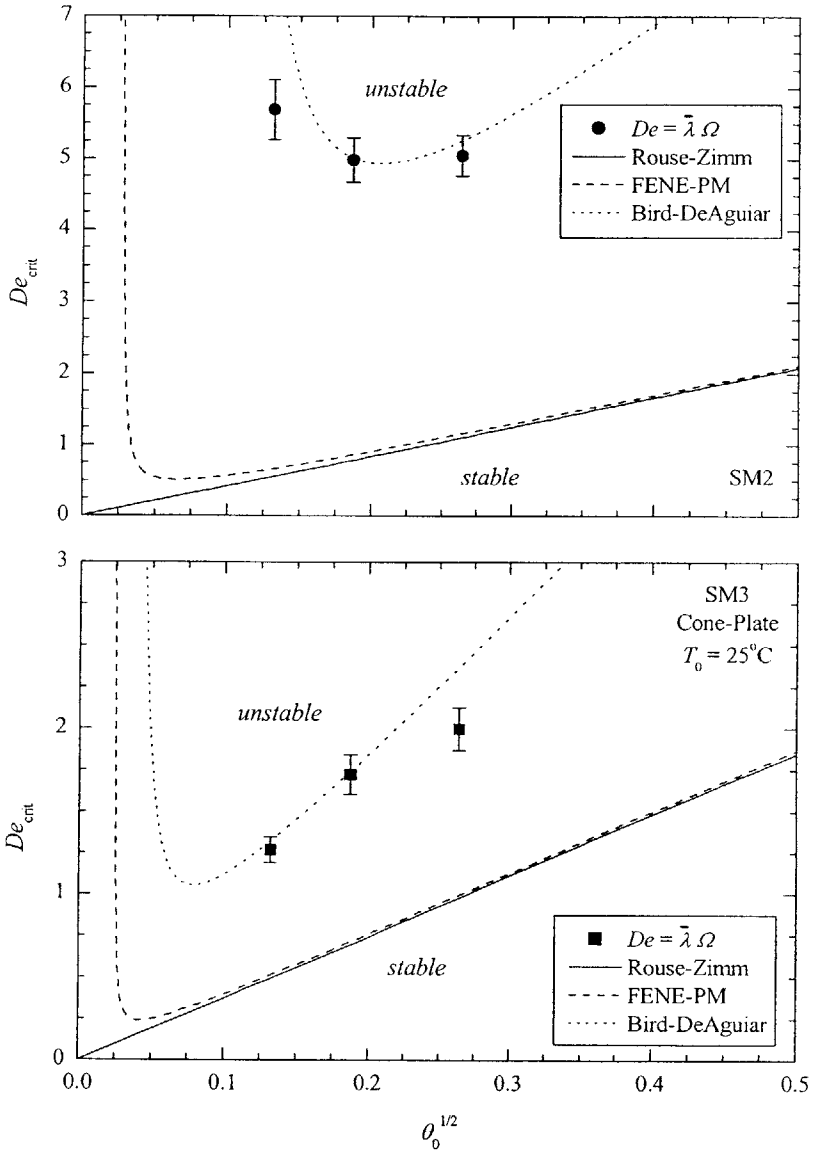

Figure 2-7 Effect of cone angle on the critical Deborah number for the onset of the purely elastic flow instability between a rotating cone-and-plate for the a) SM2 and b) SM3 test fluids.

clearly seen in Figure 2-7 by examining the two broken lines which represent the stability boundaries for the FENE-PM and Bird-DeAguiar models. The FENE-PM model qualitatively captures the onset of shear-thinning in $\Psi_1(\dot{\gamma})$ at very high shear rates (low cone angles) but seriously overpredicts the fluid elasticity at intermediate shear rates as shown in Figure 2-3. By contrast, the Bird-DeAguiar model captures, at least

semi-quantitatively, the decrease in $\Psi_1(\dot{\gamma})$ arising from hydrodynamic interactions and much more accurately predicts the observed stability boundaries.

Although it cannot be seen in Figure 2-7, at low enough shear rates (high enough cone angles), the Bird-DeAguiar model does asymptotically approach the Rouse-Zimm stability curve. Without continuing the abscissa of Figure 2-7 to large cone angles, we can easily validate this statement by inspecting the viscometric data presented in Figure 2-3. The Bird-DeAguiar model satisfies simple fluid theory and so, in the limit of low shear rates, the rate-dependent relaxation time of the model will become constant and equal to the rate-independent relaxation time of the Rouse-Zimm model. However, at these rates ($\dot{\gamma} \leq 10^{-2} s^{-1}$) the cone angles required ($\theta_0 \geq 170$ rad) would be completely unphysical.

If the shear-rate-dependent relaxation time is used in the formulation of the critical Deborah number, $De = \lambda(\dot{\gamma})\Omega$, instead of the Oldroyd relaxation time, all three models will follow the same square root dependence on cone angle as the shear-rate-independent Rouse-Zimm model in Figure 2-7. If the experimental measurements of the critical rotation rate are also reported as a critical value of the shear-rate-dependent Deborah number (using Equation 2-16 to compute the relaxation time), quantitative agreement with all three of the models can be obtained. This lends additional credence to the use of the shear-rate-dependent relaxation time when comparing experiments with linear stability theory [Avagliano and Phan-Thien 1996; McKinley *et al.* 1996; Oztekin and Brown 1993] and is the only way to accurately fit the neutral stability data if the viscometric data of the viscoelastic test fluid cannot be accurately modeled by the chosen constitutive equation.

2.3.2 *Non-isothermal Modifications to Stability of Elastic Torsional Flow*

If Equation 2-9 is evaluated for fluid SM2 in the {2cm, 2°} cone-and-plate geometry, the thermoelastic number becomes

$$\Theta_{SM2} = \frac{1}{\sqrt{a_T}} \frac{R_0}{\bar{\lambda}(T_0)} \sqrt{\frac{\eta_0(T_0)\beta(T_0)}{kT_0}} = \frac{0.011}{\sqrt{a_T}} . \qquad (2\text{-}21)$$

For temperatures greater than the reference temperature $T > T_0$, the shift factor is smaller than one and the thermoelastic number Θ will increase. We show below that when the thermoelastic number is equal to $\Theta \approx 0.061$ ($T \approx 43\,^{\circ}C$), viscous heating results in significant modifications to the flow stability curves. For temperatures less than the reference temperature $T < T_0$, the shift factor $a_T > 1$ and the thermoelastic number decreases, lowering the slope of the trajectory followed by experiments in the three-dimensional space shown

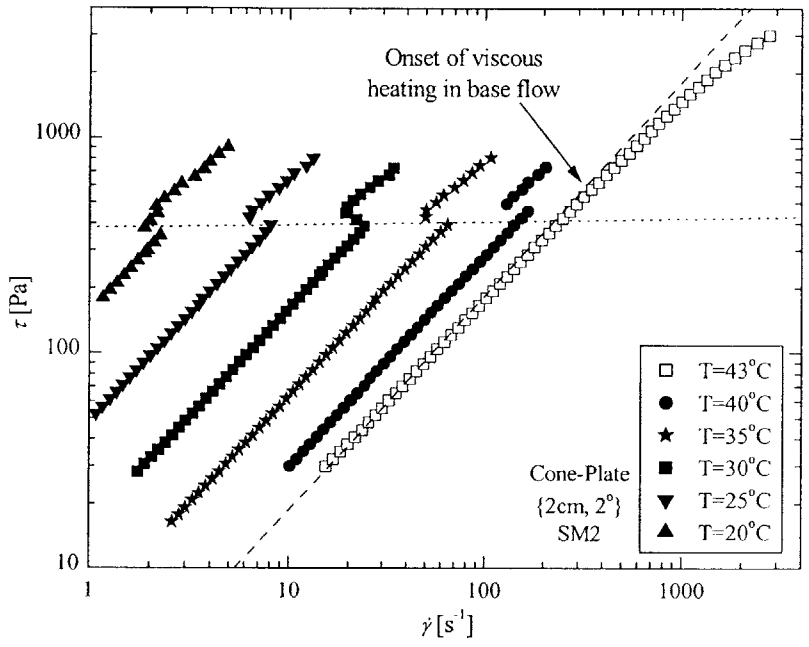

Figure 2-8 Onset of an elastic flow instability as observed in shear stress sweeps of the SM2 test fluid at various temperatures using the {2cm, 2°} cone-and-plate geometry.

in Figure 2-2.

Similar calculations of the thermoelastic number for fluids SM3 and SM1 described by Anna et al. [Anna *et al.* 2001] show that $\Theta_{SM3} = 0.0024\, a_T^{-1/2}$ and $\Theta_{SM1} = 0.092\, a_T^{-1/2}$. Viscous heating is therefore not important until temperatures of $T \approx 70\,°C$ for fluid SM3 while it is important for all temperatures greater than $T \gtrsim 10\,°C$ for fluid SM1. Indeed, experiments with fluid SM1 showed no elastic instability for any temperatures or shear rates studied. Fluid SM2 was thus chosen for the non-isothermal tests described below because its thermophysical properties allow for excellent control of the purely elastic instability at reasonable temperatures and cone angles.

Using the same testing protocol outlined in the previous section, the effect of viscous heating was systematically examined by performing torque sweeps on the SM2 fluid in the cone-and-plate geometry over a wide range of temperatures $15\,°C \leq T \leq 50\,°C$. In Figure 2-8, we show the form of the flow transition for fluid SM2 using a cone-and-plate geometry with $\{R_0, \theta_0\} = \{2\text{cm}, 2°\}$. As observed by Magda and Larson [Magda and Larson 1988] and by McKinley et al., [McKinley *et al.* 1991] the instability is subcritical in shear rate. At a temperature of 43 °C, a strong deviation in the shear stress from a linear dependence on shear

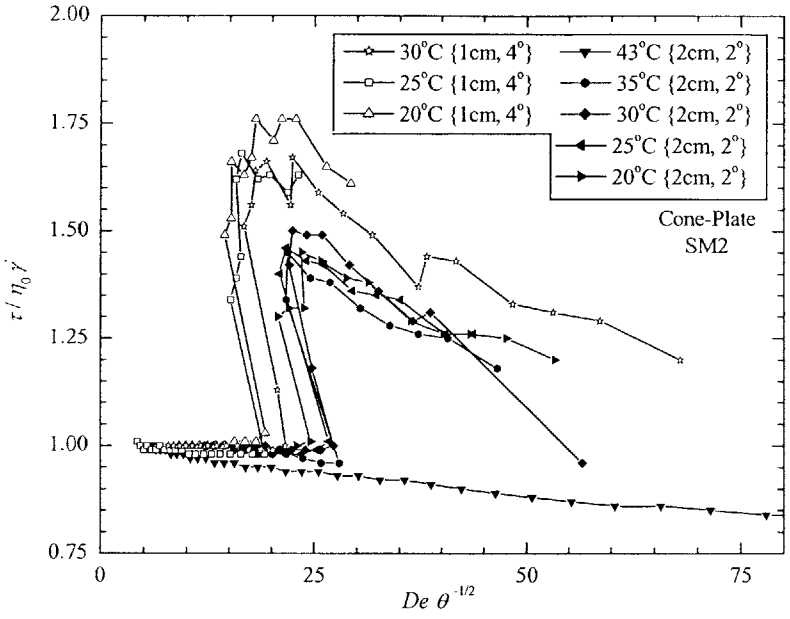

Figure 2-9 Normalized shear stress as a function of the linear stability control parameter $De\theta^{-1/2}$.

rate indicates the onset of viscous heating in the sample. Simultaneous measurement of the first normal stress difference shows that there is an even more dramatic loss of elasticity, as is shown in Figure 2-11. The result is a drastic reduction in the shear-rate-dependent relaxation time and, consequently, a failure to reach the critical conditions for the onset of the elastic instability.

In the isothermal linear stability theory, the critical Deborah number for the onset of the purely elastic flow instability is determined to be a constant, independent of temperature (see Table 2-1). When represented in terms of dimensional parameters, time-temperature superposition of the material properties leads to a linear dependence of the critical flow conditions on the test temperature. If the stability theory is expressed in terms of a critical shear stress one obtains

$$\tau_{crit} \equiv \eta \dot{\gamma}_{crit} = \frac{\eta}{\bar{\lambda}} \left(\frac{\bar{\lambda} \Omega_{crit}}{\theta_0} \right) . \qquad (2\text{-}22)$$

Substituting Equation 2-6 into Equation 2-22 one finds that the critical shear stress varies linearly with temperature

$$\tau_{crit}(T) = \tau_{crit}(T_0)\frac{T}{T_0}, \qquad (2\text{-}23)$$

where $\tau_{crit}(T_0)$ is the critical stress for the onset of instability at the reference temperature, T_0. The dotted line in Figure 2-8 represents the prediction of Equation 2-23 for the critical shear stress. This decoupled isothermal approximation correctly predicts the weak modulation in the critical conditions for onset of instability at low thermoelastic numbers, but does not take into account the strong coupling that arises at large thermoelastic numbers.

The data in Figure 2-8 can be collapsed by plotting the measured shear stress non-dimensionalized by the shear stress expected for the steady base flow, $\eta_0\dot{\gamma}$, against the control parameter expected from the linear stability theory, $De/\theta_0^{1/2}$. [Olagunju 1997]. In Figure 2-9 we plot the stability data for both the {1cm, 4°} and the {2cm, 2°} cone-and-plate geometries for the SM2 fluid over a wide range of temperatures. Although the data from the two cone angles do not superimpose exactly, the general agreement is very good. If the shear-rate-dependent relaxation time is used in the formulation of the Deborah number, the results for different cone angles would very nearly superimpose. The data show that increasing the temperature of the test fluid, and thus the Nahme number, delays the onset of the purely elastic flow instability, but has little effect on the amplitude of the fully developed time-dependent non-linear state until the thermoelastic number approaches its critical value. At that point, the instability is completely suppressed by viscous heating. This transition happens over a very small range of temperatures ($37\,°C \le T \le 43\,°C$) and we now proceed to study this region in more detail.

To highlight the effect of viscous heating on the base flow, in Figure 2-10 we show the progressive variation in the dimensionless timescale for viscous heating, $t_{heat} = Na^{1/2}\dot{\gamma}$, against the dimensionless viscoelastic timescale, De, for fluid SM2 in the {2cm, 2°} cone-and-plate rheometer as the deformation rate is increased. The filled symbols in Figure 2-10 represent steady two-dimensional flow while hollow symbols represent the unstable regime. A dashed line denoting the neutral stability curve has been superimposed on the data. At very low Nahme numbers, viscous heating is not significant and the resulting delay in the onset of the elastic instability, although clearly evident, is quite small and in agreement with Equation 2-23. At a temperature of 40°C, viscous heating begins to strongly stabilize the flow, shifting the onset of the instability upwards to a Deborah number that is 15% above the value obtained at low Nahme number. When

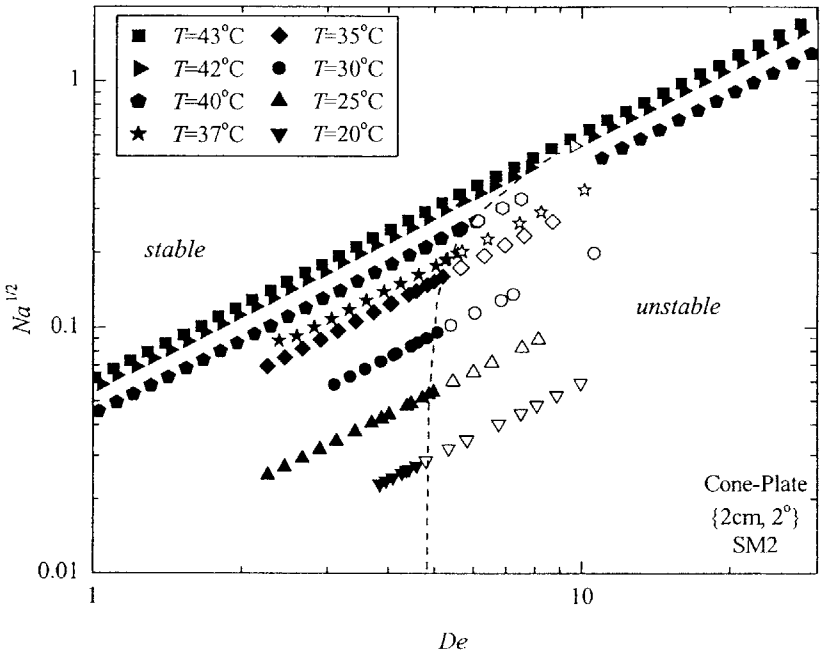

Figure 2-10 Stability diagram for the flow between a rotating {2cm, 2°} cone-and-plate geometry. As the Deborah number is increased, the flow goes from stable flow conditions represented by filled symbols '●' to unstable flow conditions represented by hollow symbols '○'. The dashed line '--' is a fit of the neutral stability curve of the form $Na_{crit} = \mathrm{K}(De_{crit} - De_{crit,0})$.

the temperature is increased still further to 43°C, the flow becomes stable at all shear rates. At this temperature, the critical thermoelastic number is $\Theta_{crit} = 0.061$ corresponding to $a^{1/2} = 0.45$ and $De_{crit} = 7.3$. In order to obtain quantitative agreement with the results of linear stability analyses it is necessary to report values of critical conditions in terms of the shear-rate-dependent relaxation time, $\lambda(\dot{\gamma})$, rather than the average relaxation time, $\overline{\lambda}$. If the fluid properties (in particular the fluid relaxation time) are allowed to vary with shear rate, the critical thermoelastic number increases by more than an order of magnitude to a value very close to one $\Theta_{crit}(\dot{\gamma}) = 0.92$.

In Figure 2-11, the critical Nahme number is plotted against the critical Deborah number for the onset of the elastic instability. When the data are plotted in this way, the critical Deborah number appears to vary as

$$Na_{crit} = K\left(De_{crit} - De_{crit,0}\right). \tag{2-24}$$

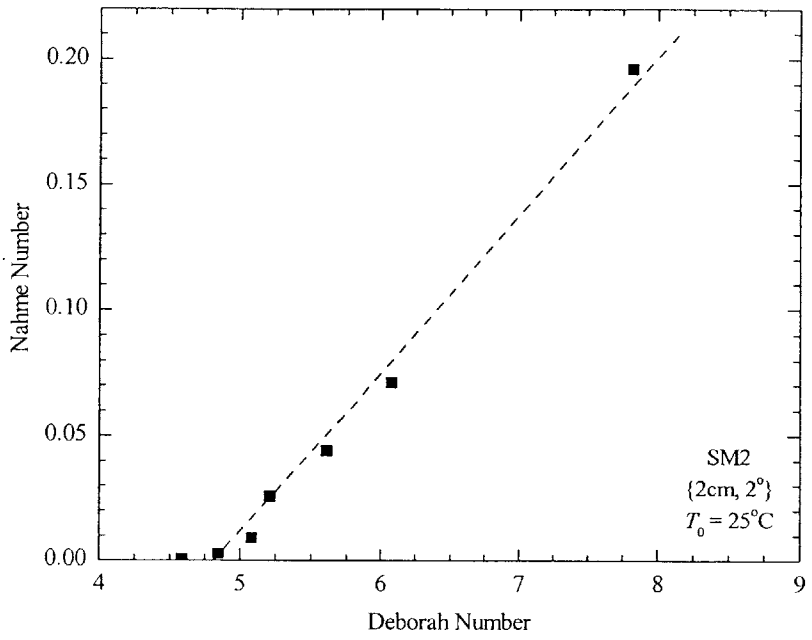

Figure 2-11 Neutral stability points '■' for the flow between a rotating {2cm, 2°} cone-and-plate geometry. The dashed line '--' is a fit of the form $Na_{crit} = K(De_{crit} - De_{crit,0})$.

where $De_{crit,0}$ is the isothermal critical Deborah number and K = 0.063 is a constant. A neutral stability curve of this form has also been superimposed over the data in Figure 2-10 and fits quite well.

The Nahme number and the Deborah number cannot be varied independently, but are related by the thermoelastic number, $\Theta = Na^{1/2}/De$, which is a constant for each experiment, independent of shear rate. A better way to express Equation 2-24 is thus in terms of the critical Deborah number and the thermoelastic number

$$De_{crit} = \frac{K}{2\Theta^2}\left(1 - \sqrt{1 - \frac{4De_{crit,0}\Theta^2}{K}}\right). \tag{2-25}$$

In the limit of small thermoelastic number, $\Theta << 1$, Equation 2-25 reduces to the isothermal critical condition. However, if the thermoelastic number of the experiment is greater than $\Theta > 1/2\sqrt{K / De_{crit,0}}$, the critical Deborah number defined by Equation 2-25 is undefined. In this limit, an experimental shear rate

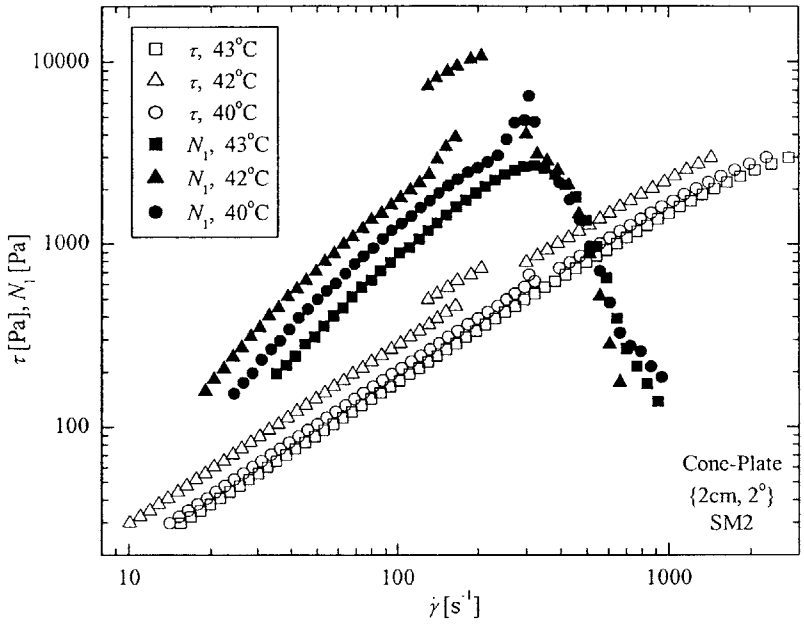

Figure 2-12 Viscometric properties for flow of SM2 fluid between a rotating {2cm, 2°} cone-and-plate geometry at three temperatures showing the effect of viscous heating on the purely elastic flow instability.

ramp, which traverses a line of constant thermoelastic number, will not intersect the neutral stability curve and the flow is found to be stabilized by viscous dissipation.. By fitting the neutral stability data to Equation 2-24, the critical thermoelastic number is predicted to be $\Theta_{crit} = 0.057$ which corresponds to a wall temperature of $T_{crit} = 42.2\,°C$.

The coupling of viscous heating effects and onset of flow instability is also manifested in a profound way in the normal stress data. We show in Figure 2-12 the shear stress and first normal stress difference as a function of shear rate for torque sweeps performed with the {2cm, 2°} cone-and-plate rheometer on the SM2 fluid for temperatures of 40 °C, 42 °C and 43 °C. As the temperature is increased from 40 °C to 43 °C, the magnitude and duration of the elastic instability is diminished while the onset is delayed to a larger critical Deborah number by viscous heating. The onset of viscous heating is characterized by a sharp decrease in the first normal stress difference and is differentiable from simple shear-thinning by the non-monotonic nature of the curves. This can be seen most clearly in measurements of the shear stress and first normal stress difference taken at 43 °C. At low shear rates $\dot{\gamma} \lesssim 60\ s^{-1}$ (Na ≈ 0.008), the viscometric data is consistent with the predictions of the Rouse-Zimm and Bird-DeAguiar models. A maximum in the shear

stress corresponding to a "thermal blow-up" is reached at a shear rate of $\dot{\gamma} \approx 2700\ s^{-1}$ ($Na \approx 12$). In a controlled stress experiment, no steady values of shear rate above this maximum shear stress are attainable [Arigo 1999]. The first normal stress difference also goes through a local maximum, but at a much lower shear rate $\dot{\gamma} \approx 320\ s^{-1}$ ($Na \approx 0.17$). This degradation of fluid elasticity results in the complete suppression of the elastic flow instability. In the experiments at 40°C and 42°C, the flow becomes unstable before viscous heating can begin to significantly degrade the elasticity. However, the instability is quickly suppressed after a critical value of Nahme number $Na_{crit} \approx 0.23$ is reached. The shear stress does begin to show noticeable nonlinear effects at these moderate shear rates, but the normal stress is clearly a much better indicator of viscous heating. These viscous heating trends are in excellent agreement with recent measurements of similar polystyrene and polyisobutylene-based Boger fluids performed by Arigo [Arigo 1999]

2.3.3 *Effect of Test Protocol on Stability Observations*

Since there are a number of important timescales characterizing different physical processes in the fluid (see Table 1), the choice of experimental test protocol and the associated observation window can have

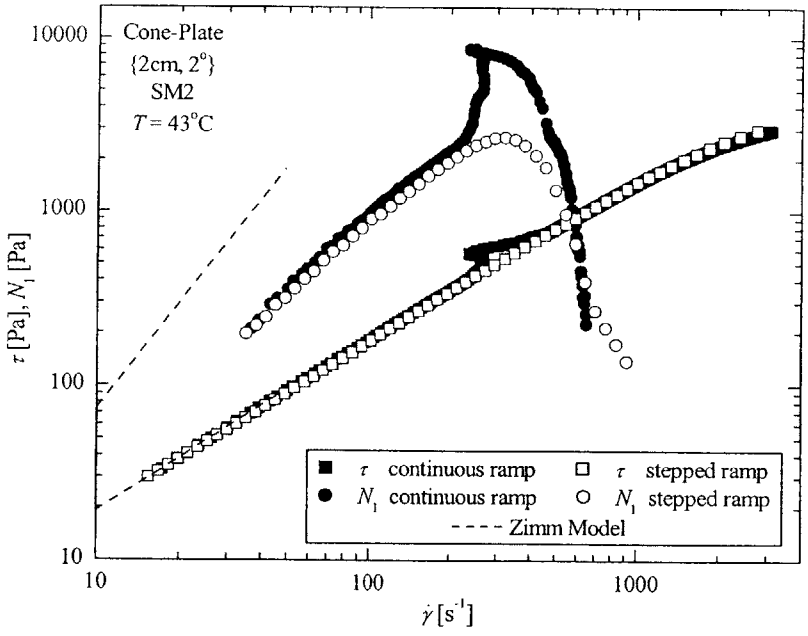

Figure 2-13 Viscometric properties for flow of SM2 fluid between a rotating {2cm, 2°} cone-and-plate geometry at $T = 40°C$ showing the effect of test protocol. The predictions of the Rouse-Zimm bead spring model are plotted as dashed lines '– –' for low shear rates.

a significant impact on the observed results of the experiments. Theoretical stability analysis [Al-Mubaiyedh *et al.* 1999; Becker and McKinley 2000] of non-isothermal viscoelastic flows assume that the base flow on to which perturbations are imposed is steady and fully developed. For the cone-and-plate geometries the timescale for thermal diffusion is 5s $\lesssim t_{thermal} \lesssim$ 10s (depending on cone geometry) and the timescale for the stress to reach steady state is $\lambda_z(T_0)$ = 31.1 seconds. If the experiment ramps in torque are imposed too quickly, then the fluid may not be able to reach thermal or structural equilibrium, resulting in the observation of a pseudo-steady-state which is in fact dependent on the speed at which one probes the material. The issue of structural equilibrium is most pertinent at low temperatures where the relaxation time is much longer than the timescale for thermal diffusion. Ramping the torque too quickly at low temperatures will result in observation of a critical Deborah number much higher than expected because the fluid stresses will not be fully developed. At higher temperatures, the relaxation time, $\lambda(T) = \lambda_z(T_0)/a_T$, decreases rapidly and it is the thermal diffusion time which becomes important.

When both scales are important, very complex dynamics may ensue. In Figure 2-13, we show measurements of the SM2 fluid in a cone-and-plate geometry with $\{R_0, \theta_0\}$ = {2cm, 2°} at a test temperature of T = 43 °C. On the basis of the steady state experiments described in Section 3.2, using step changes in the applied shear stress and a ten relaxation time observation window, viscous heating is found to completely stabilize the flow. The corresponding data for the shear stress and normal stress are shown as open symbols. As the shear rate increases, viscous heating results in an apparent shear thinning in the shear stress and a dramatic decrease in the normal force exerted on the cone. However, if a continuous stress ramp with rate of increase of $d\tau/dt$ = 5Pa/s is imposed, the data corresponding to the filled symbols is obtained and the flow appears to exhibit an elastic instability. When the underlying steady one-dimensional shear flow is stable ($\dot{\gamma} \lesssim 110\ s^{-1}$), the two curves closely parallel each other and the shear stress predictions of the Rouse-Zimm bead spring model. The departure in the first normal stress data from the predictions of the quasi-linear Rouse-Zimm model is the result of shear thinning caused by hydrodynamic interactions and can be captured by the Bird-DeAguiar model. At higher shear rates, a transient subcritical instability is observed. As the stress is increased, the shear rate initially decreases and the normal stress increases dramatically as previously observed in Figure 2-11 for lower test temperatures. However, as the thermal profile in the fluid begins to develop through the rapid azimuthal, and slower radial, diffusion of thermal energy, the effective elasticity of the fluid decreases. Eventually, the instability is effectively eliminated and the shear rate returns to a steady, stable value monotonically increasing with the imposed stress.

2.4 Discussion

In this study, we have systematically demonstrated the importance of non-isothermal flow effects on the stability of torsional flows of highly elastic polymer solutions. Two monodisperse polystyrene test fluids of different molecular weight have been used to investigate the role of the fluid rheology. The agreement with isothermal linear stability analyses for the Rouse-Zimm and Bird-DeAguiar constitutive models in both cone-and-plate and parallel-plate geometries was found to be good, especially if shear thinning in the fluid relaxation time is accounted for. It was then shown that the proper dimensionless groups to consider when investigating purely elastic instabilities in viscoelastic flows are the Deborah number and the thermoelastic number $\Theta = Na^{1/2}/De$ which measures the importance of coupling between the fluid elasticity and the nonlinearities arising from viscous heating. The thermoelastic number can be influenced by changes in geometry, molecular weight and temperature. By varying the ambient temperature of the test fluid through a fairly narrow range, it was possible to progressively delay the onset of the purely elastic flow instability through a decrease in elasticity caused by temperature gradients across the gap. At thermoelastic numbers greater than $\Theta > \Theta_{crit} \approx 0.062$, the flow instability can be eliminated entirely by the same mechanism.

When the effects of energetics on the linear stability of the viscoelastic flow within a Taylor-Couette device were investigated by Al-Mubaiyedh et al., [Al-Mubaiyedh *et al.* 1999] a new mode of different spatio-temporal character to the mode arising from isothermal linear stability analysis was predicted to be the most unstable. The critical conditions for onset of this new stationary mode of instability are much lower than those required for the isothermal mode and are also in better agreement with the experimental observations. By contrast, in earlier investigations of the viscoelastic torsional flow between a rotating cone-and-plate or between two coaxial parallel-plates, the critical conditions for onset of spiral secondary flows were observed to be consistent with the predictions of isothermal linear stability analysis [McKinley *et al.* 1991; McKinley *et al.* 1995; Olagunju 1995]. This has been confirmed by our present experiments when the thermoelastic number is small. No new mode of instability is observed and viscous heating effects (corresponding to increasing thermoelastic number) are found to progressively stabilize the subcritical bifurcation. These two studies thus do not appear to be consistent. However, very recently, Al-Mubaiyedh et al. [Al-Mubaiyedh *et al.* 2000] extended their linear stability analysis of non-isothermal viscoelastic flows to the case of pressure-driven Taylor-Dean flow. In this geometry they found that, as in the torsional flow experiments, the dominant mode of the instability does not change with the addition of viscous heating, but is instead dramatically stabilized. The thermal mode is still present, but is not the dominant mode until $Pe >> 1$.

The differences observed between the stability characteristics of viscoelastic flow in the Taylor-

Couette, Taylor-Dean and torsional geometries must be the result of differences in the symmetries of the base velocity, temperature and stress fields. When the temperature at both walls is the same and the fluid is heated through viscous dissipation, the local fluid temperature achieves a maximum at the center of the gap. It is easy to physically understand how viscous heating can stabilize any of these flows. As discussed in McKinley et al. [McKinley *et al.* 1996], purely elastic instabilities arise from an interplay between streamline curvature and elastic normal stresses. When a critical Deborah number is reached, the following dimensionless parameter is exceeded

$$\left(\frac{\lambda U}{R_c} \frac{\tau_{11}}{\eta_0 \dot{\gamma}} \right)^{1/2} \geq M_{crit}, \tag{2-26}$$

and the flow becomes unstable. The temperature increase caused by viscous heating leads to a decrease of both the viscosity and the elasticity of the test fluid and thus results in a decrease in the elastic hoop stress. The critical condition expressed in Equation 2-24 is no longer exceeded along local streamlines even though the critical conditions would have been reached globally for an isothermal flow at the same rate. This thermoelastic mechanism has been found to stabilize the isothermal elastic modes of all the flows examined, including the Taylor-Couette geometry for $Pe < 10^4$ [Al-Mubaiyedh *et al.* 1999].

In the base flow of the Taylor-Couette geometry the shear stress is uniform across the gap. Viscous heating breaks the base flow symmetry in the gradient direction. A new temporal mode of instability is caused by radial convection of thermal gradients across streamlines. It appears that the symmetry of the base stress field in Taylor-Couette flow may shift the onset of this new thermoelastic instability to much smaller Peclet numbers ($Pe \geq 10^4$), than is found in the case of Taylor-Dean flow ($Pe \geq 10^5$), in which the base-state stress field is already asymmetric [Al-Mubaiyedh *et al.* 1999; Al-Mubaiyedh *et al.* 2000].

If one applies this same reasoning to the two torsional flow geometries, then one would expect that because of the homogeneity of the stress field in the base-state of the cone-and-plate geometry, the effect of viscous heating should lead to a new mode of instability as observed in the linear stability calculations for the Taylor-Couette geometry. By contrast, one would reason that the parallel-plate geometry, in which the stress field is already radially inhomogeneous, would more closely resemble the Taylor-Dean flow geometry. However, these symmetry arguments do not agree with our experimental observation. Viscometric flow in the cone-and-plate geometry does not appear to exhibit a new mode of instability when viscous heating is included, but rather only a stabilization of the isothermal elastic spiral instability. The magnitude of viscous heating in a flow scales with the Nahme number, which for the cone-and-plate geometry can be written as

$Na = \beta r^2 \Omega^2 / k T_0$. Thus, even though the shear rate, $\dot{\gamma} = \Omega / \theta_0$, is constant in the cone-and-plate geometry, the velocity, and the resulting viscous dissipation, increases radially. Therefore, unlike the Taylor-Couette geometry, viscous heating results in non-homogeneous temperature variations in both the gradient and the neutral direction for the cone-and-plate geometry. In the parallel-plate geometry the gap between the plates is constant, but both the temperature field and shear rate (or in dimensionless terms, the Nahme-Griffiths number and the Weissenberg number respectively) will exhibit radial variations. The two torsional flows thus seem to have more in common with the Taylor-Dean geometry. Such base flow symmetry arguments may help to rationalize these differences in thermoelastic effects, however, what is ultimately required is a detailed comparison of the linearized disturbance equations for viscoelastic flow in the Taylor-Couette, Dean and torsional flow geometries.

The subcritical bifurcation in shear rate observed in the present experiments is different from the turning point in the shear stress - shear rate curve corresponding to the "thermal blow-up" seen in similar Boger fluids and highly viscous Newtonian fluids [Arigo 1999] at large Nahme numbers. This instability, which can be seen in both the shear stress and the normal stress data presented in Figure 2-12 at $T = 43\,^{\circ}\mathrm{C}$, corresponds to the point at which viscous heating reduces the viscosity so significantly that increases in applied shear rate result in a decrease of the measured shear stress necessary to drive the flow [Yueh and Weng 1996].

The effects of viscous heating will always be present to some extent in the shear flow of highly elastic fluids. These effects will be especially important in shear flows with closed streamlines in which the heat from viscous dissipation can be accumulated in the device over long periods of times. In this work, we have shown that the effect of viscous heating can be minimized by considering the functional dependence of the thermoelastic parameter in Equation 2-5 and by decreasing the ambient temperature of the test or by utilizing small devices. Such an approach has been used to minimize thermal noise in detailed studies of other hydrodynamic flow instabilities [Heslot *et al.* 1987].

CHAPTER 3 The Flow of Elastic Liquids Through an Abrupt 4:1:4 Axisymmetric Contraction-Expansion

3.1 Introduction

Recent experimental and numerical investigations have shown that the dynamical evolution of the microstructure in dilute polymer solutions undergoing a strong extensional flow is far more complex than the qualitative picture of a single dumbbell undergoing uniaxial stretching. Fluorescence imaging of individual DNA molecules by Chu and coworkers has shown that a number of distinct conformational trajectories are possible in an extensional flow. Some molecules do indeed resemble dumbbells undergoing elongation, however, many other conformations such as 'half-dumbbells', 'kinked chains' and 'folded' molecules are also observed [Perkins *et al.* 1997]. Macroscopic quantities such as polymeric stress and birefringence depend on differently-weighted ensemble averages of these possible microscopic configurations. One may expect the stress-strain characteristics of a dilute polymer solution undergoing transient uniaxial elongation to be more complex than predicted by a simple dumbbell model which only captures a single measure of the end-to-end chain length.

Doyle *et al.* have recently shown through combined birefringence, tensile stress measurements and Brownian dynamics calculations that a dilute monodisperse PS solution undergoing uniaxial extension in a filament stretching device exhibits a pronounced *stress-conformation hysteresis* [Doyle *et al.*]. That is, the stress and the end-to-end conformation (as measured by phase-modulated birefringence) evolve along one path during the transient unraveling process and a distinct second path during the relaxation back to equilibrium. The difference in these curves represents an additional energy loss associated with a hydrodynamic coupling between the externally imposed flow and the internal conformational chain dynamics which appears to only be significant when the fluid is subjected to a strong flow and large Hencky strains. Similar hysteretic effects have been observed in Brownian dynamics calculations of ensembles of bead-rod chains [Doyle *et al.* 1998; Rallison 1997] and FENE dumbbells [Lielens *et al.* 1998] and can be captured, at least qualitatively, in simple closed-form constitutive models such as the ones recently proposed by Hinch [Hinch 1994] and Rallison [Rallison 1997]. The first qualitative discussion of such ideas together with scaling estimates of the magnitudes of the resulting stress was given by Ryskin [Ryskin 1987] in his analysis of the pressure drop measurements of King and James for sink flows of dilute polymer solutions at high Reynolds numbers. This hysteresis gives rise to an additional contribution to the polymer stress which may be modeled as purely viscous (i.e. it disappears instantaneously upon the cessation of stretching) [Remmelgas

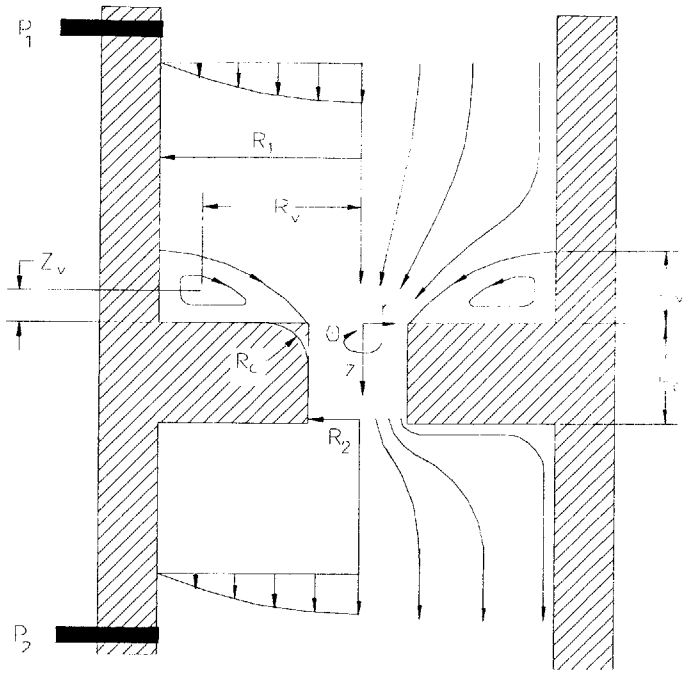

Figure 3-1 Schematic diagram of contraction geometry and definitions of important length scales.

et al. 1997] or as viscoelastic in origin with a very short characteristic relaxation time [Doyle *et al.* 1998]. Regardless of these distinctions we refer to this phenomenon as arising from an additional polymeric *dissipative stress* which removes energy from the flow. In a complex flow containing regions of extension and shear, the effects of this dissipative stress will be reflected in macroscopic observations of dynamic quantities such as pressure drops or drag coefficients.

In the present work we investigate the enhancement in the pressure drop arising from the strong converging-diverging flow of a dilute polymer solution at low Reynolds number through a 4:1:4 axisymmetric contraction-expansion. The basic orifice plate geometry for flow through an axisymmetric contraction-expansion can be seen in Figure 3-1. A fully-developed flow through a tube of radius R_1 is accelerated through an abrupt contraction of radius R_2 and is then rapidly re-expanded into a second tube of the upstream radius R_1. In the process a secondary recirculating flow may develop in the corners directly upstream and/or downstream of contraction. The elasticity of the fluid plays an important role in the flow structure and vortex formation and growth. The relative importance of the fluid elasticity is again characterized by the Deborah number $De \equiv \lambda / \mathcal{T}$ where λ is a characteristic relaxation time of the fluid and $\mathcal{T}$ is the characteristic timescale of the flow (eg. residence time in the contraction region). The flow through a contraction is a complex flow with shearing deformation near the walls and a strong nonhomogeneous

extensional flow present along the centerline and within close proximity of the contraction plane. For highly viscoelastic fluids, the recirculation region in the corners upstream of the contraction can be very strong and readily observable [Boger and Walters 1993]. For this reason and because of the geometric simplicity of the problem, viscoelastic flow through a contraction has become a standard numerical benchmark for non-Newtonian fluid dynamics calculations [Caswell 1996; Hassager 1988].

There is a great deal of literature, both experimental and numerical, dealing with flow through a contraction over a wide range of Deborah numbers and contraction ratios using a large variety of fluids and constitutive models. The experimental work has been reviewed in detail by both Boger [Boger 1987] and White, Gotsis & Baird [White *et al.* 1987] and hence we will only briefly describe some of the global characteristics observed in highly elastic polymer solutions. At low Deborah numbers, the streamlines near the contraction plane are identical to those observed in creeping flow of a Newtonian fluid with a weak 'Moffatt eddy' present in the outer stagnant corner of the upstream and downstream tube. As the Deborah number is increased, two distinctly different sequences of flow patterns can be observed for a particular contraction ratio. For some elastic fluids (eg. PAA/CS Boger fluids in a 4:1 contraction [Boger 1987; Boger and Binnington 1994]) the upstream corner vortex increases in strength and grows radially inward toward the re-entrant corner while the reattachment point grows steadily upstream. This flow regime is steady in time and substantial upstream vortex growth is observed as the Deborah number is further increased. In this case, numerical computations are able to quantitatively capture the kinematic characteristics of the flow [Coates *et al.* 1992; Purnode and Crochet 1996]. However, for other fluids (eg. PIP/PB Boger fluids in a 4:1 contraction) the corner vortex decreases in size as the Deborah number is increased and a separate, distinct 'lip' vortex [Boger 1987] forms near the re-entrant corner. The subsequent upstream vortex growth observed at higher Deborah numbers originates from outward radial growth of the lip vortex. Experimental measurements [Boger and Binnington 1990; McKinley *et al.* 1991] show that these flows are unsteady in time and three dimensional in nature. Successful simulations of a time-dependent lip vortex in an axisymmetric contraction have yet to be performed, although similar transient phenomena have been recently computed in three dimensional planar contraction geometries [Mompean and Deville 1997].

At very high Deborah numbers, the large upstream vortex observed for either of the fluid formulations described above becomes unstable to a global dynamical mode that is a sensitive function of the contraction ratio [Boger and Binnington 1990; McKinley *et al.* 1991] and is reminiscent of the melt flow instabilities observed in polymer melts [White *et al.* 1987]. These global flow instabilities have serious repercussions for industrial applications such as extrusion and injection molding where the quality of the extrudate and the flow rate are important design criteria. One of the goals of this research is to investigate

which vortex evolution pathway is followed by a dilute and monodisperse polystyrene Boger fluid which has been well characterized in both shear and extension. Polystyrene Boger fluids are purely organic in formulation like PIB/PB fluids with none of the hydrogen-bonding and polyelectrolyte issues that affect aqueous PAA solutions, but the local chain architecture is more rigid than PIB as a result of the styrene side groups. This leads to longer Kuhn statistical segment lengths in dilute solution and higher values of molecular weight between entanglements in concentrated solutions and melts of polystyrene [Ferry 1980]. It is therefore not clear *a priori* which vortex evolution pathway to expect for a PS/PS Boger fluid.

The difference in the sequence of flow transitions for two different fluids that are ostensibly identical in shear must arise from differences in the extensional rheology. It is conjectured that these differences arise from the molecular characteristics of the *equilibrium* conformations of the PAA and PIB chains [Boger and Binnington 1994]. Such conformational differences will also have a large effect on the evolution of *non-equilibrium properties* such as the transient extensional stress growth in the fluid as a function of both *strain* and *strain-rate*. In particular, the interplay between (entropic) elastic energy storage and energy dissipation during chain unraveling and the associated stress-orientation hysteresis will impact the macroscopic entrance pressure drop and the stability of the global motion as the Deborah number is increased.

Of course, observation of the fluid kinematics through flow visualization is insufficient for deducing the dynamical response of the polymeric stresses. In planar contraction flows, additional information can be obtained using pointwise birefringence and Laser Doppler Velocimetry (LDV), and these measurements can be combined to rigorously test the performance of various constitutive models [Quinzani *et al.* 1995]. The much lower Hencky strain attained in the planar geometry typically results in much less pronounced viscoelastic effects than observed in axisymmetric contractions [Ryskin 1987]; however, application of line-of-sight techniques such as birefringence in axisymmetric geometeries is not straightforward. Recently Byars et al. [Byars *et al.* 1997] have combined experimental measurements of the centerline velocity gradient of a PIB/PB fluid flowing through a axisymmetric 4:1 contraction with independent measurements of the extensional rheology performed using a filament stretching device [Ooi and Sridhar 1994] to show that even with a multimode nonlinear model it is not possible to fit both the shear rheology and the extensional rheology of a fluid with a single set of constitutive parameters. One possible cause for this discrepancy is the existence of an additional contribution to the stress in strong extensional flows which is not captured by existing dumbbell-like constitutive models.

An alternate experimental technique which can provide some limited insight into the polymeric stresses that develop during flow through a contraction is measurement of the additional or extra pressure drop resulting from the converging/diverging flow. Pressure drop measurements for axisymmetric

contraction flow of polymer solutions are not as common in the literature as visualization of flow patterns and yet they can be an effective tool for comparison of constitutive rheological predictions and for quantifying the accuracy of a numerical simulation. The majority of entrance pressure drop data have been taken as a means of estimating the extensional viscosity of a fluid [Binding and Walters 1988; Boger and Binnington 1990; Cogswell 1972; James and Chandler 1990] or to augment the information available from streak images and reattachment length measurements [Cartalos and Piau 1992; Eisenbrand and Goddard 1982], while other measurements have been taken at Reynolds numbers well beyond the creeping flow limit studied here [James and Saringer 1980]. A common observation amongst these studies is that there exists an extra pressure drop associated with the flow of a viscoelastic non-Newtonian fluid across an abrupt contraction that does not exist for a Newtonian fluid; i.e. the dimensionless pressure drop across an abrupt contraction, defined as $\mathscr{P}(De) = \Delta P_{\text{non-Newtonian}}(De, Q) / \Delta P_{\text{Newtonian}}(De = 0, Q)$, increases monotonically with Deborah number.

In general, the total pressure drop across the contraction arises from the fully-developed viscous flow through the pipe plus entrance and exit effects due to the contraction. In the present experiments, an orifice plate geometry has been chosen over other types of abrupt contractions because the extended polymer chains are allowed to relax quite quickly after exiting the contraction. The measured pressure drop is then primarily a function of the dissipative stresses that remove energy from the flow across the contraction and not due to stored elastic energy in the entropic springs that gradually relaxes in the narrow downstream tube. Such a contraction-expansion geometry may be useful in probing the dissipative contributions to the polymeric stress in a prototypical complex flow where significant differences in the extra pressure drop may be observed at the same Deborah number in PAA/CS, PIB/PB and PS/PS Boger fluids with identical shear rheology. We begin with a PS/PS fluid in the present work because the existence of a stress-conformation hysteresis has already been demonstrated experimentally and numerically [Doyle *et al.* 1998]. Furthermore, the fluid is a dilute solution of a monodisperse polymer and the results of these experiments may provide a better benchmark for theoretical comparisons than results using a similar polydisperse polymeric component.

Cartalos and Piau investigated the flow of a partially hydrolyzed polyacrylamide (HPAM) in glycerin solution through a similar orifice plate contraction-expansion [Cartalos and Piau 1992]. In these experiments, the authors found that the dimensionless pressure drop increased monotonically with deformation rate and then began to plateau at large values between $\mathscr{P}=8$ and $\mathscr{P}=18$ depending on the concentration of HPAM and the presence or absence of salt.

In the numerical literature, good agreement with experiment has been obtained for both the evolution of vortex structure [Purnode and Crochet 1996] and the upstream birefringence patterns [Beraudo *et al.*

1998]. For some fluids (eg. a molten polybutadiene rubber), the enhancement in the dimensionless pressure drop $\mathcal{F}(De)$ across a contraction is well described by the computations; however, for other materials (eg. polystyrene), the measured pressure drop is severely under predicted even though the shear rheology is well described by a multimode Leonov model [Gupta *et al.* 1997]. In fact, for dumbbell-like models (eg. the FENE-P and Oldroyd-B models) which describe the flow of dilute polymer solutions, a decrease in the dimensionless pressure drop $\mathcal{F}(De)$ is predicted in most cases as the Deborah number is increased [Coates *et al.* 1992]. Only in the limit of high Deborah numbers and fully extended polymer molecules is a small extra pressure drop predicted numerically [Keiller 1993; Szabo 1997]. This enhancement in the dimensionless pressure drop when the molecules approach full extension is consistent with observation of entrance pressure drops for rigid rod systems [Mongruel and Cloitre 1995] in which the additional non-Newtonian contribution to the extensional viscosity is explicitly dissipative because the rods cannot elongate and store energy entropically.

The systematic discrepancies between experimentally-observed entrance pressure drops and numerically-computed values arising from dissipative contributions to the total stress may play a role in other complex flows. For example, similar deviations in other integrated quantities such as the drag coefficient on spheres [Solomon and Muller 1996] and cylinders [Khomami and Moreno 1997; Liu 1997] have been observed for a variety of polymeric solutions. The work of Solomon & Muller showed that the enhancement in the viscoelastic drag coefficient $C_D(De)$ for the flow of a polystyrene Boger fluid past a sphere was larger (by up to an order of magnitude) than the results of similar experiments using different polymer solutions such as PIB Boger fluids [Solomon and Muller 1996]. Since we use a very similar PS/PS fluid in the present work, we may expect to observe dramatic increases in pressure drop similar to those observed in the drag measurements past spheres and cylinders.

The experimental apparatus and techniques are described in Section 3-2. The shear rheology of the fluid is shown to be well described by the classical bead-spring model of Rouse and Zimm. In Section 3-3, the pressure drop measurements through a 4:1:4 orifice for a Newtonian solvent are documented followed by the enhancement arising from the addition of the polymer. Flow visualization and DPIV are then combined with measurements of fluctuations in the pressure drop to document the onset of an elastic instability that leads to global oscillations in the flow as the Deborah number is increased.

3.2 Experimental

3.2.1 *Flow Geometry and Experimental Setup*

Figure 3-1 shows a schematic diagram of the contraction geometry and defines several useful length scales which we refer to extensively below. The upstream and downstream radii are denoted by the subscript 1 and 2 respectively. The length scales indicative of the vortex size and growth are described by the distance to the separation point upstream (L_v) and by the coordinates of the center of the recirculation denoted by the distance upstream of the contraction plane (Z_v) and the distance from the centerline (R_v). These distances are nondimensionalized with the diameter of the upstream tube to determine the dimensionless reattachment length $\chi \equiv L_v / 2R_1$ and the dimensionless coordinates of the vortex center $\zeta \equiv Z_v / 2R_1$ and $\xi \equiv R_v / 2R_1$. The contraction ratio is defined as $\beta \equiv R_1/R_2$.

The experimental setup has been designed to provide a versatile mechanism for systematically studying steady and time-dependent flows of elastic liquids through abrupt contractions. A schematic diagram of the apparatus is shown in Figure 3-2. A linear stepper motor (Servo Systems Co., Model 1000S) and microstepper controller (Intelligent Motion Systems, Inc., Model Panther LI) are utilized to drive fluid through the system at a constant displacement rate and hence a constant volumetric flow rate Q. The fluid flows through a plexiglass tube of radius R_1 = 1.4 cm, past three possible pressure transducer locations and through an interchangeable orifice plate. After passing beyond the contraction plane, the fluid again passes through a short section of 1.4 cm radius tubing, past the last pressure transducer location and into a collection

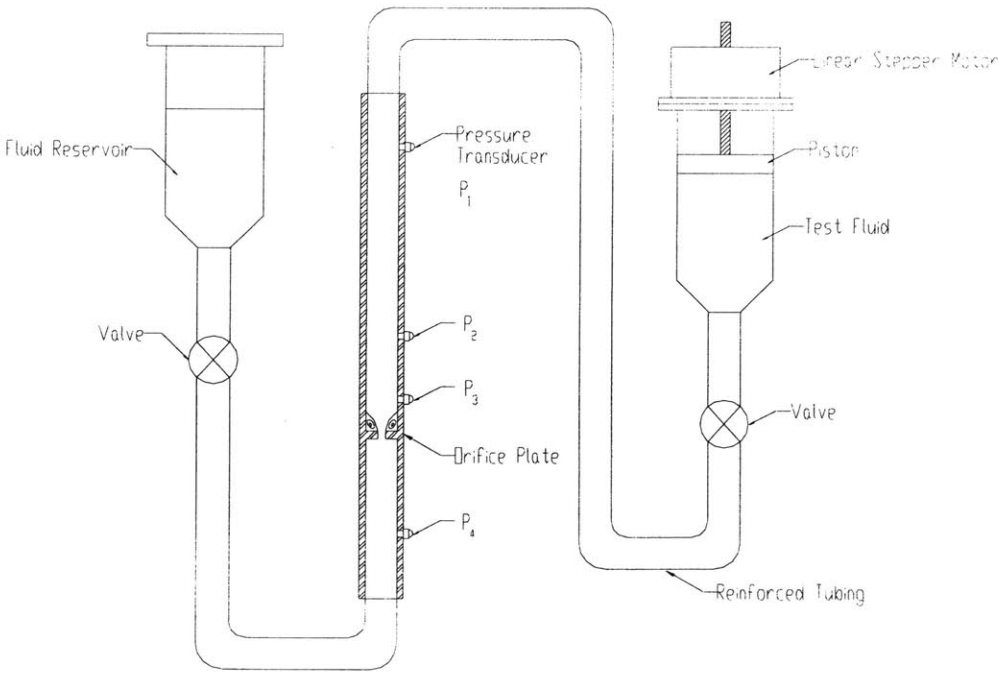

Figure 3-2 Schematic diagram of the experimental apparatus.

reservoir. When the experiment is completed the piston is retracted and the fluid is drawn in reverse back through the contraction to its original location.

The orifice plates were designed so that they could easily be replaced with a variety of different inserts containing sharp or smooth corners of various contraction ratios. In the following two chapters, this functionality will be utilized and the results reported. All experiments presented in this paper are for an orifice plate with sharp corners and a contraction ratio of $\beta = 4$ because this configuration has been established as a benchmark for numerical simulations.

During each experiment a single high-resolution pressure transducer (Endevco, Model 8510B-5) was flush mounted in one of the three upstream pressure locations and another was placed in the downstream location to measure the total pressure drop associated with flow through the contraction. The remaining upstream pressure transducer locations were sealed with screws. Table 3-1 shows the axial distance of each pressure transducer from the contraction plane. For clarity, it is useful to define several differential pressures by the location of the pressure transducers used. For instance, the pressure drop across the contraction between pressure transducers 2 and 4 is denoted as $\Delta P_{24} = (P_2 - P_4)$. Several different pressure transducers locations were created sufficiently far upstream of contraction plane to ensure that the pressure transducers were not affected by the presence of the elastically-driven growth of the upstream and downstream vortices.

	Pressure Transducer i	**Distance From Contraction Plane z_i [cm]**
Upstream:	P_1	-22.86
	P_2	-7.62
	P_3	-2.54
Downstream:	P_4	+8.26

Table 3-1 Location of the flush mounted pressure transducers with respect to the contraction plane located at $z = 0$.

As the flow rate is increased, the pressure transducers measure a combination of the pressure drop arising from fully-developed rectilinear flow in the straight pipe and the extra pressure drop caused by the presence of the orifice plate $\Delta P(Q) = \Delta P_{\text{straight pipe}} + \Delta P_{\text{ext.}}$. We are only interested, however, in the extra pressure drop which we denote as $\Delta P'_{24}$ where the prime indicates that the contribution to the total pressure drop resulting from the Poiseuille flow in the pipe connecting the pressure transducers has been removed in

order to isolate the extra pressure drop across the contraction-expansion. In other words,

$$\Delta P'_{24} = \Delta P_{24} - \frac{8QL\eta}{\pi R_2^4}, \tag{3-1}$$

where $L \equiv z_4 - (z_2 + L_c)$ is the length of straight tubing between the pressure transducers and the contraction, Q is the volume flow rate of the fluid and η is the fluid viscosity. Lastly, we define a dimensionless pressure drop

$$\mathscr{P}(De) = \frac{\Delta P'_{24}(Q, De)}{\Delta P'_{24}(Q, De = 0)}, \tag{3-2}$$

where $\Delta P'_{24}(Q, De = 0)$ is the pressure drop across the orifice of the Newtonian oligomeric polystyrene oil at a given flow rate and $\Delta P'_{24}(Q, De)$ is the pressure drop across the contraction-expansion of the viscoelastic 0.025wt% PS/PS polymer solution at the same flow rate. This dimensionless pressure drop differs from the Couette correction often used to present contraction flow pressure drop data by a constant factor and is discussed further in Section 3.3.1.

3.2.2 *Digital Particle Image Velocimetry (DPIV)*

Digital particle image velocimetry (DPIV) is a non-invasive technique for acquiring measurements of velocity vector fields over an entire flow domain. DPIV measures local velocities by determining the average displacements of particles $\overline{\Delta x}$, $\overline{\Delta y}$ in a small correlation region over a known time Δt. Two images of laser illuminated particles in a flow field are taken and broken down into correlation windows. Within each correlation window the two frames are compared and an average displacement is calculated. This displacement is then converted into a velocity through the known time difference between images.

In these experiments a DPIV algorithm is used to measure the axial and radial velocity components of the flow upstream of the axisymmetric contraction-expansion. A single beam from a 300mW Ar-ion laser (Ion Laser Technologies, Model 5500A-00) is passed through a non-Gausian optical element to obtain a 1mm thick laser light sheet of uniform intensity. The use of a single-mode optical fiber (Oz Optics Inc.) allows the light sheet to be easily directed normal to the surface of the tube to illuminate the fluid which is seeded with 50 μm diameter silvered hollow glass spheres (Potters Industries Inc) at a volume fraction of 2.1×10^{-3}. This concentration of particles corresponds to the number of particles required to achieve a minimum of 20-25 particles per 16×16 pixel correlation window [Pakdel and McKinley 1997]. Using Einstein's correction

to the viscosity of a suspension [Batchelor 1985] we may estimate the increase in the zero-shear-rate viscosity of the fluid as

$$\eta_{suspension} / \eta_{solvent} = 1 + 2.5\varphi \tag{3-3}$$

where η is the shear viscosity and φ is the volume fraction of particles. From Equation 3-1 we can estimate that the shear viscosity of the suspension will be approximately 0.53% greater than the shear viscosity of the solvent. Subsequent measurements of the viscometric properties of the suspension showed no discernable effect of the particle addition within the accuracy of the rheological measurements.

The illuminated fluid motion is videotaped using a digital video camera (Sony DCR-VX1000) aligned orthogonal to the laser light sheet. The video recorder contains 3 CCD chips and digitally records 480×720 pixel images to tape every 30th of a second using a lossless compression algorithm. Images are then captured digitally onto the hard drive of a PC where the DPIV analysis is performed. A more detailed discussion of the utility of the DPIV technique for velocity and other kinematic measurements in non-Newtonian fluids is given by Pakdel and McKinley [Pakdel and McKinley 1997].

3.2.3 *Laser Doppler Velocimetry (LDV)*

Laser Doppler velocimetry (LDV) measurements are used to supplement the global velocity vector field measurements obtained with DPIV. Primarily, we utilize LDV to take pointwise measurements of velocities near and within the throat of the contraction-expansion where DPIV measurements are not possible due to the loss of cross-correlation between sequential images in subregions where the velocity or velocity gradient of the particles become too large. To facilitate these measurements, an acrylic 4:1:4 orifice plate was created to form the contraction-expansion. LDV can generate time-resolved point velocity measurements which can be used to search for the onset of elastic flow instabilities near the contraction plane [Lawler 1986]. The test fluid is seeded with the same 50μm diameter silvered hollow glass spheres (Potters Industry) used for DPIV and flow visualization purposes. Utilizing a fast Fourier transform technique, a spectrum analyzer (Dantec Burst Spectrum Analyzer) is used to compute the velocity from the Doppler shifted frequency signal collected from a single-colored, fiber optic LDV system (Dantec Electronics Inc.) coupled with a 300mW argon-ion laser (Ion Laser Technologies). A detailed description of the LDV system used in this research is presented by Arigo et al. [Arigo *et al.* 1995]. The spectrum analyzer is an excellent tool for extracting average velocities from ensembles of Doppler bursts for slow flows, even in the presence

of noise, but because of the discrete nature and random arrival times of the Doppler bursts, spectral analysis cannot always be used to effectively resolve slow time-varying velocity profiles such as those that develop beyond the onset of flow instabilities. A Doppler frequency tracker (DISA, Model 55 N 21) is therefore used to lock into and measure the frequency and amplitude of velocity fluctuations resulting from elastic flow instabilities. These local velocity measurements are a very sensitive indicator of the critical conditions for the onset of the elastic flow instability.

3.2.4 *Flow Visualization*

The same optical configuration used for the DPIV analysis was also utilized for direct flow visualization. Digital video of the laser illuminated flow field was recorded and used to artificially generate long time exposures or 'streak' images from multiple single frames. These 'streak' images were used to record the streamlines in the flow field and were created by first thresholding many frames to remove all background light and then averaging all the images together. The resulting image is similar to the classic streak images created by exposing photographic film over a long period of time. This flow visualization technique has been used extensively for contraction flows and other complex flows throughout the field of non-Newtonian fluid dynamics [Boger and Walters 1993].

3.2.5 *Fluid Shear Rheology*

The viscoelastic fluid consists of an 0.025 wt% solution of monodisperse polystyrene (PS) (Scientific Polymer Products, Inc.) with a molecular weight of 2.25×10^6 g/mol and polydispersity of $M_w/M_n = 1.03$. The polystyrene is dissolved in oligomeric styrene (Hercules) to yield a dilute solution with $c/c^* = 0.24$. The resulting solution falls into a class of fluids first described in detail by Boger [Boger 1977/78] which are highly elastic with an almost constant viscosity. The absence of shear thinning in the viscosity allows one to investigate elastic effects of the fluid alone, while the large viscosities and long relaxation times eliminate inertial effects while permitting flows to be studied at high Deborah numbers. The use of a monodisperse polymeric constituent in the PS/PS fluid permits the rheology to be more easily compared with molecular theories for dilute solutions.

Figure 3-3 shows a master curve of the rheological properties for the 0.025wt% PS/PS solution at $T_0 = 25\,^{\circ}C$, measured with a controlled stress device (TA Instruments, Model AR1000N). The viscoelastic properties of the fluid are characterized in small amplitude oscillatory shear flow by the dynamic viscosity

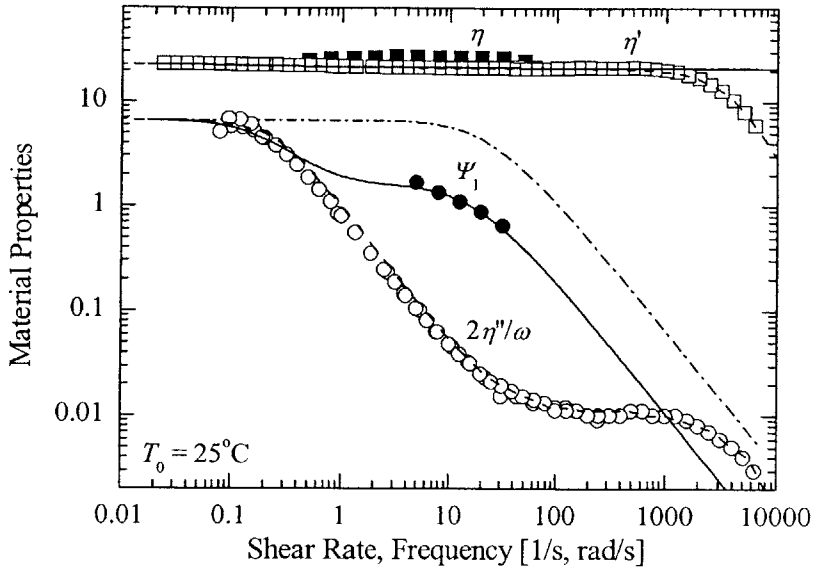

Figure 3-3 Rheological material functions of the 0.025wt% monodisperse polystyrene in oligomeric polystyrene solution. The data include: ■, steady shear viscosity, $\eta(\dot{\gamma})$ [Pa·s]; □, dynamic viscosity, $\eta'(\omega)$ [Pa·s]; ○, dynamic rigidity, $2\eta''(\omega)/\omega$ [Pa·s^2]; ●, first normal stress coefficient, $\Psi_1(\dot{\gamma})$ [Pa·s^2]; and the corresponding fits of the FENE-P, – · –, Bird-DeAguiar, —, and Zimm model, – –, respectively.

$\eta'(\omega)$ and the dynamic rigidity $2\eta''(\omega)/\omega$ which are both functions of the frequency of oscillation. In steady shear flow the fluid is characterized by the first normal stress coefficient $\Psi_1(\dot{\gamma}) = (\tau_{11}(\dot{\gamma}) - \tau_{22}(\dot{\gamma})) / \dot{\gamma}^2$ and viscosity $\eta(\dot{\gamma})$, each of which are functions of the shear rate. Figure 3-3 shows that the viscosity of the solution is approximately constant over several decades of shear rate. The fluid is strongly elastic and its first normal stress coefficient shear thins monotonically throughout the entire range over which data can be obtained.

The linear viscoelastic properties are well described by the Rouse-Zimm bead-spring model [Zimm 1956] with a longest relaxation time of $\lambda_z = 3.24$ s. The Rouse-Zimm model also predicts a zero-shear-rate viscosity of $\eta_0 = 22.8$ Pa·s, nearly all of which is contributed by the oligomeric PS solvent ($\eta_s = 21.0$ Pa·s), and a first normal stress coefficient of $\Psi_{10} = 6.66$ Pa·s^2 in the limit of zero shear rate. Table 3-2 lists the parameters used to compute the material properties.

The Rouse-Zimm model accurately predicts the frequency response of the measured dynamic rigidity $2\eta''(\omega)/\omega$. At medium frequencies, $1/\lambda_z << \omega << 1/\lambda_{ps}$ the slope of this data allows an approximate

determination of the hydrodynamic interaction parameter h^* [Larson 1988]. In the limit $h^* = 0$, the free-draining Rouse model incorporates no hydrodynamic interaction and $2\eta'' / \omega \sim \omega^{-3/2}$, whereas in the Zimm (non-free-draining) limit $h^* \approx 0.25$ and $2\eta'' / \omega \sim \omega^{-4/3}$. For the present data $2\eta'' / \omega \sim \omega^{-1.44}$ suggesting from the approximate solution of Thurston that $h^* \approx 0.1$ [Bird *et al.* 1987]. At low frequencies ($\omega \leq 0.01$ rad/s) the fluid is essentially Newtonian and the phase angle $\delta \rightarrow 90°$ so that significant experimental error is expected in the measurements. However, at high frequencies ($\omega \geq 1000$ rad/s) the Zimm model predictions deviate from the experimental measurements due to the small but finite elasticity of the oligomeric solvent. This additional elasticity can be modeled by an extra Maxwell element for the solvent with a relaxation time $\lambda_{ps} \approx 2.5 \times 10^{-4}$ s which is in good agreement with the range of values reported by Mackay and Boger [Mackay and Boger 1987] and Quinzani *et al.* [Quinzani *et al.* 1995].

	Notation	Description	Parameter
Known:	c	Concentration of High Molecular Weight Polystyrene	0.025%
	M_w/M_n	Polydispersity	1.03
	M_w	Molecular Weight [g/mol]	2.0×10^6
	$b = L^2$	Extensibility Parameter	7744
	T_0	Reference Temperature [K]	298
Fitted:	η_0	Zero Shear Rate Viscosity [Pa·s]	22.75
	η_s	Solvent Viscosity [Pa·s]	21
	λ_{ps}	Solvent Relaxation Time [s]	2.5×10^{-4}
	h^*	Hydrodynamic Interaction Parameter	0.1
	σ	Extent of Anisotropy in Stokes' Law	0.63
	β	Extent of Anisotropy in Brownian Motion Forces	1
Calculated:	λ_z	Zimm (Longest) Relaxation Time [s]	3.24
	$\overline{\lambda}$	Oldroyd Relaxation Time [s]	0.146
	Ψ_{10}	First Normal Stress Coefficient [Pa·s^2]	6.66

Table 3-2 Parameters characterizing the viscometric properties of the 0.025wt% PS/PS solution.

The solid line in Figure 3-3 represents the predictions of a single FENE-P model for the steady shear data. If the finite extensibility is computed from the molecular weight and radius of gyration of the chain we obtain $L = 93$. The FENE-P model contains no adjustable parameters, however, it is clear that a simple dumbbell model does not capture all of the physics observed at high deformation rates. The asymptotic slope

of the expression for $\Psi_1(\dot{\gamma})$ at high shear rates cannot be changed; however, a better fit, meaning that the model crosses through the experimental data and not above it, can be obtained if the extensibility parameter L is reduced to a value of $L = 15$. The much earlier onset of shear-thinning in $\Psi_1(\dot{\gamma})$ observed experimentally is most likely due to hydrodynamic interactions between the beads of the deformed chain which is not captured in the Zimm (pre-averaged) model [Magda *et al.* 1988]. An improved description requires a more detailed treatment of hydrodynamic interactions between segments of a polymer chain undergoing a steady shearing deformation. One such model that accounts for the anisotropy in the hydrodynamic drag forces in approximate form is the encapsulated dumbbell model of Bird and DeAguiar [Bird and DeAguiar 1983]. The evolution equations of the Bird-DeAguiar model can be re-written as

$$\lambda \mathbf{A}_{(1)} = -\left[f\left(tr\mathbf{A}\right)\mathbf{A} - \mathbf{I}\right] + 3\left(1-\sigma\beta\right)\frac{\mathbf{A}}{tr\mathbf{A}} - \left(1-\sigma\beta\right)\mathbf{I}, \tag{3-4}$$

$$\boldsymbol{\tau}_p = -n\mathrm{k}_\mathrm{B}T\left[f\left(tr\mathbf{A}\right)\mathbf{A} - \mathbf{I}\right] + 2n\mathrm{k}_\mathrm{B}T\left(1-\beta\right)\left[\frac{3\mathbf{A}}{tr\mathbf{A}} - \mathbf{I}\right], \tag{3-5}$$

$$\text{where} \quad f\left(tr\mathbf{A}\right) = \frac{1}{1-\dfrac{tr\mathbf{A}}{L^2}}, \tag{3-6}$$

where k_B is the Boltzman constant, n is the number of springs, λ is the relaxation time of the fluid, L is the finite extensibility of the polymer chain and the polymer conformation is given by the dimensionless second moment tensor $\mathbf{A} = \langle\mathbf{RR}\rangle$, where $\mathbf{R}$ is the end-to-end vector of the polymer chain scaled with the root mean square end-to-end length of the chain. The extent of anisotropy in the viscous drag on the beads is given by σ and the anisotropy in the velocity distribution of the beads arising from Brownian motion is given by β. When $\sigma = \beta = 1$, the FENE-P model is recovered. Our exploratory calculations suggest that to quantitatively describe the viscometric properties of dilute polymer solutions in viscous solvents, the anisotropy in the viscous drag the primary effect of importance. The Brownian motion of the beads can thus be assumed to be isotropic with $\beta = 1$. In this limit, Equation 3-4 reduces to the familiar expression for the stress in an ensemble of FENE-P dumbells while the evolution equation reduces to

$$\lambda \mathbf{A}_{(1)} = -\left[\left\{f\left(tr\mathbf{A}\right) - \frac{3\left(1-\sigma\right)}{tr\mathbf{A}}\right\}\mathbf{A} - \sigma\mathbf{I}\right], \tag{3-7}$$

The solid lines in Figure 4-3 represent the predictions of the Bird-DeAguiar model fit and are in good agreement with both the viscosity and first normal stress difference measurements.

Variations in the viscoelastic properties of the test fluid can occur due to thermal fluctuations in the laboratory test environment. To correct for these effects we employ time-temperature superposition with a shift factor

$$a_T = \frac{\eta_0(T)\, T_0 \rho_0}{\eta_0(T_0)\, T \rho} \tag{3-8}$$

to adjust the strain rate, normal stress difference and viscosity to a reference temperature of $T_0 = 25\,^{\circ}C$ [Bird *et al.* 1987]. For the temperature ranges experienced in the laboratory, we use the WLF equation to determine a_T which has been found to be valid for a wide variety of polymer solutions and melts and has the form

$$\log a_T = \frac{-a(T - T_0)}{b + (T - T_0)} \tag{3-9}$$

where a and b are constants to be determined [Bird *et al.* 1987]. Table 3-3 shows the values of the constants used to fit the temperature dependence of the 0.025wt% PS/PS solution to the WLF equation.

Notation	Parameter Value
T_0	298 K
a	16.4
b	80.5 K

Table 3-3 WLF equation parameters used to fit the temperature dependence of the 0.025wt% PS/PS solution

3.2.6 *Fluid Extensional Rheology*

To understand the kinematics of the complex flow through axisymmetric contraction-expansions, it is important to characterize the behavior of the test fluid in both shear and extension. The filament stretching rheometer and techniques developed by Anna et al. [Anna *et al.* 1999] were used to measure the transient extensional viscosity of the PS/PS solution. The theory and experimental technique of extensional rheology will be discussed in detail in Chapter 7. In Figure 3-4, the Trouton ratio, $Tr = \bar{\eta}^+ / \eta_0$, where $\bar{\eta}^+$ is

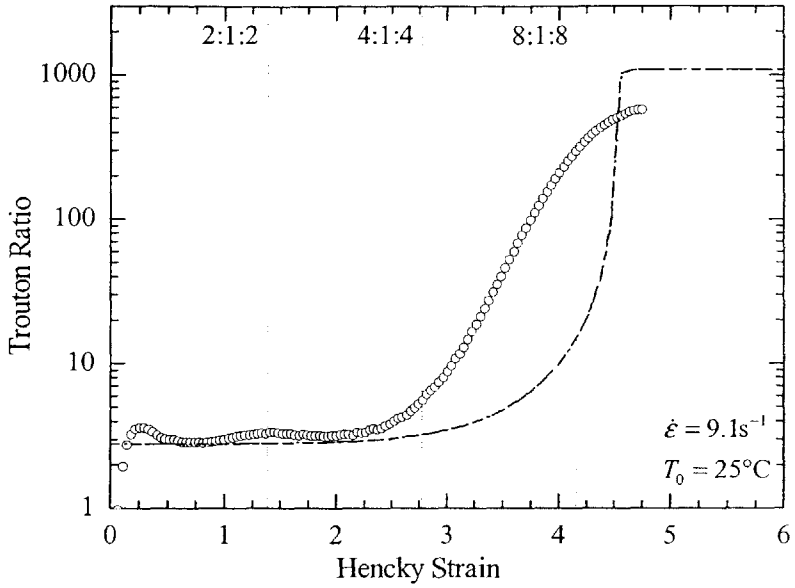

Figure 3-4 Measurements of the dimensionless transient uniaxial extension, $\overline{\eta}^+ / \eta_0$, as a function of Hencky strain, $\varepsilon = \dot{\varepsilon}t$. The data include: ○, experimental measurements of the 0.025wt% PS/PS solution taken at a strain rate of $\dot{\varepsilon} = 9.1s^{-1}$; and – –, FENE-P model fit. The maximum strain achieved along the centerline of the three contraction ratios tested is also shown.

the transient extensional viscosity is plotted against the Hencky strain, $\varepsilon = \dot{\varepsilon}t$, for a strain rate of $\dot{\varepsilon} = 9.1s^{-1}$. One important point to note is that at high Deborah numbers, $De = \lambda_z \dot{\varepsilon} = 29.5$, the Trouton ratio is relatively insensitive to changes in extension rate. At low Hencky strains, the extensional viscosity behaves in a Newtonian-like manner and the Trouton ratio is approximately equal to $Tr \cong 3\eta_s/\eta_0$. As the Hencky strain increases, the PS/PS solution strain-hardens, reaching an equilibrium at a Trouton ratio of $Tr \sim 1000$. The FENE-P and Bird-DeAguiar model fits are plotted with the experimental data. Neither of these models fit the experimental data well, overpredicting the critical Hencky strain for the onset of strain-hardening and overpredicting the equilibrium value of the extensional viscosity. It is interesting to note that the anisotropy introduced by the Bird-DeAguiar model has very limited effect in uniaxial extension even though it has a profound effect on the prediction of the first normal stress differences in shear.

3.2.7 *Dimensionless Parameters*

The relative importance of inertial to viscous effects in the flow is characterized by the Reynolds number. In the present work we define the characteristic Reynolds number based on the flow conditions at the contraction plane as

$$Re = \frac{\rho \langle v_z \rangle_2 2R_2}{\eta_0} = \frac{2\rho Q}{\pi R_2 \eta_0}, \tag{3-10}$$

where $\langle v_z \rangle_2 = Q / \pi R_2^2$ is the average axial velocity through the contraction, Q is the volume flow rate and ρ = 1.026 g/cm^3 is the density of the fluid. For all experiments performed the Reynolds number $Re < 1 \times 10^{-2}$, making it possible to neglect inertial effects and placing these experiments well within the creeping flow regime.

The Deborah number characterizes the relative importance of elastic effects to viscous effects in the flow. To determine the Deborah number we need to select both a characteristic timescale for the flow and a representative measure of the spectrum of relaxation times of the fluid. A characteristic strain rate based on the local flow conditions near the plane of the contraction is defined by $\dot{\gamma} \equiv \langle v_z \rangle_2 / R_2$. A characteristic convective time of the flow can then be taken to be $\mathcal{T} \equiv R_2 / \langle v_z \rangle_2 = \dot{\gamma}^{-1}$. The simplest choice for the fluid time scale is of course the longest or Zimm relaxation time λ_z determined from the linear viscoelastic measurements. Even though the viscosity does not have a strong rate dependence, the first normal stress coefficient does. It is therefore important to note that the relaxation time, which can be calculated from the viscometric properties of the fluid previously determined, is a function of shear rate [Bird *et al.* 1987]. In polymer melts it is customary to use a shear-rate-dependent relaxation time of the form

$$\lambda(\dot{\gamma}) \equiv \frac{\Psi_1(\dot{\gamma})}{2\eta(\dot{\gamma})} \tag{3-11}$$

The dimensionless product $\lambda(\dot{\gamma})\dot{\gamma}$ is thus equivalent to half the stress ratio [Petrie and Denn 1976].

Discrepancies between different estimates of the relaxation time have been discussed at length by Keiller *et al.* [Keiller *et al.* 1992]. For scaling purposes, in the present work the characteristic relaxation time of the 0.025wt% PS/PS solution will be given by the relaxation time evaluated in the limit of zero shear rate. After substituting for the asymptotic value of Ψ_{10} obtained from the Rouse-Zimm model the characteristic relaxation time becomes

$$\lambda_0 = \frac{\Psi_{10}}{2\eta_0} = 0.29\,\lambda_z \frac{\eta_p}{\eta_0} = 0.146\text{s} \tag{3-12}$$

The zero-shear-rate Deborah number expressed with this choice of constant characteristic relaxation time becomes $De = \lambda_0 \dot{\gamma}$. For convenience, we will report the Deborah number in the latter representation for all experiments in this paper. The *shear-rate-dependent Deborah number* of flow through a 4:1:4 axisymmetric contraction is expressed as

$$De(\dot{\gamma}) = \lambda(\dot{\gamma})\,\dot{\gamma} = \frac{\Psi_1(\dot{\gamma})\,\langle v_z \rangle_2}{2\eta(\dot{\gamma})\,R_2} \tag{3-13}$$

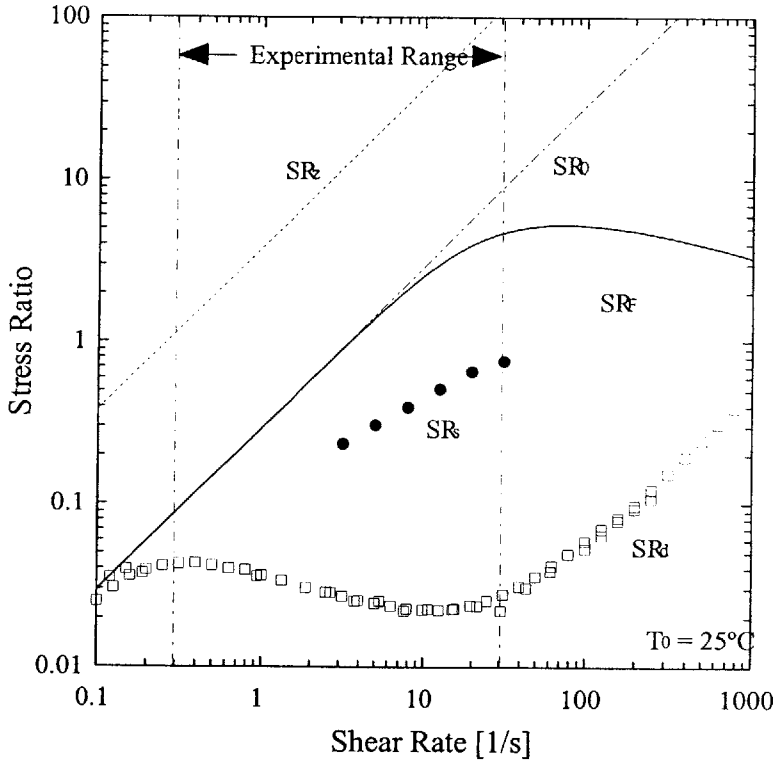

Figure 3-5 Various estimates of the stress ratio $SR \equiv \tau_{xx}/\tau_{yx}$ of the 0.025wt% PS/PS solution in steady shear. The data includes: '●', the experimental stress ratio from steady shear data $SR_s = N_1/\tau_{yx} = \Psi_1\dot{\gamma}/\eta$; '□', experimental stress ratio from dynamic data $SR_d = G'/G'' = \eta''/\eta'$; '- -', the stress ratio predicted using the longest relaxation time of the Zimm model $SR_z = 2\lambda_z\dot{\gamma}$; '– –', the stress ratio predicted using the zero-shear-rate relaxation time $SR_0 = 2\lambda_0\dot{\gamma}$; '—', the stress ratio SR_F predicted by the FENE-P model

and may also be thought of as a *Weissenberg number* [Gupta *et al.* 1997] or recoverable shear because it is a direct estimate of the ratio of the normal stress difference to the total shear stress in the fluid at a given deformation rate $\dot{\gamma}$. We refer to this generically as a stress ratio SR which was used in early publications to report the magnitude of viscoelastic effects in flow through a contraction [Petrie and Denn 1976]. Figure 3-5 shows a plot of the stress ratio, $SR \equiv N_1(\dot{\gamma}) \; / \; \tau_{12}(\dot{\gamma})$, as a function of strain rate to demonstrate the rate dependence of the elastic stress difference in the fluid. The filled circles represent the steady shear viscometric data and the short dashed line represents the linear approximation to the stress ratio if the constant relaxation time is used; $SR_0 = 2\,\lambda_0\,\dot{\gamma}$. The non-monotonicity in the dynamic data is a consequence of the additional elasticity contributed from the polymeric solvent at high deformation rates. The long dashed line represents the same approximation if the longest "Zimm" relaxation time were used $SR_z = 2\,\lambda_z\,\dot{\gamma}$ and it clearly over predicts the magnitude of elastic effects in the actual test fluid. The solid line represents the stress ratio, SR_F, predicted by the shear thinning FENE-P model. As expected, the experimental values of SR increase with strain rate and begin to approach a maximum around one. At low shear rates, the experimental values of SR approach the linear function SR_0, but throughout the range of deformation rates attained in the experiments, they remain up to an order of magnitude smaller. Even though SR_0 is clearly a better approximation than SR_z it is by no means an ideal description of the actual magnitude of the elasticity in the flow of the 0.025wt% PS/PS solution and shear-thinning effects must be incorporated to achieve a quantitative description of the data. However, even with a shear-thinning first normal stress coefficient, the FENE-P model does not accurately predict the magnitude of the stress ratio.

3.3 Results

3.3.1 *Evolution of Newtonian Pressure Drop with Flow Rate*

The pressure drop of the Newtonian oligomeric polystyrene oil through the 4:1:4 axisymmetric contraction was measured to serve as a baseline for comparison of the non-Newtonian results and to evaluate the performance of the experimental system. Figure 3-6 shows the experimentally measured transient evolution in the pressure drop (ΔP_{24}) across the 4:1:4 orifice plate for the Newtonian polystyrene oil as the characteristic strain rate $\dot{\gamma}$ is stepped from 1.7 s^{-1} to 3.2 s^{-1} in 3 equal increments of 0.5 s^{-1} and is then reduced to 0 s^{-1}. All values of pressure have been shifted to the value corresponding to a fluid with viscosity η_0 at the reference temperature of $T_0 = 25\,°C$ using the shift factor a_T discussed in section 2.4. At a specified flow rate, the pressure drop of a Newtonian fluid in creeping flow is proportional to its viscosity, so the pressure drop should scale with ambient temperature just as its viscosity does. For a non-Newtonian fluid, it would

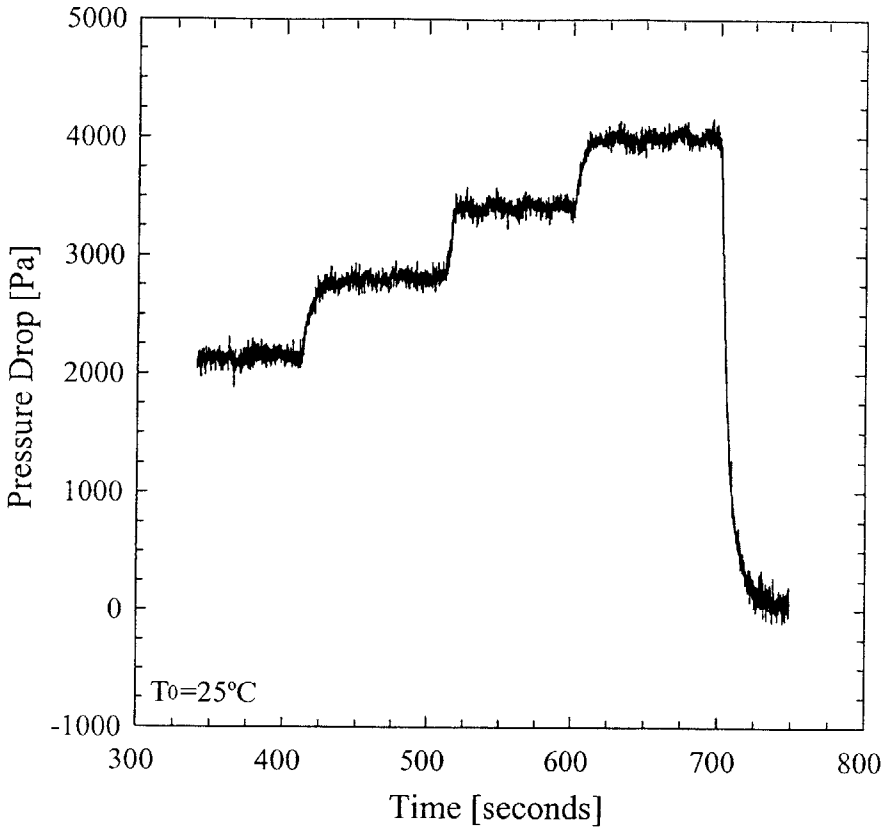

Figure 3-6 Pressure drop across the contraction ΔP_{24} for the Newtonian oligomeric PS oil demonstrating the transient response of the system as the characteristic strain rate is stepped from 1.7 s^{-1} to 3.2 s^{-1} in 3 equal increments of 0.5 s^{-1} and is then dropped to 0 s^{-1}.

be important to also shift the time axis according to the technique of *time-temperature superposition*.

Figure 3-6 demonstrates that the pressure differences over increments of $\Delta\dot{\gamma} \approx 0.5\ s^{-1}$ or smaller are easily discernible from the noise of the system which for the chosen pressure transducers was consistently around ±0.1kPa (±0.015psi). For each strain rate shown, the fluid motion approached a steady state flow after a short system lag of about 10 seconds. Similar results were observed for the Newtonian PS oil at all strain rates tested ($0.5\ s^{-1} \leq \dot{\gamma} \leq 10\ s^{-1}$) and no flow instabilities were observed under any condition.

In 1891, R. A. Sampson first solved the pressure-driven flow of a Newtonian fluid at low Reynolds number through an infinitesimally thin circular hole in an infinite rigid wall using oblate spheroidal coordinates [Sampson 1891]. Of particular interest are Sampson's results for the centerline velocity profile $v_z(z)$ and the pressure drop across the orifice which may be simply expressed in cylindrical coordinates as

$$v_{z,S} = \frac{Q}{2\pi R_2^2}\left(\frac{1}{1 + (z/R_2)^2}\right) \tag{3-14}$$

$$\Delta P_S = \frac{3Q\eta_s}{R_2^3} \tag{3-15}$$

where Q is the volume flow rate of the fluid and z is the axial distance from the orifice plane. For large contraction ratios $\beta = R_1 / R_2 >> 1$, Sampson's solution should approximate the flow near the plane of the contraction reasonably well. However, because our orifice plate is not infinitely thin, and has finite aspect ratio ($L_c / R_2 \neq 0$) there is an additional contribution to the pressure drop. This has been considered analytically by Dagan *et. al* [Dagan *et al.* 1982]. Their numerical calculations can be accurately approximated by linearly combining the pressure drop associated with Sampson flow and the pressure drop of the assumed Poiseuille flow through the orifice itself to give:

$$\Delta P_D = \frac{Q\eta}{R_2^3}\left(3 + \frac{8L_c}{\pi R_2}\right) \tag{3-16}$$

where $L_c = 0.635$ cm is the thickness of the orifice plate.

In the present experiments, $L_c / R_2 = 2$ and the additional pressure drop arising from the latter term in Equation 3-16 is not negligible. To eliminate any possible relaxation of the polymer chains in the orifice section, one ideally requires $L_c / R_2 \to 0$; however such a geometry is difficult to experimentally realize and furthermore, from a numerical perspective, the resulting corner singularities would severely compromise viscoelastic flow calculations at high Deborah number. Conversely, in the conventional benchmark of entry flow into a simple contraction ($L_c / R_2 \to \infty$) all of the stored elastic energy is slowly returned to the flow as the stretched molecules advect and relax in the downstream pipe flow and resolution of this slow downstream stress relaxation appreciably increases the domain size and computational expense of simulations.

By selecting a contraction-expansion with a finite value of L_c / R_2 the physical domain of interest is limited to a few radii upstream and downstream of the orifice and it also becomes possible to investigate the effects of varying the local radius of curvature of the re-entrant corner. We shall report on this in later publications. The value $L_c / R_2 = 2$ is in the same range as previous experimental [Cartalos and Piau 1992]

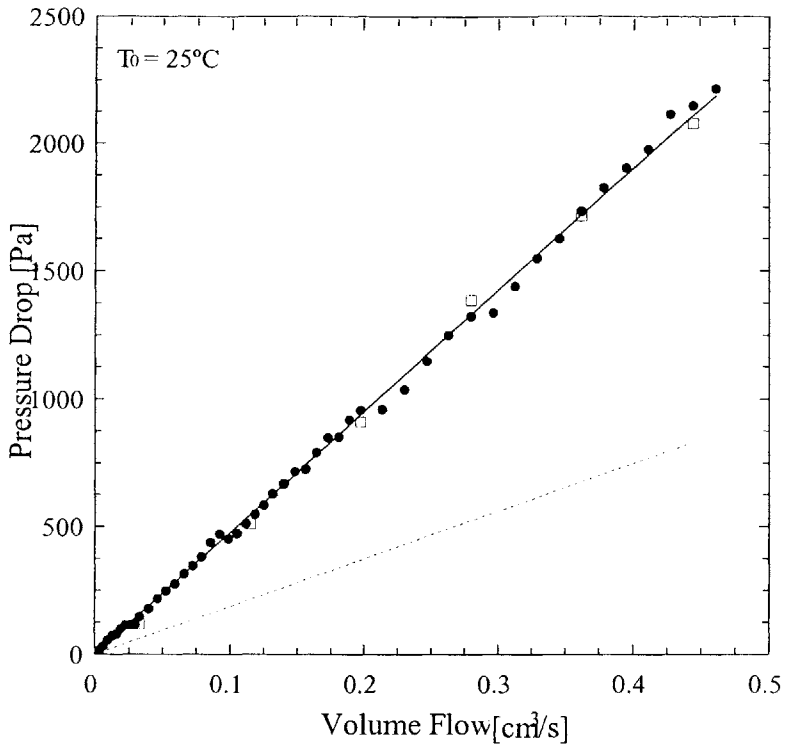

Figure 3-7 Extra pressure drop $\Delta P'_{24}$ for the Newtonian oligomeric polystyrene oil through a 4:1:4 axisymmetric contraction/expansion. The data includes: '●', experimental points taken during forward displacement through the contraction; '□', experimental points taken during backward displacement through the contraction; '—', an approximation to the numerical results of Dagan *et. al* [48]; '– –', the analytical result of Sampson [47].

and numerical [Szabo 1997] studies of viscoelastic flows through contraction-expansions.

Figure 3-7 is a comparison of the experimentally measured pressure drop $\Delta P'_{24}(Q)$ of the Newtonian PS oil through the 4:1:4 contraction with the predictions of Sampson and Dagan. Once again the pressure data has been shifted to the reference temperature of $T_0 = 25\,°C$. For creeping flows of a Newtonian fluid, the velocity field is symmetric in the converging and diverging flows near the contraction plane. Pressure measurements were performed for both forward and backward flows through the contraction to rule out any hysteresis effects. As expected, the pressure drop is linearly proportional to the volumetric flow rate. The Sampson flow prediction is systematically low, but the prediction of Dagan *et. al* is remarkably good and provides almost an exact fit to the data. Even though the experimentally manufactured orifice plate is only 0.635 cm thick, the additional viscous pressure drop, $8\,Q\,L_c\,\eta / \pi\,R_2^4$, is as large as the contribution from the Sampson converging flow.

An alternative approach commonly used in presenting contraction flow results is to report a *Couette*

correction [Boger *et al.* 1978] in which the extra pressure drop arising from the orifice is scaled with the wall shear stress in the downstream tube

$$C = \frac{\Delta P'}{2\tau_w} = \frac{\Delta P' \pi R_2^3}{8\eta_s Q}, \tag{3-17}$$

where $\tau_w = 4\eta_s \langle v_2 \rangle / R_2 = 4\eta_s Q / \pi R_2^3$. For $\beta \to \infty$, the Couette correction for a Newtonian fluid entering an abrupt contraction the Sampson solution thus predicts

$$C = \frac{1}{2}\frac{\Delta P_{Sampson}}{2\tau_w} = \frac{3\pi}{16} = 0.589, \tag{3-18}$$

which is in good agreement with simulations and measurements [Mackay *et al.* 1988].

3.3.2 *Evolution of the Non-Newtonian Pressure Drop with Flow Rate*

The pressure drop of the non-Newtonian 0.025wt% PS/PS solution through the 4:1:4 axisymmetric contraction ($\Delta P'_{24}$) was measured for Deborah numbers in the range $0.06 \le De \le 7.5$. Figure 3-8 shows the results of these experiments. The evolution in the Couette correction with increasing Deborah number is commonly reported in numerical calculations [Bernstein *et al.* 1994; Coates *et al.* 1992]. However, in the present work we chose to report values in terms of the dimensionless pressure drop $\mathscr{P}(De) = \Delta P'_{24}(Q, De) / \Delta P'_{24}(Q, De=0)$, where $\Delta P'_{24}(Q, De=0)$ is the best fit to the Newtonian pressure drop data described in §3.1.1. In the limit $De \to 0$ we therefore expect $\mathscr{P} \to 1.0$. The scatter in the data is due for the most part to a $\pm 0.1\,^{\circ}C$ uncertainty in the temperature measurements which leads, through a propagation of error analysis, to a 2% uncertainty in both the dimensionless pressure drop and the Deborah number at each point. At low Deborah numbers, when the elasticity of the fluid is negligible, one would expect the fluid to be Newtonian with a dimensionless pressure drop close to one, as confirmed in Figure 3-8. As the Deborah number is increased, the experiments show a marked increase in the dimensionless pressure drop beginning at a critical Deborah number of $De_{cri} = 0.4$. This value is quite close to a Deborah number of $De = 0.5$, at which *coil-stretch transition* occurs in a homogeneous extensional flow. Beyond this critical point the dimensionless pressure drop becomes a monotonically increasing function of the Deborah number of the form $\mathscr{P} = 1 + 0.2 (De - De_{cri})$ for $De \le 5.0$. As the Deborah number is increased still further, the dimensionless pressure drop appears to saturate, plateauing at a value of $\mathscr{P} \approx 2.1$.

The increase in the pressure drop above the Newtonian result for flows above the critical Deborah

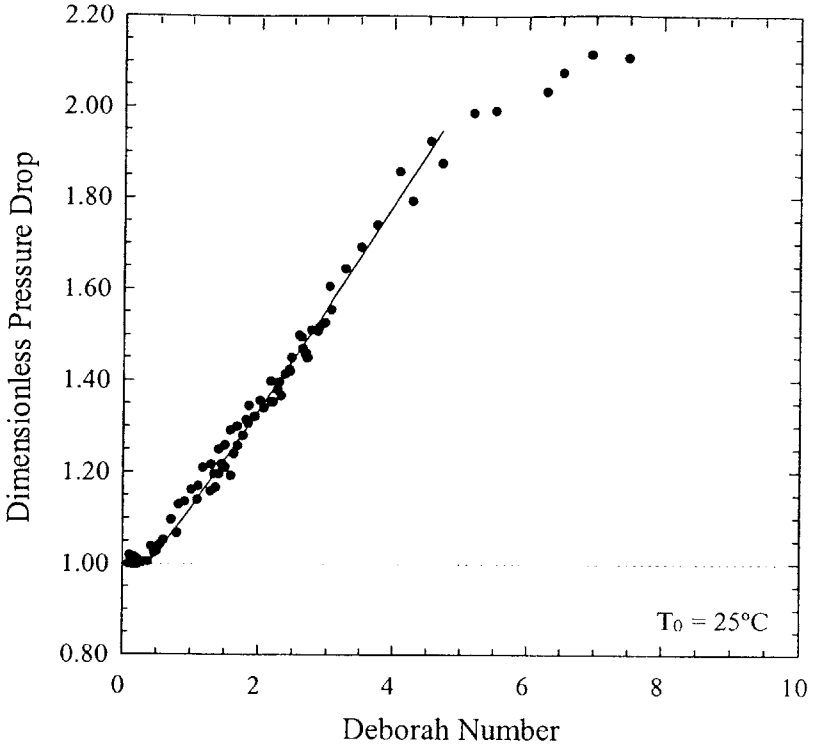

Figure 3-8 Dimensionless pressure drop $\mathcal{P}(De) = \Delta P'_{24}(De, Q) / \Delta P'_{24}(De = 0, Q)$ of the 0.025wt% PS/PS solution across the 4:1:4 axisymmetric contraction as a function of Deborah number $De = \lambda_0 \dot{\gamma}$. The figure includes: '●', experimental data; '—', linear regression of the form $\mathcal{P} = 1 + 0.2\,(De - De_{cr1})$.

number De_{cr1} is consistent with previous experimental studies for flow of polyacrylamide-based flows across a 4:1:4 orifice [Cartalos and Piau 1992] which also showed a large increase and ultimate saturation in the dimensionless pressure drop $\mathcal{P}(De)$. Large additional pressure drops have also been observed in entry flows of polymer solutions in 4:1 contractions [Binding and Walters 1988; Boger and Binnington 1990; Eisenbrand and Goddard 1982; James and Saringer 1980]. By contrast, numerical studies for both the 4:1 contraction [Coates *et al.* 1992; Keiller 1993] and the 4:1:4 orifice [Szabo 1997] show that for creeping flows of simple viscoelastic models such as the FENE-P and Oldroyd-B equations the dimensionless pressure decreases at moderate De ~O(1). In the case of FENE-P dumbbell calculations, small increases in the dimensionless pressure drop are observed as the molecules approach maximum elongation, but Szabo *et al.* report a maximum increase of approximately 10% at a Deborah number of $De = 9.5$ for a finite extensibility of $L = 5$. Simulations of viscoelastic flows into 4:1 contractions with multimode nonlinear models do show increases in the Couette correction with Deborah number [Bernstein *et al.* 1994; Gupta *et al.* 1997], however,

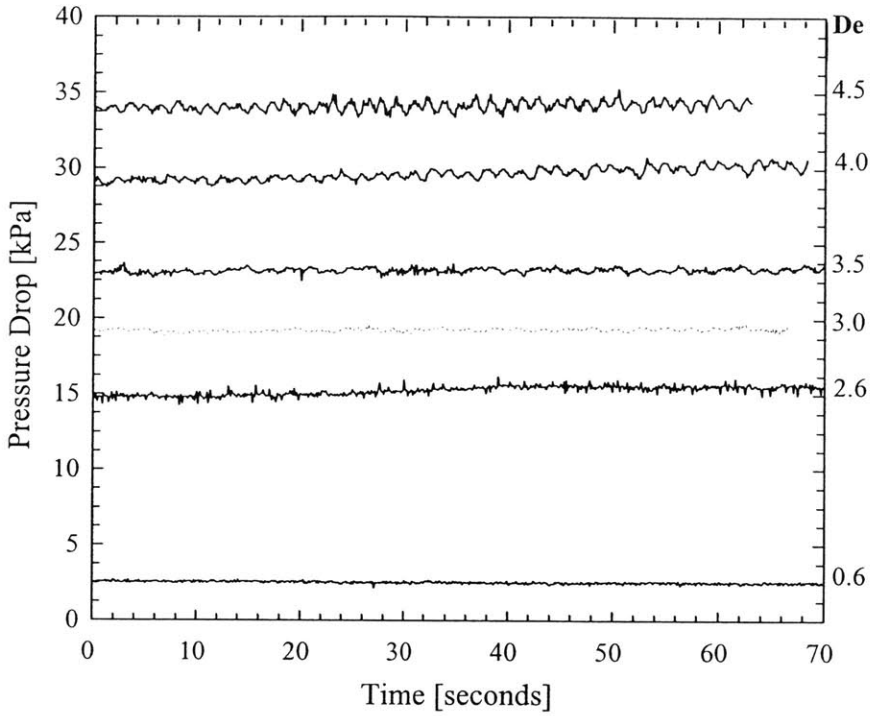

Figure 3-9 Pressure drop (ΔP_{24}) across the contraction plane as a function of time for the 0.025wt% PS/PS solution at various Deborah numbers. The oscillations in the pressure show the onset of a flow instability at a critical Deborah number of $De_l = 2.6 \pm 0.1$.

this is associated primarily with shear-thinning effects in the viscosity arising from the decrease in the scaled wall shear stress in the downstream tube at high shear rates. Such effects are not possible in the present work due to the replacement of the capillary tube downstream of the contraction plane with a diverging flow and the constant viscosity of the PS solvent. The experimentally observed increase in the pressure drop must thus arise from viscoelastic effects associated with the rapid converging and diverging flow.

While visualizing the flow of the 0.025wt% PS/PS solution, a slow non-symmetric pulsating of the enlarged corner vortices was observed at large Deborah numbers. This periodic growth and decay of the corner vortex is associated with the onset of a supercritical Hopf bifurcation. Figure 3-9 shows the temporal variation in pressure drop $\Delta P_{24}(t)$ as the flow rate and the Deborah number are increased from $De = 0.6$ to $De = 4.5$. Oscillations in the pressure drop data become visually apparent for Deborah numbers larger than $De > 2.8$ and the magnitude of these fluctuations increase dramatically with increased Deborah number. Similar pressure drop fluctuations arising from elastic instabilities in strong converging/diverging flows such as flow through banks of cylinders have been previously observed [Khomami and Moreno 1997].

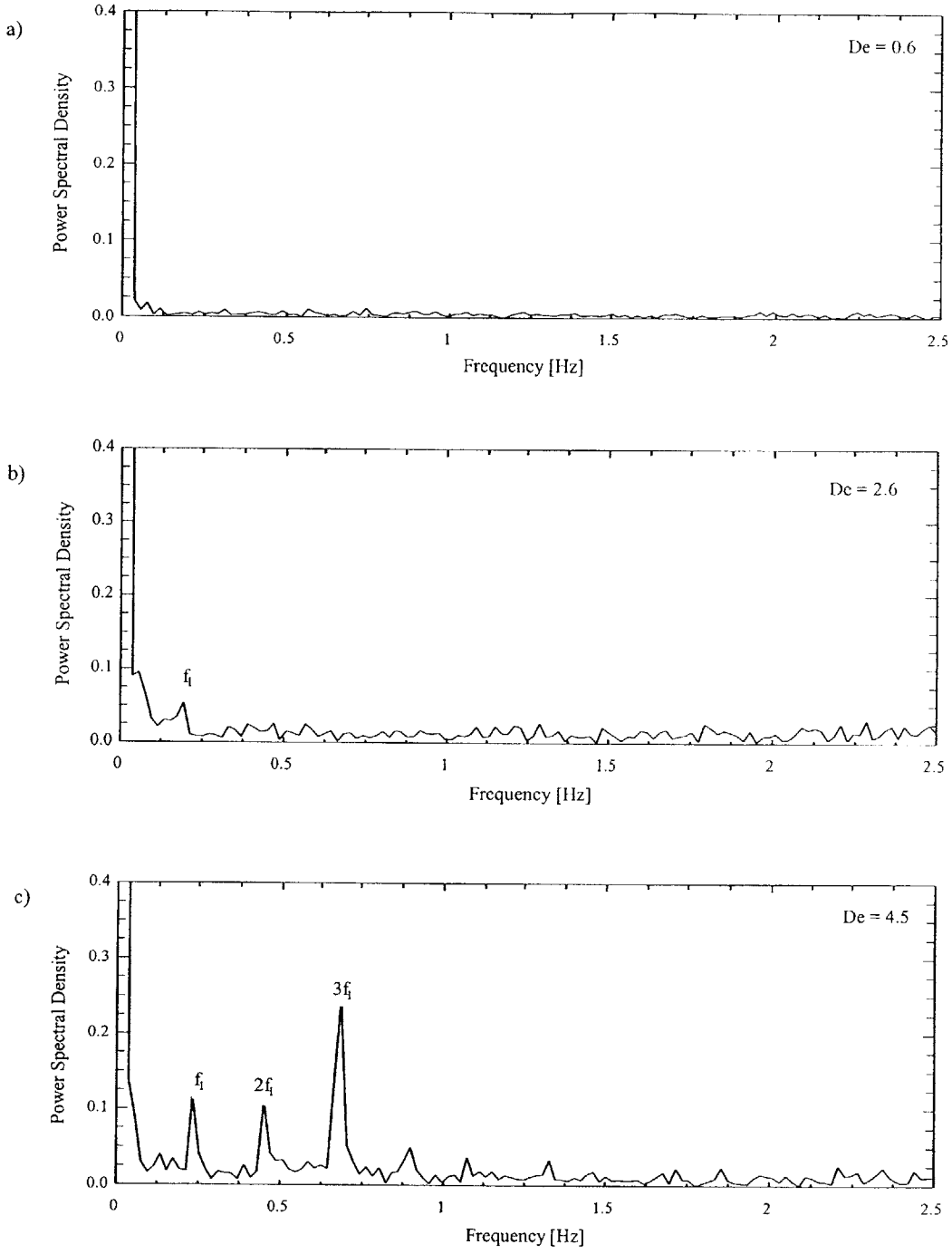

Figure 3-10 Power spectral density plots of pressure drop ΔP_{24} for 0.025wt% PS/PS solution at three different Deborah numbers a) $De = 0.6$, b) $De = 2.6$ and c) $De = 4.5$ showing the onset of a supercritical elastic flow instability.

A fast Fourier transform (FFT) was performed on the pressure drop data to determine the frequency of the vortex oscillations and to determine the critical Deborah number for the onset of this elastic flow instability. Figure 3-10 shows the power spectral density of the signal as the Deborah number is increased. Figure 3-10a shows the Fourier spectrum for $De = 0.6$; the pressure drop data is clearly stable in time, with no peaks discernable above the background noise. Figure 3-10b indicates the first signs of the onset of a local flow instability at a critical Deborah number for vortex oscillation of $De_{crit} = 2.6 \pm 0.1$. A single small peak at a the fundamental oscillation frequency $f_1 = 0.20$Hz can be discerned above the noise floor. At this critical Deborah number the oscillations observed in the pressure drop are not observable in the global flow patterns or in the vortex structure. However, at a second critical Deborah number $De_{crit} = 2.8 \pm 0.1$, onset of a global elastic instability is characterized by unsteady flow patterns and an asymmetric precessing of the corner vortices. As the Deborah number is further increased, the intensity of the pressure drop fluctuations grows in amplitude, the frequency of oscillations slowly increases and higher harmonics of the fundamental frequency begin to appear. At a Deborah number of $De = 4.5$, the FFT in Figure 3-10c contains two strong harmonics of the fundamental frequency ($f_1 = 0.23$Hz) at $f_2 = 2f_1 = 0.45$Hz and $f_3 = 3f_1 = 0.68$Hz.

Similar supercritical Hopf bifurcation were first observed by Muller while studying the flow a PIB/PB/K Boger fluid through a 4:1 contraction [Lawler 1986]. However, in contrast to our present observations and the detailed studies of McKinley *et al.* using a PIB/PB/C14 Boger fluid [McKinley *et al.* 1991], Lawler *et al.* found the flow returned to a steady two-dimensional motion as the Deborah number was increased further. The flow of the 0.025wt% PS/PS solution used in the present study remains time-dependent for all Deborah numbers tested above De_{crit}. The nature of this flow instability will be discussed in more detail in conjunction with the LDV measurements in Section 4.3.3.

3.3.3 *Flow Visualization*

Flow visualization was used to observe vortex growth and development in the upstream tube with increasing Deborah number. Figure 3-11 shows streak images created using the technique discussed in §2.2. The first image shows the particle streamlines for a low Deborah number, $De = 0.05$. At such low flow rates, the 0.025wt% PS/PS solution is essentially Newtonian and small weak recirculation zones or 'Moffatt vortices' (with characteristic concave dividing streamlines) can be seen in the stagnant corners just upstream of the contraction plane. As the Deborah number is increased, the corner vortices increase in size and strength. The presence or the absence of a lip vortex has been noted in many different studies and depends on the both the fluid used and the contraction ratio through which it is forced [Boger 1987]. In contrast to

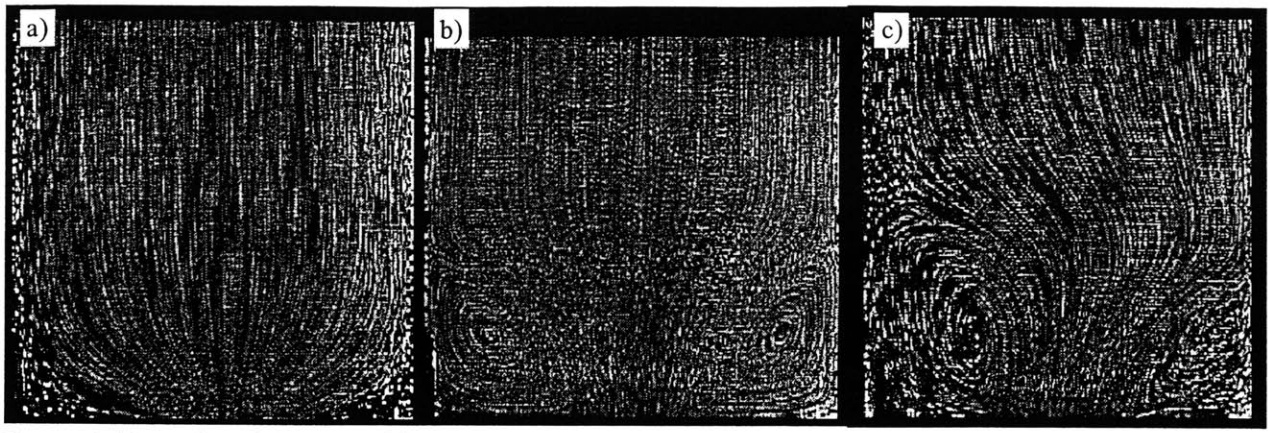

Figure 3-11 Streak images of flow upstream of the contraction for Deborah numbers of a) $De = 0.05$, b) $De = 2.6$ and c) $De = 5.5$ showing streamline patterns and upstream vortex growth.

the results of other contraction flow experiments with PIB/PB fluids [Boger 1987; McKinley *et al.* 1991], for the PS/PS fluid in the 4:1:4 contraction-expansion we do not observe the formation of a separate and distinct time-dependent lip vortex. Instead the corner vortex 'fingers' out towards the contraction entrance, the dividing streamline becomes convex and then proceeds to grow upstream. Figure 3-11b shows the streak lines for a Deborah number of $De = 2.6$. This flow demonstrates the large, convex vortices indicative of highly elastic converging flow and it also corresponds to the critical value of Deborah number for the onset of the local instability. Even though the instability is present in the pressure measurements by this point, there is no noticeable effect on the streak line images, at least for this time exposure of $\Delta t = 1.3$ seconds which is somewhat smaller than the characteristic period of the pressure oscillations. This is not the case for the streak lines in Figure 3-11c which indicate the presence of a global instability in the flow at a Deborah number of $De = 5.5$ and clearly show the non-symmetric corner vortex. Visual observations of this vortex show that the vortex boundary precesses in the azimuthal direction so that fluid elements follow a helical path into the orifice.

The precessing of the upstream vortex is demonstrated more clearly in Figure 3-12 which shows three streak images taken at a Deborah number of $De = 4.7$ at various times throughout one period of the vortex oscillation cycle. Figure 3-12a shows a symmetric flow field at time $t = t_0$. As seen in Figure 3-12b, after an additional one quarter of the fundamental period of vortex oscillation, $t = t_0 + 1 / (4 f_1)$, the symmetry is broken by a marked increase in the size of the right hand vortex and a substantial decrease in the size of the left hand vortex. If the time is increased by an additional half period to $t = t_0 + 3 / (4 f_1)$, the anti-symmetric vortex structure mirrors itself about the centerline of the upstream tube. The precession of the large vortex to the left of the upstream tube and the corresponding shift of the small vortex to the right

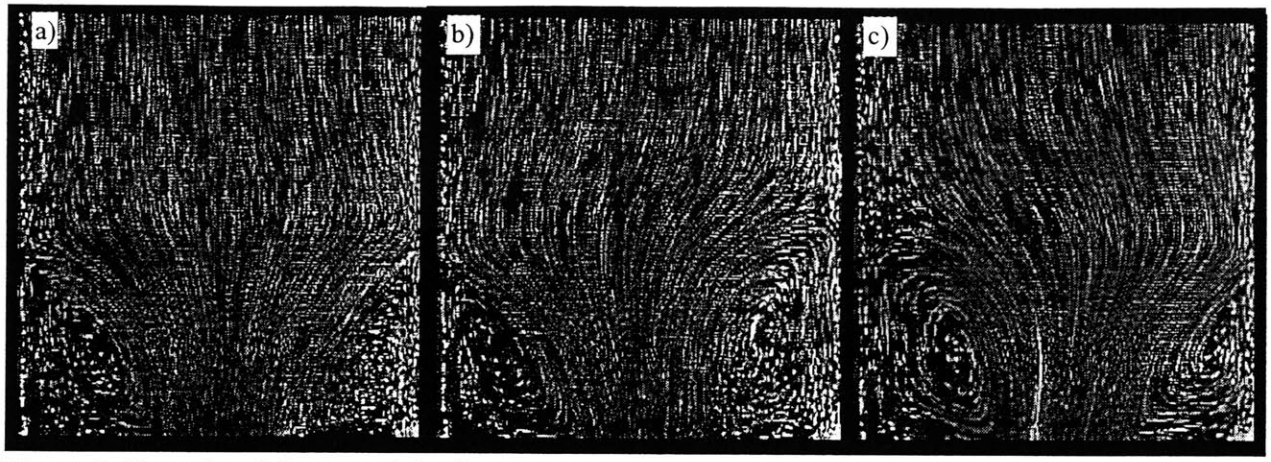

Figure 3-12 Streak images of the flow upstream of the contraction plane demonstrating the precession of the upstream corner vortex for a Deborah number of $De = 4.7$ at times corresponding to fractions of the fundamental period of oscillation, $1/f_1 = 5.1$s, a) $t = t_0$, b) $t = t_0 + 1/(4f_1)$ and c) $t = t_0 + 3/(4f_1)$.

hand side can be readily distinguished in Figure 3-12c.

Quantitative measurements of the vortex size were extracted digitally from the streak images of each experiment. Figure 3-13 shows the evolution in the dimensionless reattachment length $\chi \equiv L_v/2R_1$ and the dimensionless coordinates of the vortex center $\zeta \equiv Z_v/2R_1$ and $\xi \equiv R_v/2R_1$ as a function of Deborah number. Unfortunately, due to the weakness of the corner vortex, it is not possible to accurately locate the exact center of the corner vortex for flows at $De < 1.2$. At low Deborah numbers the dimensionless reattachment length is constant with the expected value for creeping Newtonian flow, $\chi_{\text{Moffatt}} \approx 0.17$. As the flow rate is increased the reattachment length and the axial location of the vortex center begin to increase monotonically with Deborah number. The radial location of the vortex center moves outward from the center of the tube to a radial position $R_v = 0.56R_1$ where it saturates and remains constant as the vortex grows upstream with increasing Deborah number. Once the critical Deborah number for the onset of the global elastic instability is reached, the reattachment length decreases slightly and begins to oscillate in size. At this point it becomes very difficult to determine the location of the vortex center using the streak images as a result of the global unsteadiness of the vortex structure. Consequently no values above a Deborah number of $De = 2.8$ are reported for the coordinates of the vortex center.

The trends of this data match quite well previous experimental results for contraction flows of other polymer solutions that do not lead to formation of lip vortices [Boger 1987; Boger and Binnington 1990; Byars *et al.* 1997; McKinley *et al.* 1991]. Although, to our knowledge, this is the first time that the location

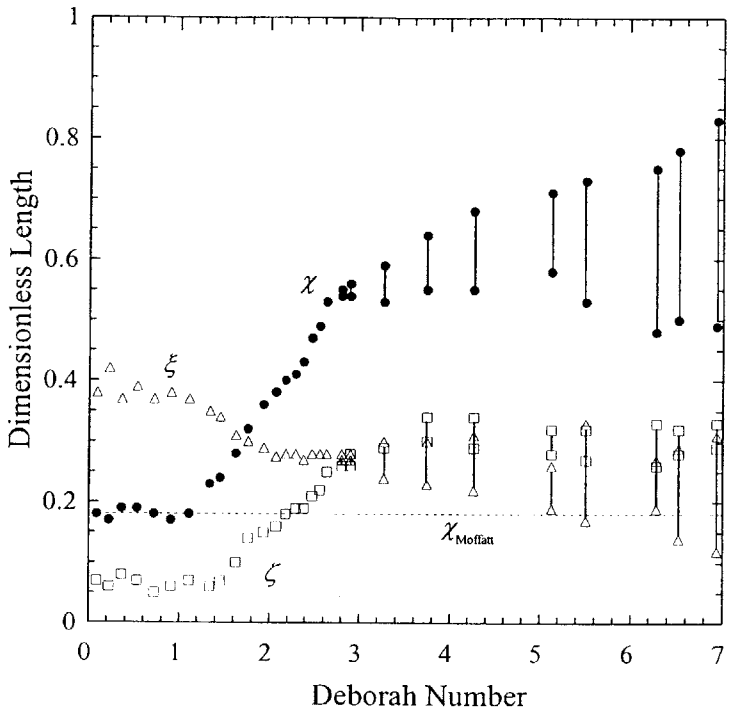

Figure 3-13 Characteristics of the upstream vortex enhancement as a function of Deborah number: '●', vortex reattachment length, $\chi = L_v / 2R_1$; '△', radial location of the vortex center, $\xi = R_v / 2R_1$; '□', the upstream location of the vortex center, $\zeta = Z_v / 2R_1$.

of the corner vortex center has been reported experimentally, it has been reported for numerical work in the past [Szabo 1997]. In the work of Szabo *et al.* the upstream vortex started as a small Newtonian vortex, began to grow outwards toward the re-entrant corner and then proceeded to grow upstream as the Deborah number is increased. Except for the 'fingering' of the corner vortex towards the re-entrant corner at the onset of vortex enhancement, the vortex behavior reported by Szabo *et al.* is qualitatively similar to the vortex growth behavior observed in the present experiments.

Figure 3-14a shows the transient dimensionless extra pressure drop $\mathscr{P}(t)$ following a step increase in the driving piston velocity from initial start-up until the onset of the elastic flow instability for a flow at a Deborah number of $De = 4.7$. Seven points have been labeled on the dimensionless pressure drop curve and the corresponding vortex center and reattachment points have been plotted in Figure 3-14b. Mirrored by the development of the corner vortex, the dimensionless pressure drop evolves in four distinct regions: a sharp jump in dimensionless pressure drop attributable to the start-up of the experimental system for times $t <$ A, a region of fast growth in the dimensionless pressure drop and vortex size for times A $< t <$ C, a region

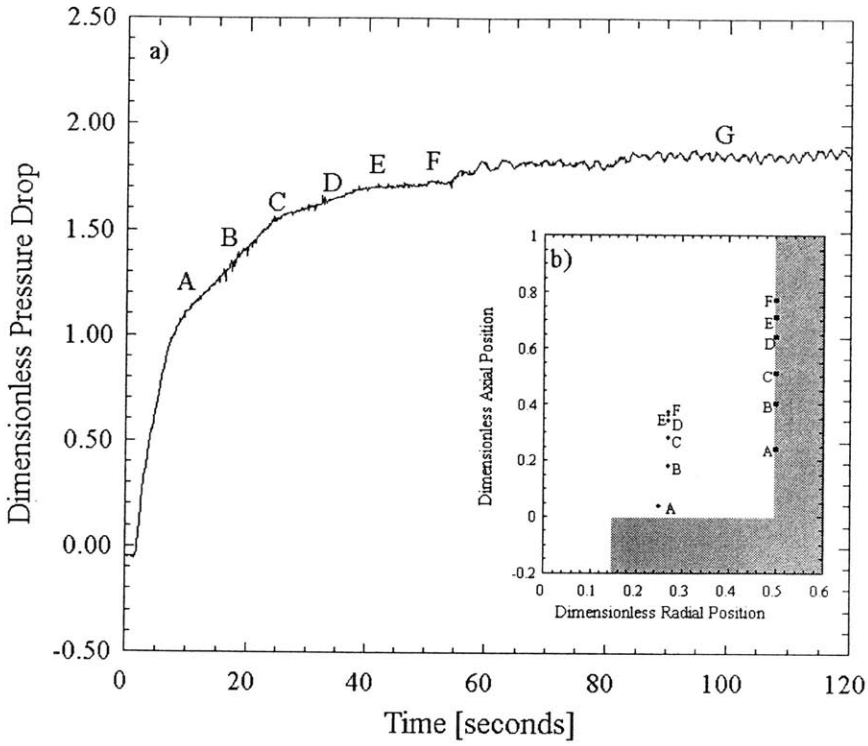

Figure 3-14 Transient dimensionless pressure drop (a) and vortex size (b) data for the flow of the 0.025wt% PS/PS solution through an axisymmetric contraction at a Deborah number of De = 4.7 from start-up to the onset of an elastic flow instability.

of slower changes in dimensionless pressure drop and vortex growth that approaches a local steady-state value of pressure drop and vortex size for times C < t < F and, finally, the onset and growth of the small amplitude oscillations in dimensionless pressure drop and vortex size associated with the elastic flow instability for t > F. This evolution of the dimensionless pressure drop and the corner vortex is in good qualitative agreement with the numerical simulations of Szabo *et al.* [Szabo 1997].

3.3.4 *Digital Particle Image Velocimetry Measurements*

We have also used the digital images of the particle motions near the contraction plane to compute instantaneous DPIV vector fields. It should be noted that there are several difficulties encountered in the implementation of DPIV technique which need to be addressed in future work. The principal difficulty arises from the limited dynamic range of digital particle image velocimetry. For particle displacements on the order of the correlation window size there is a progressive loss of information as seed particles are swept out of

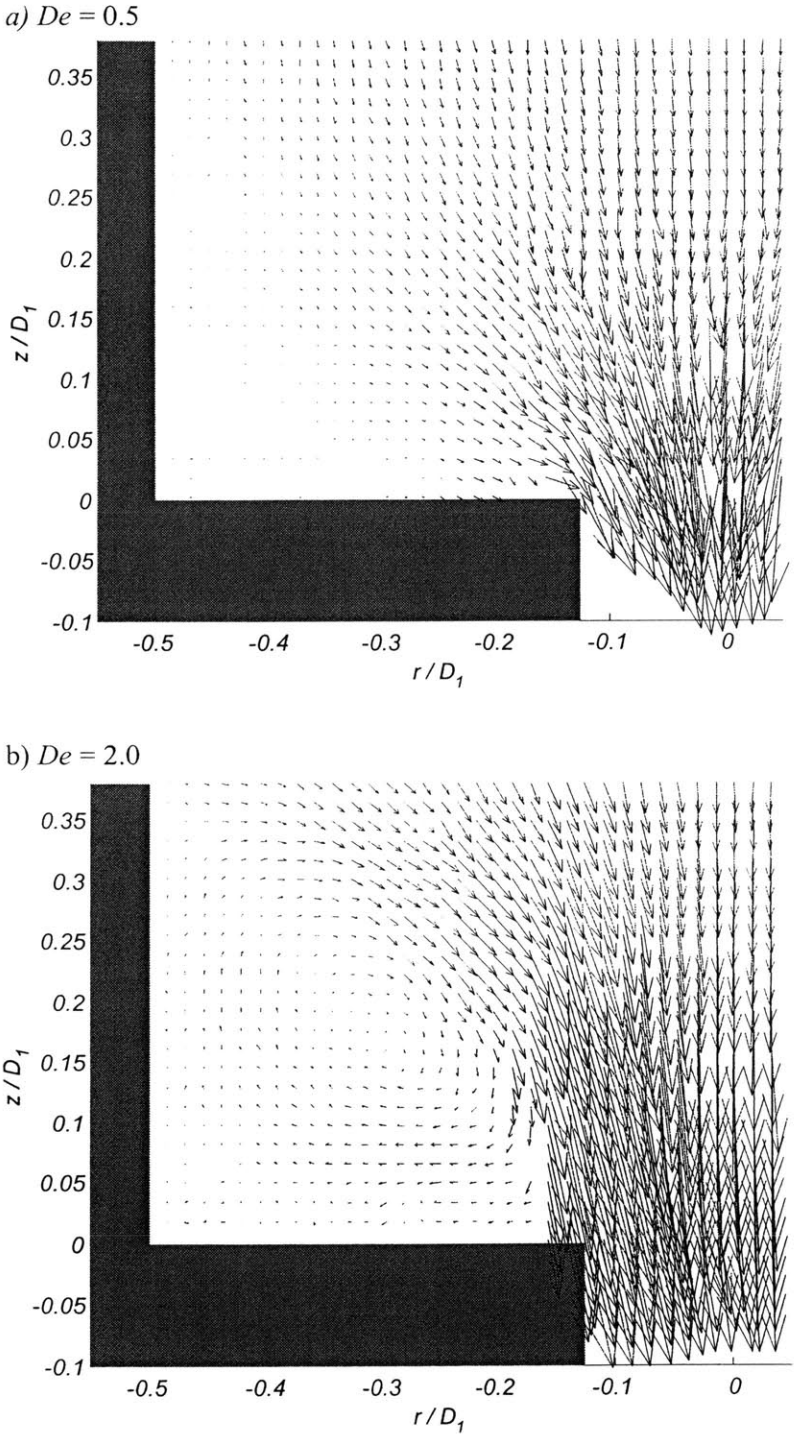

Figure 3-15 PIV vector fields for the flow of the 0.025wt% PS/PS solution into the axisymmetric contraction at Deborah numbers of a) $De = 0.5$ and b) $De = 2.0$.

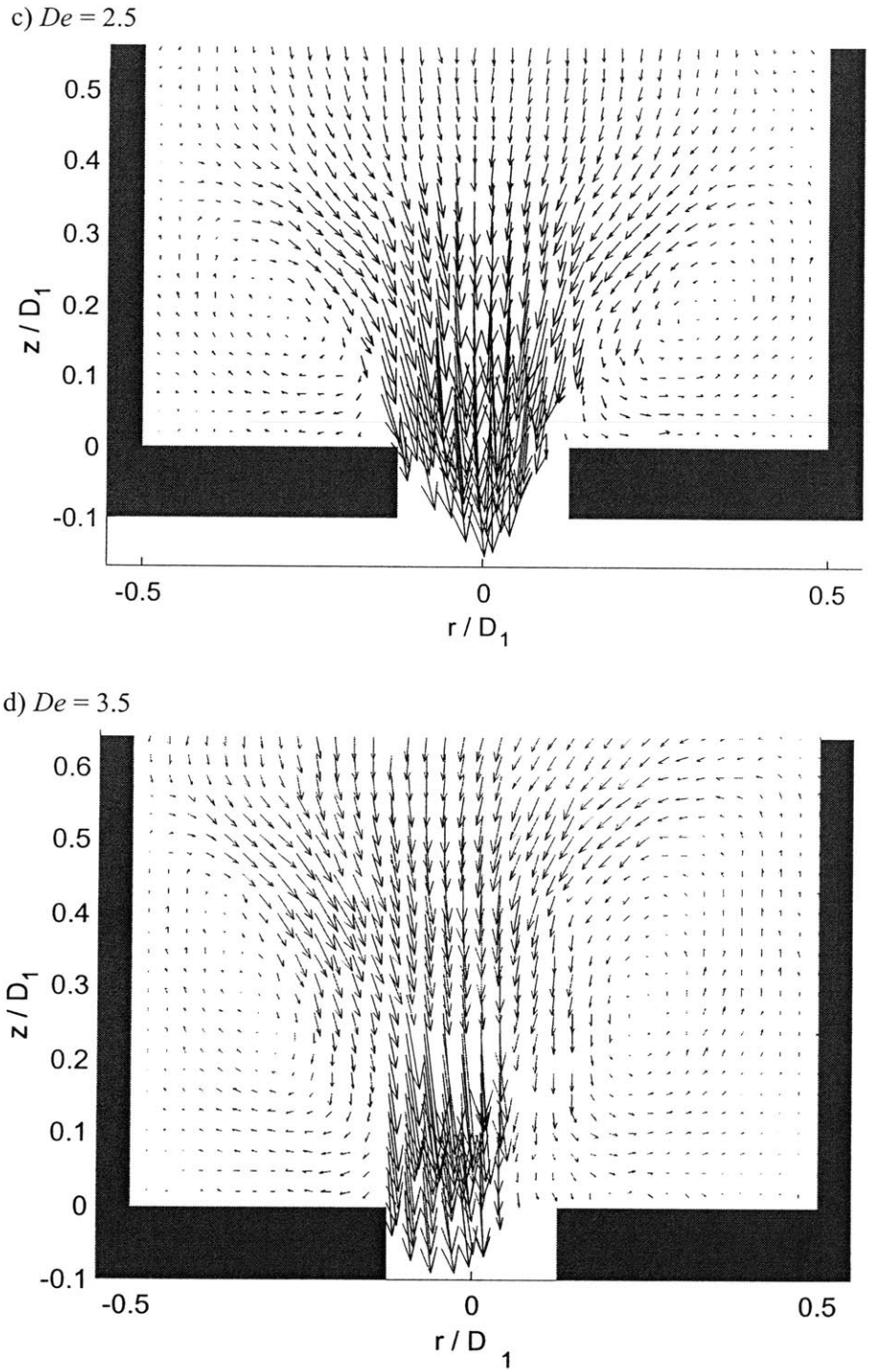

Figure 3-15 PIV vector fields for the flow of the 0.025wt% PS/PS solution into the axisymmetric contraction at Deborah numbers of c) $De = 2.5$ and d) $De = 3.5$.

the correlation region. Conversely, increasing the window size leads to a decrease in the spatial resolution that can be attained. This 'uncertainty principle' is of particular importance near the contraction plane, and the loss of particles into the throat results in uncorrelated regions as the Deborah number gets larger. Since our primary focus in the present work is on the global characteristics of the upstream vortex rather than the quantitative features of the converging flow very near the throat we have selected a field of view that can resolve the entire width of the upstream tube.

Figure 3-15 shows the results of DPIV for four Deborah numbers, De = 0.5, 2.0, 2.5 and 3.5. The vectors are scaled such that an arrow of length $\Delta z / 2R_1 = 0.1$ corresponds to a velocity of $v_z / \langle v_z \rangle_2 = 0.2$ for Figure 3-15a,b and $v_z / \langle v_z \rangle_2 = 0.1$ for Figure 3-15c,d.

At low Deborah numbers the corner vortex is so weak that it cannot be resolved readily by the DPIV algorithm, but as the Deborah number is increased, the vortex grows in strength and its structure is easily captured. Similar DPIV images have been generated for all Deborah numbers at which flow visualizations discussed in Section 3.3.2 were reported. It is hoped that these vector fields will be useful in detailed comparison between experimental and numerical work in the future.

3.3.5 *Laser Doppler Velocimetry Measurements*

Axial velocity measurements taken along the centerline of the 4:1:4 axisymmetric abrupt contraction-expansion are shown in Figure 3-16. The dimensionless velocity measurements, $v_z/\langle v_z \rangle_2$, are plotted from locations far upstream of the contraction plane, $z/R_2 > -10$, to positions inside the throat, $z/R_2 = 0.25$. In a Poiseuille flow, the velocity on the centerline is equal to twice the average velocity in the tube $v_z(r = 0) = 2\langle v_z \rangle$. Therefore, one would expect that for a constant viscosity fluid, the dimensionless centerline velocity well upstream of the contraction plane would be equal to $v_z/\langle v_z \rangle_2 = 2/\beta^2 = 0.125$, while the dimensionless velocity within the throat would be equal to $v_z/\langle v_z \rangle_2 = 2$. This is confirmed far upstream, where the shear rate is quite low and where there are no extensional effects influencing the velocity profile. As the fluid approaches the contraction, the velocity increases to conserve mass as the radius of the tube abruptly contracts. At low Deborah numbers, this increase is observed to occur smoothly, beginning at an axial position of $z/R_2 \approx -2.5$. With the initial increase in Deborah number, the velocity increase shifts slightly downstream towards the contraction plane; however, as the flow rate is increased further, the velocity gradient along the centerline is reduced and the influence of the contraction is felt by the flow further and further upstream. This latter effect takes place in conjunction with the elastic vortex growth observed in Section 3.3.3. As the fluid enters the throat, there is a sharp elastic overshoot in the velocity at all Deborah

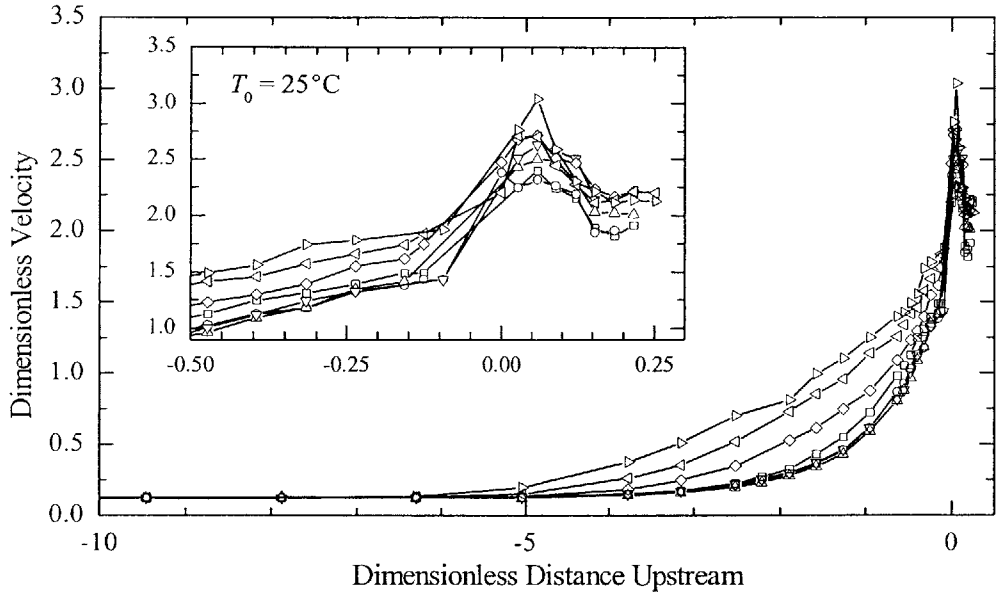

Figure 3-16 Laser Doppler Velocimetry (LDV) measurements showing the dimensionless axial velocity along the centerline, $v_z/\langle v_z \rangle_2$, as a function of dimensionless axial position, z/R_2, for the flow through a 4:1:4 axisymmetric contraction-expansion. The figure includes: □, Deborah number of De = 0.5; ○, De = 1.0; △, De = 1.5; ▽, De = 2.0; ◇, De = 3.0; ◁, De = 4.0; and ▷, De = 5.0.

numbers, including a small jump in the low Deborah number case, De = 0.5. The magnitude of this overshoot increases with Deborah number, but the location of the maximum does not change. Further downstream, the centerline velocity reduces to a value consistent with Poiseuille flow, for all but the highest Deborah numbers in which the velocity remains slightly high than $v_z/\langle v_z \rangle_2 = 2$ for the range of axial positions that can be measured with the present apparatus. Additional LDV measurements show that, the non-monotonic trend in the evolution of the centerline velocity profile is independent of contraction ratio and re-entrant corner curvature. This will be discussed in more detail in Chapters 4 and 5.

3.4 Discussion

In this work, we have measured the additional pressure drop associated with strong extensional flow of a monodisperse polymer solution through a 4:1:4 axisymmetric contraction-expansion. This large additional pressure drop is not predicted by existing numerical computations with simple dumbbell models.

Possible reasons for these discrepancies may lie in the way different models treat polymer chains. In quasilinear dumbbell models, such as the Oldroyd-B model, the entropic elasticity of the Hookean spring can store considerable amounts of energy as a polymer molecule is extended. In a Lagrangian unsteady flow such as flow through an orifice, a dumbbell is accelerated and undergoes a transient uniaxial elongation, absorbing energy as the polymer chain unravels. The stored energy is then released downstream of the contraction as the polymer chain rapidly relaxes under biaxial expansion. The result is a decrease in the global pressure drop because a portion of the energy lost in the case of a Newtonian fluid is returned to the flow. If finite extensibility is added to the dumbbell model, similar behavior is observed until the chains approach full extension; beyond this point, the polymer chains behave more like rigid rods and the additional viscous drag on the polymers increases the computed pressure drop across the contraction. However, simulations with the FENE-CR model indicate that this effect is insufficient to account for the huge increases in pressure drop across the contraction seen in this work and in the earlier work of Cartalos & Piau [Cartalos and Piau 1992].

These discrepancies between the numerical and the experimental work in a prototype complex flow support the observations made in uniaxial transient elongation by Doyle *et al.* of an additional dissipative contribution to the polymeric stress manifested in the form of a *stress-conformation hysteresis* [Doyle *et al.* 1998]. This hysteresis would result in an additional dissipative stress term present during the rapid extension of the polymer molecules. The first theoretical considerations of such phenomena were made by Ryskin [Ryskin 1987] who analyzed the pressure drop measurements of King and James [King and James 1983] for dilute polymer solutions flowing in a conical entrance region at high Reynolds number. In the resulting 'yo-yo' model the chains are envisaged to unravel in a similar manner to a yo-yo with the coiled regions near the end connected by a central rigid rod. Viscous drag on the elongating rod results in a dissipative polymeric contribution that increases linearly with the deformation rate $\dot{\varepsilon}$. No general constitutive equation was formulated by Ryskin, however, on the basis of Brownian dynamic simulations, Rallison [Rallison 1997] recently proposed one form for the additional dissipative stress

$$\boldsymbol{\tau}^{\mathrm{d}} \propto \eta_2 \left[\frac{(\boldsymbol{A}:\dot{\boldsymbol{\gamma}})\boldsymbol{A}}{tr\boldsymbol{A}} \right] \tag{3-19}$$

where $\boldsymbol{A} = \langle \boldsymbol{QQ} \rangle / Q_{eq}^2$ is the ensemble average of the mean end-to-end contour length of the molecule and η_2 is the additional contribution to the viscosity.

In recent work Yang and Khomami [Yang and Khomami] have computed viscoelastic flow past a sphere – another benchmark flow involving rapid stretching and relaxation – using the full FENE model and

'distributional hysteresis'. To capture such effects it may thus be necessary to resolve the internal dynamical structure of the chains as observed by Perkins et al. [Perkins *et al.* 1997] by performing simulations with bead-rod chain models that can capture such 'configurational hysteresis'.

Although it is not possible in a complex nonhomogeneous flow such as creeping flow through a contraction-expansion to readily estimate the additional pressure drop arising from contributions to the polymeric stress tensor of the form in Equation 3-10, it is worth noting that the additional pressure drop $\mathscr{P}$ (i.e. the pressure increase beyond that associated with the linear, Newtonian change in $\Delta P'_{24}(Q)$ with increasing flow rate, Q) does increase linearly with the Deborah number. The combined pressure drop, vortex size and DPIV measurements for a well characterized dilute monodisperse polymer solution should make the data presented in this paper suitable for a quantative comparison with future numerical simulations using such models.

It is also possible to use the pressure drop data presented above to estimate an approximate extensional viscosity using the technique developed by Cogswell [Cogswell 1972] which assumes the fluid viscosity to follow a power-law profile in shear (n = 1 in our case). The resulting equations are of the form

$$\bar{\eta} = \frac{9\pi}{64}\frac{R_2^3}{Q}\left(\frac{\Delta P_{ext}}{2\tau_w}\right)\Delta P_{ext} \tag{3-20}$$

$$\dot{\varepsilon} = \frac{4}{3\pi}\frac{Q}{R_2^3}\left(\frac{2\tau_w}{\Delta P_{ext}}\right) \tag{3-21}$$

Cogswell's extensional viscosity determined using the above expression can be approximated as a linear combination of the extensional viscosity of the solvent η_s and the extensional viscosity resulting from the dissipative contribution to the polymeric stress $\bar{\eta}^d$, $\bar{\eta} = 3\eta_s + \bar{\eta}^d(\dot{\varepsilon})$. For a rapid contraction-expansion we know that the additional pressure drop arising from the FENE-like elastic stretching is essentially zero [Szabo 1997]. We can now calculate an approximate dissipative stress from the dissipative extensional viscosity and the extension rate $\Delta\tau^d = \dot{\varepsilon}\,\bar{\eta}^d$. Figure 3-17 shows a plot of the approximate dissipative stress $\Delta\tau^d$ as a function of the extension rate $\dot{\varepsilon}$. As expected, the dissipative stress starts at zero and Coggswell's analysis correctly predicts $\bar{\eta} \approx 3\eta_s$ for low extension rates where the fluid is Newtonian. As the extension rate is increased, the dissipative stress begins to increase slowly until an extension rate of $\dot{\varepsilon} = 14\ s^{-1}$ after which it grows linearly with extension rate through the onset of the elastic flow instability (at $\dot{\varepsilon} = 17.8\ s^{-1}$) at and

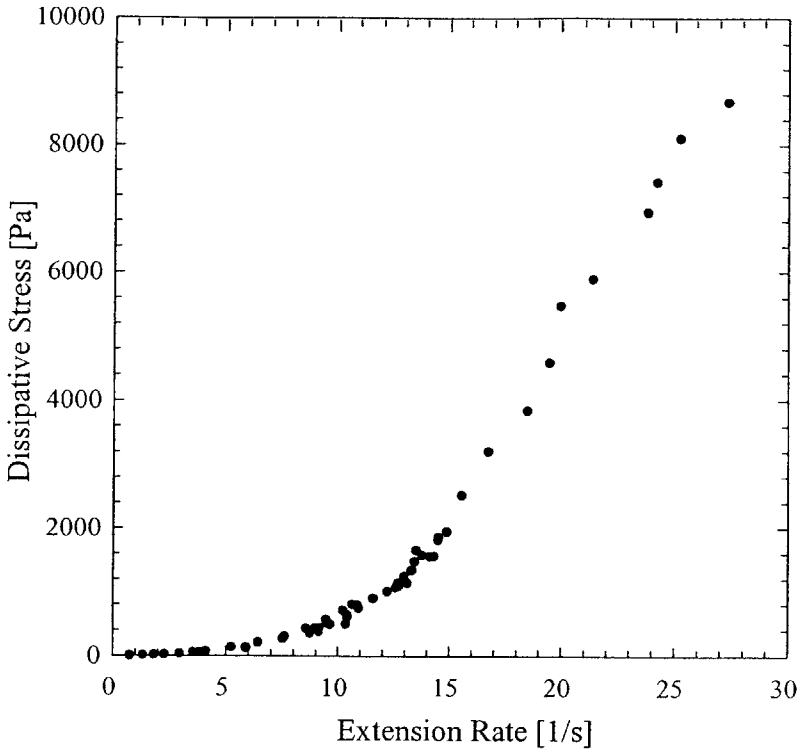

Figure 3-17 Estimated value of the dissipative stress $\Delta\tau^d$ as a function of the extension rate $\dot{\varepsilon}$ for the flow of a 0.025wt% PS/PS solution through a 4:1:4 axisymmetric contraction at a constant Hencky strain of $\varepsilon = 2.77$.

through the plateau of the dimensionless pressure drop. This approximate dissipative stress can be compared with the values given by Orr and Sridhar who experimentally determined the dissipative stress of PIB at various extension rates and Hencky strains from transient uniaxial extension measurements. The total Hencky strain experienced by a fluid element moving along the centerline of the 4:1 axisymmetric contraction region from far upstream to the middle of the throat is given by

$$\varepsilon \equiv \int_0^{t_1} \dot{\varepsilon}\, dt = \int_{v_z(-\infty)}^{v_z(z = 1/2L_c)} \frac{dv_z}{v_z} = \ln(\beta^2) = 2.77 \qquad (3\text{-}22)$$

if we assume a fully developed Poiseuille flow in the throat. Thus the dissipative stress calculated here should be compared with experiments of Orr and Sridhar conducted at Hencky strains of $\varepsilon = 2.77$. Unfortunately, at such a low Hencky strain, the experimental strain rates used by Orr and Sridhar were not large enough ($\dot{\varepsilon} < 5s^{-1}$) to demonstrate any substantial dissipative stresses in either our experiments (Figure

3-17) or theirs. However, the dissipative stress is expected to be a function of *both* the extension rate and the Hencky strain, and we can therefore qualitatively compare the two sets of experimental results; each of which tend to increase with extension rate and show maximum dissipative stresses within the experimental range on the order of $O(10^4$ Pa) [Remmelgas *et al.* 1997]. The dissipative stress will be investigated in greater detail in Chapter 7.

It is important to note that the enhanced pressure drops measured experimentally are not directly connected with the onset of any elastic instabilities. The dimensionless pressure drop begins to increase monotonically with Deborah number at $De = 0.4$ while the onset of local elastic instability does not occur until a Deborah number of $De_l = 2.6$. Thus, regardless of whether a numerical simulation can successfully predict the onset of an elastic instability, the chosen constitutive model should still be able to predict the large extra pressure drops associated with the steady motion of non-Newtonian behavior of a dilute polymeric solution before any flow instabilities occur. In fact, we note that in our experiments at controlled displacement rates, the onset of elastic instability in the converging flow of a PS/PS Boger fluid is associated with a lowering in the rate of increase in pressure driving force required. In fluids such as dilute polymer solutions with large contributions to the dissipative stress, the elastic instabilities observed in contraction flows may thus be directly connected to this additional coupling between the conformation ($\boldsymbol{A}$), the local deformation rate ($\dot{\gamma}$) and the resulting stress ($\boldsymbol{\tau}$). Certainly the magnitude of this additional polymeric stress may be expected to modify the local kinematics in the entry flow region and may help to explain why different Boger fluid formulations (eg. PAA/CS/water, PS/PS and PIB/PB systems) exhibit such different patterns of vortex growth in a 4:1 contraction. This may also account for dynamic differences in the flow observed with such fluids in other complex flow geometries; for example the large variations in the evolution of drag coefficient C_D (De) of a sphere sedimenting in a PAA, PS or PIB Boger fluid [Chmielewski *et al.* 1990; Solomon and Muller 1996]. To investigate such effects further it is necessary to measure the dimensionless pressure drops $\mathcal{P}(De)$ in different contraction ratios and for different fluids. We hope to report on such observations in the future. The pressure drop measurements and DPIV measurements coupled with the use of a monodisperse, well-characterized fluid should also make this set of experiments amenable to comparison with numerical work in this benchmark geometry.

CHAPTER 4 The Effect of Contraction Ratio on the Flow through an Abrupt Axisymmetric Contraction-Expansion

4.1 Introduction

The flow of a viscoelastic fluid through an axisymmetric contraction-expansion is a complex flow containing regions of strong shearing near the walls, nonhomogeneous uniaxial extension along the centerline upstream of the contraction plane and nonhomogeneous biaxial expansion downstream of the expansion. In this chapter, the same 0.025wt% PS/PS Boger fluid used in the experiments presented in Chapter 3 is used to investigate the kinematics of the flow through several axisymmetric contraction-expansions of different contraction ratios over a wide range of Deborah numbers. The experimental measurements include global pressure drop and local velocity measurements as well as streak images of the elastically-enhanced upstream vortex structures.

Experimental measurements of the pressure drop for polymer solutions flowing through abrupt axisymmetric contraction-expansions have shown a substantial extra pressure drop well above the value observed for a Newtonian fluid with equal viscosity at the same flow rates by Cartalos and Piau [Cartalos and Piau 1992] and again in the previous chapter. In neither case was the observed viscoelastic enhancement of the pressure drop associated with the onset of an elastic or an inertial flow instability; however, it is not even qualitatively predicted by existing steady-state or transient numerical computations with simple dumbbell models [Coates *et al.* 1992; Keiller 1993; Szabo 1997]. In fact, these models predict a significant viscoelastic *decrease* in the pressure drop with addition of polymer to a Newtonian solvent. The failure of these constitutive models to predict the correct evolution in the properties of complex flows with Deborah number may be due to an inadequate description of the internal molecular conformations of the polymer chains that arise during rapid stretching. This is evident in measurements of transient uniaxial extension where the existence of a *stress-conformation-hysteresis* has been experimentally observed [Doyle *et al.* 1998; Sridhar *et al.* 2000] and computed in bead-rod and bead-spring computations [Doyle *et al.* 1998; Li *et al.* 2000] but has yet to be quantitatively predicted by any simple closed-form differential constitutive model. A complete discussion of previous experimental and numerical studies involving pressure drop measurements in contraction flows is presented in Chapter 3.1. One of the major goals of the research presented in this chapter and the next is to determine what effects systematic changes in the contraction ratio and the curvature of the re-entrant corner will have on the magnitude and the onset of this enhanced pressure drop. Investigation of the role of lip curvature is especially important because a major computational impediment

to simulations of the viscoelastic flow through a contraction-expansion is the development of singular stress fields near a sharp re-entrant corner. The effect of changes in re-entrant corner curvature will be investigated in Chapter 5.

Measurements of the evolution in the pressure drop generate information about the global state of viscoelastic stress in the flow and are an excellent comparative tool when utilized in conjunction with measurements of the flow kinematics such as streak images and velocity measurements. There have been a great number of experimental investigations dealing with the kinematics of the flow through a contraction over a wide range of Deborah numbers, contraction ratios and re-entrant corner curvatures using a large variety of different viscoelastic fluids [Boger 1987; Boger and Binnington 1994; White *et al.* 1987]. In experiments with elastic polymer solutions two distinct pathways for evolution of the vortex growth with Deborah number have been observed, which lead to flow structures typically described in the literature as corner and lip vortices. These experimentally observed vortex growth developments are described in Chapter 3.

The sequence of flow patterns chosen by the viscoelastic fluid is a complex function of the contraction ratio and the re-entrant lip curvature. Results prior to 1987 are summarized in Boger [Boger 1987] and Table 4-1 summarizes more recent observations for several different Boger fluid formulations. In general, as the contraction ratio is increased, the flow moves from the lip vortex to the corner vortex flow regime, but the critical contraction ratio for this crossover in vortex evolution pathway is strongly dependent on the properties of the test fluid and impossible to predict *a priori*. So, why do two elastic fluids such as PIB/PB and PAA/CS Boger fluids, which have very similar viscoelastic properties, act so differently in this and other complex flows? Many researchers have postulated that the answer must arise from differences in the transient extensional rheology [Boger and Binnington 1994; Chmielewski *et al.* 1990; McKinley *et al.* 1991]. Until quite recently, reliable measurements of the extensional stress of dilute polymer solutions undergoing ideal uniaxial extension were not possible, but with the advent of the filament stretching rheometer, transient uniaxial extensional rheology measurements are now attainable [Anna *et al.* 2001; McKinley and Sridhar 2002], making it possible to test the validity of such assertions.

In addition to investigating the evolution of the pressure drop, another goal of the present study is to determine which vortex evolution path is followed by a dilute and monodisperse polystyrene Boger fluid that has been well characterized in both extension and in steady and transient shear flows. In the previous chapter, we have reported measurements for flow through a 4:1:4 contraction-expansion, but a detailed analysis of the effect of contraction ratio will generate additional insight into the trends observed in the published data on PIB/PB and PAA/CS Boger fluids listed in Table 4-1 when analyzed in conjunction with

measurements of the transient extensional rheology.

In Section 4-3, we first present observation of the enhanced pressure drop through several different contraction-expansions. Flow visualization, digital particle image velocimetry (DPIV) and laser Doppler velocimetry (LDV) are then combined to characterize the evolution in the kinematics of the fluid motion with increasing Deborah number. LDV measurements of fluctuations in the fluid velocity are then used to document the onset of an elastic instability that eventually leads to global oscillations in the flow and the development of an interesting jetting instability as the Deborah number is increased. Finally, in Section 4-4 we discuss the implications of our findings for simulation and modeling of elastic flows through contractions.

	Sharp Re-Entrant Corner	
Boger Fluid	Corner Vortex	Lip Vortex
PIB/PB [Boger and Binnington 1994; McKinley *et al.* 1991]	$\beta \geq 8$	$2 \leq \beta \leq 6.8$
PAA/CS [Boger 1987; Boger and Binnington 1994; Nguyen and Boger 1979]	$\beta \geq 4$	$\beta \leq 2$
PS/PS	$\beta = 4$	

Table 4-1 Vortex growth dynamics for several Boger fluids at various contraction ratios ($\beta = R_1/R_2$, where R_1 is the upstream radius and R_2 is the radius of the contraction).

4.2 Experimental

4.2.1 *Flow geometry*

The same axisymmetric contraction-expansion used in Chapter 3 is employed in these studies. A schematic diagram of the flow cell and the important length scales associated with it can be found in Figure 3-1. The radii of the cylindrical tubes upstream and downstream of the contraction-expansion are equal and remain constant at R_1 (=1.27cm) while the radius within the throat of the contraction is given by R_2. Several different orifice plate configurations yielding various contraction ratios ($\beta \equiv R_1 / R_2$) and contraction lengths (L_c) are listed in dimensionless form in Table 4-2.

Description	Contraction Ratio ($\beta \equiv R_1 / R_2$)	Contraction Length (L_c / R_2)
2:1:2	2	0.5
4:1:4	4	1
8:1:8	8	2

Table 4-2 Description of orifice plate geometries used in this study. In each case the value of the upstream radius is $R_1 = 1.3$cm.

As described in the previous chapter, the fluid is forced at a constant volume flow rate, Q, past two flush mounted pressure transduces, here denoted P_u and P_d, located at positions $z_u = -7.62$cm far upstream and $z_d = 8.26$cm far downstream of the contraction plane (located at $z = 0$). Again, the extra pressure drop across the contraction-expansion is isolated by removing the pressure drop resulting from the Poiseuille flow in the upstream and downstream tubing as well as the Poiseuille flow within the throat of the contraction-expansion are removed

$$\Delta P'_{ud} = \Delta P_{ud} - \frac{8Q\eta}{\pi}\left(\frac{L}{R_1^4} + \frac{L_c}{R_2^4}\right), \tag{4-1}$$

where $L \equiv (z_u - z_d) - L_c$ is the total length of straight pipe of radius R_1 between the pressure transducers and η is the viscosity of the fluid. The dimensionless pressure drop becomes

$$\mathscr{P}\left(De, R_c, \beta\right) = \frac{\Delta P'_{ud}\left(Q, De, \beta\right)}{\Delta P'_{ud}\left(Q, De = 0, \beta = 4\right)}, \tag{4-2}$$

where the pressure drop resulting from the flow of a Newtonian fluid across a 4:1:4 sharp axisymmetric contraction-expansion at a given flow rate, $\Delta P'_{ud}(Q,\ De = 0,\ \beta = 0)$, is used in the denominator to non-dimensionalize the pressure drop resulting from the flow of the non-Newtonian test fluid across each of the contraction-expansions at the same flow rate, regardless of aspect ratio.

4.2.2 *Measurement Techniques*

The flow field upstream of the axisymmetric abrupt contraction is investigated using several different techniques: digital particle image velocimetry (DPIV); laser Doppler velocimetry (LDV); and flow visualization through computer-generated streak images. A complete discussion of the DPIV and flow visualization techniques used in this paper can be found in the previous chapter.

4.2.3 *Fluid Rheology*

The viscoelastic test fluid used in these experiments is the same 0.025wt% PS/PS solution used in the experiments described in the previous chapter. A complete discussion of the fluid shear and extensional rheology can be found in Section 3.2.3. The same conventions for the definition of relaxation time, Deborah number and Reynolds number will be followed.

4.3 Results

4.3.1 *Pressure Drop Measurements*

The evolution in the total pressure drop (ΔP_{ud}) of the 0.025% PS/PS solution flowing through the three contraction-expansion geometries described in Section 4.2.1 was measured for Deborah numbers $De \leq 10.5$. In the previous chapter, it was shown that the Stokes flow solution provided by Sampson for the pressure drop through an infinitesimally thin circular hole in an unbounded rigid wall [Happel and Brenner 1965] was in good agreement with the pressure drop measurements for the flow of the Newtonian oligomeric

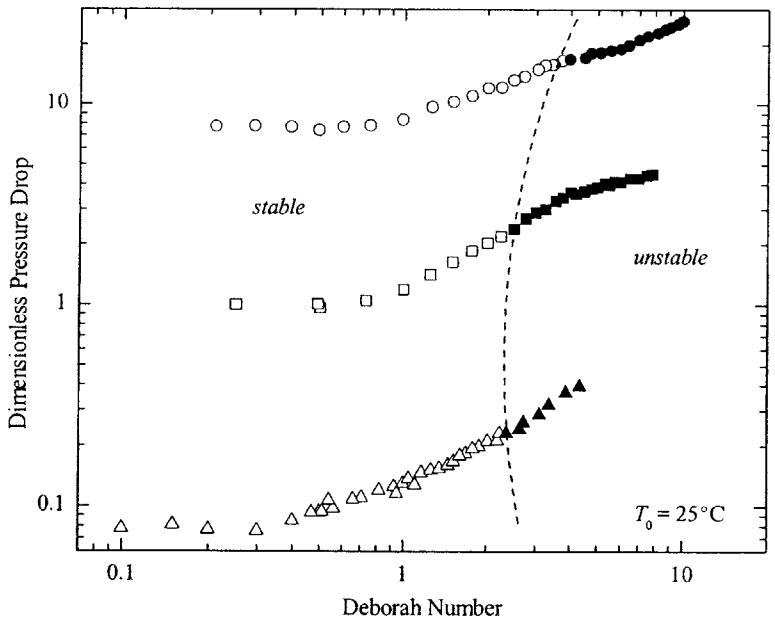

Figure 4-1 Dimensionless pressure drop measurements, $\mathcal{F}(De, \beta, R_c) = \Delta P'_{ud}(De, \beta, R_c) / \Delta P'_{ud}(Q, De = 0, R_c = 0, \beta = 0)$, of the 0.025wt% PS/PS solution across several axisymmetric contraction-expansions as a function of Deborah number, $De = \lambda_0 \dot{\gamma}$. The figure includes: ○, $\beta = 8$; □, $\beta = 4$; and △, $\beta = 2$. The hollow symbols represent stable flow conditions while the filled symbols represent unstable flow conditions.

polystyrene into a 4:1:4 contraction-expansion (corrected using Equation 4-1)

$$\Delta P'_{ud}\left(Q, De = 0, R_c = 0, \beta = 4\right) \cong \Delta P_{Sampson} = \frac{3\eta_0 Q}{R_2^3}, \tag{4-3}$$

and this value was thus used to generate the dimensionless pressure drop defined in Equation 4-2.

The effect of contraction ratio on the dimensionless extra pressure drop is shown in Figure 4-1. In the absence of elasticity, the pressure drop across the various contraction-expansions should be equal to that of a Newtonian fluid. In other words, in the limit $De \to 0$ we expect $\mathscr{P} \to (\beta/4)^3$. This is true for both the 4:1:4 and 8:1:8 contraction-expansion, however, for a contraction ratio of $\beta = 2$, the Sampson flow assumption of upstream and downstream fluid reservoirs with infinite lateral extent is no longer a good approximation. The presence of the upstream and downstream walls result in a dimensionless pressure drop considerably smaller than expected, $\mathscr{P}(De << 1, \beta = 2) \approx 0.08$. As the Deborah number is increased, the measurements for each of the contraction ratios examined show a monotonic increase in the dimensionless pressure drop beginning at a critical Deborah number. The value of the critical Deborah number increases slightly with contraction ratio, $0.3 \lesssim De_{crit} \lesssim 0.8$, but is consistently close to the Deborah number at which the *coil-stretch transition* occurs in a homogeneous extensional flow, $De = 0.5$. As the Deborah number is increased still further the rate of increase in the dimensionless pressure drop is greatly reduced. These trends in the evolution of the entrance pressure drop have been observed previously in experimental studies of polyacrylamide-based fluids [Cartalos and Piau 1992] flowing through a 16:1:16 axisymmetric contraction-expansion as well as a polystyrene-based fluids flowing (Chapter 3) through 4:1:4 axisymmetric contraction-expansions, the latter being reproduced in Figure 4-1. As stated previously, these large additional pressure drops associated with the addition of very small amounts of high molecular weight polymers to Newtonian solvents have yet to be even qualitatively simulated numerically [Coates *et al.* 1992; Keiller 1993; Szabo 1997].

The onset of an elastic flow instability is also indicated in the pressure drop data in Figure 4-1. A complete discussion of the nature of this elastic flow instability is presented in Section 4.3.4. A hypothetical sketch of the line of neutral stability motivated by previous studies of PIB/PB fluids [McKinley *et al.* 1991] is superimposed over the 2:1:2, 4:1:4 and 8:1:8 data. Limitations in the hardware and the sensitivity of our measurement techniques made it impossible to reach Deborah numbers large enough to observe an elastic instability in the 2:1:2 contraction-expansion, however, through flow induced birefringence measurements it was possible to observe the onset of an elastic instability. It is important to note that, in each case, the enhanced pressure drops measured experimentally are not directly connected with the onset of any elastic

instabilities. Thus, regardless of whether a numerical simulation can predict the onset of an elastic instability, the constitutive model should still be able to predict the large enhanced pressure drops associated with steady viscoelastic entrance flow before any flow instabilities occur

4.3.2 *Vortex Growth Dynamics*

Flow visualization was used to observe the vortex growth dynamics upstream of the contraction for the four geometries describe in Section 4.2.2 for Deborah numbers $De \leq 11$. A detailed description of the vortex growth and development in the 4:1:4 contraction-expansion with increasing Deborah number has been presented in Chapter 3 and here we focus on changes resulting from varying the contraction ratio.

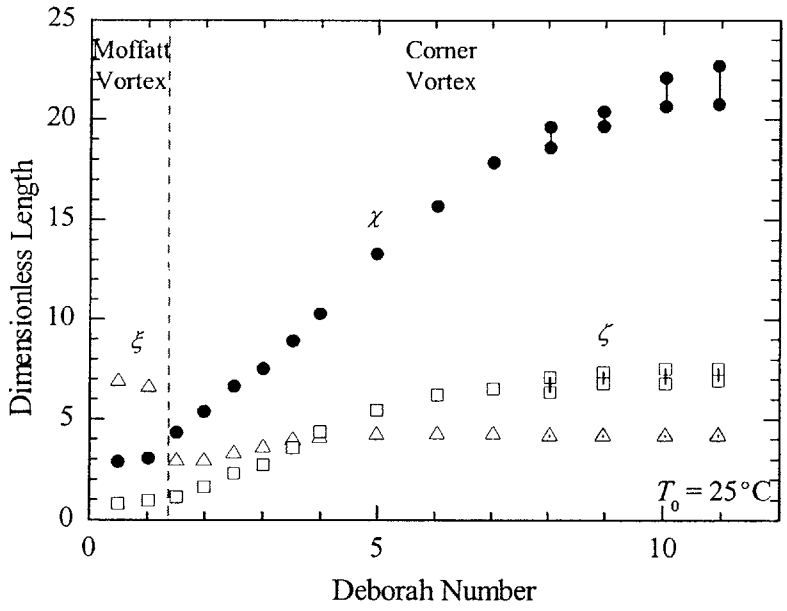

Figure 4-2 Characteristics of the upstream vortex growth dynamics as a function of Deborah number for the 8:1:8 axisymmetric contraction-expansion: ●, vortex reattachment length, $\chi = L_v / R_2$; △, radial location of the vortex center, $\xi = R_v / R_2$; and □, the upstream location of the vortex center, $\zeta = Z_v / R_2$.

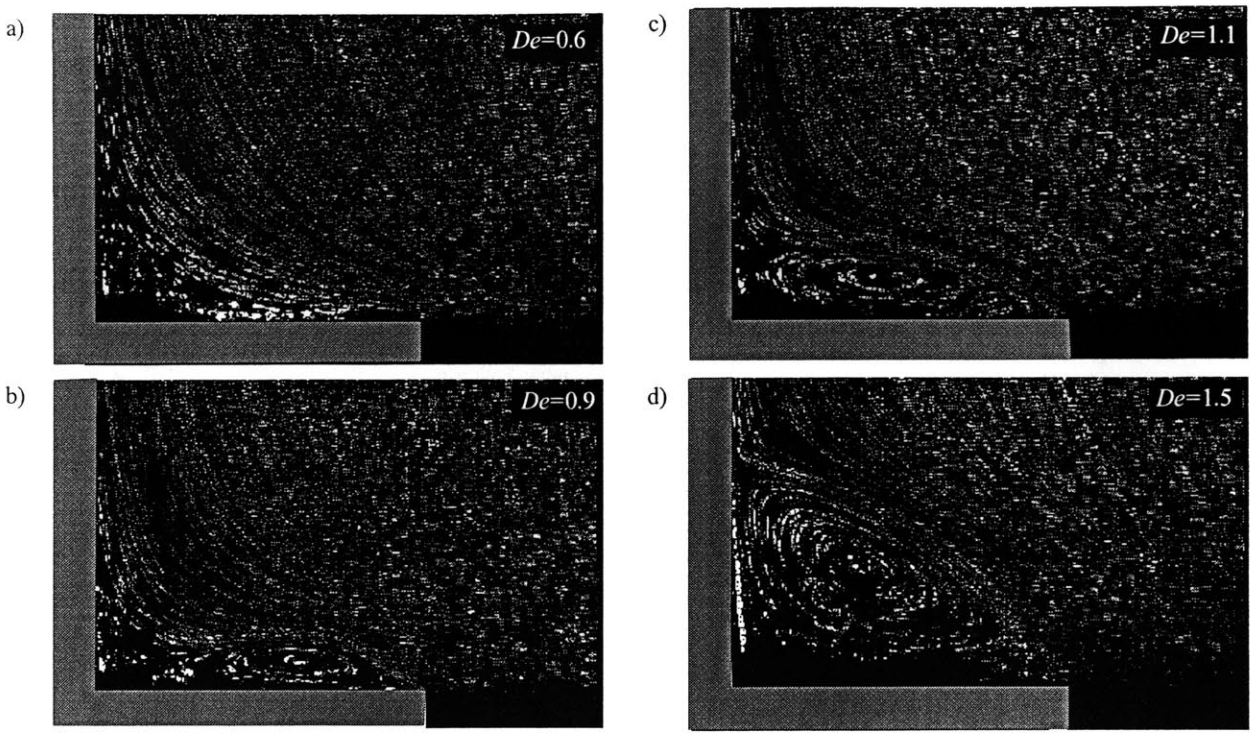

Figure 4-3 Streak images of flow upstream of a 2:1:2 axisymmetric contraction-expansion for Deborah numbers of (a) De = 0.6, (b) De = 0.9, (c) De = 1.1 and (d) De = 1.5 showing the development and growth of the lip vortex.

In Figure 4-2, the dimensionless reattachment length and coordinates of the vortex center are shown for the 8:1:8 contraction-expansion. The vortex growth dynamics for the 8:1:8 contraction expansion are similar to those described above; dominated by the presence and upstream growth of an elastic corner vortex. The principal difference arises from the onset conditions for the transitions into different vortex growth regimes. For both the 4:1:4 and the 8:1:8 contraction-expansions the critical Deborah number for the onset of observable corner vortex growth is approximately 20% larger than that for the onset of enhanced pressure drop growth. The kinematics of these two effects appear to be quite strongly correlated.

In Figure 4-3, pseudo streak images upstream of the 2:1:2 contraction-expansion are shown for Deborah numbers of De = 0.6, 0.9, 1.1 and 1.5. As observed for both the 4:1:4 and the 8:1:8 contraction-expansions, at low Deborah numbers a Moffatt vortex is present in the upstream stagnant corner as shown in Figure 4-3(a). However, in contrast to the results presented for the previous contraction ratios, as the Deborah number approaches unity, the corner vortex decreases in size and a separate and distinct 'lip' vortex forms near the re-entrant corner, Figure 4-3(b). The lip vortex then proceeds to grow outward, Figure 4-3(c),

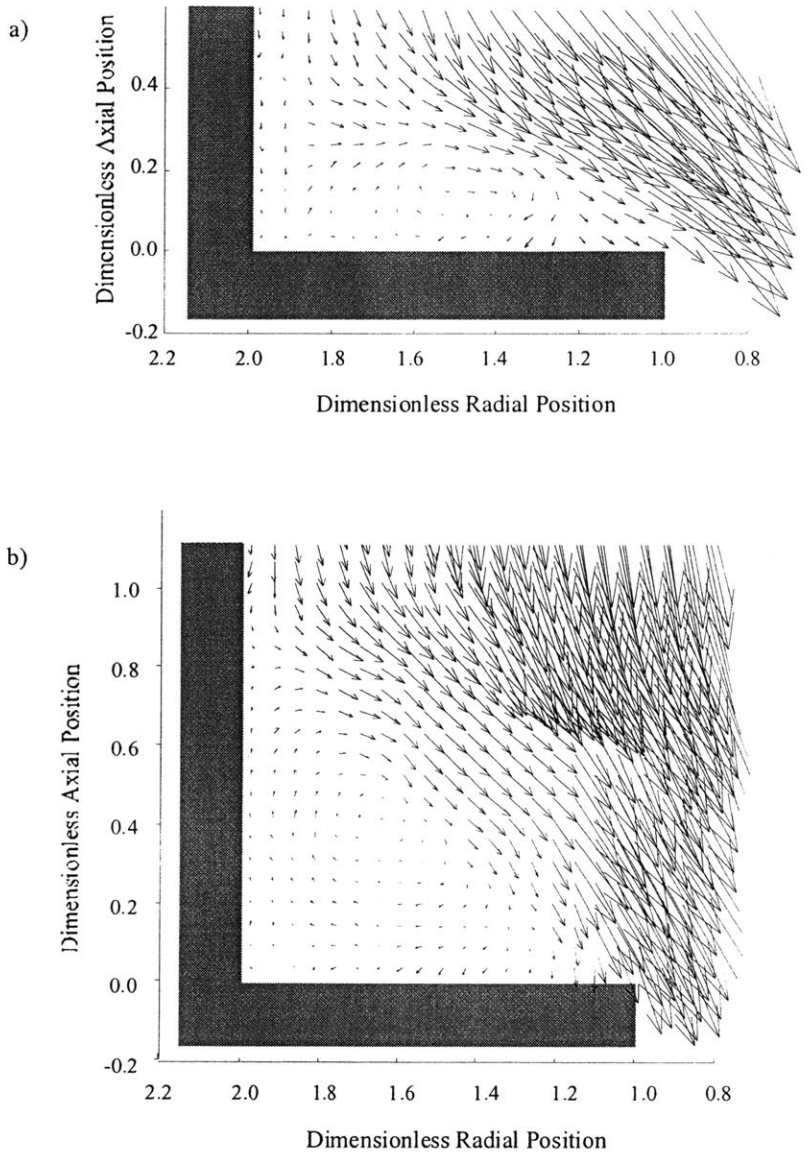

Figure 4-4 Particle Image Velocimetry (PIV) measurements of the vector fields for the recirculating flow upstream of a 2:1:2 axisymmetric contraction-expansion at Deborah numbers of (a) $De = 0.9$ and (b) $De = 1.5$.

until it reaches the stagnant corner at which point it grows upstream in a manner consistent with the corner vortex growth dynamics described above for larger contraction ratios.

Digital particle image velocimetry (DPIV) measurements for Deborah numbers of $De = 0.9$ and 1.5 are shown in Figure 4-4. These velocity vector field measurements correspond to the streak images shown in Figures 4-4(b) and 4-4(c). The vectors are scaled such that an arrow of length $l / R_2 = 0.25$ corresponds to a velocity magnitude of $v / \langle v_z \rangle_2 = 1$. The DPIV measurements in Figure 4-4(a) demonstrate the complete suppression of the corner vortex with the presence of the lip vortex. In fact, the fluid flows into the stagnant

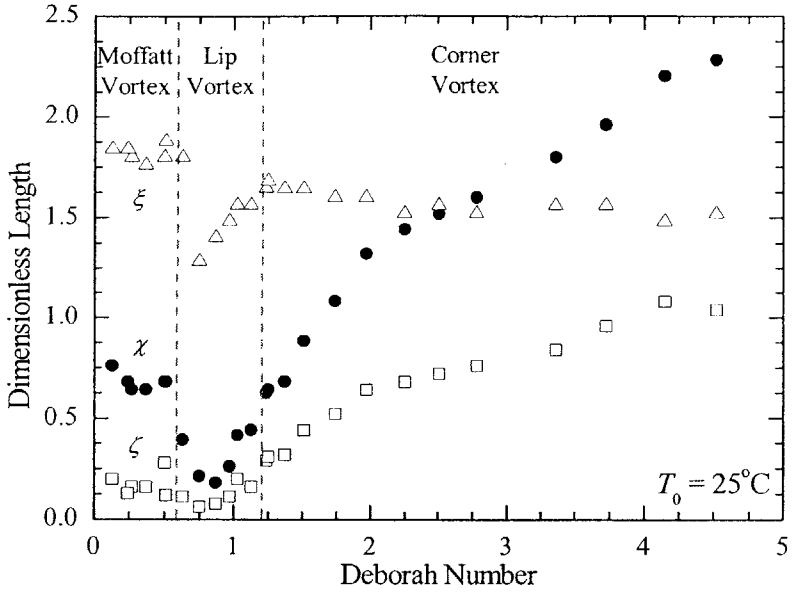

Figure 4-5 Characteristics of the upstream vortex growth dynamics as a function of Deborah number for the 2:1:2 axisymmetric contraction-expansion: ●, vortex reattachment length, $\chi = L_v / R_2$; △, radial location of the vortex center, $\xi = R_v / R_2$; and □, the upstream location of the vortex center, $\zeta = Z_v / R_2$.

corner and then reverses direction in order to flow back upstream, around the lip vortex and into the contraction. The vector field in Figure 4-4(b) is very similar to the vector field measurements of elastic corner vortices upstream of a 4:1:4 sharp contraction-expansion presented in the previous chapter. This reinforces our previous observations which indicate that once the lip vortex has reached the stagnant corner, the dynamics of the subsequent elastic vortex growth are identical to those observed in contraction ratios that do not demonstrate formation of a distinct lip vortex.

The dimensionless reattachment length and coordinates of the vortex center are shown in Figure 4-5. These measurements quantify the spatial characteristics observed in the pseudo streak images. At low Deborah numbers, the dimensionless reattachment length is again constant with the expected value for the Newtonian Moffatt vortex. As the Deborah number is increased, the reattachment length decreases drastically as the lip vortex begins to develop. At this point, the coordinates reported in Figure 4-5 shift from the disappearing Moffatt vortex to the center of the now-dominant and topologically-distinct lip vortex. As the lip vortex grows outward, the reattachment length remains quite small and the axial position of the lip vortex center remains relatively constant. Once the lip vortex has reached the stagnant corner, the radial

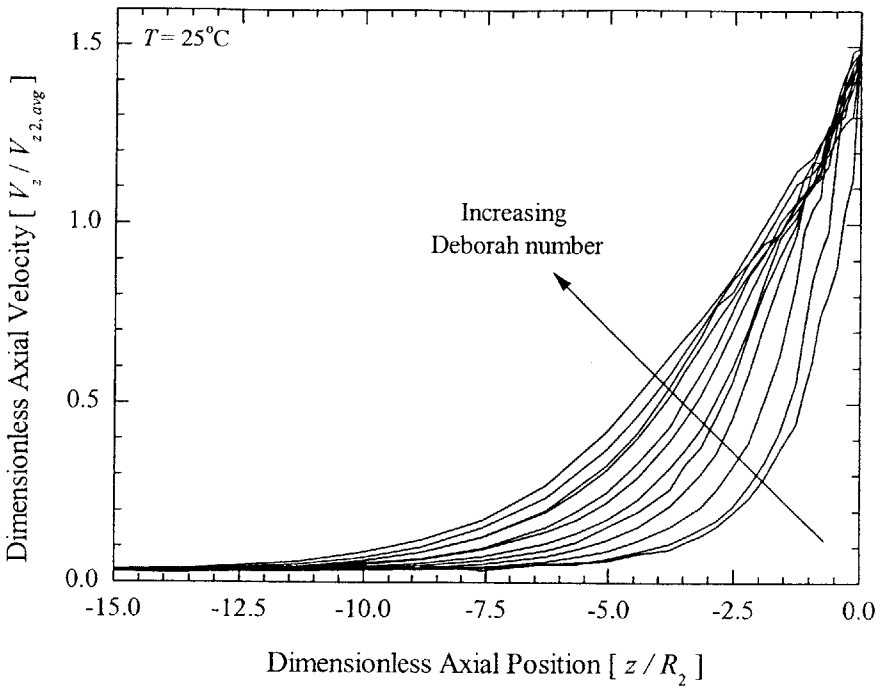

Figure 4-6 Laser Doppler Velocimetry (LDV) measurements showing the dimensionless axial velocity along the centerline, $v_z/\langle v_z \rangle_2$, as a function of dimensionless axial position, z/R_2, for the flow through an 8:1:8 axisymmetric contraction-expansion. The figure includes Deborah number from De = 1 to De = 12 increasing by a constant increment of De = 1 from right to left.

location of the vortex center saturates at $\xi \sim 1.5$ and the large elastic corner vortex begins to grow upstream. Previous experimental measurements [Boger and Binnington 1990; McKinley *et al.* 1991] indicate that the lip vortices are unsteady in time and three dimensional in nature, but within the sensitivity of our velocity and pressure measurement techniques, the lip vortex resulting from the flow of a PS/PS solution through a 2:1:2 contraction-expansion is found to be steady in time. The difference may be a consequence of the difference in operating procedure; earler studies imposed a constant pressure difference ΔP_{ud} across the contraction geometry and determined an average flow rate or velocity, whereas in the present experiments we use a fixed displacement rate and measure the ensuing pressure drop.

4.3.3 *Laser Doppler Velocimetry Measurements*

Axial velocity measurements taken along the centerline of the 2:1:2 and the 8:1:8 axisymmetric abrupt contraction-expansion to complement the data in Chapter 3. The results are shown in Figures 4-6 and

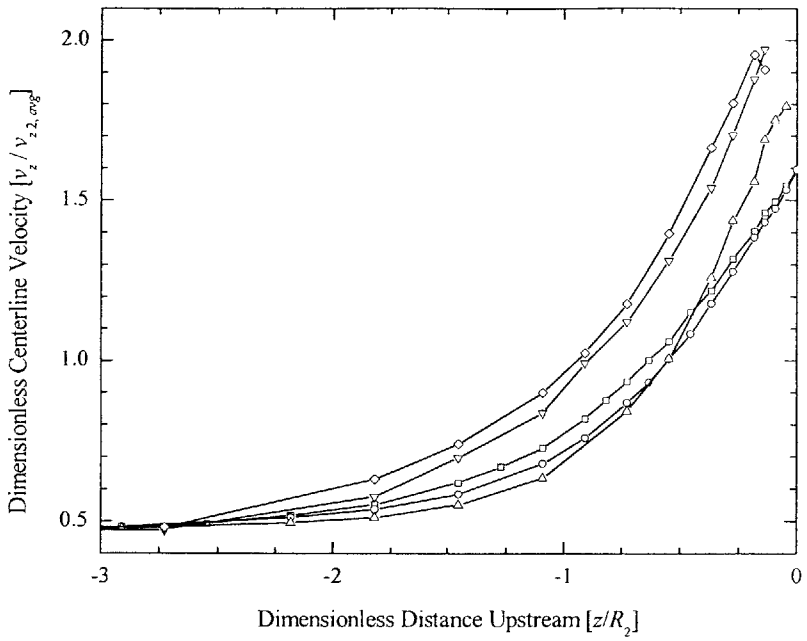

Figure 4-7 Laser Doppler Velocimetry (LDV) measurements showing the dimensionless axial velocity along the centerline, $v_z/\langle v_z\rangle_2$, as a function of dimensionless axial position, z/R_2, for the flow through an 8:1:8 axisymmetric contraction-expansion. The figure includes: □, Deborah number of $De = 0.5$;○, $De = 0.9$; ▽, $De = 2.0$; △, $De = 3.0$; and ◇, $De = 3.5$;.

4-7. The dimensionless velocity measurements, $v_z/\langle v_z\rangle_2$, are plotted from locations far upstream of the contraction plane, $z/R_2 > -10$, to positions at the contraction plane, $z/R_2 = 0$. Unlike for the 4:1:4 contraction-expansion, the contraction inserts for both these contraction ratios is made of aluminum and so no optical measurements are possible within the throat. In a Poiseuille flow, the velocity on the centerline is equal to twice the average velocity in the tube $v_z(r=0) = 2\langle v_z\rangle$. The dimensionless centerline velocity well upstream of the contraction plane should be equal to $v_z/\langle v_z\rangle_2 = 2/\beta^2$, while the dimensionless velocity within the throat would be equal to $v_z/\langle v_z\rangle_2 = 2$. In both cases, this is confirmed far upstream. In Figure 4-6, the centerline velocity profile into an abrupt 8:1:8 contraction-expansion is shown. For this large contraction ratio, the fluid must accelerate to a velocity in the throat that is 64 times larger than the velocity well upstream of the contraction plane. At low Deborah numbers, the acceleration is observed to occur smoothly, beginning at an axial position of $z/R_2 \approx -5.0$ upstream. As the Deborah number is increased, the effect of the contraction is felt progressively further upstream as the corner vortex grows towards the re-entrant corner and then upstream.

The presence of the lip vortex in the 2:1:2 contraction expansion has a significant impact on the velocity profile development as the Deborah number is increased. The velocity profiles along the centerline upstream of the abrupt 2:1:2 contraction-expansion can be seen in Figure 4-7. At low Deborah numbers, the velocity increases smoothly into the throat to a maximum velocity of $v_z/\langle v_z \rangle_2 \approx 1.5$. The growth of the elastic lip vortex at a Deborah number of $De = 0.9$ forces the test fluid to travel closer to the contraction plane before accelerating into the throat. Unlike the observations made in the 4:1:4 and 8:1:8 contraction-expansions, the velocity profile is not observed to increase monotonically upstream with elastic vortex growth. At a Deborah number of $De = 2.0$, the onset of fluid acceleration is moved even closer to the contraction plane while the maximum velocity achieved along the centerline increases to $v_z/\langle v_z \rangle_2 \approx 2.0$. The velocity profile eventually does shift monotonically further upstream beyond this Deborah number, as the elastic corner vortex grows in size and strength.

Velocity measurements using LDV were also taken at several locations moving across the contraction radially for a large range of Deborah numbers and positions. However, very little additional information is provided from these measurements that cannot be ascertained by inspecting the velocity vector fields presented in Section 4.3.2. The readers are referred to these measurements.

4.3.4 *Flow Stability*

While studying the flow of the PS solution into both the 4:1:4 and the 8:1:8 contraction-expansions, a slow non-symmetric precession of the enlarged corner vortex was visually observed at large Deborah numbers. The analysis of the oscillations in the pressure drop measurements across the 4:1:4 contraction-expansion have been presented in Chapter 3.3.2.

The onset of an elastic instability is first indicated by small amplitude oscillations in the global pressure drop and local velocity measurements which are observed to grow in magnitude with increasing Deborah number. In Figure 4-8(a), two samples of the temporal variation of the radial, $v_r(t)$, and axial, $v_z(t)$, velocity for the flow of the PS/PS Boger fluid into the 4:1:4 sharp contraction-expansion are shown at Deborah numbers of $De = 3.5$ and 7.0. These two measurements were taken at a position, $(r/R_2, z/R_2) = (0.63, -1.26)$, just above the re-entrant corner. A fast Fourier transform (FFT) of the velocity data allows a quantitative determination of the frequency and amplitude of the velocity fluctuations. In Figure 4-8(b) we show the power spectral density (PSD) at $De = 3.5$. The Fourier spectrum indicates that the elastic flow instability has a strong fundamental oscillation frequency, $f_1 = 0.15$Hz, and the existence of a small peak at the first harmonic. As the Deborah number is further increased, the intensity of the velocity fluctuations

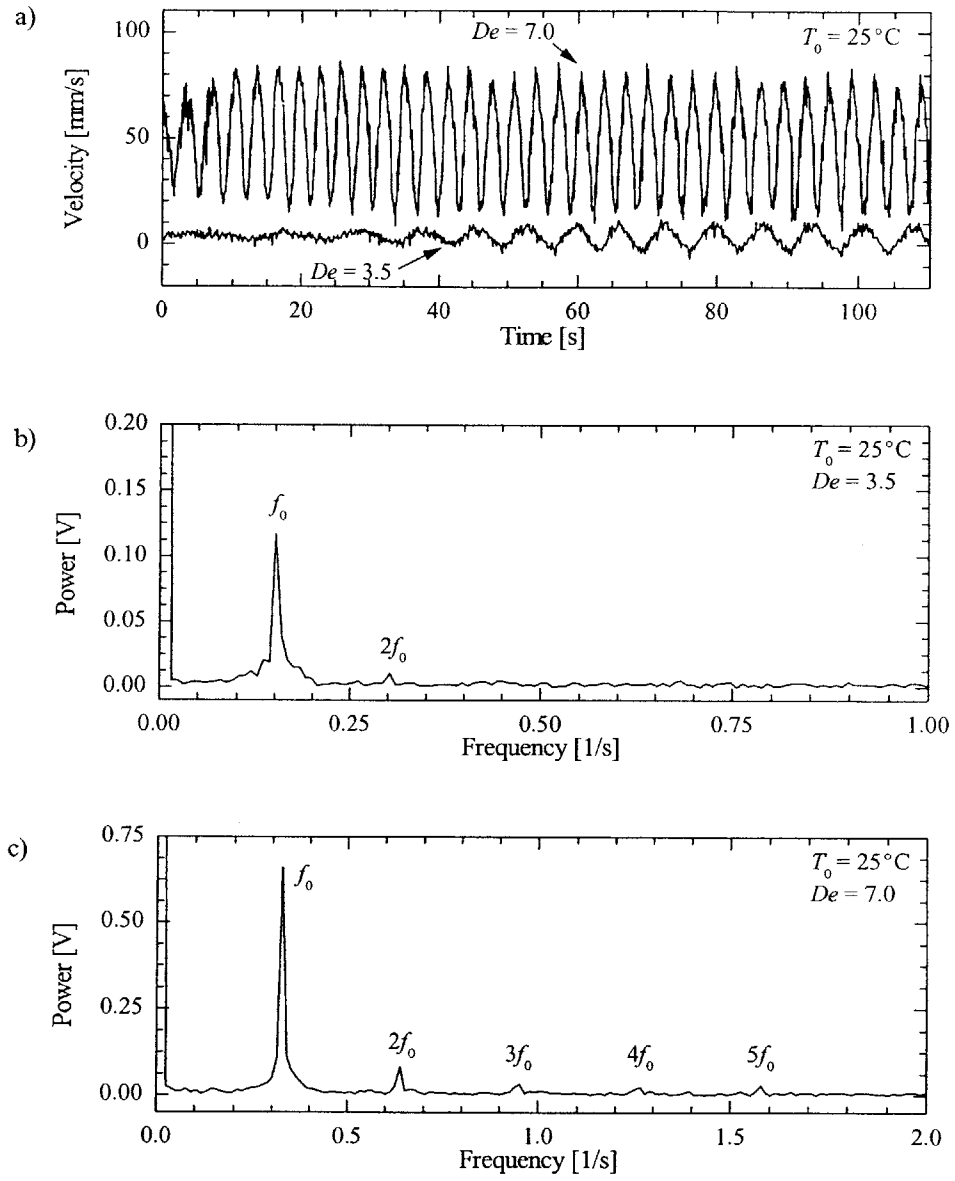

Figure 4-8 The onset of a supercritical elastic instability seen in (a) Laser Doppler Velocimetry (LDV) measurements of the flow upstream of a 4:1:4 axisymmetric contraction-expansion and power spectral density plots of (b) radial velocity measurements, v_r, at a Deborah number of $De = 3.5$ and (c) axial velocity measurements, v_z, at a Deborah number of $De = 7.0$.

grows in amplitude, the fundamental frequency of oscillation slowly increases and the higher harmonics of the fundamental frequency begin to appear. At a Deborah number of $De = 7.0$, the PSD plot in Figure 4-8(c)

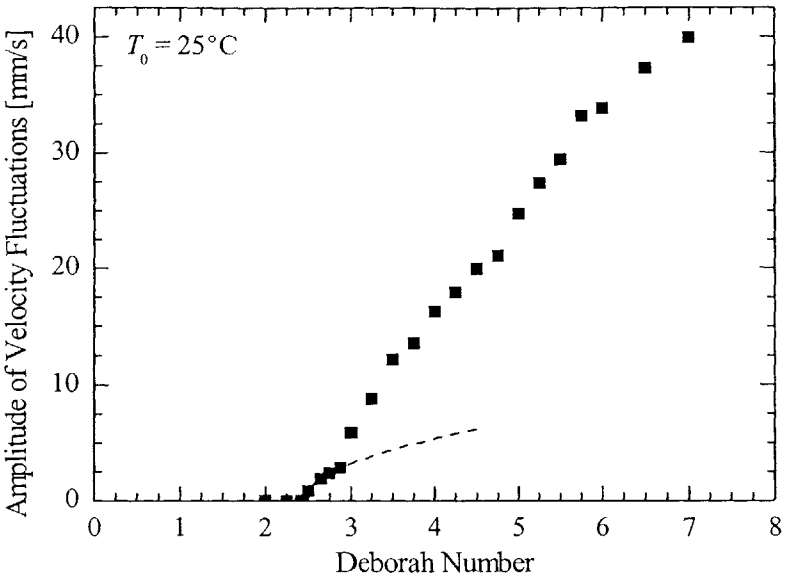

Figure 4-9 Amplitude of velocity fluctuations in the unstable upstream flow into a 4:1:4 axisymmetric contraction-expansion as a function of Deborah number. The data include: ■, experimental measurements, and —, the theoretical prediction for a supercritical Hopft bifurcation, $|\mathbf{v}| \sim (De - De_{crit})^{1/2}$.

contains four detectable harmonics of the fundamental frequency.

The variation in the amplitude and frequency of oscillation determined from the Fourier spectrum, such as those shown in Figure 4-8(a) and (b) can be used to determine the critical Deborah number for the onset of this supercritical Hopf bifurcation, are shown in Figures 4-9 and 4-10 respectively. The critical Deborah number for the onset of the periodic flow is accurately determined by fitting the these results to the asymptoticresults for a supercritical Hopf bifurcation [Iooss and Joseph 1980]

$$\left|\mathbf{v}(r,\theta,z,t)\right| \propto \left(De - De_{crit}\right)^{1/2}, \tag{4-4}$$

$$f = c_1 + c_2\left(De - De_{crit}\right), \tag{4-5}$$

where c_1 and c_2 are constants. These expressions are valid only in the linear limit, such that $(De - De_{crit}) << 1$. Theoretically, in this limit only the fundamental frequency will exist in the Fourier spectrum, however, a small first harmonic peak is present in the experiments at all but the very lowest unstable flow rate. To

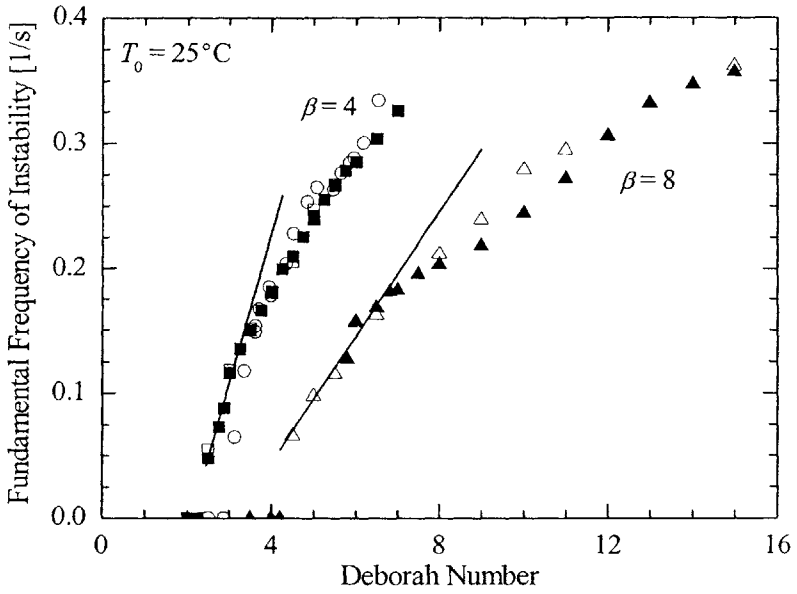

Figure 4-10 Fundamental frequency of velocity and pressure drop fluctuations in the unstable upstream flow into the axisymmetric contraction-expansions as a function of Deborah number. The data include: ■, v_z for the 4:1:4 sharp contraction-expansion; □, v_r for the 4:1:4 sharp contraction-expansion;▲, v_z for the 8:1:8 contraction-expansion;△, v_θ for the 8:1:8 contraction-expansion;○, Δp for the 4:1:4 rounded contraction-expansion; and —, the theoretical prediction for a supercritical Hopf bifurcation, $f \sim (De - De_{crit})$.

circumvent this difficulty, a cutoff for linearity is defined such that only data taken at Deborah numbers for which the amplitude of velocity fluctuations of the fundamental frequency are an order of magnitude greater than those of the first harmonic, $\left|\mathbf{v}(r,\theta,z,t)\right|_{f_0} > 10\left|\mathbf{v}(r,\theta,z,t)\right|_{2f_0}$, are used to determine De_{crit} from Equations 4-4 and 4-5. The results of these fits are superimposed on the data in Figures 4-9 and 4-10 and the critical Deborah numbers are tabulated in Table 4-4.

	Critical Deborah Number for the Onset of the Elastic Flow Instability
4:1:4 Sharp Contraction-Expansion	2.4 ± 0.1
8:1:8 Contraction-Expansion	4.2 ± 0.2

Table 4-3 Critical conditions for the onset of the supercritical Hopf bifurcation.

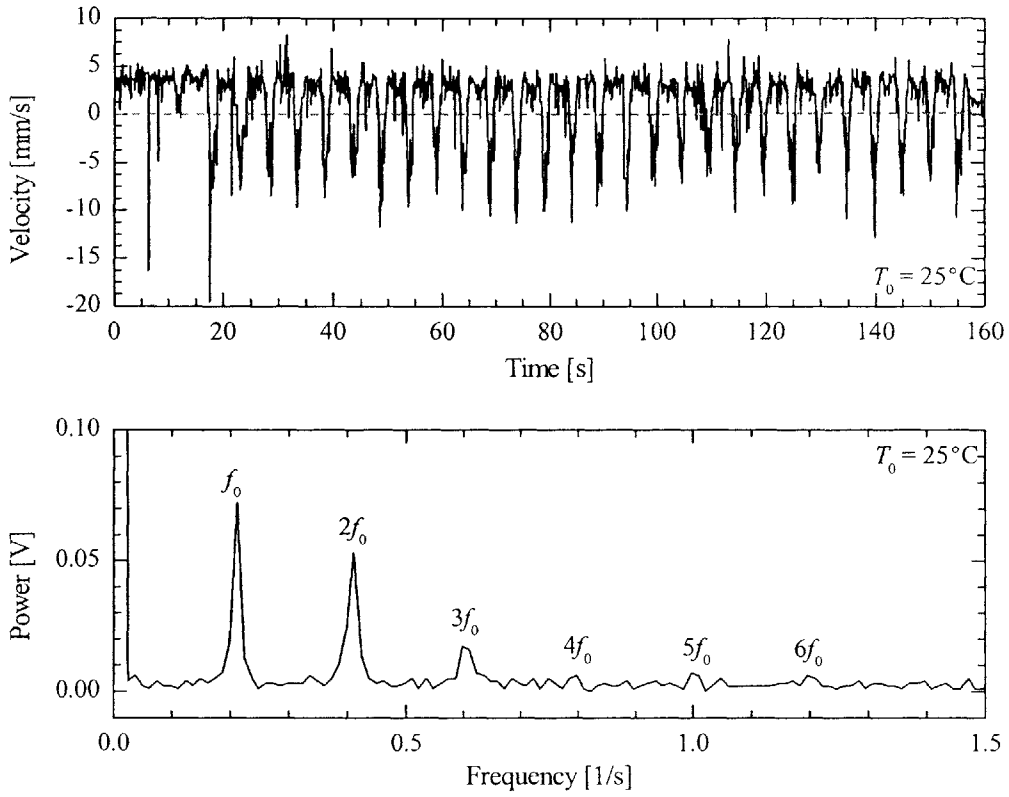

Figure 4-11 Nonlinear dynamics of jetting flow observed in (a) LDV measurements of the radial velocity at a position $r/R_2 = 1.57$ and $z/R_2 = -0.16$ upstream of the 4:1:4 axisymmetric contraction-expansion and the corresponding (b) power spectral density plot at a Deborah number of $De = 4.5$.

The initial deviation from axisymmetric stable flow conditions is well describe by linear stabilityanalysis. However, when $De >> De_{crit}$ nonlinear dynamics begin to dominate the flow kinematics. These nonlinear effects are first observed in the Fourier spectrum as higher harmonics of the fundamental frequency and the transition from a periodic to a period-doubling instability [McKinley *et al.* 1991]. Another manifestation of these nonlinear dynamics observed in the present experiments is the development of a high speed 'jetting' instability near the lip of the contraction in the 4:1:4 contraction-expansion, which has not been reported previously. After the onset of the elastic flow instability, the upstream vortex breaks symmetry and begins to precess in the azimuthal direction. The extent of this symmetry breaking in the vortex height increases with Deborah number. In conjunction with the break in symmetry, a strong jet of high speed fluid

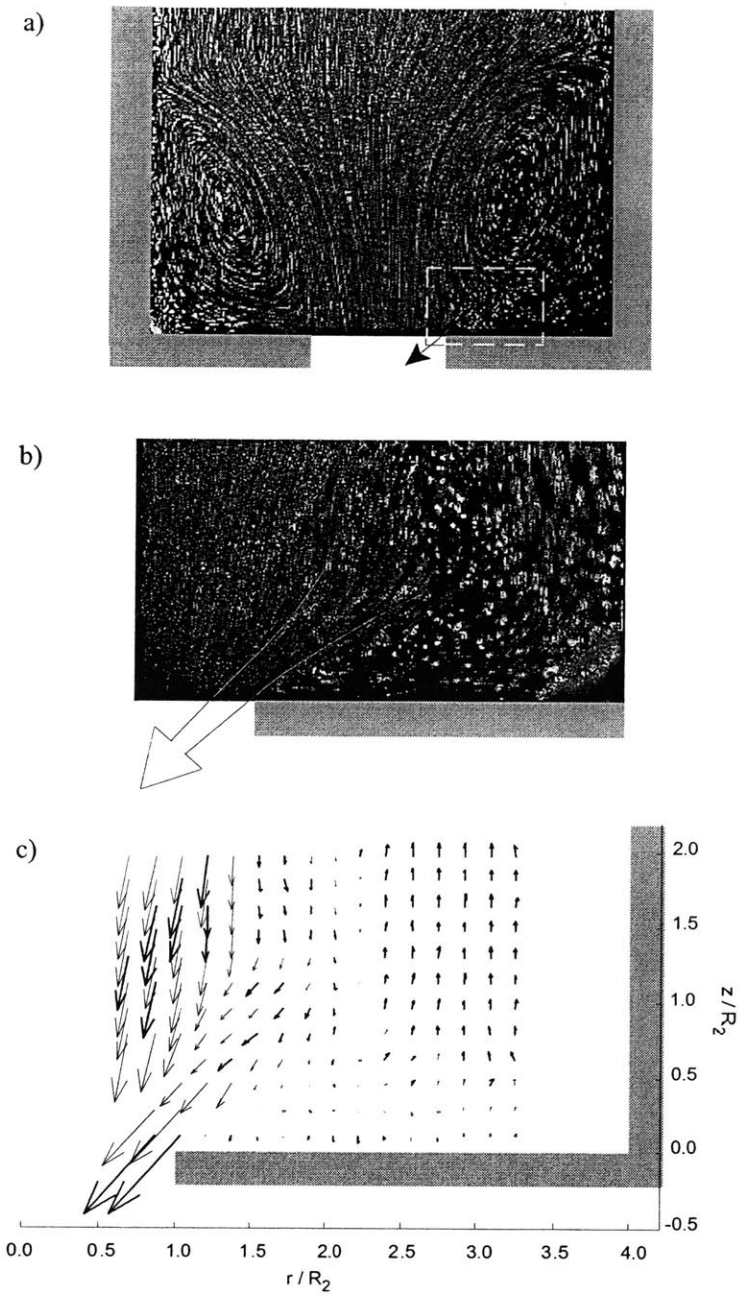

Figure 4-12 Streak images of the jetting instability upstream of a 4:1:4 axisymmetric contraction-expansion for Deborah numbers of De = 3.5 showing the (a) full view of the unstable upstream vortex and (b) a closeup of the jetting instability along with (c) PIV velocity vector field generated from the closeup images.

appears, originating from the base of the upstream vortex and flowing directly into the throat just upstream

of the contraction plane. By focusing the LDV probe at a position $(r/R_2, z/R_2) = (1.57, -0.16)$ within the vortex and just upstream of the contraction plane, it is possible to quantify this jetting flow instability. Measurements of the time-varying radial velocity are shown in Figure 4-11(a). The flow is initially steady with a velocity $v_r \approx 3.5$ mm/s ($v_r/\langle v_r \rangle_2 \approx 0.063$) directed radially outward, indicating that the probe is focused within the recirculating region of the corner vortex. As the flow develops, the jetting flow appears as large amplitude periodic spikes in the velocity measurements. These spikes are larger in magnitude, $v_r \approx -10$ mm/s ($v_r/\langle v_r \rangle_2 \approx 0.18$), than the stable recirculating flow velocity and directed inward toward the contraction entrance. The Fourier spectrum presented in Figure 4-11(b) contains several higher harmonics of the fundamental frequency including a first harmonic signal, the amplitude of which is nearly equivalent to that of the fundamental frequency. The fundamental frequency of the jetting instability is identical to the frequency of the upstream vortex precession. We therefore postulate that this instability is in fact a helical jet of fluid running the entire axial length of the upstream vortex.

Two streak images and a DPIV vector field showing this instability can be found in Figure 4-12. The global structure of the unstable vortex is seen in Figure 12(a) and a box is sketched around the location of the jetting instability which appears at the base of the precessing asymmetric upstream vortex at the point of its greatest upstream extent. This box also indicates the field of view blown up in the streak image of Figure 4-12(b) and the vector field in Figure 4-12(c). Although these close-up images were taken at the same Deborah number as the full field of view, the images were not collected simultaneously and a slight difference in the temporal development of the jetting instability was unavoidable. The vectors in Figure 4-12(c) are scaled such that an arrow of length $l/R_2 = 0.5$ corresponds to a velocity of $v/\langle v_z \rangle_2 = 1$ and clearly demonstrate the strong localized nature of this instability. For a brief video clip of this instability we encourage the reader to either visit our website or to contact the authors directly.

4.4 Discussion

4.4.1 *The Role of Transient Extensional Viscosity*

With variations in the contraction ratio, the flow field upstream of the contraction-expansion was found to evolve along two distinct vortex growth pathways. For a contraction ratio of $\beta = 2$ a steady elastic lip vortex was observed, while for contraction ratios of $4 \leq \beta \leq 8$ a corner vortex was seen. The presence or the absence of a lip vortex has been noted in many different studies and depends not only on the contraction ratio through which the fluid is forced, but also on the formulation of the fluid used. These observations are summarized in Table 4-2 which, when completed with the vortex growth data for the PS/PS

Boger fluid from this study, shows a marked similarity between the behavior of the PS/PS and PAA/CS test fluids. It has been conjectured that the differences in flow transitions for fluids with ostensibly identical shear properties question must arise from differences in extensional rheology [Boger *et al.* 1986; McKinley *et al.* 1991]. This hypothesis suggests that the differences observed in contraction flows and other complex flows arise from changes in the molecular characteristics of the equilibrium conformations of the polymer chains resulting from solvent quality or stiffness of the polymer backbone [Boger and Binnington 1994; Chmielewski *et al.* 1990; Solomon and Muller 1996]. It follows that these initial equilibrium conformational differences will also have a large effect on the evolution of non-equilibrium properties such as the transient extensional stress growth in the fluid. With the advent of the filament stretching rheometer and the advances in simulation techniques for bead-rod and bead-spring models, it is now possible to probe such hypotheses both experimentally and numerically [Li and Larson 2000].

A fluid filament experiencing a constant uniaxial extension rate in a filament stretching rheometer should, at least qualitatively, describe the uniaxial elongation of the fluid element flowing along the centerline into the contraction-expansion even if the extension rate in this case is not constant. If one assumes a fully developed Poiseuille flow in the throat of the axisymmetric contraction-expansion, then one can calculate the total Hencky strain experienced by a fluid element moving along the centerline from far upstream into the middle of the throat as

$$\varepsilon = \int_0^{t_1} \dot{\varepsilon}\, dt = \int_{v_z(z=-\infty)}^{v_z(z=0.5L_c)} \frac{dv_z}{v_z} = 2 \ln \beta. \tag{4-6}$$

Dotted lines representing the total accumulated strain of a fluid element traveling along the centerline into each of the geometries tested are superimposed over the extensional rheology data in Figure 4-13. These measurements seem to reinforce our previous conjecture. The PS/PS solution flowing into the 2:1:2 contraction-expansion demonstrates no significant strain-hardening while the extensional viscosity of the PS/PS solution flowing into the 4:1:4 and especially the 8:1:8 contraction-expansions is greatly enhanced. Thus, in the case of a PS/PS test fluid, a simple doubling of the extensional viscosity along the centerline is enough to eliminate the lip vortex. If this result could be generalized to other polymeric fluids, real physical insight might be achieved. Unfortunately, in similar extensional rheology tests of the same PIB/PB Boger fluid used by McKinley et al. [McKinley *et al.* 1991] which are also shown in Figure 4-13, the lip vortex is present at all contraction ratios, $\beta < 8$, corresponding to Trouton ratios up to $Tr \approx 150$; well past the Trouton

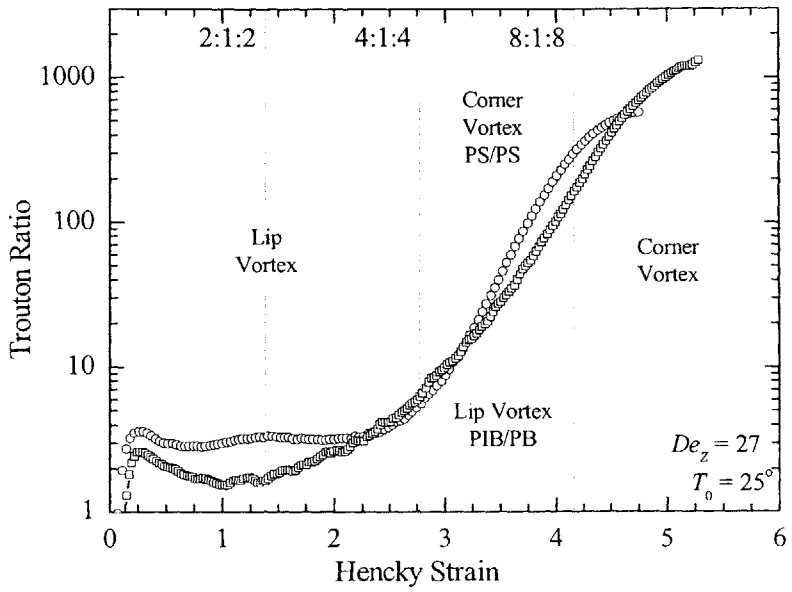

Figure 4-13 Uniaxial extensional measurements of Transient Trouton ratio, $\overline{\eta}^+ / \eta_0$, as a function of Hencky strain, $\varepsilon = \dot{\varepsilon} t$, for the 0.31wt% PIB/PB solution, □, and the 0.025wt% PS/PS solution, ○, taken at a Deborah number of $\lambda_Z \dot{\varepsilon} = 27$, where λ_Z is the Zimm relaxation time. The maximum strain achieved along the centerline of the 2:1:2, 4:1:4 and 8:1:8 contractions-expansions are indicated by the dashed lines.

ratio at which the flow of the PS/PS Boger fluid begins to demonstrate elastic corner vortex growth.

Although these two fluids demonstrate similar behaviors in extension, it is still important to point out their differences. The Trouton ratio of the monodisperse, dilute PS/PS solution grows more quickly and can be up to 50% larger than the Trouton ratio of polydisperse, semidilute PIB/PB at moderate Hencky strains. Li and Larson [Li and Larson 2000] used a bead-spring simulation to show that for a dilute high molecular weight polymer dissolved in a good solvent, both the stress and the birefringence rise much more rapidly with strain than for the same polymer dissolved in a theta solvent. Differences in solvent quality between these two Boger fluid formulations, the PS being dissolved in a slightly better solvent than the PIB, may still hold the key to differences in the kinematics and the dynamics of the flow. The effect of solvent quality has been systematically investigated in several model complex flows, for example viscoelastic flow past falling spheres. In a series of experiments performed by Solomon and Muller [Solomon and Muller

1996] using high molecular weight PS fluids, the increase in the drag coefficient above that expected for a Newtonian fluid was found to increase with increasing solvent quality. Unfortunately, this argument is not entirely consistent throughout the literature. Chmielewski et al. [Chmielewski *et al.* 1990] compared the drag past a falling sphere for two different Boger fluids. They found that the drag increased over the Newtonian value for the PIB solution in a close to theta solvent (polybutene), but the drag decreased below Newtonian for a PAA solution in a good solvent (corn syrup/water). These results are not consistent with our argument which would hold that because the PAA is dissolved in a better solvent than the PIB and it should demonstrate a more rapidly strain hardening extensional viscosity and a larger drag coefficient. The difference in this case may be the result of the shear thinning in the solution viscosity of the PAA/CS/H_2O fluid which is of the same order of magnitude (25%) as the reduction in drag.

In our experiments, the enhanced pressure drop measurements across the contraction-expansions were found to be qualitatively independent of both the contraction ratio and the radii of curvature of the re-entrant corner. However, even with rounded re-entrant corners, these large additional pressure drops have not been predicted by any existing numerical simulations using simple dumbbell models [Coates *et al.* 1992; Keiller 1993; Szabo 1997]. The evidence suggests that these discrepancies arise because of the inability of current bead-spring constitutive models to properly describe the extensional rheology of the polymer solutions. Most notable is the failure of these constitutive models to qualitatively predict the stress-conformation hysteresis first observed by Doyle et al. in measurements of uniaxial transient elongation [Doyle *et al.* 1998; Sridhar *et al.* 2000]. To capture such effects it may be necessary to resolve the non-equilibrium internal dynamical structure of the polymer chains recently observed by Perkins et al. [Perkins *et al.* 1997] by performing simulations with bead-rod chain models that can capture such 'configurational hysteresis'. However, an excellent description of the extensional viscosity alone might not be adequate to accurately model the flow into an axisymmetric contraction-expansion. Observations of the polystyrene Boger fluid in transient uniaxial extensional demonstrate no sign of strain hardening or of the dissipative stress suggested by stress-conformation hysteresis at the small strains achieved by a fluid element traveling along the centerline of the 2:1:2 axisymmetric contraction-expansion ($\varepsilon = 1.386$) and yet the pressure drop measurements still show a dramatic enhancement. Presumably, this results from the much larger deformations experienced by fluid elements passing near the re-entrant corner singularity but this cannot be confirmed until simulation are performed using a suitable constitutive model.

4.4.2 *The Normal Stress Ratio*

A combined knowledge of the shear and extensional properties of these polymeric fluids should ideally provide a means of predicting the vortex growth dynamics *a priori*. As the contraction ratio is increased at a fixed Deborah number, the shear rate at the tube walls upstream of the contraction decreases as $\dot{\gamma}_1 \propto \frac{1}{\beta^3}$, while at the same time, the accumulated strain along the centerline increases as $\varepsilon \propto \ln\beta$. Thus, there are two competing effects which contribute to the fluid's choice of vortex growth evolution; namely, extensional stresses and shear induced normal stresses. It is clear from these simple estimates of the strain and deformation that a lip vortex is present for elastic test fluids for contraction ratios which generate very little extension of the polymer chain along the centerline; they may therefore be considered to be elastically shear-dominated. For a given contraction ratio, the extensional stresses increase dramatically as the Deborah number is increased; whereas, for most Boger fluids, the first normal stress difference tends to saturate due to shear thinning arising from finite extensibility effects. A large elastic vortex then supplants the lip vortex. Similarly, as the contraction ratio is increased, the extensional stresses developed within the contraction flow dominate the normal stress difference arising from shear and, once again, a corner vortex replaces the lip vortex.

We have argued that the flow kinematics associated with the transition from lip to corner vortex appear to be driven by a change in the dynamics from a shear dominated to an extension dominated flow. A possible means of quantifying this transition is to compare the normal stresses generated by the shear flow along the walls to the extensional stresses resulting from the elongational flow along the centerline. We thus consider a dimensionless normal stress ratio defined as

$$\aleph = \frac{N_1/\eta_0\dot{\gamma}}{(\tau_{zz}-\tau_{rr})/\eta_0\dot{\varepsilon}} = \frac{S_R(\dot{\gamma})}{T_R(\varepsilon)}, \tag{4-7}$$

where $T_R(\varepsilon)$ is the Trouton ratio evaluated at the total Hencky strain accumulated along the centerline of the contraction-expansion and $S_R(\dot{\gamma})$ is the shear-rate-dependent stress ratio. Although, we differentiate explicitly between the extension rate $\dot{\varepsilon}$ and the shear rate $\dot{\gamma}$, in a nonhomogeneous flow, such as the one considered here, it is sufficient to approximate both as $\dot{\gamma} \approx \dot{\varepsilon} \approx \langle v_z \rangle_2/(R_2 + R_c)$. Arigo and McKinley [Arigo and McKinley 1998] used this dimensionless group to help rationalize the differences in the wake developing downstream

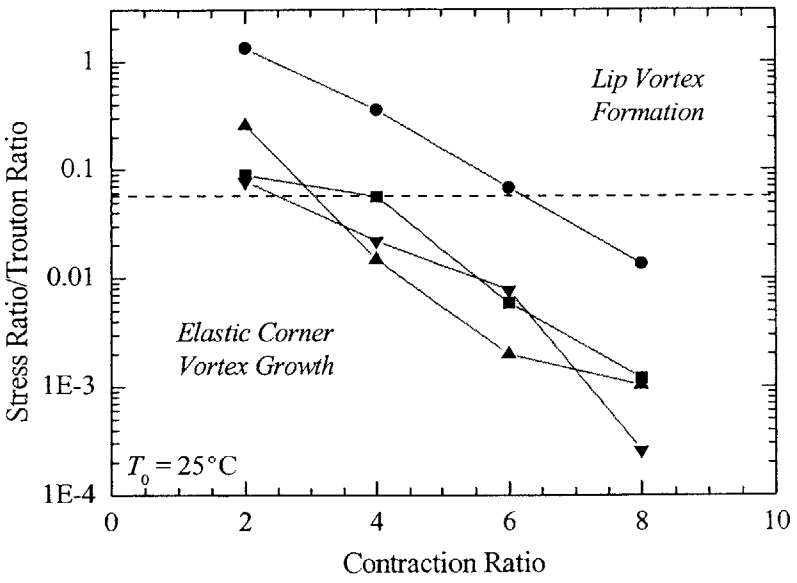

Figure 4-14 The normal stress ratio, $\aleph = SR/TR$, as a function of contraction ratio evaluated at the deformation rate corresponding to the onset conditions for upstream vortex growth. The data includes: ▪, the 0.025wt% PS/PS solution ($\langle v_z \rangle_2 / R_2 = 5.1 s^{-1}$); •, the 0.31wt% PIB/PB solution ($\langle v_z \rangle_2 / R_2 = 9.2 s^{-1}$) from [McKinley *et al.* 1991]; and two PAA/CS solutions ▲, Fluid C ($\langle v_z \rangle_2 / R_2 = 0.14 s^{-1}$) and ▼, Fluid E ($\langle v_z \rangle_2 / R_2 = 2.5 s^{-1}$) from [Stokes 1998].

of spheres sedimenting in dilute and concentrated viscoelastic fluids, however, to our knowledge it has not been used to compare differences between different ideal elastic Boger fluids. In Figure 4-14, the normal stress ratio ($\aleph$) is plotted as a function of contraction ratio for the PS/PS, PIB/PB and PAA/CS Boger fluids used in contraction flow publications and this research [Boger and Binnington 1994; McKinley *et al.* 1991; Nguyen and Boger 1979]. Of course, this normal stress ratio is also a function of deformation rate and should be represented as a two-dimensional surface, $\aleph(\beta, De)$. Here we have chosen to evaluate the normal stress number at the deformation rate ($\langle v_z \rangle_2 / R_2$) corresponding to the onset of the first significant elastic vortex growth. The shear and extensional rheological data used to calculate the normal stress number for the PIB/PB and PS/PS Boger fluids can be found in Figures 3-3, 3-4 and 4-13 and in McKinley et al. [McKinley *et al.* 1991], while analogous shear and extensional rheology data for PAA/CS Boger fluids can be found in Stokes [Stokes 1998]. The PAA/CS Boger fluids characterized by Stokes [Stokes 1998] are similar, but not identical, to the test fluids used by Nguyen and Boger [Nguyen and Boger 1979], so two

representative solutions denoted Fluid C (η_0 = 1.5Pa·s) and Fluid E (η_0 = 23Pa·s) by the author have been chosen for comparison. Note that the extensional rheology of PAA/CS solutions is extremely difficult to measure in a filament stretching rheometer because of the tendency of the corn syrup solvent to crystallize at the surface of the fluid filament. At low Hencky strains, the resulting 'skin' on the PAA/CS filament results in an overprediction of the Trouton ratio and a large uncertainty in the normal stress ratio for the 2:1 contraction. At moderate to large Hencky strains ($\varepsilon \geq 3$), however, the skin does not affect the extensional data.

It can be seen from Figure 4-14, that there is a marked difference between the normal stress ratio calculated for the PS/PS and the PAA/CS solutions and for the PIB/PB solution. The normal stress ratio decreases monotonically with contraction ratio. For an ideal elastic liquid, which can be modeled at the most elementary level by the Oldroyd-B model, $\aleph$ can be expressed analytically for $De > 0.5$ by the following expression

$$\aleph = \frac{2\eta_p \lambda_1 \dot{\gamma}^2}{3\eta_s \dot{\varepsilon} + \frac{\eta_p \dot{\varepsilon}}{2\lambda_1 \dot{\gamma} - 1} \exp\left[2\varepsilon\left(1-(2\lambda_1\dot{\varepsilon})^{-1}\right)\right]} = \frac{2(\eta_p/\eta_s)De}{3 + \frac{(\eta_p/\eta_s)}{2De-1}\exp\left[2\varepsilon\left(1-(2De)^{-1}\right)\right]} \tag{4-8}$$

where $\dot{\gamma} \approx \dot{\varepsilon} \approx \langle v_z \rangle_2/(R_2 + R_c)$ and $\varepsilon = 2\ln\beta$. The magnitude of this ratio thus depends on the ratio η_p/η_s (which depends on solvent quality and polymer concentration), the Deborah number and the contraction ratio.

Over the entire range of contraction ratios examined, the normal stress ratio of the PS/PS and PAA/CS solutions are significantly smaller than the normal stress ratio of the PIB/PB solution. A line can be drawn through the data at a normal stress ratio of $\aleph \approx 0.055 \pm 0.005$ which divides the data into regimes of elastic corner vortex growth ($\aleph \leq 0.055$) and lip vortex growth ($\aleph \geq 0.055$). As the Deborah number, and subsequently the tensile normal stress difference in extension, increase, we expect the normal stress ratio to decrease monotonically and the lip vortex regime to eventually give way to elastic corner vortex growth. This is the first quantitative evidence to suggest that the kinematics of the flow can be systematically rationalized on the basis of rheological information. It would be interesting to compare these observations with Brownian dynamics computations of the ratio of elastic stress differences in shear to first normal stress differences in extension as the solvent quality or excluded volume is systematically modified.

The principal remaining difference between different experimental observations of the lip vortex is now the time-dependent characteristic observed in different elastic fluids. Possible explanations here may include the method of observation used (e.g. time-averaged streak photography or time-resolved LDV and DPIV measurements) and, perhaps more importantly, the driving mechanism used. In the present work, we use a constant volumetric displacement rate, whereas the majority of previous studies have imposed a constant global pressure drop across the test geometry. This important difference in experimental control parameters leads to different dynamics in many other bifurcating systems (e.g. spurt and stick slip in melt extrusion) and may prove to be a useful avenue for future research studies.

CHAPTER 5 The Effect of Lip Curvature on the Flow through an Abrupt Axisymmetric Contraction-Expansion

5.1 Introduction

In this chapter, the 0.025wt% PS/PS Boger fluid is used to investigate the kinematics of the flow through several axisymmetric contraction-expansions of varying lip curvatures over a wide range of Deborah numbers. The experimental techniques utilized in the previous two chapters will again be used to determine what effects systematic changes in curvature of the re-entrant corner will have on the magnitude and the onset conditions of the enhanced pressure drop, vortex growth dynamics and flow stability. Investigation of the role of lip curvature is especially important because a major computational impediment to simulations of the viscoelastic flow through a contraction-expansion is the development of singular stress fields near a sharp re-entrant corner [Caswell 1996].

	Sharp Re-Entrant Corner		Rounded Re-Entrant Corner	
Boger Fluid	Corner Vortex	Lip Vortex	Corner Vortex	Lip Vortex
PIB/PB [Boger and Binnington 1994; McKinley *et al.* 1991]	$\beta \geq 8$	$2 \leq \beta \leq 6.8$	$\beta \geq 8$	$2 \leq \beta \leq 6.8$
PAA/CS [Boger 1987; Boger and Binnington 1994; Nguyen and Boger 1979]	$\beta \geq 4$	$\beta \leq 2$	$\beta > 4$	$\beta \leq 4$
PS/PS	$\beta \geq 4$	$\beta = 2$		

Table 5-1 Vortex growth dynamics for several Boger fluids at various contraction ratios and re-entrant corner radii of curvature.

As observed in Chapters 3 and 4, the sequence of flow patterns chosen by the viscoelastic fluid is a complex function of the contraction ratio as well as the re-entrant lip curvature. The effect of lip curvature on the vortex growth dynamics is summarized in Table 5-1. Boger and Binnington [Boger and Binnington 1994] presented a systematic photographic study using PIB/PB and PAA/CS Boger fluids while the vortex growth dynamics observed using a similar PIB/PB Boger fluid were discussed by McKinley et al. [McKinley *et al.* 1991]. These previous studies show that, for the PIB/PB Boger fluid at the contraction ratios examined, rounding the re-entrant corner leads to increases in the critical Deborah numbers for flow transitions, but

does not qualitatively change the kinematics of the flow field. However, rounding the re-entrant corner of the 4:1 contraction with a radius of curvature equal to 36% of the contraction radius ($R_c = 0.36R_2$) results in a dramatic change in the vortex evolution for the PAA/CS solution [Boger and Binnington 1994]. Streak images recorded upstream of the sharp re-entrant corner, clearly demonstrate the growth dynamics of a corner vortex. However, the nature of the contraction flow was completely changed by rounding the re-entrant corner. The formation of the expected corner vortex is suppressed and supplanted by a lip vortex [Boger and Binnington 1994]. Boger and Binnington thus argue that the evidence suggests that rounding the re-entrant corner is equivalent to decreasing the contraction ratio.

In Section 5-3, we first present observation of the enhanced pressure drop for several different re-entrant lip curvatures. Flow visualization, and digital particle image velocimetry (DPIV) are then used to characterize the evolution in the kinematics of the fluid motion with increasing Deborah number. Finally, in Section 4-4 we discuss our finding.

5.2 Experimental

5.2.1 *Flow Geometry*

A schematic diagram of the axisymmetric contraction-expansion and the important length scales associated with can be found in Chapter 3, Figure 3-1. Several different orifice plate configurations with various re-entrant corner radii of curvature (R_c) are used in this study and are listed in dimensionless form in Table 5-2. The configurations investigated in the previous two chapters are included for completeness.

Description	Contraction Ratio ($\beta \equiv R_1 / R_2$)	Re-entrant Lip Curvature (R_c / R_2)	Contraction Length (L_c / R_2)
2:1:2	2	< 0.01	0.5
4:1:4	4	< 0.01	1
4:1:4 Rounded	4	0.5 upstream only	1
8:1:8	8	< 0.01	2
8:1:8 Rounded	8	0.18 upstream and downstream	2

Table 5-2 Description of orifice plate geometries used in this study. In each case the value of the upstream radius is $R_1 = 1.3$cm.

In this chapter, we define a dimensionless pressure drop that similar to the definition presented in

$$\mathscr{P}\left(De, R_c, \beta\right) = \frac{\Delta P'_{ud}\left(Q, De, R_c, \beta\right)}{\Delta P'_{ud}\left(Q, De = 0, R_c = 0, \beta = 4\right)}, \tag{5-1}$$

where the pressure drop resulting from the flow of a Newtonian fluid across a 4:1:4 sharp (R_c = 0) axisymmetric contraction-expansion at a given flow rate, $\Delta P'_{ud}(Q,\ De = 0,\ R_c = 0,\ \beta = 0)$, is used in the denominator to non-dimensionalize the pressure drop resulting from the flow of the non-Newtonian test fluid across each of the contraction-expansions at the same flow rate, regardless of re-entrant lip curvature.

5.3 Results

5.3.1 *Pressure Drop Measurements*

The effect of re-entrant corner curvature on the dimensionless pressure drop is shown in Figurse 5-1 for the 4:1:4 contraction-expansion with sharp ($R_c < 0.01R_2$) and rounded ($R_c = 0.5R_2$) re-entrant corners and

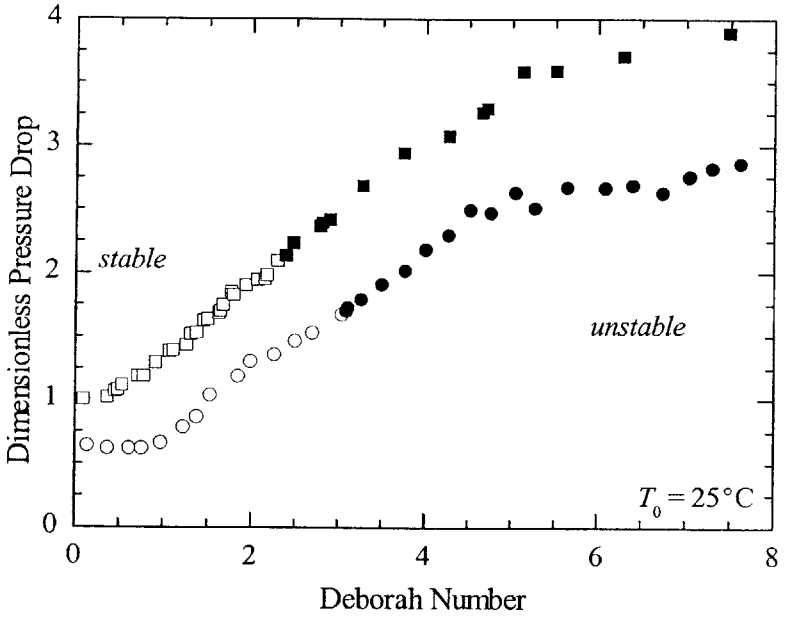

Figure 5-1 Dimensionless pressure drop measurements, $\mathscr{P}(De, \beta, R_c)$, of the 0.025wt% PS/PS solution across two 4:1:4 axisymmetric contraction-expansions with different entrance lip curvature as a function of Deborah number, $De = \lambda_0 \nu$. The figure includes: □, $\beta = 4$ and $R_c = 0$; and ○, $\beta = 4$ and $R_c = 0.5\ R_2$. The hollow symbols represent stable flow conditions while the filled symbols represent unstable flow conditions.

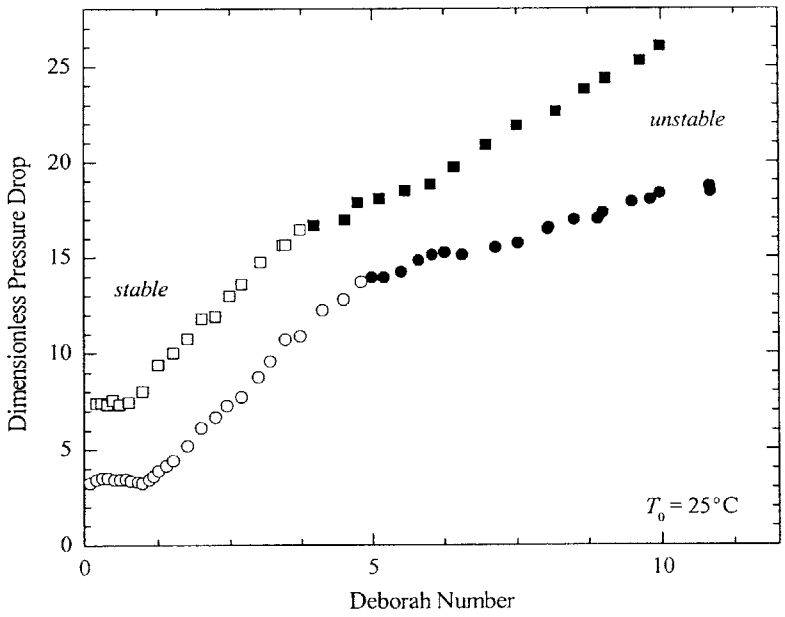

Figure 5-2 Dimensionless pressure drop measurements, $\mathscr{P}(De, \beta, R_c)$, of the 0.025wt% PS/PS solution across two 8:1:8 axisymmetric contraction-expansions with different entrance lip curvature as a function of Deborah number. The figure includes: □, $\beta = 8$ and $R_c = 0$; and ○, $\beta = 8$ and $R_c = 0.18\ R_2$. The hollow symbols represent stable flow conditions while the filled symbols represent unstable flow conditions.

Figure 5-2 for the 8:1:8 contraction-expansion with sharp ($R_c < 0.01R_2$) and rounded ($R_c = 0.18R_2$) re-entrant corners. The resulting plots are very similar to Figure 4-1, showing all the same qualitative features. At low Deborah numbers, the dimensionless pressure drop is Newtonian-like for all re-entrant corner curvatures and contraction ratios. The limiting value of the dimensionless pressure drop at low Deborah number for the rounded re-entrant corner is small, $\mathscr{P} \approx 0.35$ for $\beta = 4$ and $\mathscr{P} \approx 3.4$ for $\beta = 8$, because the presence of the re-entrant corner curvature has essentially been ignored in Equation 5-1. Recall that for a sharp contraction-expansion the dimensionless pressure drop at low Deborah numbers will be equal to $\mathscr{P}(De << 1) = \beta^3/64$. The regions of strong enhanced pressure drop and the onset of the elastic instability are still present even when the re-entrant corner has been rounded. In fact, the only noticeable effect is a shift of onset conditions for different flow regimes to higher Deborah numbers with increasing re-entrant corner curvature. This is consistent with an overprediction of the characteristic deformation rate near the throat, which is at present taken to be the deformation rate within the contraction throat, $\dot{\gamma} = \langle v_z \rangle_2 / R_2$, independent of re-entrant corner curvature. We return to discuss this shift in onset conditions in Section 5.4.

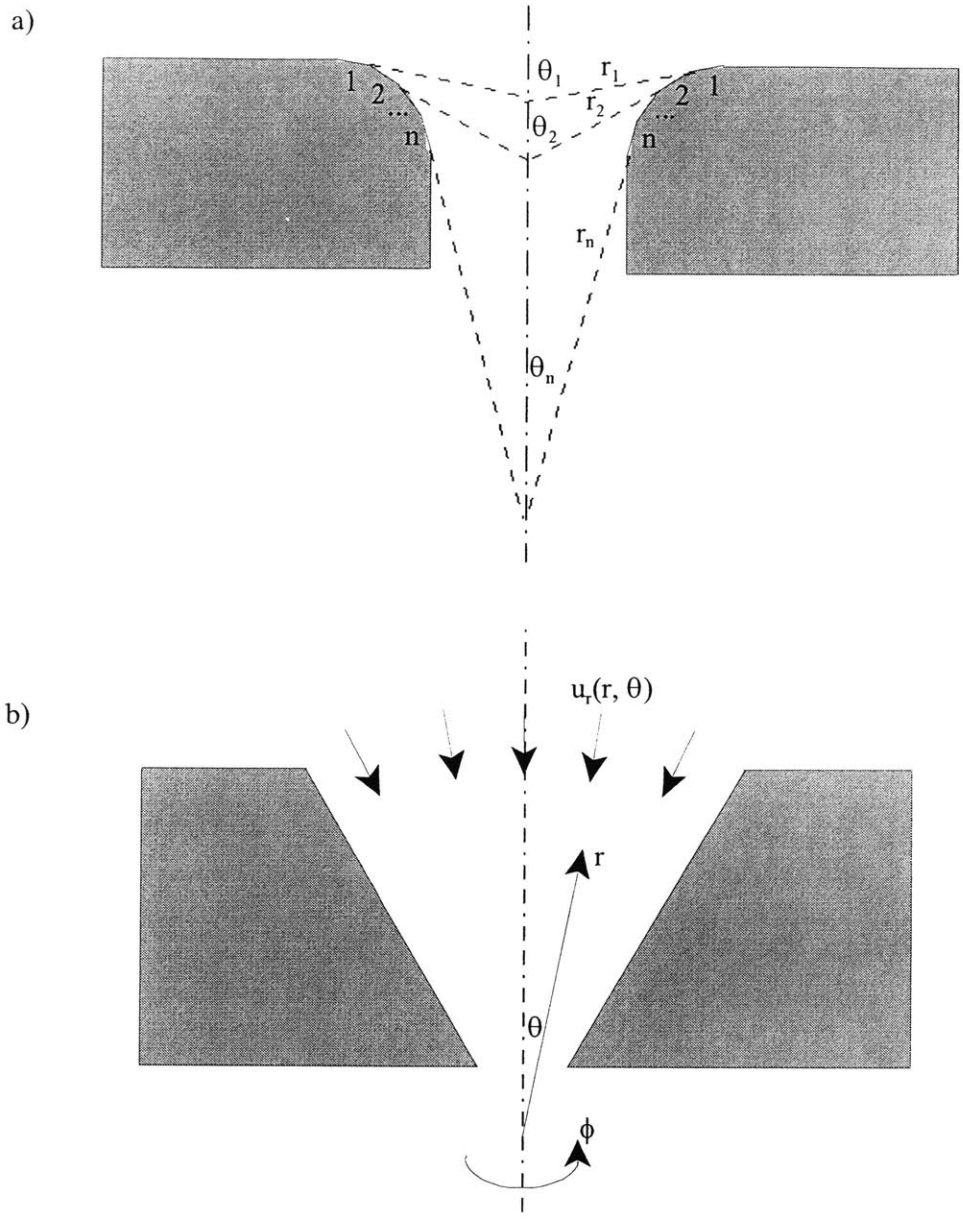

Figure 5-3 Schematic diagram of flow into (a) an axisymmetric contraction-expansion with a curved re-entrant corner and (b) a conical section.

These experiments show that the existence of enhanced pressure drop measurements above and beyond the Newtonian pressure drop ($P > 1$) do not depend qualitatively on re-entrant corner curvature nor on the onset of elastic instabilities. Thus, numerical simulations should be able to remove the singularity associated with the sharp re-entrant corner and without hindering the ability of the constitutive model to predict the large enhanced pressure drop seen in experiments.

A systematic numerical study of the effect of lip curvature on the pressure drop across a contraction-expansion has yet to be performed for either a Newtonian or a non-Newtonian fluid. The pressure drop across the curved re-entrant corner can be estimated for a Newtonian fluid by adding the pressure drop contribution from a series of short conical sections approximating the shape of the curved lip. This idea is illustrated by the schematic diagram in Figure 5.3. As the number of conical sections, n, is increased, this approach should converge to a value approximately equal to the pressure drop across the rounded re-entrant corner.

The flow of a Newtonian fluid into a conical section at low Reynolds number was solved exactly by Hamel in 1917 [Happel and Brenner 1965]. The fluid velocity and pressure gradients are given by

$$\begin{aligned} u_r &= -\frac{1}{2\eta r^2}\left[\sin^2\alpha - \sin^2\theta\right], \\ \frac{\partial P}{\partial \theta} &= \frac{2K'}{r^3}\cos\theta\sin\theta, \\ \frac{\partial P}{\partial r} &= \frac{K'}{r^4}\left[2\cos^2\theta - \sin^2\theta\right], \end{aligned} \tag{5-2}$$

where α is the cone angle at the wall and

$$K' = \frac{3Q\eta}{2\pi\left[\cos^3\alpha + \frac{3}{2}\sin^2\alpha - 1\right]}. \tag{5-3}$$

The pressure drop along the wall ($\theta=\alpha$) thus becomes

$$\Delta P = \frac{K'}{3}\left[2\cos^2\alpha - \sin^2\alpha\right]\left(\frac{1}{r_1^3} - \frac{1}{r_2^3}\right). \tag{5-4}$$

The curved re-entrant corner can be mapped to an arbitrary number of conical sections. In Figure 5-4, the dimensionless pressure drop across the curved lip which is defined as

$$\frac{\Delta P_{cone\ flow}}{\Delta P_{Sampson}} = \frac{\Delta P_{cone\ flow}}{\frac{3\eta Q}{R_2^3}}, \tag{5-5}$$

is plotted as a function of the number of conical sections for a 4:1:4 axisymmetric contraction-expansion with

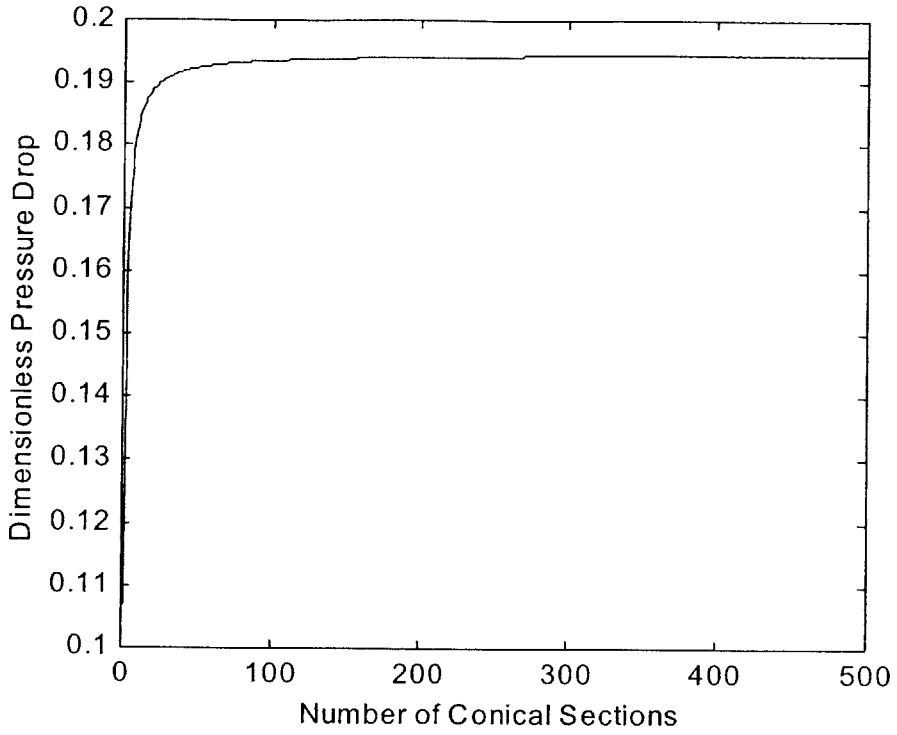

Figure 5-4 Dimensionless pressure drop across the curved re-entrant lip calculated as a function of the number of conical sections used to approximate form of lip for a 4:1:4 contraction-expansion with an upstream re-entrant corner curvature of $R_c/R_2 = 0.5$.

a lip radius of curvature of $R_c = 0.5R_2$. The analytical model quickly converges using less than 300 conical sections. By calculating the pressure drop, $\Delta P_{cone\ flow}$, for each contraction geometry, the total dimensionless Newtonian pressure drop across the axisymmetric contraction-expansion can thus be estimated for an arbitrary re-entrant corner curvature

$$\frac{\Delta P'_{curved\ contraction}}{\Delta P_{Sampson}} = \frac{\Delta P_{Sampson}\left(R_2 + R_c\right) + \Delta P_{cone\ flow} - \Delta P_{Poiseuille}\left(R_c\right)}{\Delta P_{Sampson}\left(R_2\right)},$$
$$= \frac{R_2^3}{\left(R_2 + R_c\right)^3} + \frac{\Delta P_{cone\ flow}}{\frac{3\eta Q}{R_2^3}} - \frac{8}{3\pi}\frac{R_c}{R_2}, \tag{5-6}$$

where the extra pressure drop resulting from the curved contraction, $\Delta P'_{curved\ contraction}$, is defined by Equation 4-1. In Figure 5-5, we show that using this simple analysis, the experimentally measured dimensionless

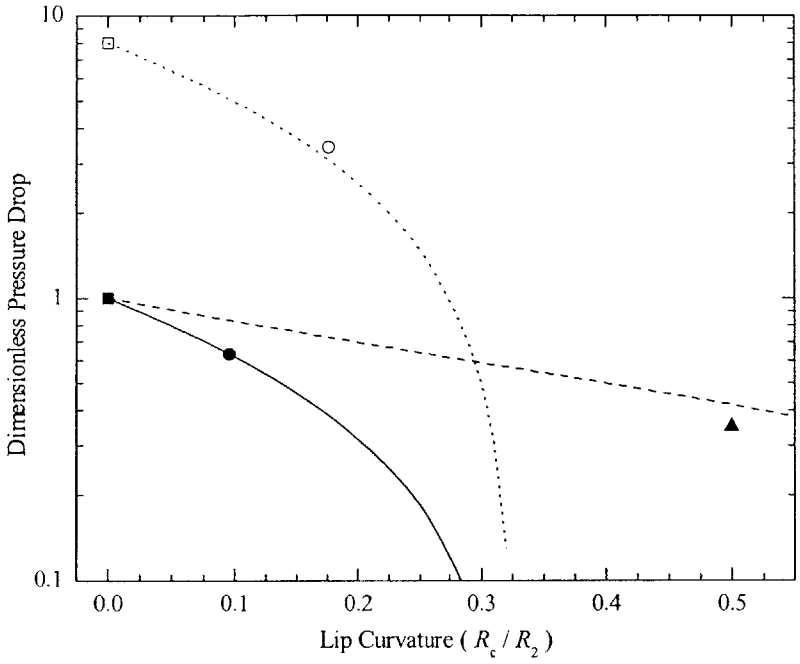

Figure 5-5 Dimensionless pressure drop as a function of degree of dimensionless lip curvature. The data include: '■', 4:1:4 axisymmetric contraction-expansion with R_c = 0 upstream and downstream; '●', β = 4, R_c = 0.1 upstream and downstream; '▲', β = 4, R_c = 0.5 upstream only; '□', β = 8, R_c = 0 upstream and downstream; '●', β = 8, R_c = 0.18 upstream and downstream; and the analytical predictions from Equation 5-6.

pressure drop in the limit of small Deborah numbers $De << 1$ is predicted quite well for both the 4:1:4 and the 8:1:8 axisymmetric contraction-expansions with various degrees of lip curvature. Data from several other lip curvatures are needed to demonstrate the robustness of this analytical model, however, one can conclude from Figure 5-5 that the dimensionless pressure drop is extremely sensitive to the small changes in re-entrant lip curvature. This is evident both from the experimental data and the analytical model predictions. This analysis will be used again in Section 5.4.1 when the data are rescaled to remove the effects of re-entrant lip curvature and generate a series of master curves.

5.3.2 *Vortex Growth Dynamics*

Flow visualization was used to observe the vortex growth dynamics upstream of the contraction for the geometries describe in Section 5.2.1 for Deborah numbers $De \leq 7$. The pseudo-streak images on the left-

hand side of Figure 5-6 show the vortex growth and development of the vortex upstream of the sharp 4:1:4 contraction-expansion at Deborah numbers of De = 1.6, 2.6 and 3.6 while the images on the right-hand side show the vortex development upstream of the 4:1:4 rounded contraction-expansion at the same Deborah numbers. These images demonstrate the dramatic delay in corner vortex development that results from the introduction of curvature to the re-entrant corner. At low Deborah numbers the 0.025wt% PS/PS solution is essentially Newtonian and Moffatt vortices are present in the stagnant corners just upstream of the contraction plane. An example of the flow patterns observed before the vortex growth and the increase in the pressure drop is shown in Figure 5-6(d). As the Deborah number is increased, the corner vortices increase in size and strength, Figure 5-6(a) and 6(e). The corner vortex 'fingers' out towards the contraction

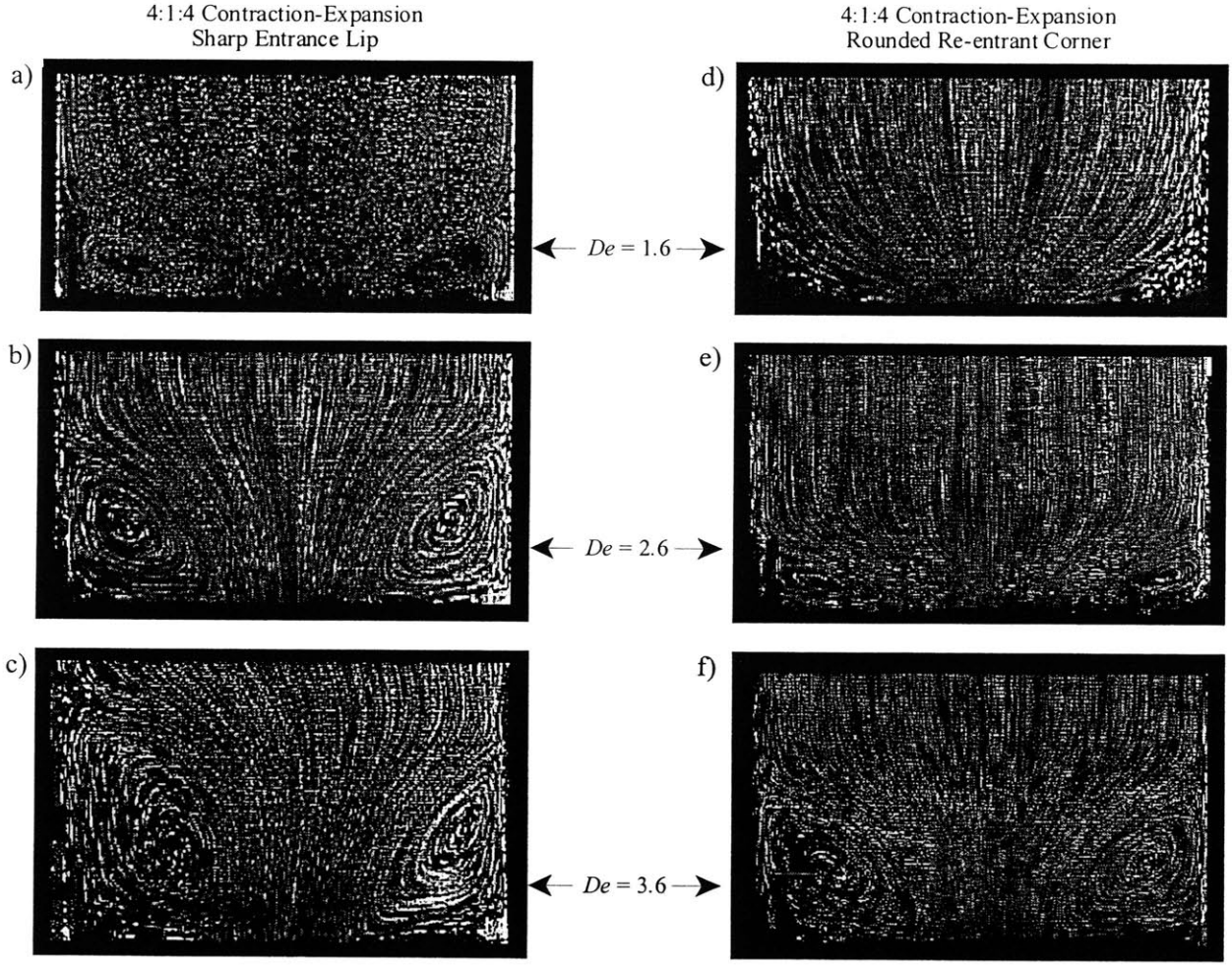

Figure 5-6 Streak images comparing the flow upstream of a 4:1:4 axisymmetric contraction-expansion with (a)-(c) a sharp entrance lip, $R_c = 0$, and (d)-(f) a rounded entrance lip, $R_c = 0.5\ R_2$, taken at identical Deborah numbers of (a),(d) De = 1.6, (b),(e) De = 2.6, and (c),(f) De = 3.6.

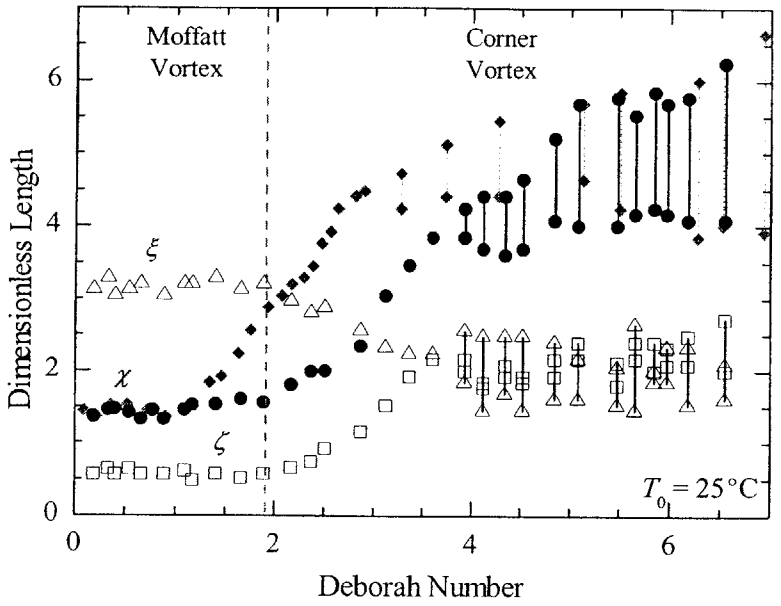

Figure 5-7 Characteristics of the upstream vortex growth dynamics as a function of Deborah number for the 4:1:4 axisymmetric contraction-expansion with rounded entrance lip, $R_c = 0.5\ R_2$,: ●, vortex reattachment length, $\chi = L_v / R_2$; ▵, radial location of the vortex center, $\xi = R_v / R_2$; □, the upstream location of the vortex center, $\zeta = Z_v / R_2$; and ♦, vortex reattachment length for the 4:1:4 contraction-expansion with sharp entrance lip, $R_c = 0$.

entrance and the dividing streamline becomes convex. As the Deborah number is increased still further, a pronounced increase in the dimensionless pressure drop is observed and the corner vortex begins to grow upstream, Figure 5-6(b) and 6(f). In Figure 5-6(c), the presence of a global instability in the flow is evident from the non-symmetric corner vortex. Visual observations and LDV measurements of this vortex show that the vortex boundary precesses in the azimuthal direction so that fluid elements in fact follow a helical path into the orifice.

The vortex growth dynamics of the 4:1:4 rounded contraction-expansion are quantified in Figure 5-7 through measurements of the dimensionless reattachment length and coordinates of the vortex center as a function of Deborah number. To motivate the discussion of re-entrant corner curvature effects, the reattachment length of the 4:1:4 sharp contraction-expansion has been superimposed over the complete set of 4:1:4 rounded contraction-expansion data presented in Chapter 3. At low Deborah numbers, the dimensionless reattachment length is constant with the expected value for creeping Newtonian flow. As the

flow rate is increased, the reattachment length and the axial location of the vortex center begin to increase monotonically with Deborah number. The radial location of the vortex center moves inward from the stagnant corner to a position $\xi \sim 2$ which then remains constant as the vortex grows upstream with increasing Deborah number. Upon the onset of the elastic flow instability, all of the measured lengths begin to oscillate with the unsteady motion of the vortex. These data show the same general functional dependence on Deborah number as our earlier measurements for the sharp 4:1:4 contraction-expansion presented in Chapter 3. The principal result of rounding of the re-entrant corner is to cause a delay of the vortex growth dynamics to higher Deborah number.

5.3.3 *Flow Stability*

As has been described in detail in both Chapter 3 and 4, the 0.025wt% PS/PS solution becomes unstable to a slow non-symmetric precession of the enlarged corner vortex at large Deborah numbers. Laser

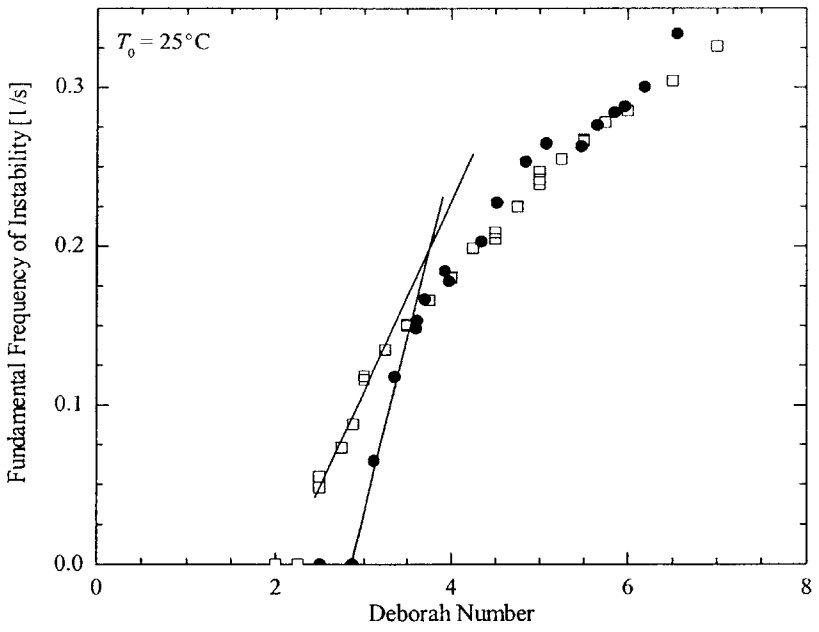

Figure 5-8 Fundamental frequency of velocity and pressure drop fluctuations in the unstable upstream flow into the axisymmetric contraction-expansions as a function of Deborah number. The data include: □, v_r and v_z for the 4:1:4 sharp contraction-expansion; ●, Δp for the 4:1:4 rounded contraction-expansion; and —, the theoretical prediction for a supercritical Hopf bifurcation, $f \sim (De - De_{crit})$.

Doppler velocimetry measurements are coupled with pressure drop measurements across the rounded 4:1:4 contraction-expansion to characterize the elastic flow instability. In Figure 5-8, the fundamental frequency of the elastic instability is plotted as a function of the Deborah number. The fit to linear stability theory, Equation 4-3, is superimposed over the data. The experimental data agrees well with the linear stability theory for a supercritical Hopf bifurcation for $(De - De_{crit}) < 1$, but as explained in Section 4.3.4, the data deviates from the linear stability theory predictions as the Deborah number is increased. The critical conditions for the onset of the subcritical Hopf bifurcation for all the contraction ratios and radii of curvature are presented in Table 5-2. The data from Chapters 3 and 4 are included for completeness. Rounding the re-entrant corner delays the onset of the elastic instability but does not change its mode. As the magnitude of the instability and its frequency grow, it is interesting to note that the data from the sharp and the rounded 4:1:4 contraction-expansion superimpose. Thus, even though the effect of re-entrant lip curvature strongly affects the linear onset conditions of the elastic instability, it appears to be much less important to the nonlinear dynamics that govern the upstream kinematics at much larger Deborah numbers.

	Critical Deborah Number for the Onset of the Elastic Flow Instability
4:1:4 Sharp Contraction-Expansion	2.4 ± 0.1
4:1:4 Rounded Contraction-Expansion	3.1 ± 0.2
8:1:8 Sharp Contraction-Expansion	4.2 ± 0.2
8:1:8 Rounded Contraction-Expansion	4.8 ± 0.2

Table 5-3 Critical conditions for the onset of the supercritical Hopf bifurcation.

5.4 Discussion

In the research presented in Chapters 3, 4 and 5, we have presented a comprehensive set of experimental measurements of the complex flow of a dilute monodisperse polystyrene solution into axisymmetric contraction-expansions of various contraction ratios and re-entrant corner curvatures. The rheological properties of the test fluid have been well characterized in both shear and extension, making these experiments a demanding comparative tool for constitutive models and numerical simulations.

An enhanced pressure drop associated with the extensional flow of the viscoelastic fluid across an axisymmetric contraction-expansion but not directly connected with the onset of an elastic instability was observed for all geometries tested. Measurements of the flow kinematics for each geometry were also made

with streak images, LDV and DPIV. The general evolution of the pressure drop measurements and the flow kinematics were found to be independent of the radius of curvature of the re-entrant corner, although the critical conditions for the transitions in pressure drop and vortex growth are a function of both the lip curvature and the contraction ratio. LDV and pressure drop measurements were used to characterize a supercritical Hopf bifurcation at large Deborah numbers which resulted in a global elastic instability, breaking the symmetry of the large enhanced upstream vortex and precessing in the azimuthal direction. This instability was observed for the 4:1:4 and 8:1:8 contraction-expansions irrespective of lip curvature.

5.4.1 *Scaling of the Effects of Lip Curvature*

The experiments with curved re-entrant corners support earlier observations in PIB/PB [Boger and Binnington 1994; McKinley *et al.* 1991] and PAA/CS elastic fluids [Boger 1987; Boger and Binnington 1994; Nguyen and Boger 1979] and suggest that numerical simulations should be able to remove the singularity associated with the sharp re-entrant corner without affecting the ability of the constitutive model to predict the large enhanced viscoelastic pressure drop seen in experiments. The qualitative similarity seen in Figures 5-1, 5-1 and 5-7 between the evolution in the vortex dimensions (ζ, ξ and χ) and the extra pressure drop ($\mathscr{P}$) with increasing Deborah number in the 4:1:4 contraction-expansions with sharp and rounded re-entrant corners suggest that it should be possible to collapse the data into a single generic response for a given contraction ratio. The principal effect of smoothing the re-entrant corner is to increase the radius of curvature and decrease the rate of deformation along the streamlines entering the contraction by removing the re-entrant corner singularity. For a low Reynolds number flow, an appropriate estimate of the residence time for a fluid element in the vicinity of the curved throat region is given by $\mathsf{T} \approx (R_2+R_c)/\langle v_z \rangle_2$. The Deborah number then becomes $De = \lambda \langle v_z \rangle_2/(R_2+R_c)$. This simple scaling of the abscissa does a remarkable job of collapsing the vortex growth data for the 4:1:4 sharp and rounded re-entrant corners onto a single curve, as shown in Figure 5-9a, even matching the transition to time-dependent flow.

Changing the local curvature of the lip entrance also affects the value of the entrance pressure drop for the creeping flow of a Newtonian fluid that is used to scale the ordinate axis in Figure 5-9b. As defined in Equation 5-1, the dimensionless pressure drop tends to be underpredicted ($\mathscr{P} < 1$) for geometries with curved re-entrant lips. Comparison of the dimensionless pressure drop data after appropriately shifting the Deborah number in the manner described above supports the expectation that the extra pressure drop at high Deborah numbers following upstream vortex growth is independent of the specific details of the local lip curvature. The principal effect of the lip is experienced at low Deborah number when the converging flow

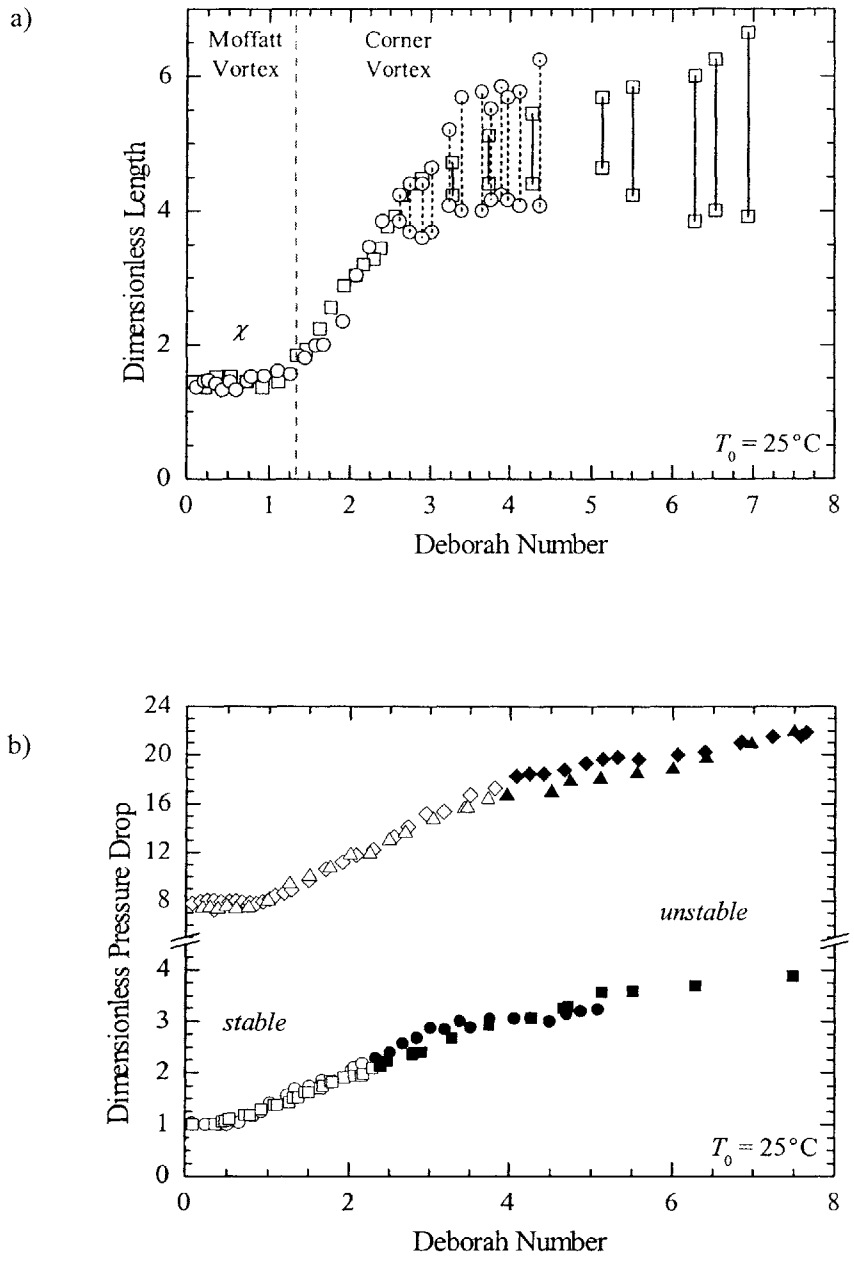

Figure 5-9 Master curves of (a) reattachment length and (b) dimensionless pressure drop measurements, $\mathcal{F}(De, \beta, R_c)$, for the flow of the 0.025wt% PS/PS solution across two 4:1:4 axisymmetric contraction-expansions with different entrance lip curvature as a function of Deborah number shifted to account for re-entrant corner curvature (see text for details). The figures include: □, $\beta = 4$ and $R_c = 0$; ○, $\beta = 4$ and $R_c = 0.5\ R_2$; △, $\beta = 8$ and $R_c = 0$; and ◇, $\beta = 8$ and $R_c = 0.5\ R_2$.

near the contraction plane is of the Sampson type. The dimensionless pressure drop (which we always scale with the Sampson flow solution for entrance in a sharp orifice $\Delta P_S = 3\eta_0 Q/R_2^3$) can thus be adjusted through the addition of a Couette-like, creeping flow correction, $C_s(\beta, R_c) = \mathcal{P}_{sharp}(De = 0) - \mathcal{P}_{curved}(De = 0)$, to take into account the pressure drop corresponding to the Newtonian flow through the curved entrance region. In Figure 5-9b, the results of this scaling of the dimensionless pressure drop $\mathcal{P}_{shifted} = \mathcal{P}_{curved} + C_s(\beta, R_c)$ is shown for two cases: the 4:1:4 sharp and rounded contraction-expansions where the Couette-like correction was found from experiments to be $C_s(R_c/R_2 = 0.5, \beta = 4) = 0.35$ and the sharp and rounded 8:1:8 contraction-expansions where $C_s(R_c/R_2 = 0.18, \beta = 8) = 4.6$. The latter data are presented to demonstrate the robustness of this scaling over several contraction ratios and radii of curvature. It is dangerous to generalize based on experimental data with only two values of radius of curvature ($R_c = 0.18R_2$ and $0.5R_2$), but this rescaling of the Deborah number also collapses quite well the trends of vortex reattachment length reported in the literature for PIB/PB Boger fluids [McKinley *et al.* 1991]. It would be very interesting to see if this simple incorporation of curvature effects on vortex size and pressure drop is supported by numerical calculations in which the radius of curvature of the re-entrant corner is systematically varied over a broad range.

The pressure drop measurements, LDV and DPIV measurements, and the streak images coupled with the use of a monodisperse dilute polymer solution, well characterized in shear and extension, make this set of experiments presented in Chapters 3,4 and 5 a useful tool for forming comparisons with theoretical and numerical work.

CHAPTER 6 Flow Induced Birefringence Measurements of the Flow through an Axisymmetric Contraction-Expansion

6.1 Introduction

Flow induced birefringence has typically been used only in two-dimensional flows of polymer melts and solutions such as planar contractions and planar extension because it is a line of sight technique. In these two-dimensional flows, where the conformation does not vary along the path of the light, Figure 6-1 shows that flow induced birefringence can generate a pointwise measure of the anisotropic conformation field. If the stress-optic rule is determined to be valid, then these measurements of polymer coil deformation can be converted directly to polymer stress. Direct comparison of these experimental measurements is possible with numerical simulations using any desired constitutive model [Beraudo *et al.* 1998]. The early measurements of flow induced birefringence were obtained by taking full field photographs of light having passed through crossed polarizers placed on either side of a flow cell [Boger and Walters 1993; Janeschitz-Kriegl 1983]. Quantitative stress field measurements are then calculated from these images by counting fringes [Beraudo *et al.* 1998; Fuller 1995; Mackay and Boger 1988; White *et al.* 1987]. The resolution of this technique is coarse as it is constrained by both the temporal and spatial resolution of the imaging camera and is only applicable for highly birefringent materials such as polymer melts. More advanced point-wise high resolution flow induced birefringence measurement techniques using polarized laser light have been developed over the past 20 years [Frattini and Fuller 1984; Fuller 1995]. Quinzani *et al.* [Quinzani *et al.* 1994; Quinzani *et al.* 1995] used laser Doppler velocimetry (LDV) and a two color birefringence technique developed by Chow and Fuller [Chow and Fuller 1984] to probe the flow of a 5% PIB/tetradecane solution through an abrupt 4:1 planar contraction. The measured centerline velocities were converted to strain rates by differentiation and used to calculate the fluid stress predicted by various constitutive models [Quinzani *et al.* 1995]. The predictions of the constitutive models were able to qualitatively reproduce the flow induced birefringence measurements of the stress for this nonhomogeneous planar elongational flow, however, these experiments were limited by the low range of Deborah numbers ($De < 0.8$), the influence of inertia and the small Hencky strains achieved. Two-dimensional flow induced birefringence measurements have also been used very successfully in homogenous transient uniaxial elongation experiments [Doyle *et al.* 1998]. A detailed account of these experiments will be presented in Chapter 7.

In an axisymmetric or three-dimensional geometry the molecular conformation does vary along the line of sight. This nonhomogeneous flow results in an integrated measure of the flow induced birefringence

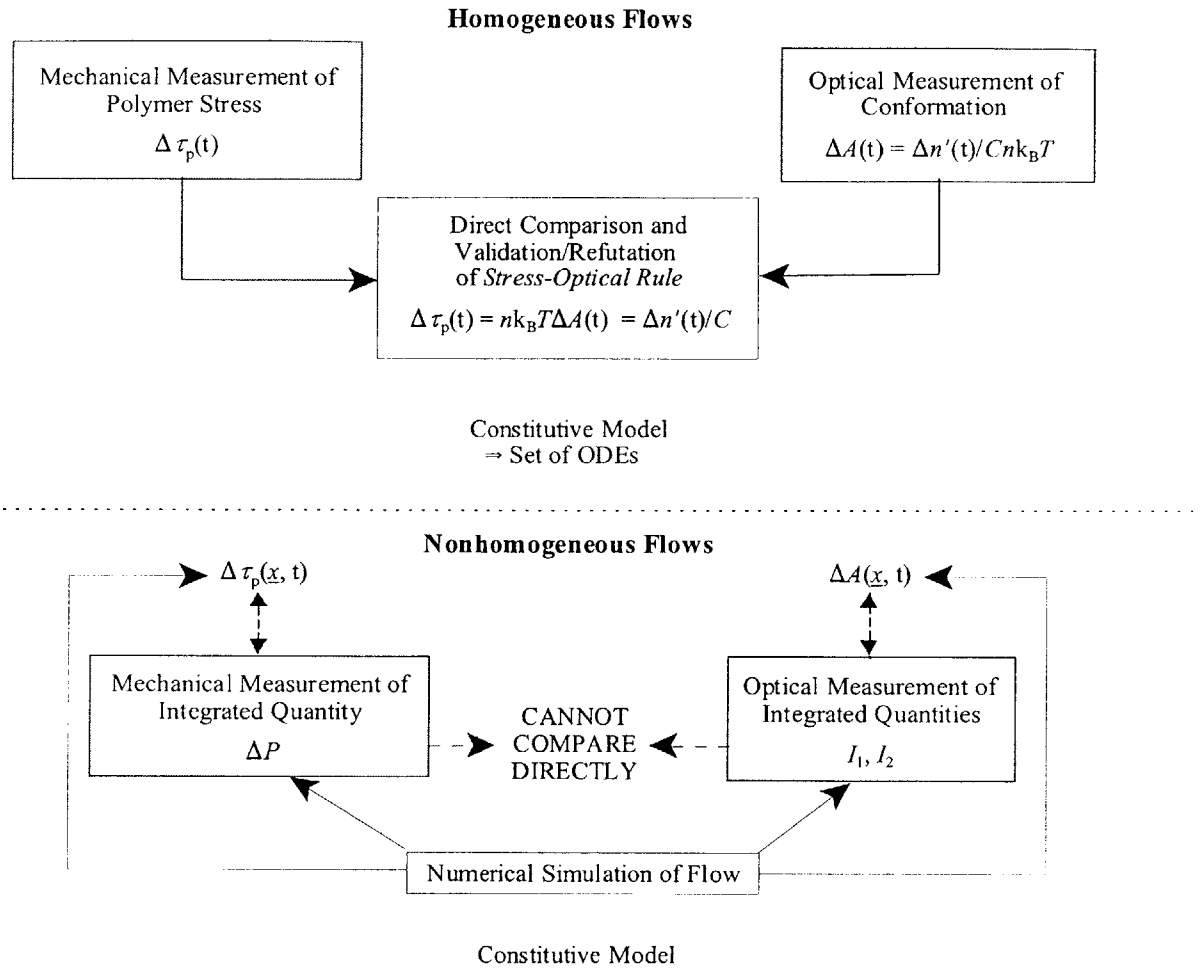

Figure 6-1 Flow chart outlining the means of quantitative comparison between numerical simulation and experimentally obtained optical and mechanical measurements of homogeneous and inhomogeneous polymeric flows.

and subsequently the anisotropic conformation. The pioneering work in this area was performed by Li and Burghardt [Li and Burghardt 1995] who investigated the axisymmetric stagnation flow of a polystyrene Boger fluid past a cylindrical obstruction with a hemispherical cap. Li and Burghardt demonstrated that even though a pointwise measure of the conformation field could not be achieved, axisymmetric flow induced birefringence (AFIB) is an excellent tool for comparison between the results of numerical simulations and experiments [Li and Burghardt 1995; Li *et al.* 1998; Li *et al.* 2000]. As shown in Figure 6-1, to perform such a comparison in nonhomogeneous flows, the conformations and stresses in the flow field upstream and downstream of a contraction-expansion can be numerically computed using a chosen constitutive model. The results of these numerical simulations can be integrated along the path of the laser beam and systematically compared to the experimentally measured conformation fields. Some recent research by Yu

et al. [Yu *et al.* 1998] used axisymmetric flow induced birefringence to investigate the extensional flow into capillary nozzle submerged in a fluid reservoir. Poor agreement was found upon comparison with numerical simulations. As in two-dimensional flows, these flow induced birefringence measurements can thus be instrumental in determining the validity and gauging the performance of various constitutive models in complex flows.

In this chapter, the experimental technique of axisymmetric flow induced birefringence measurements is introduced. Measurements of axisymmetric flow birefringence are presented for the 0.025wt% PS/PS Boger fluid upstream and downstream of a 2:1:2 and a 4:1:4 contraction-expansion over a large range of Deborah numbers. The results demonstrate a region of strong polymer alignment and upstream extension for both contraction ratios with a weak region of biaxial compression downstream of the expansion. The region of extension is found to grow in magnitude and move upstream as the Deborah number is increased while the region of biaxial compression is found to be insensitive to changes in Deborah number. The flow induced birefringence measurements are then used to explore the different vortex growth mechanisms observed at different contraction ratios. Lastly, axisymmetric flow induced birefringence is demonstrated to be a very sensitive means of detecting elastic flow instabilities.

6.2 Theory of Flow Induced Birefringence (FIB)

The molecular polarizability and hence the macroscopic refractive index of a typical linear homo-polymer chain is different in the direction parallel to and normal to the chain backbone [Fuller 1995]. Flow-induced birefringence utilizes this refractive index mismatch to probe the microscopic deformation of polymer chains. Optical birefringence measurements are noninvasive and extremely sensitive to small changes in the local orientation and deformation of the polymer chain. For this reason, flow-induced birefringence measurements have been used quite extensively to examine steady and transient flows of polymeric fluids [Fuller 1995]. By passing light of a known polarization state and frequency through the polymeric fluid sample and measuring the resulting change in polarization state, flow-induced birefringence can be used to determine the local anisotropy in the conformation of the polymer chains [Fuller 1995]. The resulting expression for the birefringence is

$$\frac{\Delta n'}{C} = n\mathrm{k}_\mathrm{B}T\Delta A, \tag{6-1}$$

where $\Delta n'$ is the measured birefringence, C is the *stress-optical coefficient*, $n\mathrm{k}_\mathrm{B}T$ is the elastic modulus of

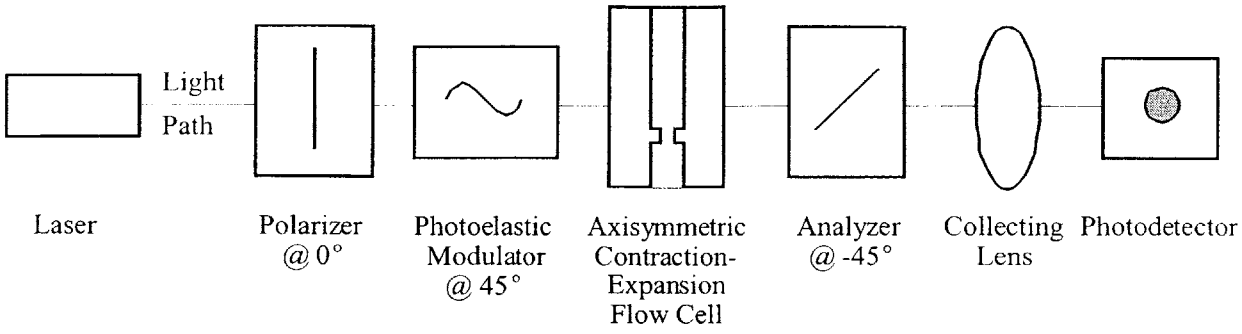

Figure 6-2 Schematic diagram of axisymmetric flow induced birefringence optical train.

the fluid, and $\Delta A = A_{11} - A_{22}$ is a measure of the anisotropy in the average conformation of the polymer chain. The polymer conformation is characterized by the dimensionless second moment tensor, $\boldsymbol{A} = \langle \boldsymbol{QQ} \rangle / Q_{eq}^2$, where $\boldsymbol{Q}$ is the end-to-end vector of the polymer chain. The theoretical value of the stress optic coefficient is given by [Fuller 1995]

$$C = \frac{2\pi \left(n'^2 + 2\right)^2}{45 n \, k_B T} \left(\alpha_1 - \alpha_2\right), \tag{6-2}$$

where isotropic index of refraction is $n' = 1.5468$ and the difference in polarizability is $(\alpha_1 - \alpha_2) = -1.45 \times 10^{-23}$ cm^3 resulting in a value of $C = -6.4 \times 10^{-9}$ Pa^{-1} for the 0.025wt% PS/PS solution [Brandrup and Immergut 1989]. However, to be consistent with the values in the literature of polystyrene in an aromatic solvent, a stress-optic coefficient value of $C = -5.0 \times 10^{-9}$ Pa^{-1} will be used in all of our FIB calculations [Doyle *et al.* 1998].

The optical path for the polarization modulated flow birefringence system employed in this research is shown in Figure 6-2 and is similar in design to the optical train first introduced by Frattini and Fuller [Frattini and Fuller 1984]. The polarized laser light is generated by a 20 milliwatt, 632nm Helium-Neon laser (Uniphase 1135P). The light passes through a linear polarizer (Karl Lambrecht Corp. MGT3E8-90) oriented at 0° from the vertical axis of the flow cell. The polarized light then passes through a photo-elastic modulator (Hinds Instruments 0385-0) oscillating at 44kHz and oriented at 45°. The light is sent through the flow cell and then a second linear polarized (Karl Lambrecht Corp. MGT3E8-90) oriented at -45°. Finally, the light passes through a collecting lens before striking on the photodetector (New Focus 1601).

The output from the photodetector is split and fed through a low pass filter (EG&G 5113) to determine the DC intensity and a pair of lock-in amplifiers (EG&G 7260) to measure the amplitude of the

signal in phase with the fundamental frequency and out of phase with first harmonic of the dual-crystal modulator. These measurements are recorded on a PC through a data acquisition card interfaced with Labview. The intensity the light entering the photodetector is given by:

$$\begin{aligned} I(t) &= I_{dc} + I_{\omega}\sin\omega t + I_{2\omega}\cos 2\omega t, \\ I_{\omega} &= 2\mathrm{J}_1(A_c) I_{dc} M_{34} = 2\mathrm{J}_1(A_c) I_{dc}\sin\delta\cos 2\chi, \\ I_{2\omega} &= 2\mathrm{J}_2(A_c) I_{dc} M_{32} = 2\mathrm{J}_2(A_c) I_{dc}[1-\cos\delta]\sin 2\chi\cos 2\chi, \end{aligned} \tag{6-3}$$

where M_{34} and M_{32} are the components of the Mueller matrix corresponding to the optical train shown in Figure 6-2a and A_c is the amplitude of the electro-optical modulation calibrated such that the Bessel function of the first kind of order zero is equal to $\mathrm{J}_0(A_c) = 0$ [Frattini and Fuller 1984]. The advantage of using a modulation technique is that it is possible to simultaneously measure the retardation, $\delta = (2\pi\,\Delta n\, d)/\lambda_{light}$, and the extinction angle, χ, where d is the pathlength of the laser and λ_{light} is the wavelength of the laser light. Solving Equations 6-3 for the retardation and extinction angle, one finds

$$\begin{aligned} \delta &= \cos^{-1}\left(\frac{-M_{32}^2 \pm \sqrt{1-M_{34}^2-M_{32}^2}}{M_{34}^2+M_{32}^2}\right), \\ \chi &= \frac{1}{2}\cos^{-1}\left(\frac{M_{34}}{\sin\delta}\right). \end{aligned} \tag{6-4}$$

In the flow through an axisymmetric geometry such as the contraction-expansion, the molecular conformation of the polymer coil varies along the path of the light resulting in an integrated measure of the flow-induced birefringence. If the retardation is small, $\delta << 1$, then the integrated version of Equation 6-3 becomes

$$\begin{aligned} \bar{M}_{34} &= \bar{\delta}\cos 2\bar{\chi} = \int_0^d \frac{2\pi\Delta n'}{\lambda}\cos 2\chi\ \mathrm{d}l \\ \bar{M}_{32} &= \frac{\bar{\delta}^2}{2}\sin 2\bar{\chi}\cos 2\bar{\chi} = \int_0^d \left(\frac{2\pi\Delta n'}{\lambda}\right)^2 \frac{l}{2}\cos 2\chi\sin 2\chi\,\mathrm{d}l \end{aligned} \tag{6-5}$$

where l is the path of the light through the birefringent material and $\bar{\delta}$ and $\bar{\chi}$ are spatially averaged effective

values of the retardation and extinction angle and $\bar{M}_{32}$ and $\bar{M}_{34}$ are the spatially averaged Mueller matrices [Li and Burghardt 1995]. Equation 6-4 still holds for the effective values of retardation and extinction angle, however, deconvoluting Equation 6-5 to calculate local measures of $\delta(r,z)$ and $\chi(r,z)$ is an ill-posed problem, although it has been attempted in the past [Yu *et al.* 1998]. Numerical simulations must be used to compare measured and computed values of $\bar{M}_{32}$ and $\bar{M}_{34}$ directly [Li *et al.* 2000].

6.3 Flow cell design and calibration

The flow cell used for the FIB measurements is shown in Figure 6-3 and was created by boring a circular hole through a block of low birefringence glass (Schott BK7). Several easily interchangeable aluminum contraction-expansions inserts were designed to fit tightly within the glass flow cell. The contraction ratio and aspect ratio of the inserts were chosen to be consistent with those used in Chapters 3 and 4 to measure macroscopic flow parameters such as pressure drop and fluid velocities. The results of AFIB for a 4:1:4 and 2:1:2 sharp contraction-expansion are presented in this chapter. To establish a seal between the flow cell and upstream and downstream tubing, the glass is mounted within an aluminum

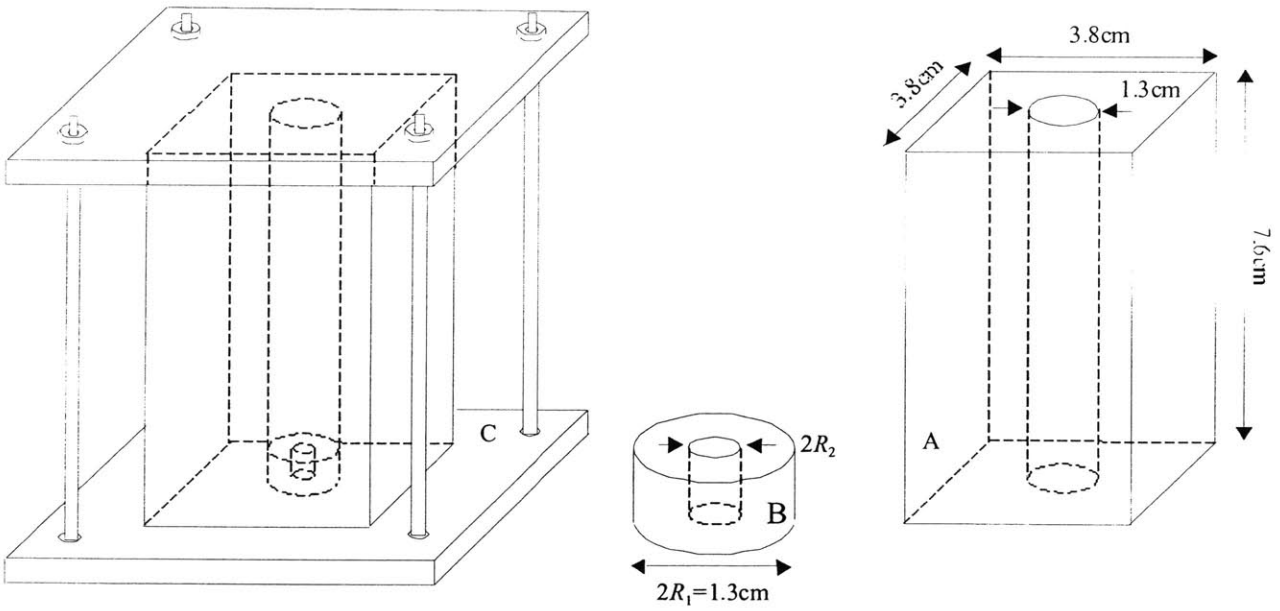

Figure 6-3 Schematic diagram of flow cell used for flow induced birefringence measurements of the axisymmetric contraction-expansion. The flow cell is comprised of: A) a block of low birefringence glass; B) a removable aluminum contraction-expansion; and C) an aluminum superstructure.

superstructure and held under constant compression. The same linear displacement stepper motor and fluid reservoir setup used in Chapters 3 through 5 is again used to drive the 0.025wt% PS/PS Boger fluid through the contraction-expansion. The birefringence optical train is rigidly mounted to an optical rail (Klinger). In order to probe the birefringence within the entire flow field, the flow cell, fluid reservoir and motor assembly are mounted on a three axis computerized stage (Compumotor 4000 and Parker 102793Q) with a $\pm 2\mu m$ position accuracy and 10cm of travel in all directions. The flow cell was carefully aligned with the optical train along all three axes.

One of the major difficulties in this technique is quantifying and subsequently removing any parasitic birefringence in the system. The chief source of parasitic birefringence is the glass used to construct the flow cell. The glass contains unknown residual stresses from the fabrication process. The birefringence associated with these residual stresses can be neglected in the final analysis of the optical path if one chooses a low birefringence optical glass such as Schott BK7. The flow cell is exposed to both a constant compressive stress exerted by the aluminum superstructure as well as an internal pressure field dependent on flow conditions. The effect of these stresses can be minimized by using a glass with an extremely small stress-optic coefficient, however, in these experiments they can not be ignored.

The two components of the Mueller matrices $\bar{M}_{32}$ and $\bar{M}_{34}$ are dependent not only on the flow-induced birefringence, but also on the parasitic birefringence of the glass. To calculate the retardation and extinction angle of the fluid, it is necessary to first determine the compression-induced and pressure-induced retardation and extinction angle, δ_c, χ_c and δ_p, χ_p respectively, so they may be systematically removed from the measured flow signals. If the retardation of any of three birefringence signals is large, this process can be a very difficult exercise in Mueller calculus [Azzam 1978; Fuller 1995]. However, if the retardation is assumed to be small, $\delta << 1$, then the contribution to the total birefringence signals of each component (flow, pressure and compression) become additive

$$\bar{M}_{34} = \delta_c \cos 2\chi_c + \delta_p \cos 2\chi_p + \bar{\delta}_{FIB} \cos 2\bar{\chi}_{FIB}. \tag{6-6}$$

Again, the overbars indicate quantities that have been integrated along the path of the incident beam. Li and Burghardt [Li and Burghardt 1995] examined the practical limits for the small angle assumption when used in the removal of the parasitic birefringence. They found an error of 5-10% in the flow induced birefringence calculated from Equation 6-6 for parasitic birefringence values on the order of $\delta \approx 0.1$-0.2 radians. To avoid incurring such errors in our measurements, the full Mueller matrix was solved to determine the flow induced birefringence at each point.

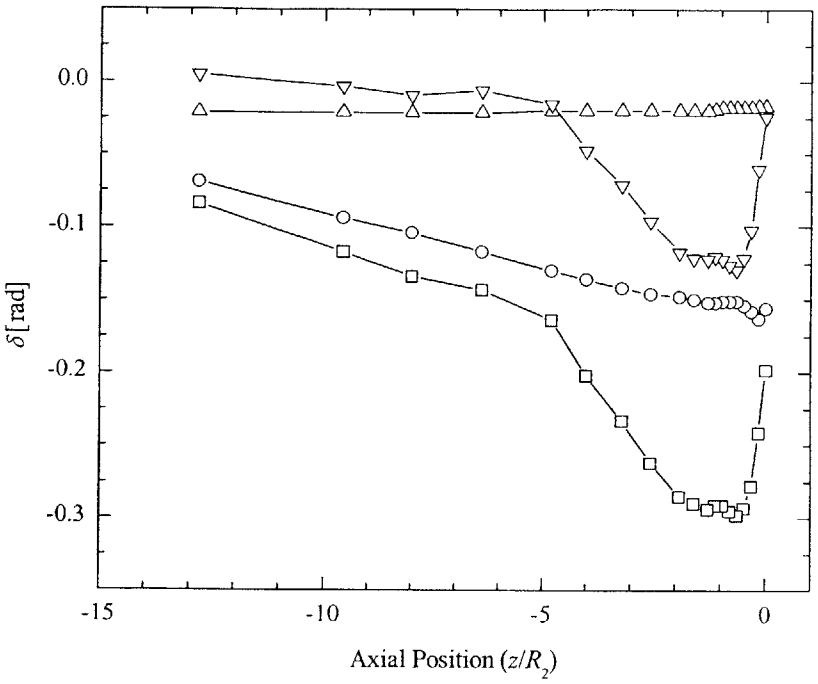

Figure 6-4 Axisymmetric flow induced birefringence measurements of the 0.025wt% PS/PS Boger fluid along the centerline upstream of a contraction-expansion at a Deborah number of $De = 4.0$. The data include: '○', contribution of compressive stress; '△', pressure; '▽', flow-induced birefringence; and '□' the total measured retardation.

Due to a strong mismatch in the indices of refraction between the flow cell glass ($n' = 1.5151$) and the polystyrene Boger fluid ($n' = 1.5468$), curvature effects make it possible to take FIB measurements only along or very near to the centerline of the flow cell. To make measurements off of the centerline, the test fluid must be closely index-matched to the flow cell glass. The only way to reduce the index of refraction of the 0.025wt% Boger fluid is to add an additional solvent component with a much lower index of refraction. Unfortunately, this would significantly alter the rheological properties to the test fluid. The decision was made not to index match because the chief goal in this research was to take centerline measurements of polymer chain deformation and orientation to compliment the macroscopic flow measurements reported in Chapters 3 through 5. Since axisymmetric flow induced birefringence measurements integrate the conformations of the molecules across the entire flow field, these centerline measurements actually succeed in sampling the entire flow field in one single integrated measure of effective retardation. As a consequence of the limitation to centerline birefringence measurements, the orientation of

the projection of the polymer coils on the *r-z* plane is always aligned with the *z* axis. In other words, the extinction angle is equal to $\bar{\chi} = 0°$. If the system is aligned properly, then $\bar{M}_{32}$ will be vanishingly small compared with $\bar{M}_{34}$. For this reason, it is therefore unnecessary to include an expression for $\bar{M}_{32}$ in Equation 6-6. If, however, measurements were possible across the entire radius of the flow cell, then the birefringence optical train shown in Figure 6-3 would need to be altered by adding quarter-wave plates after the photo-elastic modulator and before the analyzer. These changes would reproduce the system used by Li and Burghardt [Li and Burghardt 1995], making the expression for $\bar{M}_{32}$ linear, rather than quadratic, in retardation. The disadvantage of adding quarter wave plates to a birefringence optical train is that they can introduce a additional error into a measurement that is already very difficult to make.

In Figure 6-4, the procedure for systematically removing the pressure and compressive contributions to the total retardation signal is illustrated for the axisymmetric flow-induced birefringence measurements taken along the centerline upstream of the contraction plane ($z < 0$) at a Deborah number of $De = 4.0$. The magnitude of the compression induced birefringence in the glass is of the same order as the flow induced birefringence in the fluid while the retardation caused by the fluid pressure is relatively small. Both of the parasitic birefringence sources in the glass are strongly dependent on axial position and must be calibrated at each measurement point upstream. The compression-induced birefringence is isolated by performing measurements of the flow cell in the absence of flow and at zero hydrostatic pressure. This calibration is independent of flow conditions, but does depend on the exact loading of the glass in the aluminum superstructure and could change over time if the flow cell experiences a change in temperature or a slight shift in position. To minimize systematic errors, a calibration is performed before every experiment.

The determination of the proper calibration for the pressure induced birefringence in the flow cell is a little more difficult. Pressure transducers are mounted upstream and downstream of the contraction-expansion. A valve is closed downstream of the flow cell and the linear stepper motor is used to compress the fluid and increase the pressure within the flow cell. This static pressure increase should result in no appreciable change in the compressive parasitic birefringence, nor will it cause the fluid to flow resulting in microstructural deformation. The change in birefringence is measured as a function of fluid pressure and is shown in Figure 6-5. The retardation is found to increase linearly with a slope of 4.8×10^{-4} rad/kPa while the extinction angle remains constant at a value of 83°. Ideally, the extinction angle should be at 90°, however, these extinction angle measurements are extremely sensitive to very small fluctuations in the $I_{2\omega}$ signal. Using the slope of the retardation as a function of static pressure, the stress-optic coefficient of the

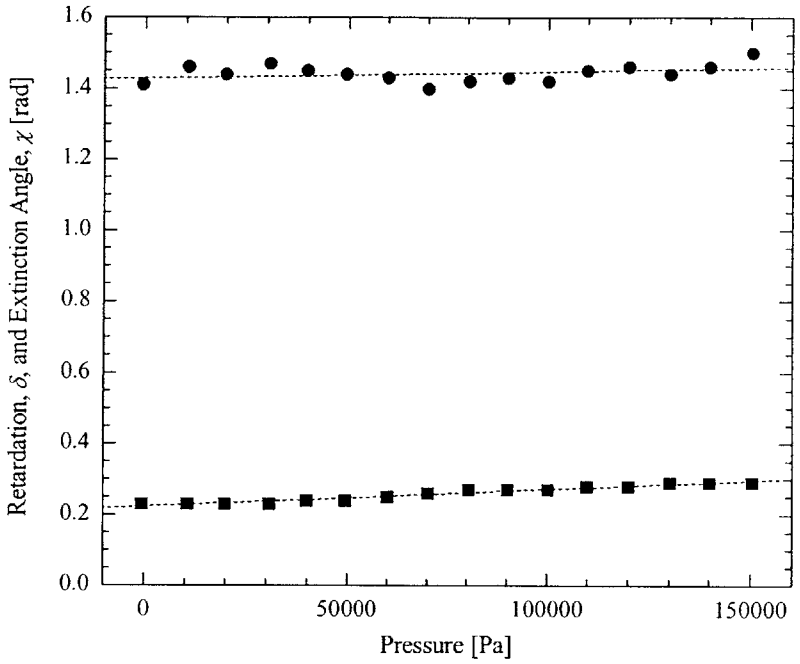

Figure 6-5 The retardation and extinction angle for the pressure induced parasitic birefringence in the flow cell glass at a position $r/R_2 = 0$ and $z/R_2 = 10$ upstream of the contraction plane. The data include: '■', retardation; '●', extinction angle; and '- -' the linear fit for each set of data.

glass is calculated to be 1.9×10^{-12} Pa^{-1}, well within the range quoted by the manufacturer. During a given experiment, the axial pressure profile is calculated from a single pressure measurement far upstream and the assumption of the Poiseuille pressure drop in the straight tube leading to the contraction plane. The stress-optic coefficient of the glass is then used to determine the appropriate value of the pressure induced retardation at each measurement location upstream of the contraction plane.

6.4 Results and Discussion

6.4.1 *4:1:4 Contraction-Expansion*

The procedure described in the previous section is used to remove the parasitic birefringence and isolate the effective retardation from all the data presented in this and the following section. The measurements are left in the form of an effective retardation, $\overline{\delta}$, but one could just as easily convert the measurements into an effective birefringence, $\Delta\overline{n}'$, or an effective conformation, $\Delta\overline{A}$. The extinction angle,

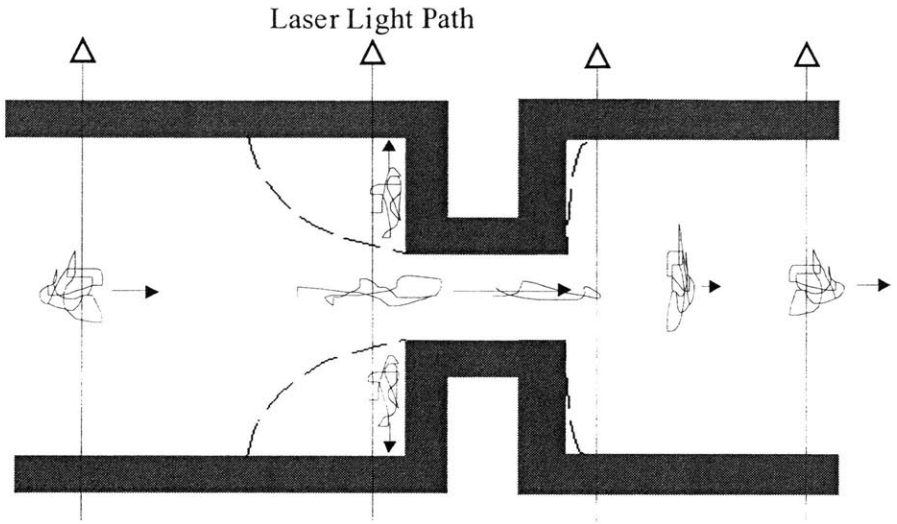

Figure 6-6 Schematic diagram depicting polymer coil orientation and elongation as it passes along the centerline of an axisymmetric contraction-expansion.

as expected, is found to be very close to 0 for all experiments performed.

A schematic diagram of the polymer chain deformation in the flow upstream and downstream of the contraction-expansion is presented in Figure 6-6 to assist with the interpretation of the effective retardation data. Figure 6-6, is intended to help emphasize that these nonhomogenous birefringence measurements are in fact integrals of the polymer coil conformation along the entire path of the interrogating laser beam. Far upstream and downstream, the polymer coils orient and elongate in the flow direction due to the shear flow along the tube walls and close to the contraction the extensional flow along the centerline. However, very near the contraction and expansion planes, the polymer coils away from the centerline are compressed with respect to the direction of the flow because of the strong shear in the recirculating vortex upstream of the contraction wall. A laser passing through the fluid near the contraction plane will therefore first encounter a region of axial chain compression followed by a zone of axial chain extension near the centerline and finally another region of compression. The result is a complicated effective retardation signal dependent not only on the relative magnitude of the polymer coil compression and extension, but on the size of each region of influence as well.

In Figure 6-7, the retardation measured along the centerline upstream of the 4:1:4 contraction-expansion is shown at several Deborah numbers for the 0.025wt% PS/PS Boger fluid. The retardation of the low Deborah number experiments in Figure 6-7 is extremely small, almost indistinguishable from the background noise. As the Deborah number is increased, the shear deformation caused by radial outflow

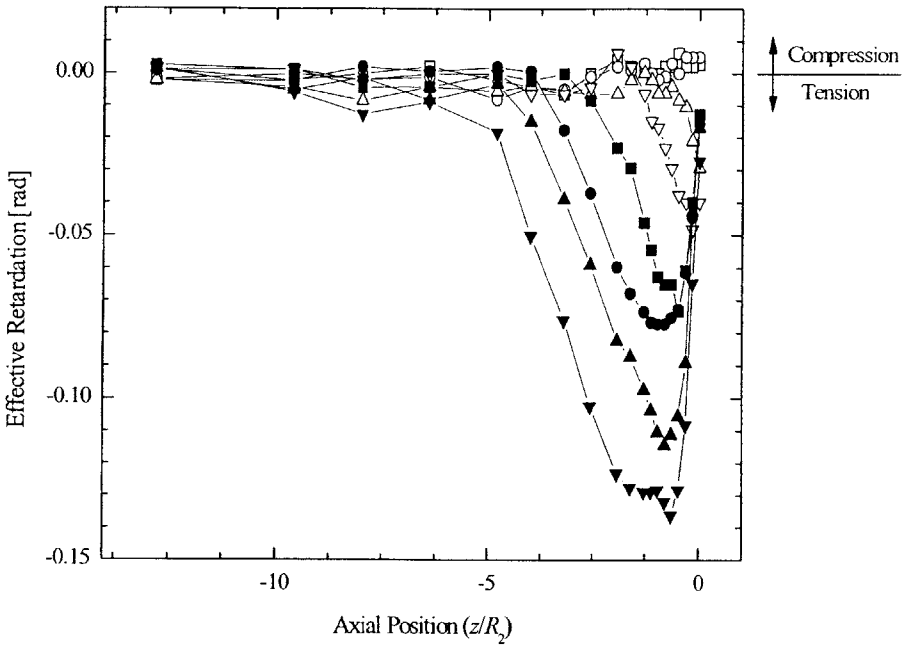

Figure 6-7 Equivalent retardation measurements of the 0.025wt% PS/PS Boger fluid along the centerline upstream of a 4:1:4 axisymmetric contraction-expansion. The data include: '□', a Deborah number of De = 0.5; '○', De = 1.0; '△', De = 1.5; '▽', De = 2.0; '■', De = 2.5; '●', De = 3.0; '▲', De = 3.5; and '▼', De = 4.0.

along the plane of the contraction, $z/R_2 \approx 0$, results in a weak axial compression of the polymer chain, $\bar{\delta} > 0$. As the Deborah number is increased, an extension of the polymer chains, $\bar{\delta} < 0$, is observed. This extension is the result of the strong extensional flow along the centerline upstream of the contraction plane. The influence of the shear flow along the contraction plane is still observable, although the flow near the contraction wall has reversed and the compression is due to a radial outflow near the contraction plane, $z/R_2 \approx 0$. The magnitude and upstream influence of the chain elongation increases concurrently with the growth and development of the corner vortex described in Chapter 3.

The effective retardation measurement far upstream is an opportunity to compare the experimental results to the predictions of theory. Assuming the stress optic law is valid for these small shearing deformations we can write [Fuller 1995]

$$\begin{aligned} \Delta n' \sin 2\chi &= 2C\tau_{12}, \\ \Delta n' \cos 2\chi &= 2C\left(\tau_{11} - \tau_{22}\right), \end{aligned} \tag{6-7}$$

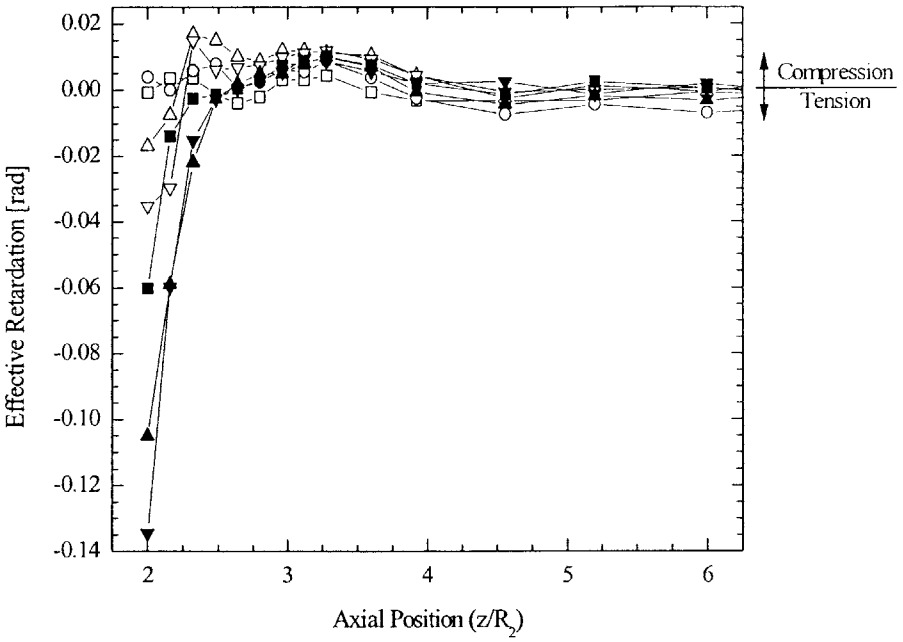

Figure 6-8 Equivalent retardation measurements of the 0.025wt% PS/PS Boger fluid along the centerline downstream of a 4:1:4 axisymmetric contraction-expansion. The data include: '□', a Deborah number of De = 0.5; '○', De = 1.0; '△', De = 1.5; '▽', De = 2.0; '■', De = 2.5; '▲', De = 3.5; and '▼', De = 4.0.

where the subscript 1 represents the flow direction, z, and the subscript 2 represents the shear direction, r. Solving for the birefringence and extinction angle variation along the centerline we find

$$\Delta n'(r) = C\left(4\tau_{rz}^2(r) + \left(\tau_{rr}(r) - \tau_{zz}(r)\right)^2\right)^{1/2},$$
$$\chi(r) = \frac{1}{2}\tan^{-1}\left[\frac{2\tau_{rz}(r)}{\tau_{rr}(r) - \tau_{zz}(r)}\right]. \tag{6-8}$$

If it were possible to take measurements off of the centerline, then the direction of light propagation would not be coincident with the chord of the circular cross section of the flow cell. For off centerline measurements, the laser light path is more easily expressed in terms of Cartesian coordinates. The full analysis for a general axisymmetric flow has been presented previously by Li and Burghardt [Li and Burghardt 1995] and will not be reproduced here.

If the fluid motion is assumed to be a Poiseuille flow far upstream of the contraction and the fluid is assumed to be a Oldroyd-B fluid, constant viscosity and first normal stress coefficient, the shear stress and first normal stress difference can be easily calculated as a function of the radius

$$\begin{aligned}
\tau_{rz} &= \frac{4Q\eta}{\pi R_1^3}\left(\frac{r}{R_1}\right) = \tau_w\left(\frac{r}{R_1}\right), \\
N_1 &= \left(\tau_{zz} - \tau_{rr}\right) = \Psi_{10}\left(\frac{4Q}{\pi R_1^3}\right)^2\left(\frac{r}{R_1}\right)^2 = 2\tau_w\frac{De}{\beta^3}\left(\frac{r}{R_1}\right)^2, \\
N_2 &= 0,
\end{aligned} \tag{6-9}$$

where τ_w is the shear stress at the wall, Q is the volume flow rate and the Deborah number, De, and the contraction ratio, β, are defined as in Chapter 3. Substituting Equations 6-9 and 6-8 into Equation 6-5 the integral expressions for the shear flow in a tube become

$$\begin{aligned}
\bar{\delta} &= \left(\frac{2\pi C}{\lambda}\right) 2\int_0^{R_1} N_1(r)\,dr = \left(\frac{2\pi C}{\lambda}\right) 2\int_0^{R_1} 2\tau_w\frac{De}{\beta^3}\left(\frac{r}{R}\right)^2 dr, \\
\bar{\chi} &= 0.
\end{aligned} \tag{6-10}$$

Integrating Equation 6-10 we find that for the 0.025wt% PS/PS Boger fluid

$$\bar{\delta} = \frac{32\pi}{3}\frac{C\eta R_1}{\bar{\lambda}\lambda_{light}}\frac{De^2}{\beta^6} = 0.091\frac{De^2}{\beta^6}. \tag{6-11}$$

The polymer deformation that should result from the shear flow along the tube walls tube far upstream of the 4:1:4 contraction-expansion is not significant enough to be observed at these low flow rates as Equation 6-10 predicts a value for the Mueller matrix to be less than This value is well below the resolution of our AFIB system and therefore all of the retardation measurements approach zero far from the contraction upstream. However, as the contraction ratio is decreased, the birefringence signal upstream will increase as $(R_{2,4:1:4}/R_{2,2:1:2})^6$ for a fixed Deborah number. For the 2:1:2 contraction-expansion it is possible to quantify the shear induced orientation and stretching of the polymer chains upstream. The results of these experiments will be presented in Section 6.4.2.

To investigate the flow downstream of the contraction-expansion, the direction of the stepper motor is reversed and the test fluid is drawn through the contraction-expansion into the flow cell. The retardation

along the centerline downstream of the axisymmetric contraction-expansion is shown in Figure 6-8 for the Deborah numbers presented in Figure 6-7. For small Deborah numbers, the effective fluid retardation is again found to be essentially zero. As the Deborah number is increased, a region of compression is observed to form roughly one contraction radius downstream of the re-expansion, $z/R_2 \approx 3$. Note that the throat is of length $L_c = 2R_2$ and thus the expansion plane is located at a position, $z/R_2 = 2$. This region of compression results from the biaxial expansion of the test fluid suddenly decelerating as it passes out of the throat [Townsend and Walters 1994]. This effect is similar to the die swell phenomenon observed at the exit of a narrow capillary. The extent of the biaxial expansion is limited by the presence of the downstream walls. The magnitude and position of this compression region appear to be independent of Deborah number. At still larger Deborah numbers, the extensional flow upstream of the contraction and the strong shear flow within the contraction couple to produce a region of residual molecular extension just downstream of the re-expansion plane. This region of extension begins with a effective retardation comparable in magnitude to the maximum extension observed upstream and decays very quickly entering the region of biaxial compression. In fact, we can estimate the effective retardation of the fluid exiting the throat from the effective retardation measurements upstream of the contraction. The resonance time of a fluid element traveling along the centerline to pass through the contraction is equal to

$$\Delta t_{resonance} = \frac{L_c}{2\langle v_z \rangle_2} \tag{6-12}$$

The conformation of the polymer coils and therefore the birefringence signal will decay on the fluid relaxation timescale. The birefringence signal at the expansion plane can thus be estimated as

$$\bar{\delta}\left(z = 2R_2\right) = \bar{\delta}\left(z = 0\right)e^{-\left(\Delta t/\bar{\lambda}\right)} = \bar{\delta}\left(z = 0\right)e^{-\left(\frac{L_c}{2R_2}\right)\left(\frac{1}{De}\right)}. \tag{6-13}$$

For the 4:1:4 contraction-expansion Equation 6-13 simplifies to

$$\bar{\delta}\left(z = 2R_2\right) = \bar{\delta}\left(z = 0\right)e^{-\left(\frac{1}{De}\right)}. \tag{6-14}$$

For the Deborah number $De = 4.0$ test Equation 6-14 predicts that the effective retardation should be 78% of the upstream retardation, $\bar{\delta}\left(z = 2R_2\right) = 0.78\,\bar{\delta}\left(z = 0\right)$. Although the experimental measurements suggest a value closer to 90%, this quick estimate does remarkably well considering that it neglects the deformation caused by the shear flow along the walls within the throat.

6.4.2 *2:1:2 Contraction-Expansion*

In Figure 6-10, the retardation measured along the centerline upstream and downstream of the 2:1:2 contraction-expansion is shown for a wide range of Deborah numbers. The throat is of length $L_c = 0.5R_2$ and the expansion plane is located at a position, $z/R_2 = 0.5$. The results of the axisymmetric flow induced birefringence measurements are qualitatively similar to the 4:1:4 contraction-expansion. At low Deborah numbers, very little polymer chain deformation is observed until the coil has reached the immediate vicinity of the contraction plane. As the Deborah number is increased, a region of strong extension appears upstream of the contraction, increasing in strength and extent as the vortex grows. The effect of shearing along the contraction plane, so prominent in the case of the 4:1:4 contraction-expansion, is almost nonexistent. The effective retardation is not considerably affected near the contraction plane. This may be a reflection on the

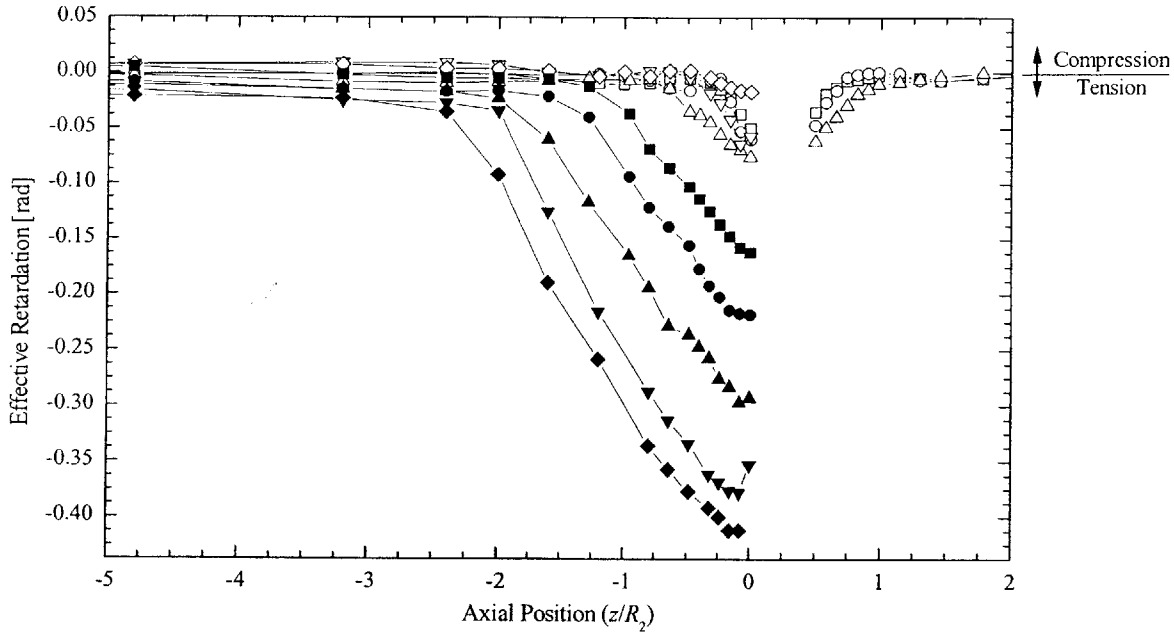

Figure 6-9 Equivalent retardation measurements of the 0.025wt% PS/PS Boger fluid along the centerline upstream and downstream of a 2:1:2 axisymmetric contraction-expansion. The data include: '◇', a Deborah number of $De = 0.25$; '□', $De = 0.5$; '▽', $De = 0.75$; '○', $De = 1.0$; '△', $De = 1.5$; '■', $De = 2.0$; '●', $De = 2.5$; '▲', $De = 3.0$; '▼', $De = 3.5$; and '◆', $De = 4.0$.

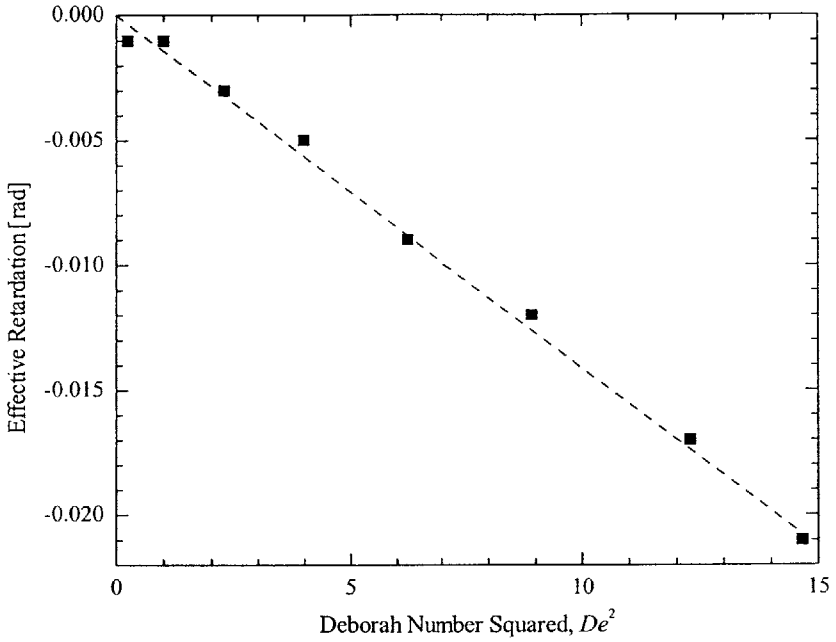

Figure 6-10 Equivalent retardation as a function Deborah number squared for the flow induced birefringence measurements of the 0.025wt% PS/PS Boger fluid far upstream of the contraction plane. Data include: '■', experimental data; and '- -', theoretical fit assuming a Poiseuille velocity profile and a Oldroyd-B fluid.

comparable strength of the recirculating vortices, but more likely, it is a byproduct of this spatial averaging birefringence technique. By reducing the contraction ratio from $\beta = 4$ to $\beta = 2$, the lateral extent of the region of compression has been reduced by a factor of two while the radial extent of the region of extension has been doubled. This simple geometrical argument suggests that the effect of shearing along the contraction plane will be reduced by a factor of about four while the maximum effective retardation should be roughly twice as large. This is indeed the case. Downstream of the re-expansion, the region of compression found in the 4:1:4 contraction-expansion is observed, but is found to be extremely weak. The change in pipe diameter is not large enough to result in any significant biaxial compression of the polymer coils.

Far upstream of the contraction plane, a weak extension in the polymer chains is observed and found to increase monotonically with Deborah number. In Figure 6-12, the value of the $\overline{\delta}$ measured far upstream ($z \leq -5R_2$) is plotted as a function of Deborah number squared. As predicted by Equation 6-11, the effective

retardation of the shear flow in a pipe is found to increase quadratically with Deborah number. It is possible to calculate the stress-optic coefficient of the test fluid from the slope. Using the average single mode Oldroyd-B relaxation time, $\bar{\lambda}$, defined in Section 3.2.5 to determine the Deborah number, the stress optic coefficient is calculated to be $C = -1.0\times10^{-9}$ Pa^{-1}. This value is quite a bit smaller then the range of values often quoted in the literature for polystyrene in an aromatic solvent, -6.0×10^{-9} Pa^{-1} $< C < -3.0\times10^{-9}$ Pa^{-1} [Rajagopalan *et al.* 1992; Wales and Janeschitz-Kriegel 1968]. Unfortunately, the value of the stress optic coefficient determined from this procedure is dependent on the choice of relaxation time. To calculate the average relaxation time we have used the first normal stress coefficient in the limit of zero shear rate, Ψ_{10}. For the Maxwell model, a more appropriate first normal stress coefficient may be the value at the knee observed in the steady shear rheological data and reproduced by the Bird-DeAguiar model in Section 3.2.5. After re-evaluating the relaxation time using this value of $\Psi_{plateau}$ we find $\lambda = 0.035$s. Refitting the data, the stress optic coefficient becomes $C = -4.1\times10^{-9}$ Pa^{-1}, a much more realistic value. To obtain a truly independent measure of the stress optic coefficient, an experimental technique independent of Deborah number must be employed. Li and Burghardt [Li and Burghardt 1995] demonstrated just such a technique for shear flow in a pipe by using birefringence measurements taken off of the centerline. Unfortunately, because the present test fluid is not index-matched to the refractive index of the optical glass, we were unable to unambiguously calculate the stress optic coefficient of the 0.025wt% PS/PS Boger fluid.

6.4.3 *Effect of Vortex Growth Mechanism on Flow Induced Birefringence Measurements*

The vortex growth mechanisms for a 2:1:2 and a 4:1:4 contraction-expansion are quite different. As described in detail in Chapter 4, in the case of the 2:1:2 contraction-expansion a 'lip' vortex is observed to form near the re-entrant corner, grow towards the salient corner and then move upstream with increasing Deborah number. This 'lip' vortex is not observed for a 4:1:4 or an 8:1:8 contraction-expansion. Instead, the Moffatt corner vortex is observed to grow out of the salient corner towards the re-entrant corner before expanding upstream at high Deborah numbers. By measuring the evolution in the flow induced birefringence upstream of several different contraction-expansions over a large range of Deborah numbers, we hope to find qualitatively different birefringence growth patterns from which we can garner further physical insight into the configuration of the polymer chains in these complex flows.

In Figure 6-11, a close up of the flow induced birefringence measurement upstream and downstream of the 2:1:2 contraction-expansion is presented for the data previously shown in Figure 6-9. The Deborah numbers are chosen to emphasize the flow transition which occurs upon the formation of the elastic 'lip'

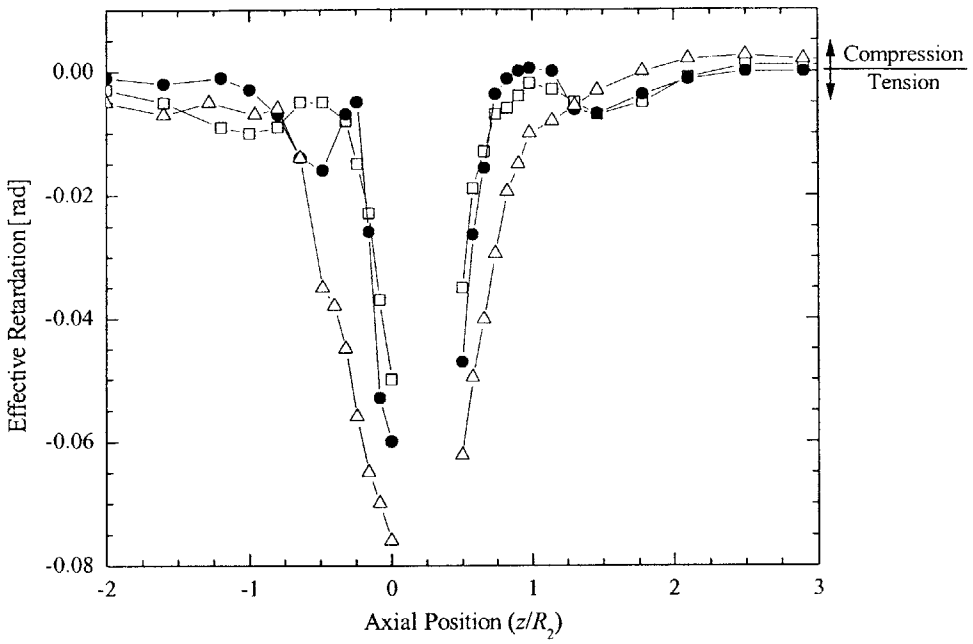

Figure 6-11 Equivalent retardation measurements of the 0.025wt% PS/PS Boger fluid along the centerline upstream and downstream of a 2:1:2 axisymmetric contraction-expansion for Deborah numbers near the onset condition of the elastic 'lip' vortex. The data include: '□', a Deborah number of $De = 0.5$; '●', $De = 1.0$; and '△', $De = 1.5$.

vortex. At a Deborah number of $De = 0.5$, the fluid traveling from far upstream experiences a modest extension beginning at a position of $z/R_2 \approx -1.5$. The elastic 'lip' vortex has yet to develop at the re-entrant corner, instead a Newtonian Moffatt vortex is present in the salient corner. The Moffatt vortex extends upstream a distance of $z/R_2 = -0.68$. Birefringence measurements taken just below the upper extent of the Moffatt vortex demonstrate a small positive shift in the effective retardation measurement corresponding to the contribution of the weakly sheared polymer coils recirculating within the Newtonian vortex. The influence of the contraction is felt just upstream of the contraction plane where the fluid is quickly stretched over the final $z/R_2 \approx -0.25$. The flow is quasi-Newtonian and fore-aft symmetric at these low Deborah numbers and Reynolds numbers. The upstream flow induced birefringence pattern is mirrored almost perfectly downstream of the re-expansion. Streak images and velocity measurements demonstrate the existence of the elastic 'lip' vortex at a Deborah number of $De = 1.0$. The influence of the lip vortex on the effective retardation measurement is quite pronounced. The polymer coil begins to feel the effect of the contraction a distance $z/R_2 \approx -1.0$ upstream. Halfway to the contraction plane, the polymer coils have

accumulated an effective retardation of $\bar{\delta} \approx -0.015$ rad. At this Deborah number, the 'lip' vortex extends a distance $z/R_2 = -0.3$ upstream of the contraction plane. The axial compression of the polymer coils recirculating within the 'lip' vortex is nearly large enough to negate the effective retardation signal. This result cannot be explained away through geometric arguments. The distance that the laser traverses through the regions of compression upstream of the contraction wall is equal to the distance the laser travels across the extensional flow upstream throat. The influence of these two effects should therefore be weighted equally in the effective retardation measurement. This implies that a polymer coil flowing over the lip vortex is compressed in the axial direction (or extended in the radial direction) as strongly as a polymer coil accelerating into the throat. As the polymer chain passes over the elastic 'lip' vortex, it rotates 90° as it is drawn and strongly extended into the throat. Downstream of the re-expansion, the flow induced birefringence measurements are similar to the results for a Deborah number of $De = 0.5$. The effect of the upstream lip vortex is not felt downstream of the re-expansion. By a Deborah number of $De = 1.5$, the elastic 'lip' vortex has reached the outer corner of the contraction geometry and begun to grow upstream in the form of an elastic corner vortex. A polymer coil traveling from far upstream of the contraction plane is slightly extended by the upstream shear flow. If one looks very closely, the influence of a very weak compression can be inferred just below the top of the corner vortex, $z/R_2 = -0.8$, but the dramatic effect of the 'lip' vortex is not reproduced by the corner vortex. The polymer chains are extended over the entire height of the corner vortex as the fluid is accelerated into the contraction. Downstream of the re-expansion, the polymer extension is carried much further downstream. A region of modest compression is observed at a position $z/R_2 \approx -2.0$ downstream.

Unlike the 2:1:2 contraction-expansion, the 4:1:4 contraction-expansion in Figures 6-8 and 6-9 does not reveal any new or interesting behavior even upon closer inspection. At a Deborah number, $De = 0.5$, the effective retardation is nearly zero both upstream and downstream of the contraction-expansion. The effective retardation measurements above a Deborah number of $De > 0.5$ demonstrate the formation of a strong extensional flow that increases monotonically in strength and upstream extent as the Deborah number is increased. The growth of this region of polymer coil extension is similar to the development of the birefringence signal for the 2:1:2 contraction-expansion after the 'lip' vortex has disappeared and the corner vortex has dominated the flow.

From the plot of effective retardation for the 2:1:2 contraction-expansion, it is possible to make an approximate lower bound estimate of the deformation of the polymer coils flowing around the elastic 'lip' vortex. Assuming that all of the polymer chains in the compressive region upstream of the contraction plane

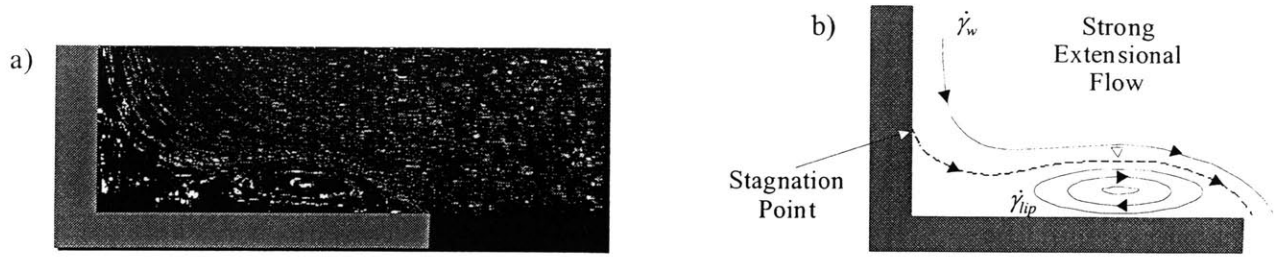

Figure 6-12 Streak image (a) and schematic diagram (b) of elastic 'lip' vortex upstream of a 2:1:2 contraction-expansion at a Deborah number of $De = 0.9$.

are extended equally, the anisotropic conformation and the retardation are related by

$$\Delta A = \frac{\delta\lambda_{light}}{4\pi R_2 Cnk_B T} = -4.2\times10^3\,\overline{\delta}. \tag{6-15}$$

Thus, a retardation of $\overline{\delta} = -0.015$ radians corresponds to an anisotropic conformation of $\Delta A \approx 65$ or about 0.75% of the maximum extension of the polymer coil. Although, the polymer coils are not greatly extended, they can still exert a considerable amount of elastic stress, $\Delta A \rightarrow \Delta\tau$.

The total accumulated Hencky strain and hence the tensile stress of a fluid element moving along the centerline increases with the contraction ratio, however, at a fixed Deborah number the deformation due to shearing along both the contraction plane and the upstream walls will decrease with contraction ratio. Unfortunately, it is not possible to unambiguously identify the origin of the molecular deformation close to the elastic lip vortex from the nonhomogeneous AFIB measurements presented in this thesis. However, several possibilities exist. In Figure 6-12, a streak image and a schematic diagram of the elastic 'lip' vortex upstream of a 2:1:2 axisymmetric contraction-expansion for a Deborah number of $De = 0.9$ are presented to help the reader visualize the possible sources of the axial compression observed in the AFIB measurements. The polymer coils flowing over the 'lip' vortex may be deformed by the shear flow near the upstream walls of the contraction plane. These polymer coils may then rotate with the streamlines entering the corner and pass over the lip vortex resulting in an extension in the radial direction. However, even if we assume that the only the most highly deformed polymer chains from the upstream wall pass over the lip vortex the most generous estimates of the polymer deformation lead to an effective retardation of only

approximately $\overline{\delta} \approx 0.002$ radians. Another alternative is that the polymer coils are deformed by the shear flow along the contraction plane. This effective retardation associated with this shear flow is more difficult to estimate. However, to achieve a change in the effective retardation of $\overline{\delta} = 0.015$ radians, the shear rate along the contraction plane would have to be stronger than in the contraction itself. This is highly unlikely. If this was the primary cause of the axial compression, one would also expect to observe a more obvious impact on the flow induced birefringence measurements directly above the contraction plane. The most probable source of the axial compression of the polymer coils observed near the elastic 'lip' vortex is the strong extensional flow upstream of the contraction. In the absence of a large elastic corner vortex, the contraction can be thought of as a sink, drawing fluid from all points upstream and accelerating it into the throat. As seen in Figure 6-12, the presence of an elastic 'lip' vortex results in a stagnation point just upstream of the salient corner and a separating streamline dividing the upstream converging flow from the recirculating vortex. The fluid located along this separating streamline is elongated radially inward as it is accelerated towards and then around the re-entrant corner. It is certainly plausible that the extend of this deformation is comparable to the amount of extension measured along the centerline. This hypothesis is supported by spatially resolved flow induced birefringence measurements taken upstream of a abrupt 4:1 planar contraction [Quinzani *et al.* 1994].

6.4.4 *The Normal Stress Ratio*

In Chapter 4,we argued that the flow kinematics associated with the transition from an elastic 'lip' to an elastic corner vortex are driven by the change in the dynamics from a shear dominated to an extension-dominated flow. This flow transition was quantified by the normal stress ratio

$$\aleph = \frac{N_1/\eta_0\dot{\gamma}}{(\tau_{zz}-\tau_{rr})/\eta_0\dot{\varepsilon}} = \frac{S_R(\dot{\gamma})}{T_R(\varepsilon)}, \tag{6-16}$$

which compares the normal stresses generated by the shear flow along the upstream walls to the extensional stresses resulting from the elongational flow along the centerline. The normal stress ratio was evaluated for several different Boger fluids using values of the stress ratio and the Trouton ratio obtained from steady shear and homogeneous transient uniaxial extension measurements. The Poiseuille flow far upstream of the contraction plane is indeed a steady shear flow, however, the flow along the centerline is not a homogeneous extensional flow. The strain rate imposed upon a fluid element traveling along the centerline increases

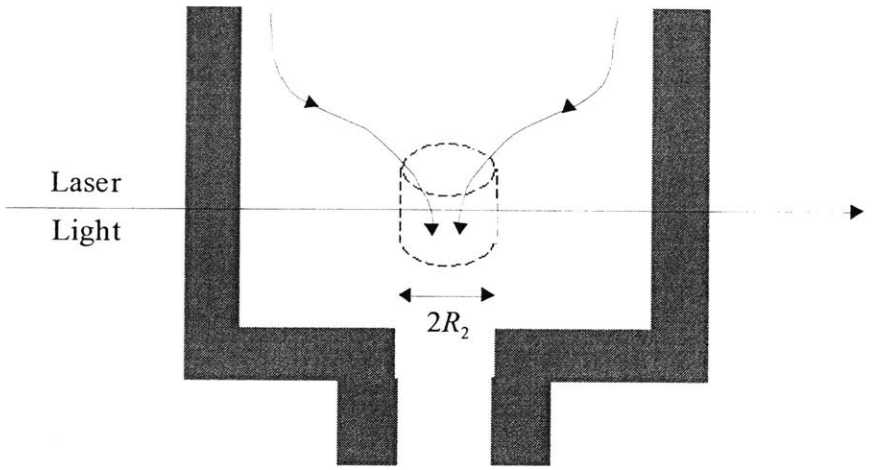

Figure 6-13 Schematic diagram of flow into an axisymmetric contraction-expansion illustrating the plug flow assumption used to calculate the normal stress ratio from AFIB measurments.

monotonically as it flows towards the contraction. A better method for evaluating the normal stress ratio may be to use the flow induced birefringence measurements obtained in this chapter to calculate an average measure of the elastic stress exerted by a polymer coil *in situ* for both the 2:1:2 and 4:1:4 contraction expansion. The normal stress ratio becomes

$$\aleph = \frac{N_{1,wall}}{(\tau_{zz} - \tau_{rr})_{max}}, \tag{6-17}$$

where $N_{1,wall}$ is the first normal stress difference at the wall measured far upstream of the contraction plane and $(\tau_{zz} - \tau_{rr})_{max}$ is the maximum tensile stress achieved within the flow. To calculate these stresses from the effective retardation measurements presented in Figures 6-7 and 6-9, certain assumptions must be made. First, the stress optic law is assumed to be valid, $\Delta n' / C = \Delta \tau$. This is a dangerous assumption especially for the extensional flow along the centerline where strong deformations can result in the failure of the stress optic law at moderate stresses [Doyle *et al.* 1998]. If the stress optic law is determined to be invalid, then without a loss in applicability, the normal stress ratio can be rederived as a polymer chain deformation ratio comparing the change in the anisotropic conformation resulting from the shear flow along the upstream walls to the conformation change induced by the elongational flow along the centerline. To make the analysis simpler, the viscosity and relaxation time of the fluid are assumed to be constant across the diameter of the

pipe. The first normal stress difference generated by the Poiseuille flow far upstream can be calculated from Equation 6-10

$$\bar{\delta} = \left(\frac{4\pi CR_1}{3\lambda}\right) 2\tau_w \frac{De}{\beta^3} . \tag{6-18}$$

Recalling from Equation 6-9 that

$$N_{1,wall} = N_1\left(r = R_1\right) = 2\tau_w \frac{De}{\beta^3}, \tag{6-19}$$

the first normal stress difference at the wall far upstream is found to be

$$N_{1,wall} = \frac{3\lambda_{light}}{4\pi CR_1} \bar{\delta}_{upstream} . \tag{6-20}$$

Near the contraction plane, the contribution to the effective retardation signal is assumed to be localized to a region of radius R_2 directly upstream of the throat. This assumption is illustrated by Figure 6-13. The average stress in this region can be calculated directly from the effective retardation measurements and Equation 6-1

$$\bar{\delta}_{contraction} = \frac{4\pi CR_2}{\lambda_{light}} \left(\tau_{zz} - \tau_{rr}\right)_{centerline} . \tag{6-21}$$

The normal stress ratio thus becomes

$$\aleph = \frac{N_{1,wall}}{\left(\tau_{zz} - \tau_{rr}\right)_{centerline}} = \frac{\frac{3\lambda}{4\pi CR_1} \bar{\delta}_{upstream}}{\frac{\lambda}{4\pi CR_2} \bar{\delta}_{contraction}} = \frac{3}{\beta} \frac{\bar{\delta}_{upstream}}{\bar{\delta}_{contraction}} \tag{6-22}$$

In Figure 6-14, the normal stress ratio evaluated from flow induced birefringence measurements upstream of a 2:1:2 and a 4:1:4 contraction-expansion is plotted as a function of Deborah number. The normal stress ratios for both contraction-expansions demonstrate the same qualitative trends. The normal stress ratio grows from zero at low Deborah numbers, increases quickly with the initial formation of the

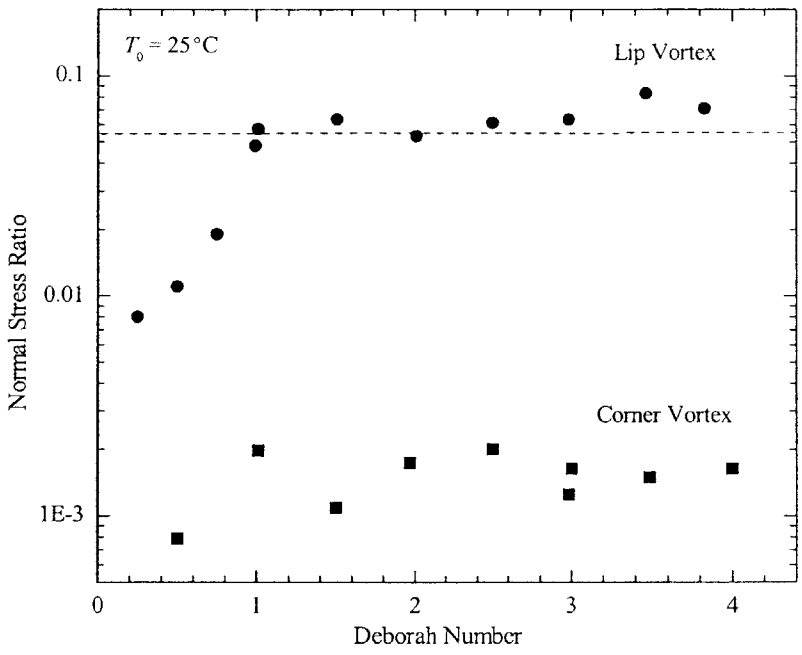

Figure 6-14 Normal stress ratio evaluated using the flow induced birefringence measurements of the 0.025wt% PS/PS Boger fluid upstream of the 2:1:2, '●', and 4:1:4, '■', contraction-expansions.

elastic vortex structure and plateaus as the vortex grows further upstream. The difference in the magnitude of the normal stress ratio for these two contraction ratios is considerable. At the onset of elastic vortex growth, the normal stress calculated from the birefringence measurements upstream of the 2:1:2 contraction-expansion remains roughly constant at a value of $\aleph_{2:1:2} \approx 0.06$ while the value of the normal stress ratio for the 4:1:4 contraction-expansion is over an order of magnitude smaller, $\aleph_{4:1:4} \approx 0.002$. Recalling that in Chapter 4 an elastic 'lip' vortex was observed for all fluids, independent of geometry, when the normal stress ratio was greater than these results are consistent with our previous findings.

To extend and complete this research, axisymmetric flow induced birefringence measurements are required for both the PIB/PB and the PAA/CS Boger fluids used in the contraction flow literature [Boger and Binnington 1994; McKinley *et al.* 1991; Nguyen and Boger 1979]. Such experiments could yield additional support that the concept of a normal stress ratio developed in this thesis is the proper dimensionless group

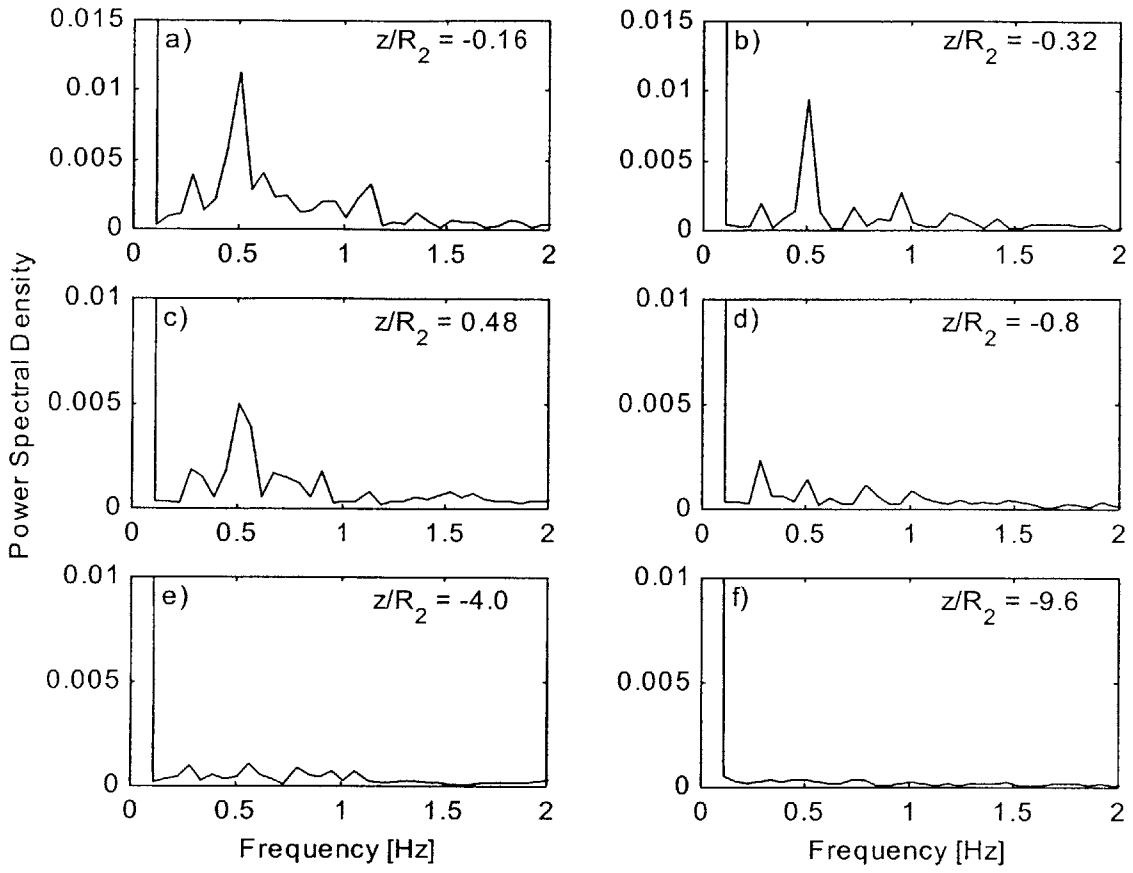

Figure 6-15 Power spectral density of flow induced birefringence measurements of the 0.025wt% PS/PS Boger fluid upstream of a 4:1:4 contraction-expansion at a Deborah number of $De = 4.0$. The data include experimental measurement at positions : a) $z/R_2 = -0.16$; b) $z/R_2 = -0.32$; c) $z/R_2 = -0.48$; d) $z/R_2 = -0.8$; e) $z/R_2 = -4.0$; and f) $z/R_2 = -9.6$ upstream.

to characterize *a priori* the vortex growth mechanisms upstream of a sudden contraction.

6.4.5 *Characterization of Elastic Instability*

Flow induced birefringence measurements have been used in the past to observe flow instabilities. Wheeler *et al.* [Wheeler *et al.* 1998] used flow induced birefringence to detect the loss of stability of steady shear flows of an wormlike micelle solution of CPyCl and NaSal. They observed a shear induced ring structure that oscillated both spatially and temporally. The flow induced birefringence measurements proved to be a valuable, sensitive tool for characterizing the onset of elastic flow instabilities.

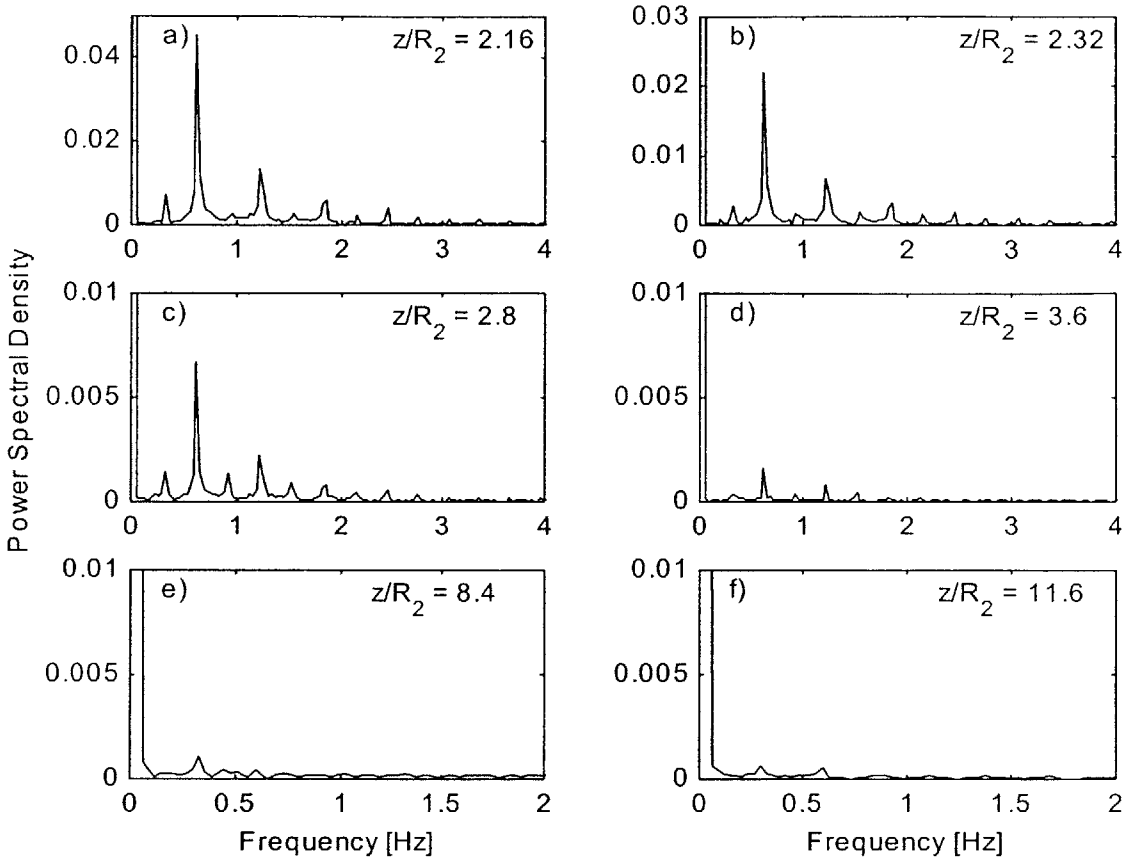

Figure 6-16 Power spectral density of flow induced birefringence measurements of the 0.025wt% PS/PS Boger fluid downstream of a 4:1:4 contraction-expansion at a Deborah number of $De = 4.0$. The data include experimental measurement at positions : a) $z/R_2 = 2.16$; b) $z/R_2 = 2.32$; c) $z/R_2 = 2.8$; d) $z/R_2 = 3.6$; e) $z/R_2 = 8.4$; and f) $z/R_2 = 11.6$ downstream.

In Figure 6-16 the power spectral density of the flow induced birefringence signal is plotted as a function of frequency for several locations upstream of the 4:1:4 contraction-expansion at a Deborah number of $De = 4.0$. The fundamental frequency of the elastic instability is observed to be $f_1 = 0.23$ Hz. This fundamental frequency is in agreement with the observations made in Chapter 3 using laser Doppler velocimetry and pressure drop measurements. A strong peak is observed at the first harmonic, $2f_1 = 0.46$Hz, for measurements taken close to the contraction plane. Moving further upstream, the intensity of the higher harmonics decays and the fundamental frequency becomes dominant. At a position just above the top of the elastic corner vortex, Figure 6-16e, the instability is still apparent, but the intensity of the small amplitude oscillations in the flow induced birefringence signal has decayed greatly. Much further upstream, Figure 6-16e, the instability has disappeared completely.

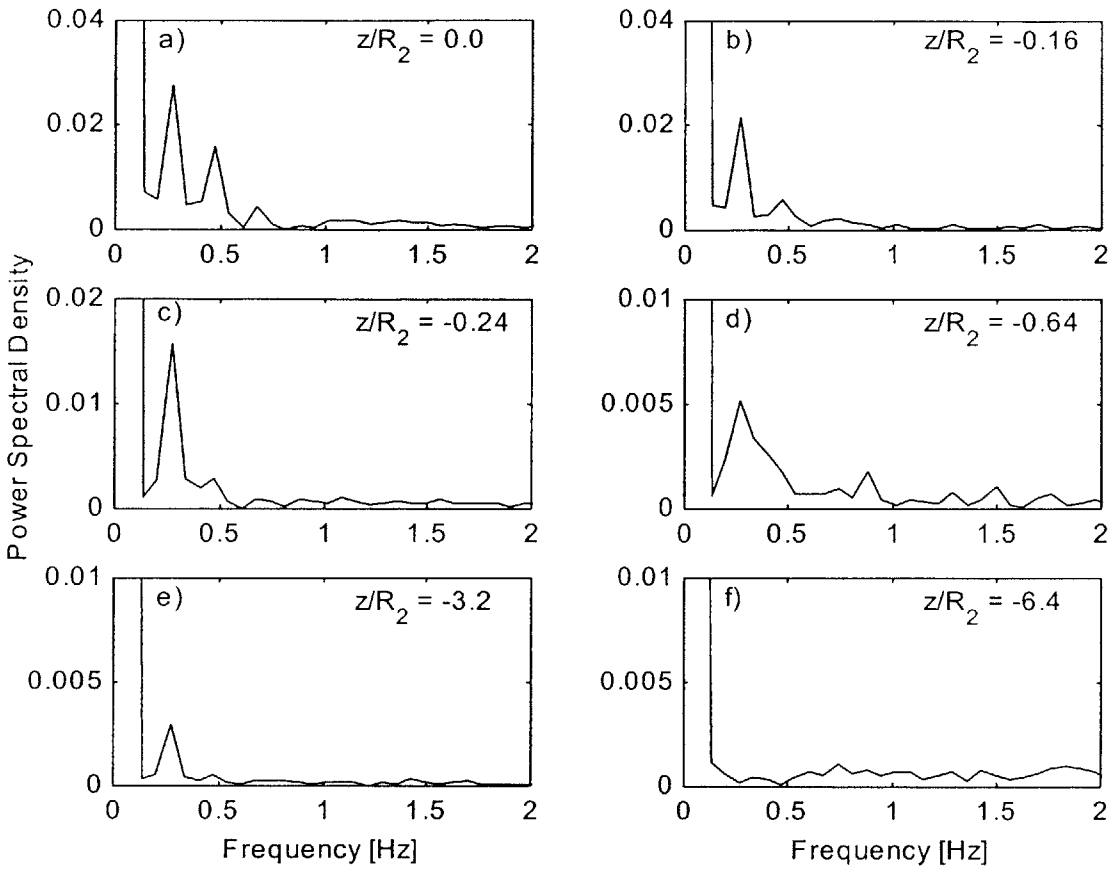

Figure 6-17 Power spectral density of flow induced birefringence measurements of the 0.025wt% PS/PS Boger fluid upstream of a 2:1:2 contraction-expansion at a Deborah number of $De = 4.0$. The data include experimental measurement at positions : a) $z/R_2 = 0.0$; b) $z/R_2 = -0.16$; c) $z/R_2 = -0.24$; d) $z/R_2 = -0.64$; e) $z/R_2 = -3.2$; and f) $z/R_2 = -6.4$ upstream.

The power spectral density of the flow induced birefringence downstream of the 4:1:4 contraction-expansion is shown in Figure 6-18. For the same Deborah number, $De = 4.0$, the intensity of the observed instability downstream of the re-expansion is greater than it is upstream of the contraction by almost one order of magnitude. The strength and number of higher harmonics has also increased. The signature of this power spectral density distribution is similar to the nonlinear jetting instability reported in Chapter 3. The instability is observed far downstream of the re-expansion. At positions up to $z/R_2 = 11.6$ downstream, Figure 6-18f, the influence of the upstream instability remains clearly present, although its intensity has significantly decayed. This is in contrast to the flow upstream of the contraction, where the instability is observed to be confined to the region within the elastic corner vortex.

Streak images, laser Doppler velocimetry measurements and pressure drop measurements were all

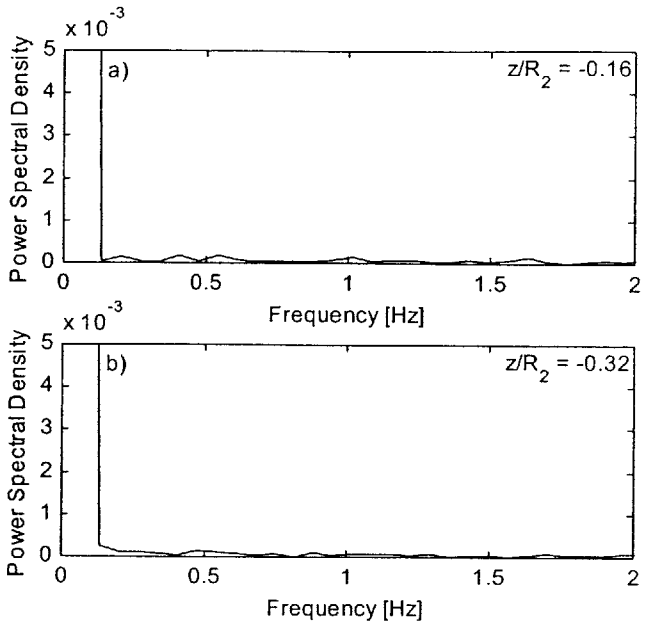

Figure 6-18 PSD of flow induced birefringence measurements of the 0.025wt% PS/PS Boger fluid upstream of a 2:1:2 contraction-expansion at a Deborah number of De = 1.0. The data include experimental measurement at positions : a) z/R_2 = -0.16 and b) z/R_2 = -0.32.

used in previous chapters to investigate the stability of the 2:1:2 contraction-expansion. None of these measurement techniques proved sensitive enough to observe an elastic instability at the Deborah numbers tested. In Figure 6-19, the power spectral density is plotted as a function of frequency for the flow induced birefringence measurements taken at several positions upstream of a 2:1:2 contraction-expansion at a Deborah number of De = 4.0. These flow induced birefringence measurements clearly demonstrate the presence of an elastic flow instability with a fundamental frequency f_1 = 0.27 Hz. The critical Deborah number for the onset of this supercritical Hopf bifurcation is found to be De_c = 2.3±0.3. In terms of vortex growth, this Deborah number corresponds to strong elastic corner vortex which extends to a position z/R_2 = -1.5 upstream of the contraction plane. The elastic 'lip' vortex is once again found to be completely stable. To emphasize this point, two power spectral density plots for the flow upstream of a 2:1:2 contraction-expansion at a Deborah number of De = 1.0 are plotted in Figure 6-19. At this Deborah number, the lip vortex has been observed using both streak images and DPIV. The two upstream positions for which AFIB measurements are presented in Figure 6-19 correspond to locations within the elastic 'lip' vortex. At these points and all other locations upstream and downstream investigated, the flow is found to be stable.

Flow induced birefringence measurements are only possible downstream of the re-expansion for Deborah numbers less than or equal to $De \leq 2.0$, all of which were found to be stable. Flow induced

birefringence measurements have thus proven to be a very sensitive measurement technique for investigating flow stability of polymeric fluids.

CHAPTER 7 Non-homogeneous Transient Uniaxial Extensional Rheometry

7.1 Introduction

A great deal of recent research has focused on understanding the extensional behavior of polymeric fluids [McKinley and Sridhar 2002]. The dynamical response of polymeric fluids in extension, especially mobile dilute polymer solutions, is quite different than in simple shear. For this reason, extensional rheology is a topic of great interest and importance to the polymer community. It is widely recognized that to generate physically consistent constitutive models capable of predicting the behavior of these elastic liquids in complex flows such as the flow into an axisymmetric contraction-expansion, it is absolutely essential to first understand the behavior of these elastic fluids in homogenous uniaxial extension [Ghosh *et al.* 2001].

Numerous devices including the four roll mill, the spin-line rheometer, the opposed jet device and the capillary rheometer have been used in the past to investigate the extensional behavior of polymeric solutions. Unfortunately, each device is plagued by an unknown prestrain history and some degree of shearing in the flow field. The filament stretching rheometer has emerged as an accurate device for reproducibly measuring the response of a fluid to an imposed homogeneous uniaxial extensional flow field [Anna *et al.* 2001].

In this chapter the concepts of extensional rheology and the filament stretching rheometer (FiSER) are introduced. The technique of flow induced birefringence measurements in extensional flows is presented and discussed. The results of homogenous uniaxial elongation are first presented to validate the experimental setup and measurement techniques. The results of nonhomogeneous uniaxial elongation in which the elongational strain rates experienced by a fluid element entering a 4:1:4 axisymmetric contraction-expansion is reproduced by the filament stretching rheometer are then presented. Simultaneous measurements of stress and conformation demonstrate the presence of a stress-conformation hysteresis as seen in homogeneous uniaxial elongational experiments. The magnitude of the additional energy dissipation is quantified for the strain rate profiles observed in the 4:1:4 axisymmetric contraction at various Deborah numbers. The dissipation is found to monotonically increase with Deborah number.

7.2 The Filament Stretching Rheometer (FiSER)

The filament stretching rheometer was originally introduced by Matta and Tytus [Matta and Tytus 1990] as a "falling plate device." By placing a small amount of fluid between two cylindrical plates and allowing the bottom cylinder to fall under gravity they were able to impose a nearly pure extensional flow

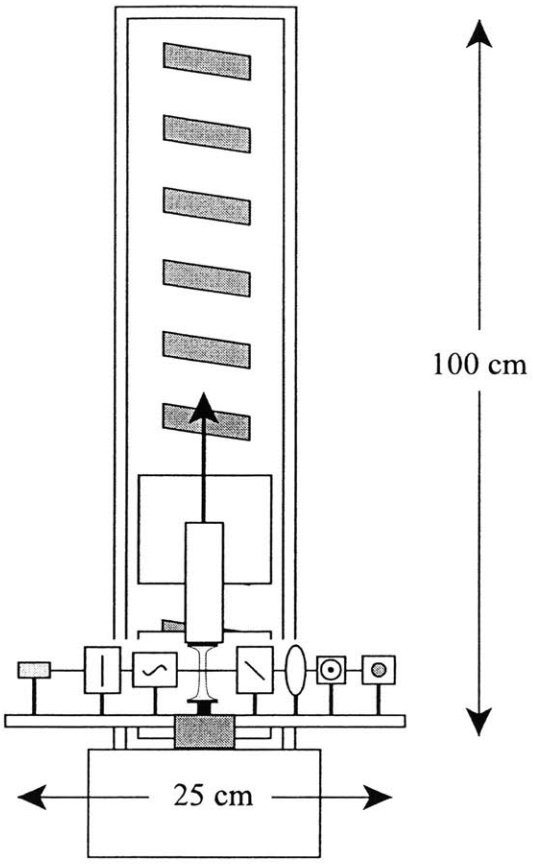

Figure 7-1 Schematic diagram of the filament stretching device (FiSER III).

field. Sridhar and coworkers [Sridhar and Gupta 1991; Sridhar *et al.* 1991; Tirtaatmadja and Sridhar 1993] extended the work of Matta and Tytus by creating a filament stretching device that, by controlling the velocity of the bottom plate, could impose a nearly homogeneous uniaxial extension on the fluid filament while simultaneously measuring the force on the top endplate. This allowed Sridhar and coworkers to measure the evolution in the transient extensional viscosity of the fluid filament from equilibrium to steady state extension. Many other research groups around the world have since developed filament stretching rheometers of various designs and operating spaces [Anna *et al.* 2001]. A recent paper by Anna et al. [2001] reported the results of an interlaboratory comparison of filament stretching rheometers in which several different instruments were used to study three dilute polystyrene-based elastic fluids. The results validated the technique by demonstrating that even though extensional rheology has proven to be difficult measurement to make, quantitative agreement can be achieved by instruments of different design.

The filament stretching device used to make all the measurements presented in this chapter, FiSER

III, is shown in Figure 7-1. FiSER III was originally designed and built by Spiegelberg and Tripathi to measurement the extensional rheology of polymer melts and is the third generation of filament stretching rheometers in Professor McKinley's lab, following very closely the successful design of Anna [2000]. In this device, an initially cylindrical filament of fluid is stretched between two circular endplates. The linear stage consists of two brushless linear DC motors which are used to impose a known velocity profile on the two platens to which the top endplate and the measurement equipment is mounted. The upper motor controls the velocity profile of the top endplate while the lower motor, traveling at half the velocity of the upper motor, ensures that an array of measurement devices is kept at the midpoint of the stretching fluid filament. The motion control system is manufactured entirely by Compumotor (model 6250). The system has a resolution of 200μm in its vertical positioning, a maximum travel of 100cm, a maximum velocity of 100cm/s and a maximum acceleration of 6000cm/s^2. The imposed velocity profiles and the data acquisition are controlled entirely through Labview. A load cell (Futek Model L2338) is mechanically isolated from the linear stage and mounted to the lower endplate. The force transducer has a maximum measurable load of

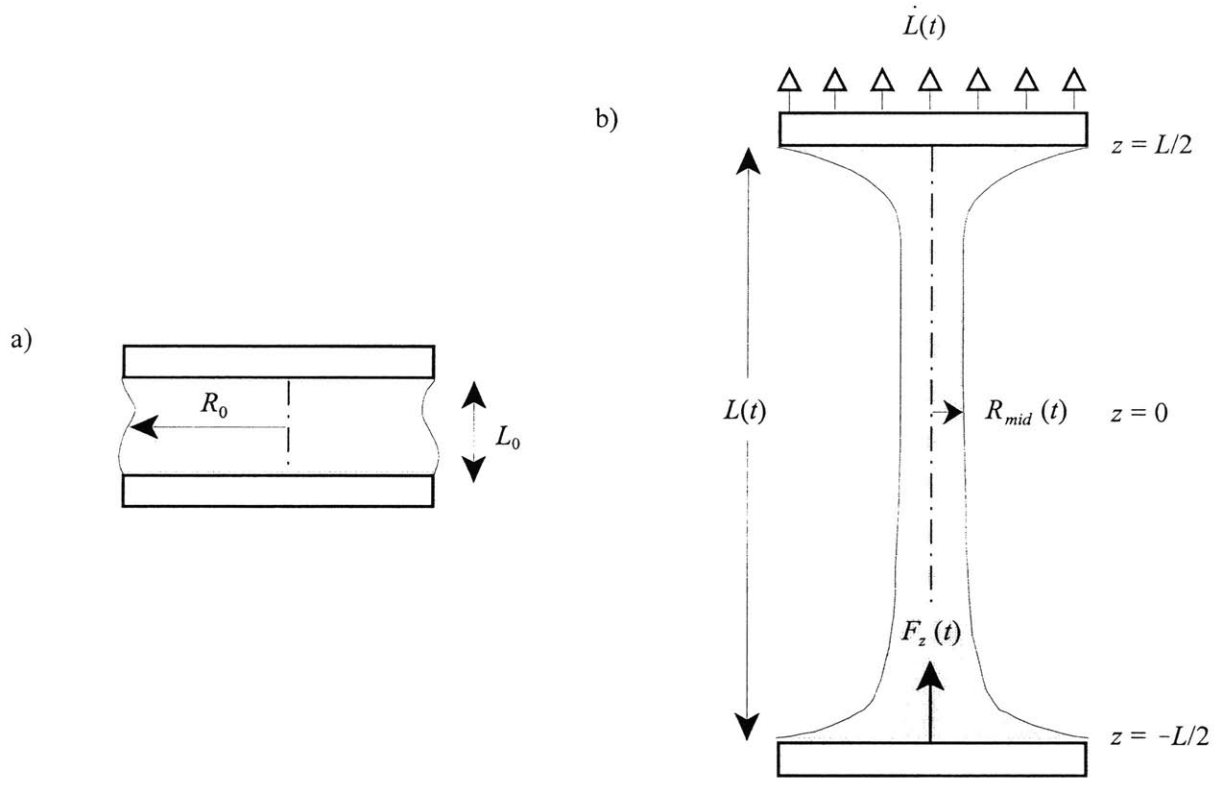

Figure 7-2 Sketch of a fluid filament being stretched by a filament stretching rheometer. The initial conditions are shown in (a), while a filament in mid stretch is shown in (b).

10g with a resolution of ±5mg. The dynamic response time of this load cell was reported to be approximately 78ms by Anna et al. [2001]. The midpoint diameter is measured with a laser micrometer (Omron Z4LA) mounted on the lower platen. The resolution of the laser micrometer is ±20μm. A flow induced birefringence (FIB) measurement optical train is also mounted to the lower platen. The FIB system is discussed in more detail in section 7.3. Accurate knowledge of the fluid temperature is required to ensure accurate knowledge of the rheological properties of the fluids. Before each experiment, a thermocouple is placed within the fluid sample and the experimental temperature of the fluid is recorded. Due to the short duration of these experiments, the temperature is assumed to remain constant throughout the course of the experiment even though the ambient temperature can vary by several degrees over the course of an hour.

In Figure 7-2, a sketch of a typical fluid filament within the filament stretching rheometer is shown. In this figure, $L(t)$ is the time evolving length of the filament, $R_{mid}(t)$ is the midpoint radius of the filament, $F_z(t)$ is the force exerted by the filament on the endplate, $\dot{L}(t)$ is the velocity of the endplate, and L_0 and R_0 are the initial length and radius of the fluid filament. The goal of extensional rheometry is to impose a motion with a constant stretch history. In other words, an initially cylindrical filament must remain cylindrical, thinning uniformly in the radial direction as it is elongated axially. As indicated schematically in Figure 7-2, the imposed flow field is not quite uniform. The initial fluid loading is not a perfect cylinder, Figure 7-2a, because the fluid sags under gravity. Gravity affects not only the initial filament shape, but may also affect the filament shape over the course of the entire stretch, causing an asymmetry in the fluid filament by draining some of the fluid from the top endplate. The result is a low extension rate limit below which the effect of gravity cannot be neglected [Anna *et al.* 2001]. The no-slip condition at the endplates results in a second nonuniformity. As shown in Figure 7-2b, as the filament is stretched, a thin film of fluid remains attached to the rigid endplates. The resulting filament shape deviates from the desired ideal cylinder, more closely resembling a classic wineglass shape. At short times and small initial aspect ratios, L_0/R_0, the no-slip condition at the endplate surface results in a shear dominated flow and eventually can lead to elastic endplate instabilities at large strain rates [Spiegelberg and McKinley 1996]. The operating space for a generic filament stretching rheometer is described in detail by Anna *et al.* [2001].

In an ideal homogeneous uniaxial extensional flow the ends of the cylinder separate exponentially in time [Bird *et al.* 1987],

$$L(t) = L_0 \, e^{\dot{E}t}, \tag{7-1}$$

where $\dot{E}$ is the imposed, constant stretch rate. However, as described above, the non-slip condition at the

endplates does no allow the fluid filament to assume the shape of an ideal cylinder. The small volume of fluid that remains at the endplates does not deform appreciably and the central fluid filament sees a time-dependent effective stretch rate based on the fluid radius, $\dot{\varepsilon}_{eff}(t)$, that is larger than the stretch rate imposed on the endplates,

$$\dot{\varepsilon}_{eff}(t) = -\frac{2}{R_{mid}(t)}\frac{dR_{mid}(t)}{dt}. \tag{7-2}$$

In fact, a lubrication approximation can be used to demonstrate that the effective deformation rate is precisely equal to $\dot{\varepsilon}_{eff} = 3/2\dot{E}$ at small strains [Anna *et al.* 1999].

The total deformation of the system can be described in terms of a Hencky strain. For the case of the ideal filament, the Hencky strain can be expressed as

$$\varepsilon_L = \ln\left(\frac{L(t)}{L_0}\right) = \dot{E}t. \tag{7-3}$$

However, for the nonideal filament, the total Hencky strain becomes an integral of the effective strain rate over all time,

$$\varepsilon_{eff} = \varepsilon_D = \int_0^t \dot{\varepsilon}_{eff}(t')\,dt' = -2\ln(R_{mid}/R_0). \tag{7-4}$$

If a constant stretch rate is applied to the endplates, this test is classified as a Type II experiment [Kolte *et al.* 1997]. If the test is designed in such a way that the effective strain rate is constant $\dot{\varepsilon}_{eff} = \dot{\varepsilon}_0$, than the test is classified as a Type III experiment. To accurately determine the desired material properties of the elastic fluid, Type III experiments must be performed. An effective technique for generating Type III tests from Type II master curves will be discussed in detail in Section 1.4.3.

The strength of the extensional flow is characterized by the Deborah number which is the ratio of the longest characteristic relaxation time of the fluid, λ_Z, to the characteristic timescale of the kinematics, $\dot{\varepsilon}_0^{-1}$,

$$De = \lambda_Z \dot{\varepsilon}_0. \tag{7-5}$$

Filament stretching rheometers have historically been used to measure the transient extensional viscosity of polymeric fluids in homogenous uniaxial extension

$$\bar{\eta}^{+} = \frac{\langle \tau_{zz} - \tau_{rr} \rangle}{\dot{\varepsilon}_0}, \tag{7-6}$$

where $\langle \tau_{zz} - \tau_{rr} \rangle$ is the principal elastic tensile stress difference generated within the filament. In a detailed force balance of the filament stretching rheometer, Szabo [Szabo 1997] showed that the principal elastic tensile stress difference generated within the filament could be calculated from the total force measured by the load cell, F_z, if the weight of the fluid, the surface tension and the inertia of the fluid are taken into account

$$\langle \tau_{zz} - \tau_{rr} \rangle = \frac{F_z}{\pi R_{mid}^2} + \frac{1}{2}\frac{\rho g\left(\pi L_0 R_0^2\right)}{\pi R_{mid}^2} - \frac{\sigma}{R_{mid}} + \frac{1}{2}\frac{\rho\left(\pi L_0 R_0^2\right)\ddot{L}_z}{\pi R_{mid}^2}, \tag{7-7}$$

where σ is the surface tension of the fluid, ρ is the density of the fluid and $\ddot{L}_z$ is the acceleration of the endplate. The last term of equation 7-7 is due to the fluid inertia and is, in practice, negligibly small. In homogenous uniaxial extension a dimensionless extensional viscosity, the Trouton ratio, is often formed

$$Tr = \frac{\langle \tau_{zz} - \tau_{rr} \rangle}{\eta_0 \dot{\varepsilon}_0} = \frac{\bar{\eta}^{+}}{\eta_0}. \tag{7-8}$$

However, if the extension rate is not constant, then the Trouton ratio may not be the best dimensionless form of the primary tensile stress. If we look at the form of the polymeric stress for the ith mode of a Hookean dumbbell model,

$$\boldsymbol{\tau}_i = -n\,\mathrm{k_B}\,T\left(\boldsymbol{A}_i - \mathbf{I}\right), \tag{7-9}$$

then a self consistent choice to nondimensionalize the stress is the elastic modulus, $n\mathrm{k_B}T$, where n is the number density of polymer chains in the solution and $\mathrm{k_B}$ is the Boltzmann constant. This choice will become even more intuitive when flow induced birefringence measurements are discussed in Section 7-3.

The elastic modulus can be derived directly from physical arguments for a Hookean dumbbell model like the Rouse-Zimm model. For the 0.025wt% polystyrene solution, the elastic modulus becomes, $n\mathrm{k_B}T$ = 0.28 Pa. However, to compare our experimental measurements to theory, we will use a single relaxation time

constitutive model such as the Oldroyd-B or FENE-P model. As described in Section 3.2.7, to convert from a multimode model to a singlemode model one must first determine the appropriate relaxation time to use. The simplest choice for the fluid relaxation time scale is the longest relaxation time, λ_z, however using the Zimm timescale does not accurately describe the entire relaxation spectrum for a single mode model. Alternatively, a viscosity weighted average or of the relaxation spectrum can be used

$$\bar{\lambda} = \frac{\Psi_{10}}{2\eta_{p,0}} \tag{7-10}$$

This average relaxation time is known as the Oldroyd relaxation time of the fluid. For the Rouse-Zimm spectrum in which the time constant and viscosity of each relaxation mode is related to the longest or Zimm mode by a simple recursion relation [Bird *et al.* 1987] this becomes

$$\bar{\lambda} = \frac{\sum_{j=1}^{N_m} j^{-2(2+\sigma)}}{\sum_{j=1}^{N_m} j^{-(2+\sigma)}} \lambda_z. \tag{7-11}$$

where $\sigma \approx -1.40\,(h^*)^{0.78}$ and h^* is the hydrodynamic interaction parameter [Bird *et al.* 1987]. However, for rheologically simple fluids, the predictions of the Rouse-Zimm model and the Oldroyd-B model must agree in the limit of zero shear rate

$$\eta_{p,0} = n\,\mathrm{k_B}\,T\lambda_Z \sum_j j^{-(2+\sigma)} = \left(n\,\mathrm{k_B}\,T\right)_{\text{Oldroyd}} \bar{\lambda}, \tag{7-12}$$

$$\Psi_{1,0} = 2n\,\mathrm{k_B}\,T\lambda_Z^2 \sum_j j^{-2(2+\sigma)} = 2\left(n\,\mathrm{k_B}\,T\right)_{\text{Oldroyd}} \bar{\lambda}^2. \tag{7-13}$$

To satisfy these two equations, the value of the elastic modulus must be modified slightly from the value obtained through physical arguments. This is achieved through a slight modification to the number density of polymer chains, n. The new value of the elastic modulus, denoted $(n\mathrm{k_B}T)_{\text{Oldroyd}}$, is give by

$$\left(n\,\mathrm{k_B}\,T\right)_{\text{Oldroyd}} = n\,\mathrm{k_B}\,T\frac{\lambda_Z}{\bar{\lambda}}\sum_j j^{-(2+\sigma)} = n\,\mathrm{k_B}\,T\frac{\left(\sum_j j^{-(2+\sigma)}\right)^2}{\sum_j j^{-2(2+\sigma)}}. \tag{7-14}$$

For the 0.025wt% polystyrene solution at $T = 25\,^{\circ}\mathrm{C}$,

$$\left(n\,\mathrm{k_B}\,T\right)_{\mathrm{Oldroyd}} = 3.26\;n\,\mathrm{k_B}\,T = 0.98\,\mathrm{Pa}\,. \tag{7-15}$$

This method for calculating the elastic modulus has been followed by several groups in the past [Doyle *et al.* 1998; Spiegelberg and McKinley 1996] and will be used throughout this manuscript.

7.3 Flow Induced Birefringence (FIB)

Much of the theory behind flow induced birefringence has been presented previously in Chapter 6. The reader is referred to Section 6.1 for many of the introductory details which will not be repeated in this chapter. Some of the earliest birefringence measurements in extensional flows of polymer solutions were performed by Keller and coworkers [Muller *et al.* 1988; Pope and Keller 1977; Pope and Keller 1978]. Flow induced birefringence measurements were performed in the four-roll mill, the opposed jet device and the cross-slot device and used to determine the degree of chain orientation in extensional flows. This work represents the first experimental documentation of the existence of a coil-stretch transition, observed at a Deborah number of $De = 1$. Talbott and Goddard [Talbott 1978; Talbott and Goddard 1979] developed a technique for measuring birefringence in slender fluid filaments drawn by a fiber spinner. By measuring the birefringence along the spinline and coupling it directly to simultaneous measurements of the tension within the fiber, Talbott and Goddard were able to demonstrate the breakdown of the stress-optic law for semi-dilute separan solutions at very low stresses, $\Delta\tau \approx 2\mathrm{kPa}$.

The first flow induced birefringence measurements of dilute and semi-dilute polymer solutions undergoing transient uniaxial elongation in a filament stretching device were reported by Doyle et al. [Doyle *et al.* 1998]. Experimental measurements and Brownian dynamic simulations revealed the existence of a 'stress-conformation' hysteresis [Doyle *et al.* 1998]. Doyle et al. found that in a strong stretching flow, the average configuration and resulting stress in a polymer chain evolve along different paths during stretching and relaxation. This hysteresis was shown to arise from non-equilibrium coupling between the macroscopic flow field and the internal degrees of freedom of the fluid microstructure. These experiments, for all their success, were not without their limitations. To avoid scattering and spreading of the polarized laser light, the initial diameter of the filament was increased and the initial aspect ratio greatly reduced. This resulted in a shear dominated flow at small strains. To minimize the effect of gravity, the filament was immersed within a Plateau tank containing a low viscosity, neutrally buoyant fluid. The experiments were further limited in the amount of total strain, $\varepsilon_{\max} = 3.5$, that could be applied to the filament and were thus unable

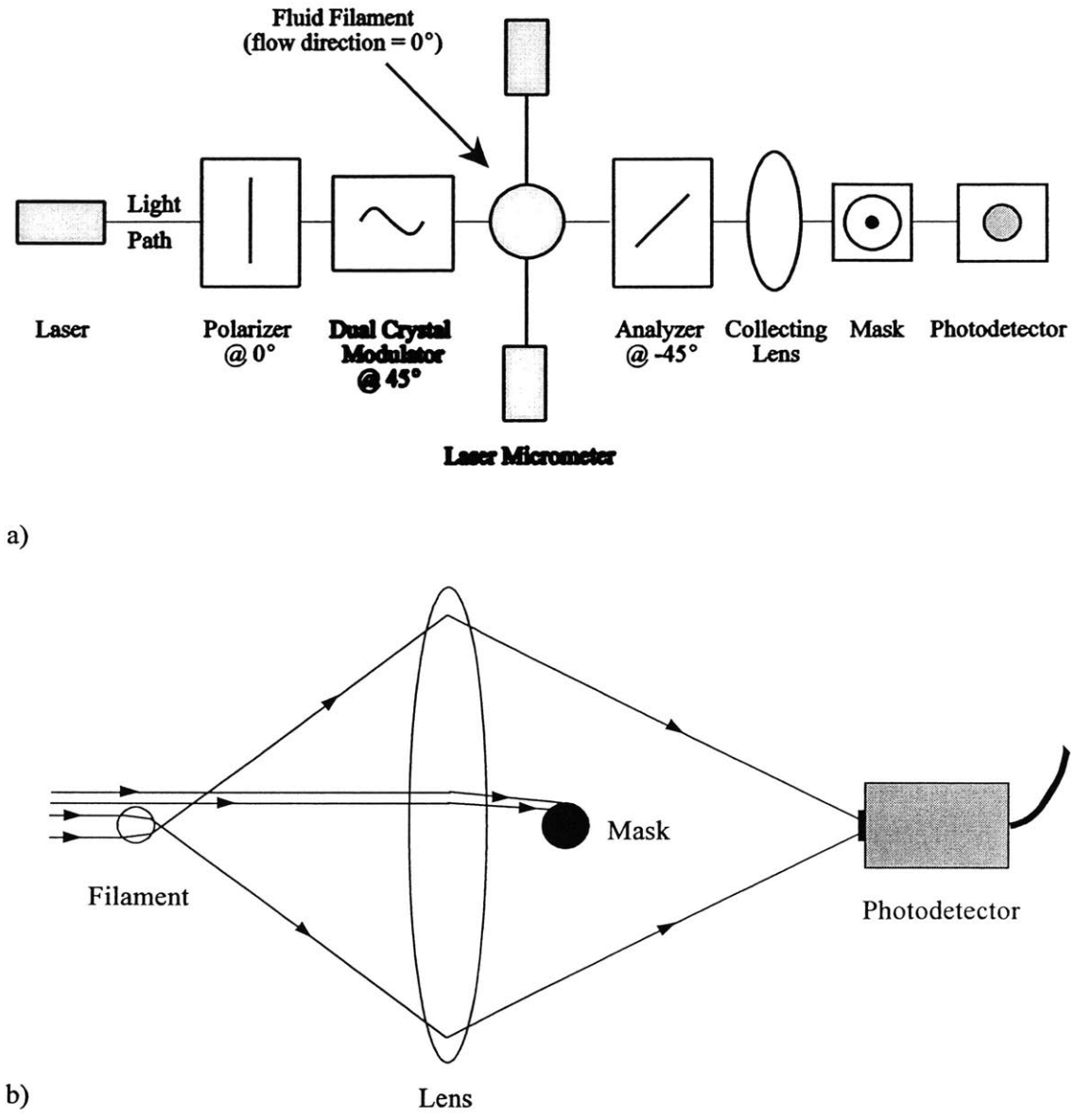

Figure 7-3 Schematic diagram or a) the flow induced birefringence optical train and b) the masking technique.

to reach the steady-state extension of the test fluid. Recently, Sridhar and coworkers [Sridhar *et al.* 2000] have developed an in-air flow induced birefringence system for their filament stretching rheometer which does not require immersion in a Plateau tank. Sridhar and coworkers were able to reach large strains, $\varepsilon \simeq 5.5$, for both steady and unsteady uniaxial extension flows.

The optical path for the polarization modulated flow birefringence system employed in this research is shown in Figure 7-3a and is similar in design to the system pioneered by Frattini and Fuller [Frattini and

Fuller 1984]. The kernel of the current birefringence system was developed at NASA's Glenn Research center for use in filament stretching experiments in microgravity. The rigors of unmanned sounding rocket experimentation require that the system be robust, compact and sensitive. These requirements prove advantageous in earth's gravity as well. The system is light, insensitive to mechanical vibration and can be successfully mounted to the lower platen of the filament stretching rheometer. The operation and calibration of this system with its unconventional dual-crystal electro-optical modulator have been presented previously by Mackey and coworkers [Mackey *et al.* 1999]. The polarized laser light is generated by a 4.5 mW, 635nm laser diode (Thorlabs CPS43AP05ME). The light is first passed through a linear polarizer (New Focus 5524) oriented at 0° from the vertical axis of the filament stretching rheometer. The polarized light is then sent through a dual-crystal electro-optical modulator oscillating at 44kHz and oriented at 45°. After passing through the filament, the light reaches a second linear polarized (Newfocus 5524), known as the analyzer, which is oriented at -45°. Finally, the light passes through a biconvex collecting lens (Newport KBX39) and a mask before impinging on a photodetector (Thorlabs PDA55).

There are several major difficulties associated with successfully taking optical measurements of a thinning fluid in a filament stretching rheometer. The radial curvature of the filament acts like a cylindrical lens, fanning the laser light and dramatically reducing the intensity of the light reaching the photodetector. As the filament shrinks, the magnitude of the light spreading will increase. Depending on the axial strain imposed, the filament may become smaller than the cross section of the incoming laser beam and allow laser light which has passed around the filament to reach the photodetector. To correct both of these problems, a lens and a mask were arranged as shown in Figure 7-3b. A similar idea was presented and analyzed by Talbott [Talbott 1978]. The lens is placed such that the diverging light exiting the filament (which acts as a cylindrical lens) is refocused onto the photodetector. The light that passes around the filament is not spread and is blocked by the mask which is composed of a black cylindrical rod of diameter, d_{mask} = 2.0mm. By mounting the mask vertically, directly behind the collecting lens, the minimum amount of light which has passed through the filament is blocked. Alternatively, the mask can be reduced in size and placed at the focal point of the lens [Talbott 1978]. A simple ray tracing analysis by Talbott [Talbott 1978] showed that the error associated with assuming that the path length of the laser light through the fluid is equal to the filament diameter is negligible. At the onset of stretching the filament, the no slip condition at the endplates and the sagging due to gravity result in a strong axial curvature. The degree of off-axis vertical deflection of the laser beam is a complicated function of the stretch rate, fluid properties and the initial loading of the sample. For a strain hardening fluid, the filament will approach an ideal cylinder at moderate strains. The effects of axial curvature are thus only present at early times. However, as the filament thins and elongates, the lateral

position of the filament can shift due to air currents, slight misalignment of the rheometer or mechanical vibration. To lessen the impact of both these problems a large area photodetector (3mm × 3mm) was used. The advantage of this large area photodetector is a reduced sensitivity to filament location and axial curvature. The disadvantage is an enhanced sensitivity to ambient light which must then be minimized. Even with this large area photodetector, short-time birefringence measurements were rendered impossible by the axial curvature of the filament. Fortunately, at small strains, the polymer coils have not been extended far enough to generate an appreciable birefringent signal and the interesting physics is easily observable at larger strains.

The output from the photodetector is split and fed through a low pass filter (EG&G 5113) to determine the DC intensity and a pair of lock-in amplifiers (EG&G 7260) to measure the amplitude of the signal in phase with the fundamental frequency and out of phase with first harmonic of the dual-crystal modulator. These measurements are recorded on a PC through a data acquisition card interfaced with Labview. The intensity the light entering the photodetector is again given by:

$$\begin{aligned} I(t) &= I_{dc} + I_{\omega}\sin\omega t + I_{2\omega}\cos 2\omega t, \\ I_{\omega} &= 2\mathrm{J}_1(A_c) I_{dc} M_{34} = 2\mathrm{J}_1(A_c) I_{dc}\sin\delta\cos 2\chi, \\ I_{2\omega} &= 2\mathrm{J}_2(A_c) I_{dc} M_{32} = 2\mathrm{J}_2(A_c) I_{dc}\left[1-\cos\delta\right]\sin 2\chi\cos 2\chi, \end{aligned} \tag{7-16}$$

where M_{34} and M_{32} are the components of the Mueller matrix corresponding to the optical train shown in Figure 7-3a and A_c is the amplitude of the electro-optical modulation calibrated such that the Bessel function of the first kind of order zero is equal to $J_0(A_c) = 0$ [Frattini and Fuller 1984]. The advantage of using a modulation technique is that it is possible to calculate both the retardation, $\delta = (2\pi\,\Delta n\, d)/\lambda_{light}$, and the extinction angle, χ, simultaneously,

$$\begin{aligned} \delta &= \frac{4\pi\Delta n' R_{mid}(t)}{\lambda_{light}} = \cos^{-1}\left(\frac{-M_{32}^2 \pm M_{34}^2\sqrt{1-M_{34}^2-M_{32}^2}}{M_{34}^2+M_{32}^2}\right), \\ \chi &= \frac{1}{2}\cos^{-1}\left(\frac{M_{34}}{\sin\delta}\right). \end{aligned} \tag{7-17}$$

where d is the optical pathlength equal to $d = 2R_{mid}(t)$ and λ_{light} is the wavelength of the laser light. The direction of the stretch is aligned with the optics at 0° from vertical. The extinction angle, and therefore the $I_{2\omega}$ signal, should be vanishingly small. Assuming the small retardation approximation, $\delta << 1$, is valid and

$\chi = 0$

$$M_{34} = \delta, \qquad M_{32} = 0, \tag{7-18}$$

and Equation 6-19 simplifies to

$$\delta = \frac{\sqrt{2} I_{\omega}}{2 \mathrm{J}_1 (A_c) I_{dc}}, \qquad \chi = 0, \tag{7-19}$$

where the squareroot appears in the denominator of the expression for the retardation because in practice, I_{DC} is an RMS voltage. The validity of these assumptions will be confirmed in Section 7.4.1.

7.4 Results and Discussion

7.4.1 *Steady Stretch Rates*

In order to validate our flow induced birefringence experimental setup and measurement technique, a series of experiments were performed in the filament stretching rheometer at a constant imposed stretch rate. The spectrum of stretch rates and final Hencky strains were chosen to facilitate comparison with the literature [Doyle *et al.* 1998; Sridhar *et al.* 2000]. In Figure 7-4, the DC intensity, I_{DC}, of the birefringence system and the two ratios, $R_{\omega} = M_{34}$ and $R_{2\omega} = M_{32}$, are plotted as a function of time for a constant stretch rate of $\dot{\varepsilon}_0 = 1.0\,\mathrm{s}^{-1}$ and a final Hencky strain of $\varepsilon = 5$. An inherent advantage of this ratiometric technique is the insensitivity of the two ratios to variations in the pathlength and the amount of scattering of the laser light, both of which lead to dramatic changes in the DC intensity over the course of the stretch. At early times, the signal is weak because of the axial curvature of the filament. In the present configuration, reliable birefringence measurements are not possible until a strain of $\varepsilon = 1$. At these small strains, the filament is subject to a reverse-squeeze shear flow which results in a very weak, positive birefringence signal. Recall that the retardation and thus the birefringence can be calculated directly from measurements of R_{ω} using Equation 7-19. As time progresses and the accumulated Hencky strain increases to values greater than $\varepsilon >$ 2, the polymer coils begin to orient with the flow and unravel. The birefringence signal grows increasingly negative until the flow is stopped. Observation of the polymer coil relaxation process is then possible until

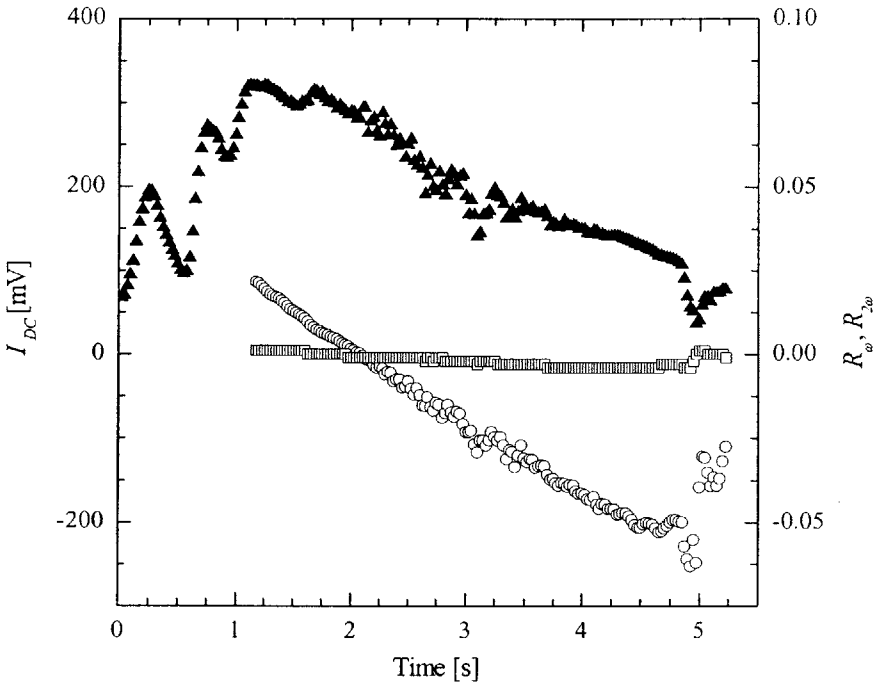

Figure 7-4 Flow induced birefringence measurements as a function of time for a constant stretch rate of $\dot{\varepsilon}_0 = 1.0\,\mathrm{s}^{-1}$ and a final Hencky strain of $\varepsilon = 5$. The data include: '▲', I_{DC}; '○', $R_\omega = M_{34}$; and '□', $R_{2\omega} = M_{32}$.

the filament fails or is deflect out of the laser's path as it drains under gravity. The results in Figure 7-3 also demonstrate the validity of the two assumptions made in the previous section. The first assumption, that the stretch direction is aligned with the 0° orientation of the optical train, is confirmed by the vanishingly small values of $R_{2\omega}$ throughout the entire stretch. The small angle approximation used to derive Equation 7-19 is also proven to be justifiable. The magnitude of R_ω never grows larger than 0.05.

In Figure 7-5, the polymeric contribution to the tensile stress is plotted against the birefringence divided by the stress optic coefficient for the experiment shown in Figure 7-4, a constant stretch rate of $\dot{\varepsilon}_0 = 1.0\,\mathrm{s}^{-1}$ and a final Hencky strain of $\varepsilon = 5$. Also included in Figure 7-5 is the theoretical prediction of the FENE-P model. The polymer contribution to the tensile stress is calculated by subtracting the viscous stress from Equation 7-8

$$\Delta\tau_p = \langle \tau_{zz} - \tau_{rr} \rangle - 3\eta_s \dot{\varepsilon}. \tag{7-20}$$

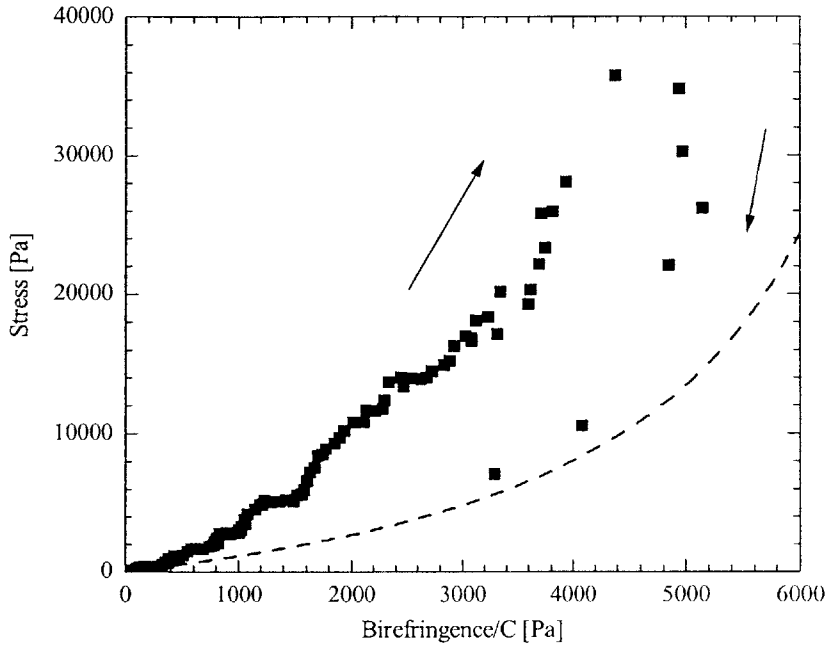

Figure 7-5 Polymer contribution to the elastic tensile stress difference as a function of birefringence/C for a filament stretching experiment of the 0.025wt% PS/PS solution at a constant stretch rate of $\dot{\varepsilon}_0 = 1.0\,\mathrm{s}^{-1}$ and a final Hencky strain of $\varepsilon = 5$. The data include: '▪', experimental data; and '- -', FENE-P model prediction.

A stress-conformation hysteresis is observed similar to that first noted by Doyle et al. [Doyle *et al.* 1998]. During the start-up of the stretch, the data follows the left-hand side of the loop while during relaxation the data follow the right-hand side of the hysteresis loop. The FENE-P model cannot even qualitatively capture the hysteresis loop because it does not contain sufficient physical information about the internal configurations of the chains to determine the polymer stress. In the FENE-P model the stress is a single valued function of the polymer conformation and thus the birefringence [Doyle *et al.* 1998] is also single valued. As expected, the FENE-P model does agree quite well with the experimental data during the latter stages of relaxation. If a conformation dependent FENE dumbbell model [Doyle *et al.* 1998] or the FENE-G model [Ghosh *et al.* 2001] is used, then the hysteresis loop can be qualitatively predicted. A quantitative prediction which properly predicts the transient behavior of this experimentally observed hysteresis loop in extensional flow has yet to be achieved with any known constitutive model.

Similar hysteresis loops can be generated for filament stretching experiments performed at the same

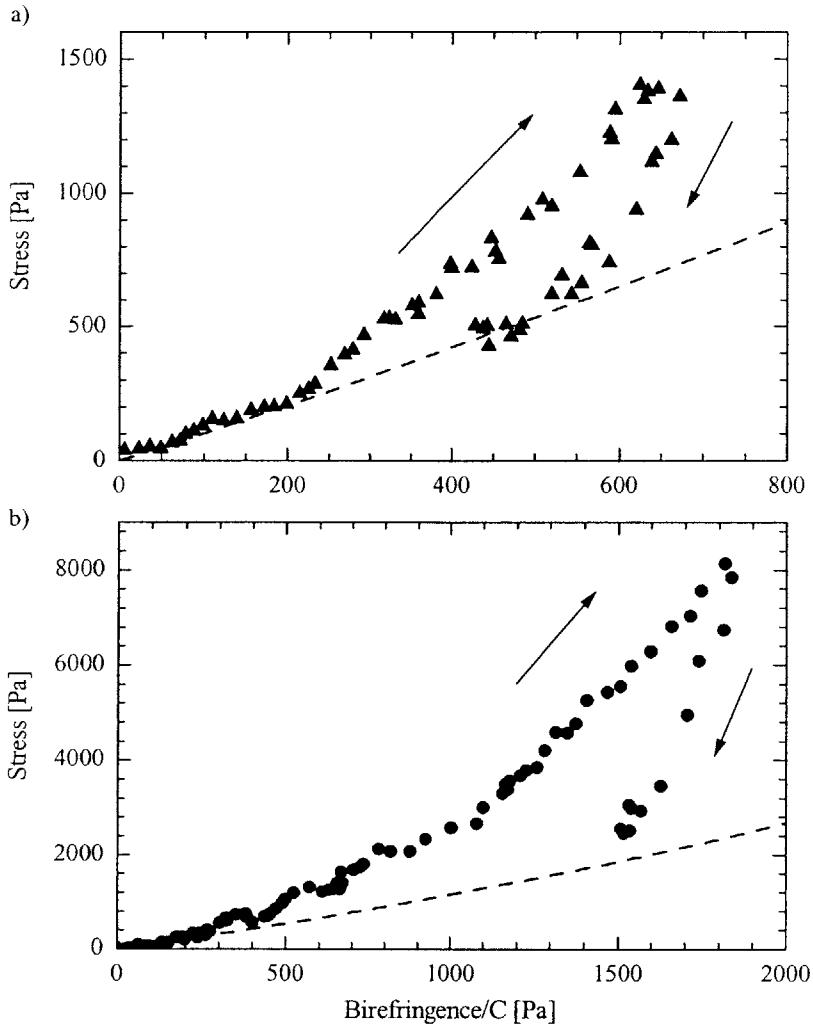

Figure 7-6 Polymeric tensile stress as a function of birefringence/C for a filament stretching experiment of the 0.025wt% PS/PS solution at a constant stretch rate of $\dot{\varepsilon}_0 = 1.0\,\mathrm{s}^{-1}$ and a final Hencky strains of a) $\varepsilon = 3$ and b) $\varepsilon = 4$. The data include: '▲', experimental data for $\varepsilon = 3$; '•', experimental data for $\varepsilon = 4$; and '- -', FENE-P model predictions.

strain rate, but to different final Hencky strains. In Figure 7-6, the polymeric stress is plotted against the birefringence/C for a constant stretch rate of $\dot{\varepsilon}_0 = 1.0\,\mathrm{s}^{-1}$ and final Hencky strains of $\varepsilon = 3$ (Figure 7-5a) and $\varepsilon = 4$ (Figure 7-5b). As before, the predictions of the FENE-P model are included in these plots. The magnitude of the hysteresis loop decreases with final strain. At these lower strains, the FENE-P model

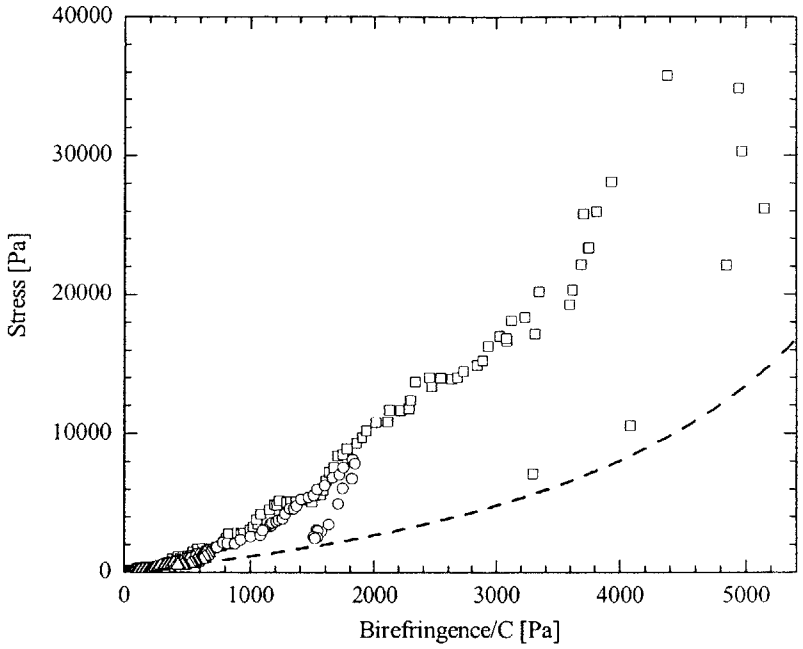

Figure 7-7 Polymeric tensile stress as a function of birefringence/C for a filament stretching experiment of the 0.025wt% PS/PS solution at a constant stretch rate of $\dot{\varepsilon}_0 = 1.0\,\mathrm{s}^{-1}$. The data include: '▲', experimental data to a final Hencky strain of $\varepsilon = 3$; '•', experimental data to $\varepsilon = 4$; '■', experimental data to $\varepsilon = 5$; and '- -', FENE-P model predictions.

predictions represent the data well during the initial onset of the stretch. The experimental data does not begins to deviate from the FENE-P model predictions until a value of approximately $\Delta n'/C \approx 250$ Pa and a stress of $\tau_p \approx 250$ Pa have been reached. These values represent the upper limit for the validity of the stress-optic rule for this dilute polymer solution. The stress-optic rule is commonly used to convert measurements of birefringence to stress in polymer melt experiments where it is valid up to much larger stresses, typically $\Delta\tau \approx 10^5$ Pa [Janeschitz-Kriegl 1983].

One way to appreciate how quickly the stress, birefringence and the magnitude of the hysteresis loop grow with increasing total Hencky strain is to plot all three of these experiments in a single figure as shown in Figure 7-7. At these scales, the $\varepsilon = 3$ experiment is almost unperceivable. Figure 7-7 also demonstrates the repeatability of these filament stretching experiments and the flow induced birefringence system in general. All three experiments superimpose quite nicely, following the same path in stretch and then again in the last stages of the relaxation process.

If the stretch rate is now changed, but the final Hencky strain held constant a new set of observations

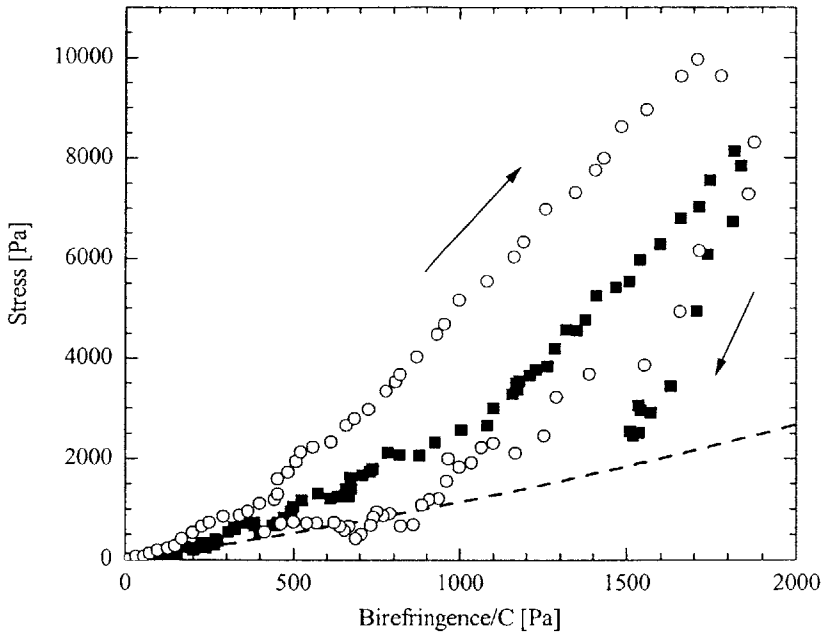

Figure 7-8 Polymeric tensile stress as a function of birefringence/C for a filament stretching experiment of the 0.025wt% PS/PS solution to a final Hencky strain of $\varepsilon = 3$. The data include: '○', experimental data at a constant stretch rate of $\dot{\varepsilon}_0 = 1.5\text{s}^{-1}$; '■', experimental data at a constant stretch rate of $\dot{\varepsilon}_0 = 1.0\text{s}^{-1}$; and '- -', FENE-P model predictions.

can be made. In Figure 7-8, the results of two filament stretching experiments terminated at a Hencky strain of $\varepsilon = 4$ are shown. The first experiment, at a constant stretch rate of $\dot{\varepsilon}_0 = 1.0\text{s}^{-1}$, has been shown previously in Figure 7-6. The second experiment is conducted at a stretch rate 50% larger than the first, $\dot{\varepsilon}_0 = 1.5\text{s}^{-1}$. The birefringence in each experiment grows to a value of $\Delta n'/C \approx 1800$ Pa before the stretch is stopped. The amount of chain orientation and unraveling, is found to be independent of rate of deformation and only dependent on the total amount of accumulated strain. The stress, however, is linearly dependent on the strain rate. This same observation has been made in the literature where the Trouton ratio was found to be independent of Deborah number above a Deborah number of $De = 1$ [Anna *et al.* 2001]. Both experiments, do, however, relax along the same path suggesting that there is a universal relaxation process independent of strain and strain rate.

It has been hypothesized in Chapters 3 and 4 that this stress-conformation hysteresis may

significantly contribute to the enhanced pressure drop through axisymmetric-contractions and the enhanced drag observed in other complex flows [Chmielewski *et al.* 1990; Solomon and Muller 1996]. However, taking a 4:1:4 contraction-expansion for example, the total accumulated Hencky strain along the centerline is only $\varepsilon = 2.77$. At these low strains, a constant stretch rate experiment shows very little hysteresis as indicated in Figure 7-6a. However, it is possible a nonhomogeneous uniaxial extension created to reproduce the strain rate profile a fluid element experiences as it travels along the centerline upstream of an axisymmetric contraction-expansion would demonstrate more substantial hysteresis and reveal some interesting new piece of the physical puzzle.

7.4.2 *4:1:4 Contraction-Expansion Centerline Profiles*

In the previous chapter, measurements of the axisymmetric flow induced birefringence along the centerline of the 4:1:4 contraction-expansion were reported for the flow of the 0.025wt% polystyrene Boger

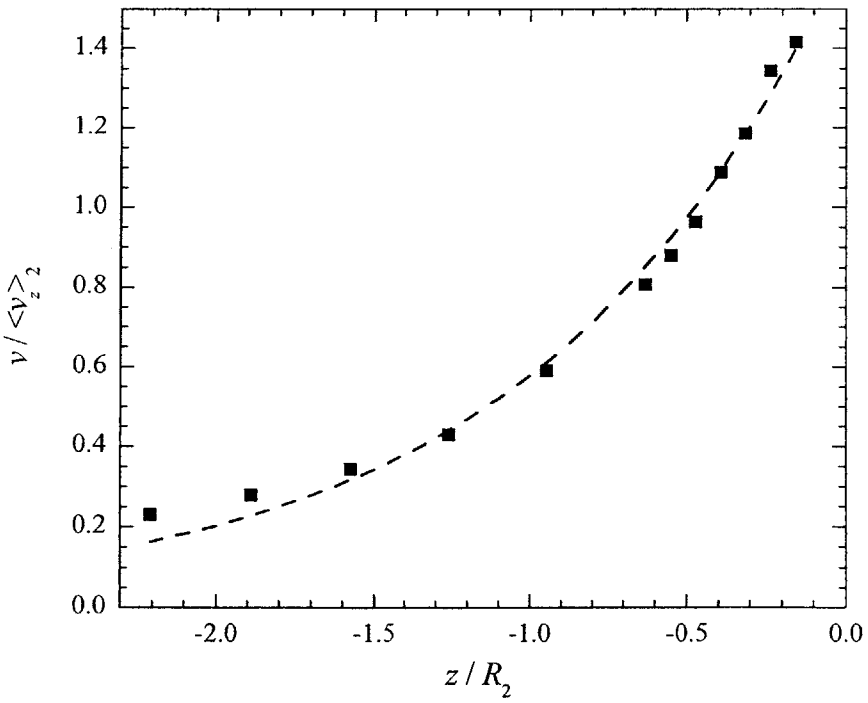

Figure 7-9 Centerline velocity profile upstream of a 4:1:4 axisymmetric contraction-expansion for a Deborah number of $De = 1.5$. The data include: '■', experimental data and '--', fit of the form $v/\langle v_z \rangle_2 = B \exp(Cz/R_2)$.

fluid. As expected, these birefringence measurements demonstrated significant orientation and elongation of the polymer chain upstream of the contraction-expansion. However, to gain more physical insight into this complex flow, it would be informative to simultaneously measure the stress and birefringence in the fluid passing through the contraction-expansion. Unfortunately, the only available measure of stress in the contraction-expansion is the global pressure drop which is, in fact, the quantity into which we hope to gain some physical insight. Instead of measuring the stress and birefringence of a fluid element within the contract-expansion flow, we can isolate that fluid element and expose it to the identical time sequence of strain rates in the filament stretching rheometer.

The fluid element traveling along the centerline of the contraction-expansion is exposed to a transient nonhomogeneous extensional flow. To determine the exact strain rate profile required, the velocity profiles presented in Section 3.3.5 are analyzed. The centerline LDV measurements upstream of the 4:1:4 axisymmetric contraction-expansion at a Deborah number of $De = 1.5$ are shown in Figure 7-9. As in Section 3.3.5, the velocities are nondimensionalized by the average velocity within the contraction, $\tilde{v}_z \equiv v_z / \langle v_z \rangle_2$, the distance upstream is nondimensionalized by the radius of the throat, $\tilde{z} \equiv z / R_2$, and the time is nondimensionalized by the shear rate, $\tilde{t} \equiv t \langle v_z \rangle_2 / R_2$, An Eulerian velocity profile of the form

$$\tilde{v}_z(z) = \mathrm{A} + \mathrm{B}\,\mathrm{e}^{\mathrm{C}\tilde{z}} \tag{7-21}$$

is found to fit the data quite well for all Deborah numbers up to $De = 4.5$. Recall that a fluid element in the Sampson flow theory [Happel and Brenner 1965], experiences a velocity profile given by $\tilde{v}_z \sim 1/\left(z^2+1\right)$. In Equation 7-21, A, B and C are constants. The value of A corresponds to twice the average upstream dimensionless velocity, $\mathrm{A} = 2/\beta^3$. However for the purpose of converting Equation 6-23 to a Lagrangian velocity profile analytically, we have chosen set to A to zero, A = 0, and refit the data to determine new values of B and C. The effect of this change is to limit the distance upstream for which the exponential fit is valid. Table 7-1 lists the values of the constants used to fit the velocity profiles at various Deborah numbers.

To calculate the proper velocity profile of the filament stretching rheometer endplates, we must first determine the strain rate profile of a fluid element traveling along the centerline of the contraction-expansion. By integrating Equation 7-21, the Lagrangian position of a fluid element $\tilde{z}\left(z_0, t_0\right)$ can be determined as a

function of time

$$\tilde{z} = -\frac{1}{C}\ln\left(BC\left(t_0 - \tilde{t}\right)\right), \tag{7-22}$$

where t_0 is a dimensionless time constant related to the initial dimensionless upstream position of the fluid element, z_0,

$$t_0 = \frac{1}{BC}e^{-Cz_0}. \tag{7-23}$$

Throughout the course of these experiments, z_0 will be set such that $\tilde{v}_z\left(z_0\right) = 2/\beta^3$. Equation 7-22 is then differentiated to determine the fluid velocity as a function of time

$$\tilde{v}(t) = \frac{1}{C\left(t_0 - \tilde{t}\right)}. \tag{7-24}$$

Deborah Number	B	C	t_0	z_0
0.500	1.694	0.849	4.697	-2.250
1.000	1.587	0.922	4.470	-2.037
1.500	1.665	1.048	4.000	-1.854
2.500	1.585	0.752	5.204	-2.427
3.500	1.750	0.557	7.468	-3.562

Table 7-1 Values for the exponential fit to the centerline velocity profiles upstream of a 4:1:4 axisymmetric contraction-expansion.

The strain rate of the fluid as a function of time thus becomes

$$\dot{\tilde{\varepsilon}} = \frac{d\tilde{v}}{d\tilde{z}} = \frac{d\tilde{v}}{d\tilde{t}}\frac{d\tilde{t}}{d\tilde{z}} = \frac{1}{\left(t_0 - \tilde{t}\right)}, \tag{7-25}$$

while the total accumulated strain as a function of time is given by

$$\varepsilon = \int_0^{\tilde{t}} \dot{\tilde{\varepsilon}}\, d\tilde{t}' = \ln\left(\frac{t_0}{t_0 - \tilde{t}}\right). \tag{7-26}$$

From Equation 7-25 it is evident that the shear rate diverges, $\dot{\varepsilon} \to \infty$, as $\tilde{t} \to t_0$. This occurs well downstream of the throat, $z = 0$, and therefore does not pose a problem for our analysis.

Recall that in the filament stretching rheometer, the total Hencky strain for an ideal stretch is given by

$$\varepsilon = \ln\left(\frac{L(t)}{L_0}\right). \tag{7-27}$$

Substituting into Equation 7-26 and exponentiating both sides, we can calculate the appropriate endplate separation

$$L(t) = L_0\left(\frac{\mathrm{t}_0}{\mathrm{t}_0 - \tilde{t}}\right), \tag{7-28}$$

and the velocity profile of the endplate

$$\dot{L}(t) = L_0 \frac{\langle v_z \rangle_2}{R_2} \frac{\mathrm{t}_0}{\left(\mathrm{t}_0 - \tilde{t}\right)^2}. \tag{7-29}$$

required to simulate the transient nonhomogeneous uniaxial extension experienced by a fluid element traveling along the centerline upstream of a 4:1:4 axisymmetric contraction-expansion. The calculated profiles corresponding to a Deborah number of $De = 1.5$ are shown in Figure 7-10 in dimensional form. Note that the strain rate monotonically increases with time. The experiments are terminated when the Hencky strain equals the total strain accumulated within the contraction. For the 4:1:4 contraction-expansion, $\varepsilon = 2\ln(\beta) = 2.77$. Hence, the total time for the stretch, t_f, can be expressed as a function of the contraction ratio β and the time constant t_0

$$t_f = t_0\left(1 - \frac{1}{\beta^2}\right) \tag{7-30}$$

Upon completion of the stretch, the platens are stopped and the relaxation of the fluid filament is observed. Although the strain rate profile during stretch will mimic the conditions upstream of the

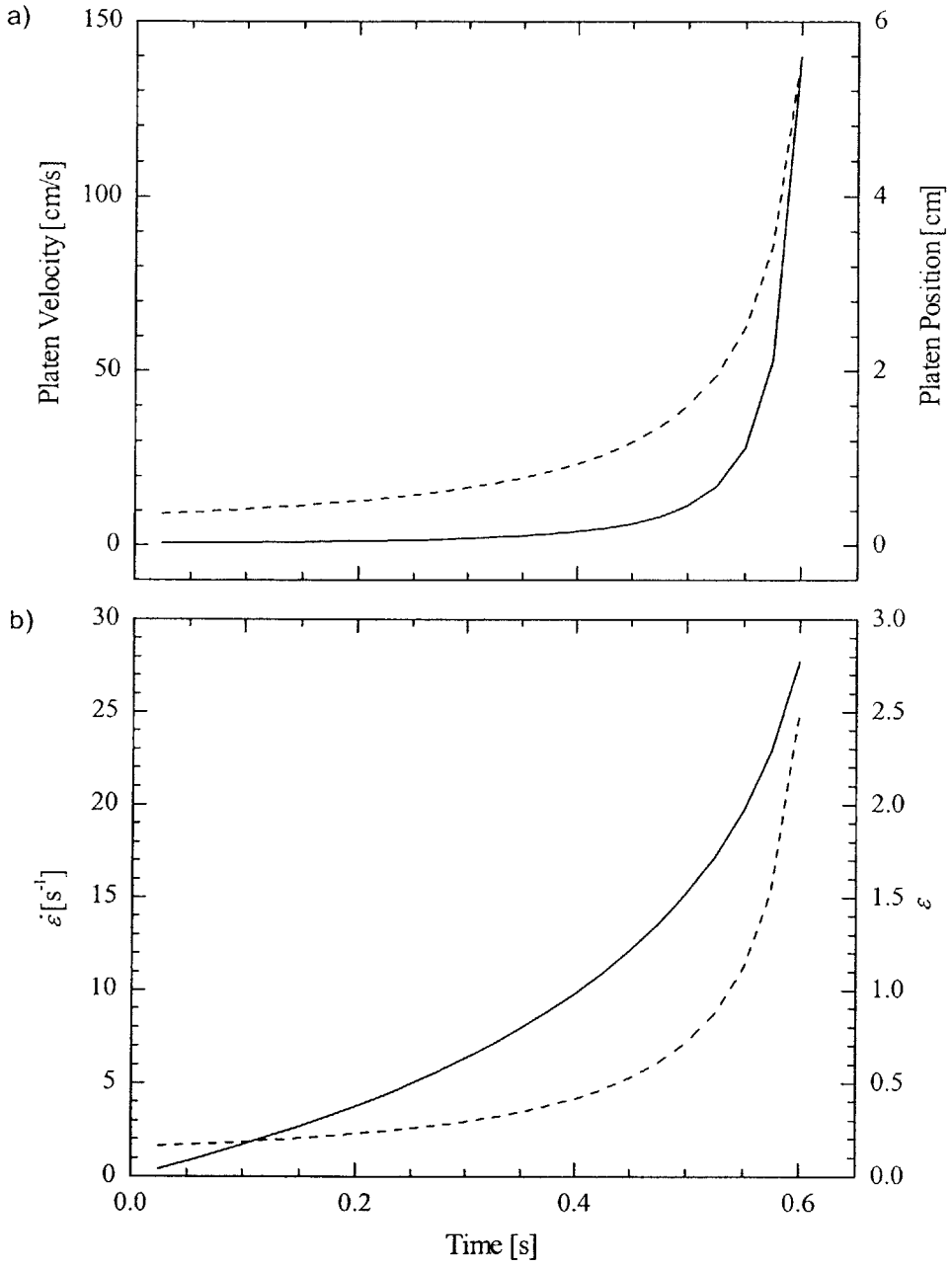

Figure 7-10 Deformation profiles for a fluid filament being stretched simulating the centerline profile into a 4:1:4 contraction-expansion at a Deborah number of De=1.5. The data in a) include: '--', endplate position and '–', endplate velocity. The data in b) include: '--', strain rate and '–', total accumulated strain.

contraction-expansion, the relaxation process does not correspond to the region of biaxial compression downstream of the expansion. Theoretically, the downstream compression could be imposed by the filament stretching device, however, in practice the slender fluid filament will buckle under such a compressive loading.

7.4.3 *Imposition of Proper Flow Kinematics*

To perform a successful filament stretching experiments, whether homogenous or nonhomogeneous in time, one must first determine the correct flow kinematics. In the previous section, the desired endplate separation, $L(t)$, and velocity, $\dot{L}(t)$, for an ideal stretch have been derived. It must be reiterated that the experiments in the filament stretching rheometer are not truly ideal. The profiles generated by Equations 7-28 and 7-29 will result in a new form of Type II experiment where the strain rate profile is no longer constant

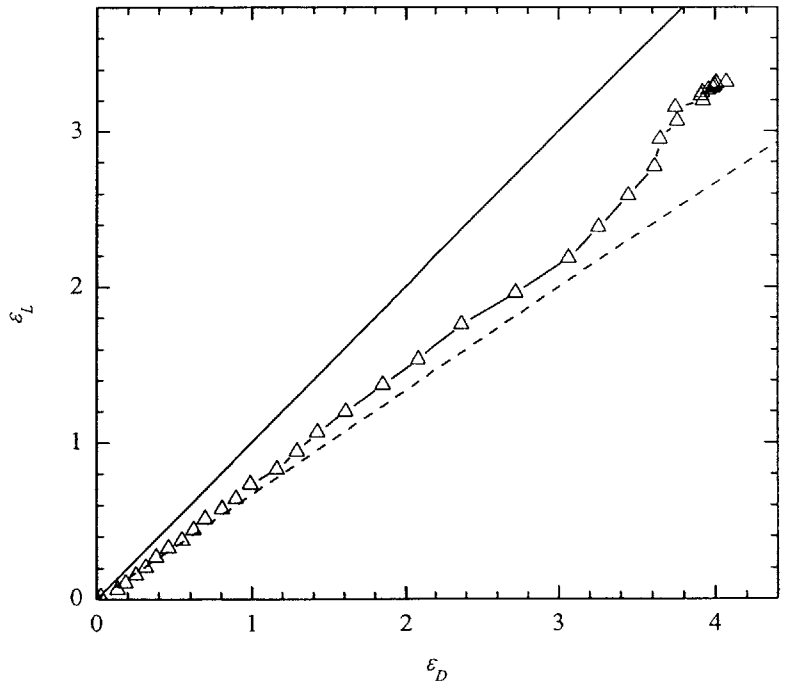

Figure 7-11 'Master curve' for the 0.025wt% PS/PS solution. The data include: '△', experimental stretch of the centerline strain rate profile upstream of a 4:1:4 contraction-expansion at a Deborah number of De = 1.5; '–', the ideal cylinder prediction; and '--', the lubrication approximation prediction.

as in Section 7-1, but is time dependent. The technique developed by Anna et al. [Anna *et al.* 1999] and Orr and Sridhar [Orr and Sridhar 1999] is used to convert from a Type II experiment, where the endplate separation follows the desired strain rate profile, to a Type III experiment, where the midfilament diameter decreases with the desired strain rate profile.

A 'master curve' is generated in Figure 7-11 which compares the Hencky strain based on plate separation, ε_L, with the Hencky strain based on midfilament diameter, ε_D, for the Type II profile simulating the flow into a 4:1:4 contraction-expansion at a Deborah number of $De = 1.5$. Also shown in Figure 7-11 are lines corresponding to an ideal stretch and the lubrication approximation. At the onset of extension, the filament follows the lubrication approximation quite closely. The filament then begins to strain harden eventually approaching the prediction of the ideal cylinder. The plot can be used to convert this nonideal Type II experiment into a nearly ideal Type III experiment using an inversion process discussed in great detail in the literature [Anna *et al.* 1999; Orr and Sridhar 1999]. A spline is used to fit the data and determine a functional relationship between the endplate separation and the filament diameter, $\varepsilon_L(\varepsilon_D)$. The proper Type III endplate velocity and position profiles are then determined by evaluating ε_L at all points in the desired strain rate profile ε_D. This profile is of course identical to the Type II profile but now the proper strain is achieved in the midfilament diameter rather than the filament length. In homogeneous uniaxial elongation tests with dilute polymer solutions, the 'master curve' has been found to be a weak function of Deborah number and so a new 'master curve' must be generated from a Type II experiment for each successive strain rate profile to ensure that the resulting Type III profile generated is as close to ideal as possible [Anna *et al.* 1999].

In Figure 7-12a, the strain based on the midfilament diameter, ε_D, for a Type II and Type III experimental stretches are compared with the ideal strain profile upstream of a 4:1:4 contraction-expansion at a Deborah number of $De = 1.5$. The strains achieved in the Type II experiment greatly overshoot the ideal profile while the Type III test is nearly indistinguishable from the ideal curve. To take a closer look at the quality of the Type III profile, the diameter error

$$\delta_D = \frac{D_{mid} - D_{ideal}}{D_{ideal}} \tag{7-31}$$

is shown in Figure 7-12b as a function of time. Through the 'master curve' inversion procedure it is possible to maintain an error of less than 5% for the duration of the experiment. Similar results have been reported in the literature for homogeneous uniaxial extension [Anna *et al.* 2001].

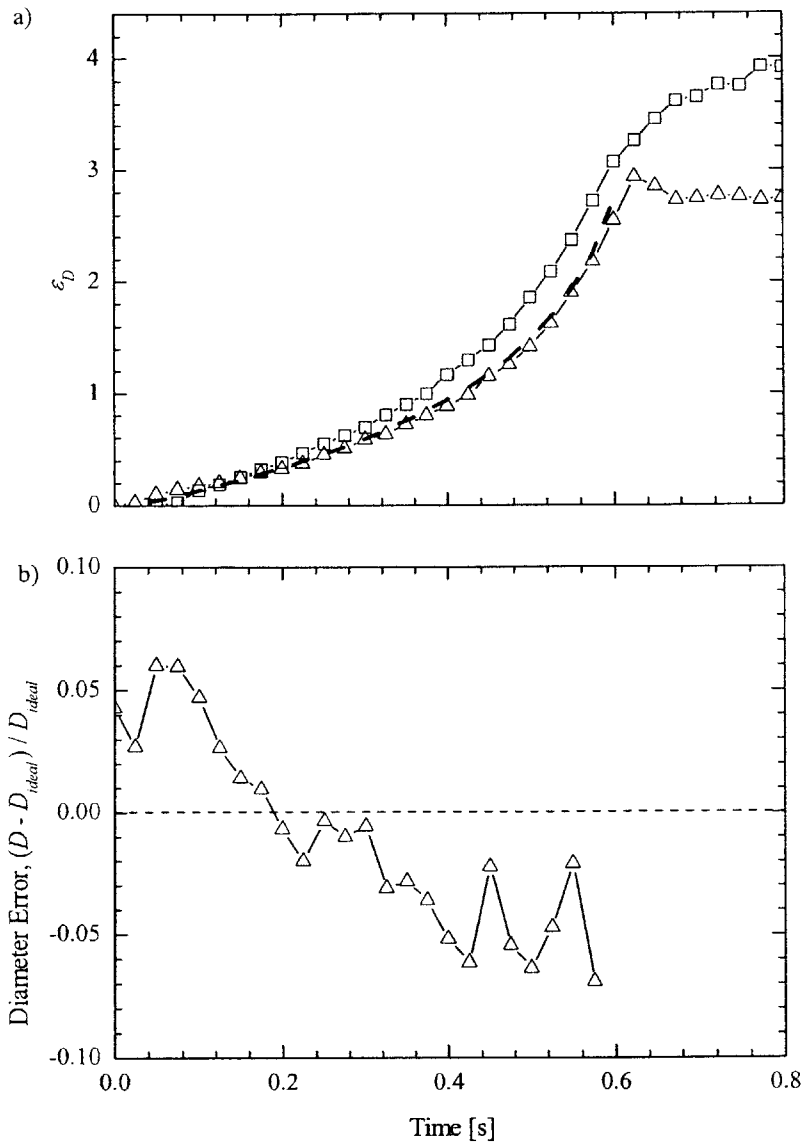

Figure 7-12 The a) strain based on the midfilament diameter and b) diameter error as a function of time for the 0.025wt% PS/PS fluid. The data include: '□', Type II and '△', Type III experimental stretch of the centerline strain rate profile upstream of a 4:1:4 contraction-expansion at a Deborah number of De = 1.5; and '- -', the ideal strain profile.

7.4.4 *Transient Measurement of Extensional Flow into a Axisymmetric 4:1:4 Contraction-Expansion*

Using the velocity profiles generated in Section 7.4.2 and the 'master curve' inversion procedure

liquids through energy loss argument associated stress-conformation hysteresis. Therefore, all the filament stretching results presented in this section will compare the polymeric tensile stress with the average conformation of the polymer chain.

In Figure 7-13, the results of the Type II and III experiments described in the previous section are shown. The strain profile is equivalent to that observed upstream of a 4:1:4 contraction-expansion at a Deborah number of $De = 1.5$. A significant hysteresis loop is observed in the Type II experiment shown in Figure 7-13 a. The magnitude is similar to the constant uniaxial stretch rate results presented in Section 7.4.1. The chains are aligned with the flow direction and significantly extended, reaching a final conformation of almost $\Delta A = 2200$. This stretch represents about 25% of the maximum extension of the polystyrene chain. This initial experiment is very encouraging, however, one must note that the final midfilament Hencky strain for this Type II experiment is $\varepsilon_D = 4.1$, which is significantly larger than the desired value of $\varepsilon_D = 2.77$. A Type III experiment is thus required to insure that the proper strain rate profile and final Hencky strain are applied to the fluid filament.

The results of the corresponding Type III experiment are shown in Figure 7-13b. The scale of the conformation axis has purposely been set to exactly one tenth of Figure 7-13a to emphasize the dramatic difference between the two experiments. By converting from a Type II to a Type III experiment, both the final Hencky strain and the strain rates applied to the fluid filament have been reduce, drastically decreasing the stresses and conformation achieved. As a result, even with signal conditioning and filtering, the Type III measurements are considerably more noisy than the Type II measurements. Note that the maximum conformation measured for the Type III experiment is only $\Delta A = 250$, just 3% of the maximum extension of the polymer coil. Fortuitously, a small hysteresis loop still exists. These stress vs. conformation plots are analogous to the stress vs. strain plots often used to investigate material properties in solid mechanics. In both cases, the area enclosed by the hysteresis loop has units of energy per unit volume. In solid mechanics, this energy represents the amount of work required to plastically deform an elastic solid. For a viscoelastic fluid, it represents the work done by a purely dissipative stress coupled to the non-equilibrium kinematics of the extensional flow whose physical origins are not well understood. To quantify the energy dissipation per unit volume, the polymeric tensile stress is numerically integrated over the entire hysteresis loop

The energy dissipation per unit volume is made dimensionless by dividing the elastic tensile stress by the elastic modulus of the test fluid

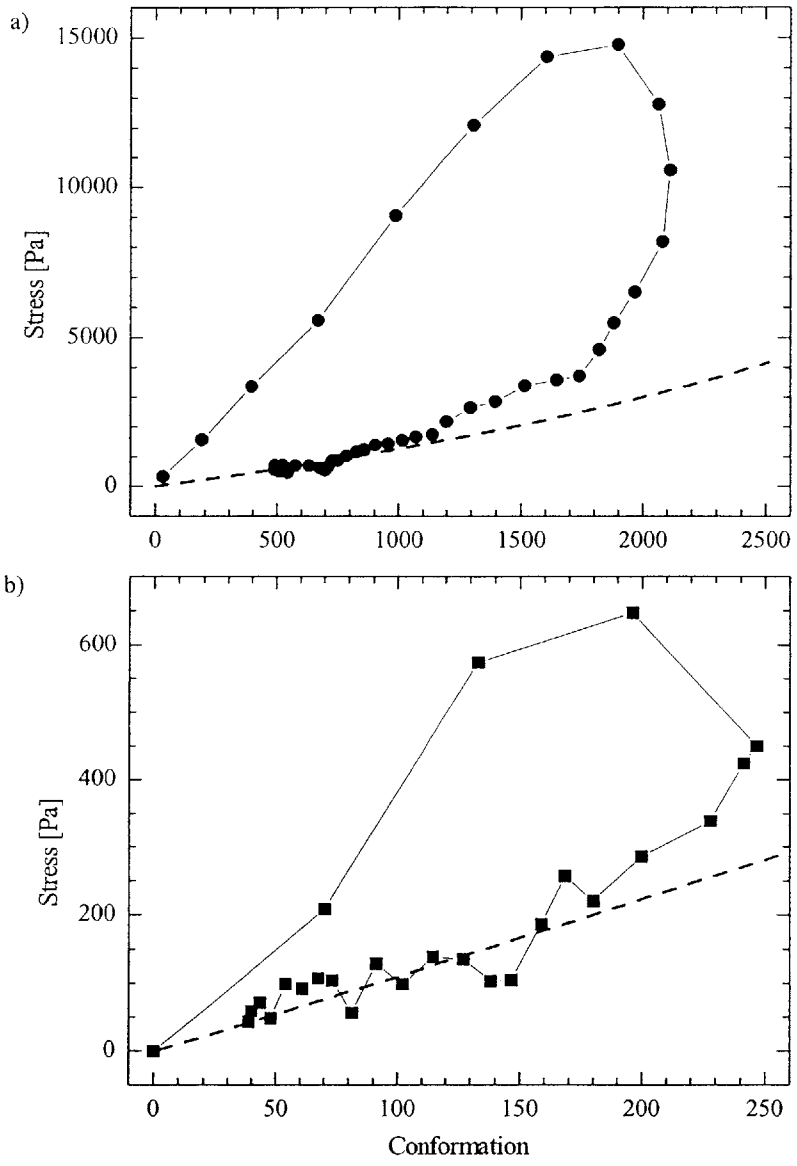

Figure 7-13 Polymeric tensile stress as a function polymer coil conformation for the 0.025wt% PS/PS solution. The data include: a) '●', Type II, and b) '■' Type III experimental stretch of the centerline strain rate profile upstream of a 4:1:4 contraction-expansion at a Deborah number of De = 1.5; and '--', FENE-P model predictions.

outlined in Section 7.4.3 it is now possible to directly observe the stress growth and polymer coil conformation of a fluid element traveling along the centerline into an axisymmetric contraction-expansion. The direct aim of this research is to explain the additional pressure drop observed in the flow of elastic

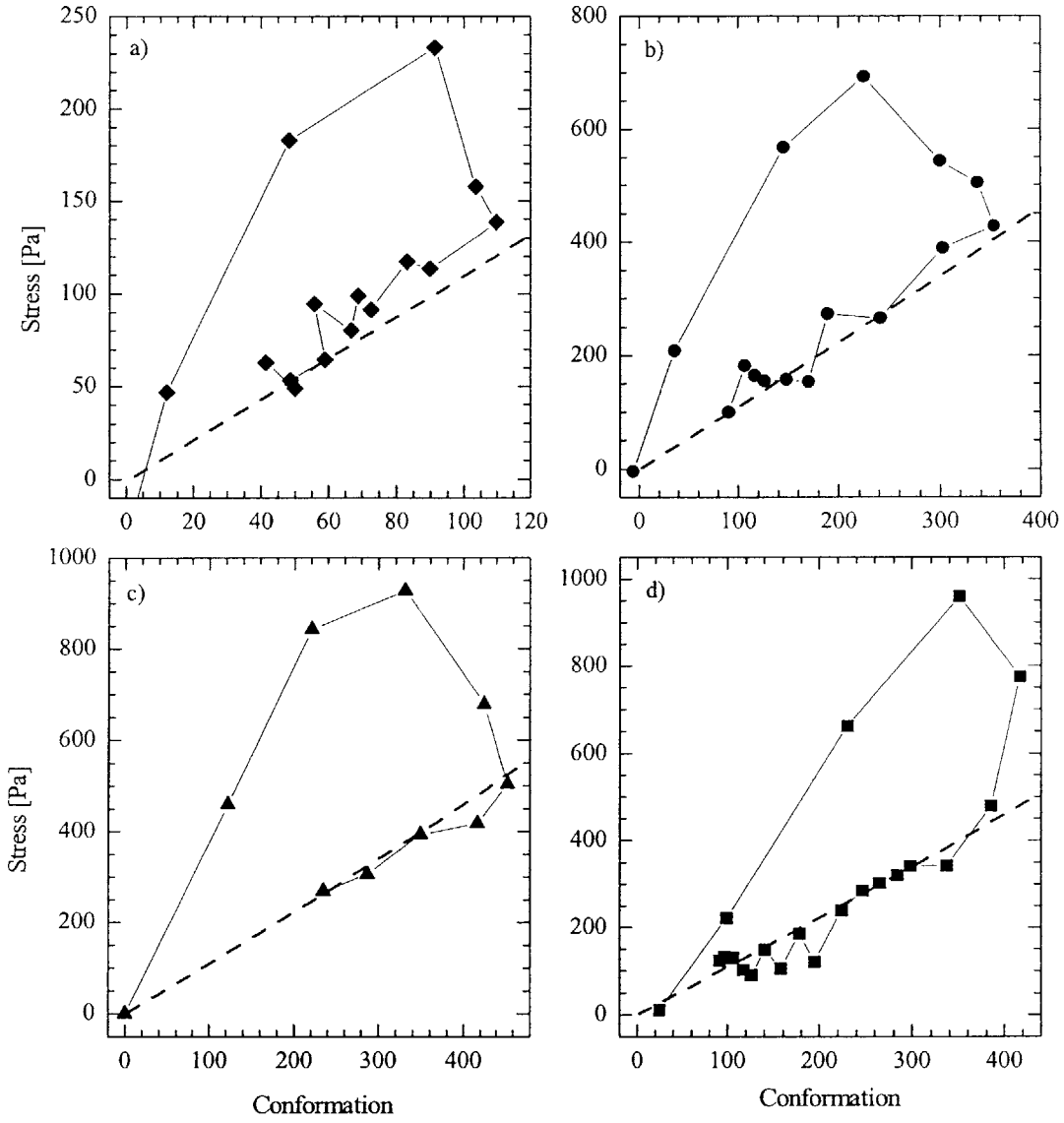

Figure 7-14 Polymeric tensile stress as a function polymer coil conformation for the 0.025wt% PS/PS solution for the Type III experimental stretch of the centerline strain rate profile upstream of a 4:1:4 contraction-expansion at several different Deborah numbers . The data include: a) '♦', $De = 0.5$; b) '●', $De = 1.0$; b) '▲', $De = 2.5$; d) '■' , $De = 3.5$; and '--', the FENE-P model predictions.

$$E_D = \int \frac{\tau_p}{n\,\mathrm{k_B}\,T}\, d\Delta A. \tag{7-32}$$

If the experimental data does not continue to zero conformation during the relaxation process, the hysteresis loop is closed using the FENE-P model predictions from the last data point to the origin. For the Type II experiment, the dimensionless dissipation energy is equal to $E_D = 1.1\times10^7$ while for the Type III experiment $E_D = 1.6\times10^5$, a difference of two orders of magnitude.

The series of experiments outlined in Table 7-1 were performed for the strain rate profiles equivalent to those observed along the centerline upstream of a 4:1:4 contraction-expansion at Deborah numbers between $0.5 \le De \le 3.5$. Representative plots of the stress-conformation hysteresis loops for each of these Deborah numbers is presented in Figure 7-14. At a Deborah number of $De = 0.5$, Figure 7-14 a, very little polymeric tensile stress or polymer stretch is generated. The dissipative energy loss associated with this stretch profile is minimal. As the Deborah number is increased, the stress, conformation and dissipative energy loss all increase. The initial stretch rates of the low Deborah number experiments are not large enough to result in significant chain orientation or unraveling. For these filament stretching experiments, the applied extension rates grow with increasing Deborah number, but the total accumulated Hencky strain is fixed at $\varepsilon_D = 2.77$. Beyond a Deborah number of $De = 1.5$, a plateau of $\Delta A \approx 400$ in the polymer chain deformation is observed even as the stress continues to grow. This is analogous to the observations made in Section 7.4.1 for constant stretch rate profiles.

In Figure 7-15, the dissipative energy loss is plotted against Deborah number for the Type III filament stretching experiment of the centerline strain rate profile upstream of a 4:1:4 contraction-expansion. The results for each Deborah number were repeated several times and the average value of dissipative energy loss is plotted along with error in these measurement which is typically on the order of ±15%. This error is the caused by noise in the birefringence and force measurements as well as the profile error associated with the Type II to Type III 'master curve' inversion procedure. The results are quite conclusive. Recalling the pressure drop measurements across a 4:1:4 contraction-expansion presented in Section 3.3.2, no additional pressure drop was observed until a Deborah number of $De \approx 0.5$ was reached. This critical Deborah number agrees quite well with the onset conditions for significant energy dissipation. Figure 7-15 also includes a fit to the experimental data of the form $E_D = 1.58\times10^6\,(De - 0.48)^{0.5}$. The fit is in excellent agreement with the experimental data, however, it does not match the predictions of recent constitutive models. Take, for example, the Rallison dissipative stress model [Rallison 1997]. The form of the model is similar to a FENE-

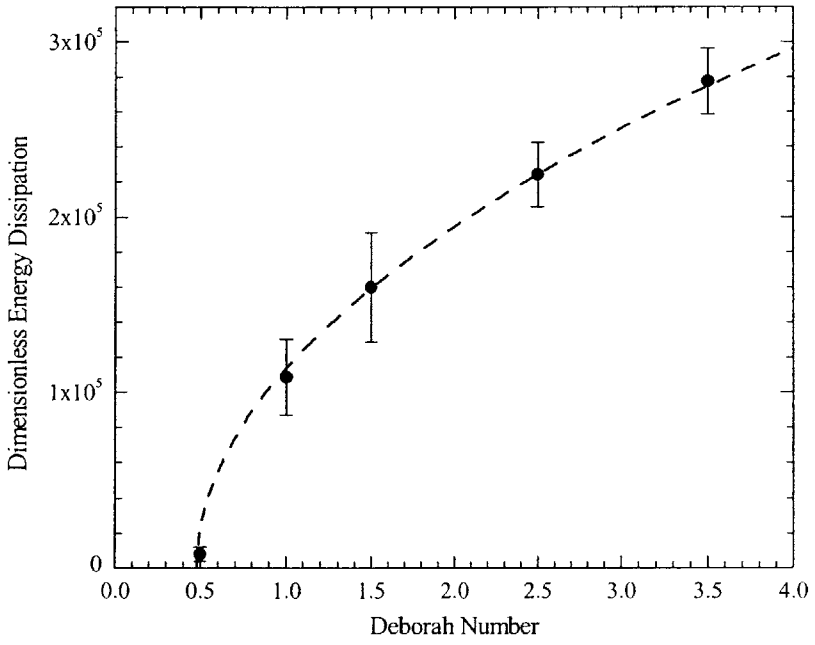

Figure 7-15 Dimensionless energy dissipation as a function of the Deborah number of the centerline stretch rate profile into a 4:1:4 contraction-expansion for the 0.025wt% PS/PS solution. The data include: '•', experimental data; and '- -', a fit of the form $E_D = 1.58\times10^6\,(De - 0.48)^{0.5}$.

P model except the polymeric stress term now has an additional purely dissipative component which relaxes immediately after secession the flow

$$\begin{aligned} \lambda \boldsymbol{A}_{(1)} &= -\left(f\left(\operatorname{tr}\boldsymbol{A}\right)\boldsymbol{A} - \boldsymbol{I}\right), \\ \boldsymbol{\tau}_p &= \frac{\eta_p}{\lambda}\left(f\left(\operatorname{tr}\boldsymbol{A}\right)\boldsymbol{A} - \boldsymbol{I}\right) + \eta_2\left(\frac{\boldsymbol{A}:\dot{\boldsymbol{\gamma}}\boldsymbol{A}}{\operatorname{tr}\boldsymbol{A}}\right), \\ f\left(\operatorname{tr}\boldsymbol{A}\right) &= \left(1 - \frac{\operatorname{tr}\boldsymbol{A}}{L^2}\right)^{-1} \end{aligned} \tag{7-33}$$

For strong deformations, the dissipative component of the polymeric stress in Equation 7-33 and therefore the total energy dissipation increases linearly with Deborah number. This scaling was verified for the stretch profiles used in these filament stretching experiments through numeric integration of Equation 7-33.

The discrepancies between the experimental observations and the constitutive model predictions at low Deborah numbers could be the result of several things. First, the Rallison dissipative model is known

to uniformly overpredict the transient extensional viscosity, but especially at small strains. The model predicts very little difference in the maximum conformation for any of the stretch rate profiles, $\Delta A_{max}(De{=}0.5)/\Delta A_{max}(De{=}3.5) \approx 0.8$ whereas the experiments clearly demonstrate a strong dependence on the stretch profile for the low Deborah number experiments, $\Delta A_{max}(De{=}0.5)/\Delta A_{max}(De{=}3.5) \approx 0.25$. Another possible cause of the discrepancy may be gravitational sagging in the experimental measurements. Anna *et al.* [Anna *et al.* 2001] demonstrated that a critical Deborah number for gravitational sagging could be determined from the ratio of the Bond number to the Capillary number

$$\frac{Bo}{Ca} = \frac{\rho g R_0}{\eta \dot{\varepsilon}}, \tag{7-34}$$

which characterizes the relative importance of gravitational forces to viscous forces throughout the stretch. When this ratio is order $Bo/Ca \approx 1$, gravitational sagging will influence the filament stretching results. From this dimensionless group a critical strain rate for gravitational sagging to become important

$$\dot{\varepsilon}_{sag} = \frac{\rho g R_0}{\eta}, \tag{7-35}$$

when $Bo/Ca = 1$. Finally, a critical Deborah number can be defined

$$De_{sag} = \lambda_z \frac{\rho g R_0}{\eta}. \tag{7-36}$$

For the current filament stretching experiments and 0.025wt% PS/PS solution, $De_{sag} = 3.43$ at $T = 25\,^{\circ}\mathrm{C}$. In the worst case, the strain rate profile for a Deborah number $De = 0.5$, only the first $\varepsilon = 0.5$ strain units are affected by gravitational sagging. Beyond that point, $\dot{\varepsilon} >> \dot{\varepsilon}_{sag}$ and gravitational effects can be ignored. Thus, it is unlikely that gravitational sagging is the cause of the discrepancy between experiments and theory or the reason why the energy dissipation decreases so quickly as the Deborah number decreases to $De = 0.5$.

By tailoring the strain rate profile within the filament stretching rheometer to reproduce the extensional flow along the centerline upstream of a 4:1:4 contraction-expansion, it is possible to simultaneously measure the stress and conformation of a polymer coil in a prototypical complex flow. The resulting measurements of stress-conformation hysteresis lead us to conclude that the energy loss of a

polymeric solution in extension is directly related to the additional pressure drop and drag coefficients observed for these same fluids in complex flows. If one hopes to accurately model a polymer solution in complex flows, it is therefore essential that the chosen constitutive model can quantitatively reproduce the stress and polymer conformation in transient extensional flows. With the current state of the art bead-spring constitutive models this is not yet possible. Additional microstructural information is required to capture the physics of a polymer coil unraveling in a strong flow. The challenge is creating such a model that is also computationally tractable. A significant innovation has recently been put forth by Ghosh et al. [2001] who incorporated a rate dependent finite extensibility parameter into a standard FENE model. Their results are encouraging in transient extensional flows, but more work and further refinement of their idea remains.

CHAPTER 8 Conclusions

The work presented in this thesis provides new insights into understanding the physical mechanisms governing the flow of elastic liquids. Specifically, the role of the shear and the extensional rheology of dilute polymer solutions on the stability of two complex flows has been investigated. The first set of experiments presented consists of a series of viscometric flows between a rotating cone-and-plate and plate-and-plate geometry. As illustrated in Figure 8-1, the complexity of this problem stems from the interaction between the flow geometry, fluid shear rheology and the thermophysical properties of the fluid. Shear flows with closed streamlines such as these can generate a considerable of amount of heat through viscous dissipation. Polymeric fluid are very poor thermal conductors. Even if the wall temperature is held constant, a nonhomogenous temperature profile can result in the fluid, strongly affecting the local fluid elasticity and the flow stability. In these simple shear experiments, the extensional rheology of the elastic liquid is unimportant. However, the second set of experiments presented in this thesis, the flow through an axisymmetric abrupt contraction-expansion, is a prototypical complex flow containing regions of both strong shear and extension. As shown in Figure 8-1, to understand the kinematics, flow transitions and state of stress for these experiments it is essential that one first understands both the shear and extensional rheology.

The combination of large elastic normal stresses and streamwise curvature can lead to flow destabilization. In Chapter 2 of this thesis, the importance of non-isothermal flow effects on the stability of torsional flows of highly elastic polymer solutions was demonstrated. Three monodisperse polystyrene test fluids of different molecular weights were used to investigate the role of the fluid shear rheology. It was shown that the proper dimensionless groups to consider when investigating thermal modifications to purely elastic instabilities in viscoelastic flows are the Deborah number and the thermoelastic number $\Theta = Na^{1/2}/De$ which measures the importance of coupling between the fluid elasticity and the nonlinearities arising from viscous heating. The thermoelastic number is independent of shear rate and can be influenced by changes in geometry, molecular weight and temperature. By varying the wall temperature (and thus the initial temperature of the test fluid) through a fairly narrow range, it was possible to significantly change the thermoelastic number. The onset conditions and scaling with changes in geometry of the subcritical Hopf bifurcation observed at small thermoelastic numbers, $\Theta << 1$, were shown to be in quantitative agreement with isothermal linear stability analyses for the Rouse-Zimm and Bird-DeAguiar constitutive models for both the cone-and-plate and the parallel-plate geometries. As the thermoelastic number was increased, the onset of the purely elastic flow instability was progressively delayed because of a decrease in local elasticity

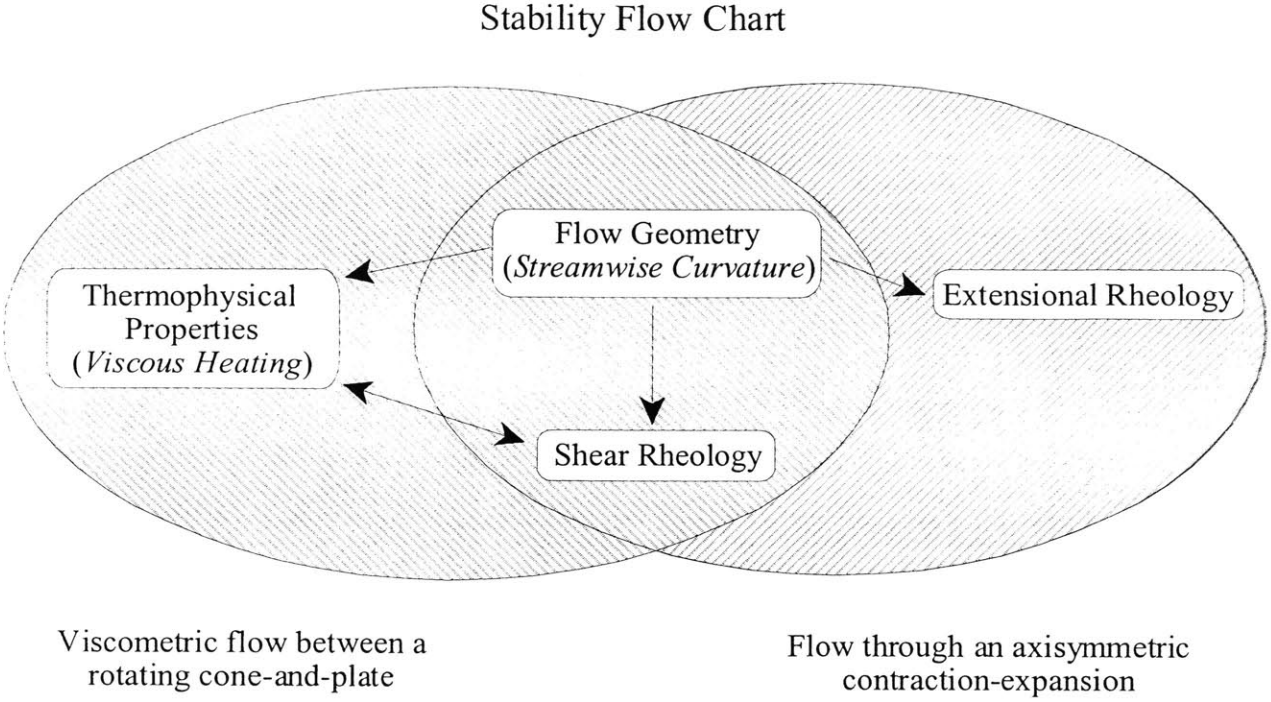

Figure 8-1 Stability flow chart illustrating the interplay between flow geometry, rheology and thermophysical properties for the experiments performed in this thesis.

caused by the temperature gradients across the gap induced by viscous dissipation. The mode of stability remained the same. The critical Deborah number for the onset of the elastic instability was found to increase linearly with the Nahme number, $Na = K(De_{crit} - De_{crit,0})$. In terms of the thermoelastic number, the critical Deborah number becomes $De_{crit} = K / 2\Theta^2 (1 - (1 - 4De_{crit,0}\Theta^2 / K)^{1/2})$. At thermoelastic numbers greater than $\Theta > \Theta_{crit} \approx 0.062$, the elastic flow instability was eliminated entirely. Thus, the thermoelastic number is an excellent new tool for predicting *a priori* the importance of non-isothermal effects and may be a key to controlling the stability of many industrial polymer processes.

Recently, Olagunju *et al.* [2001] performed the non-isothermal linear stability analysis for the flow of an Oldroyd-B fluid between a rotating cone-and-plate. The results of their work agree quite well with the experiments presented in this thesis. In their paper, they derive an expression for the equilibrium fluid temperature within the gap. As a simple extension of this thesis work, experimental measurement of the temperature profile between the cone-and-plate would not only be an excellent means of comparison to the theory of Olagunju *et al.* [2001] it would allow for the observation of the time evolution of the fluid temperature before and after the onset of the elastic instability. Perhaps these measurements will also aid in explaining the different critical shear rates and Nahme numbers associated with the maximums observed

in the shear stress and the first normal stress difference measurments during "thermal blow-up."

In the work presented in Chapters 3-6 of thesis, the flow of an ideal monodisperse, dilute polystyrene solution through an axisymmetric abrupt contraction-expansion has been extensively investigated. Several different contraction ratios and re-entrant lip curvatures were studied over a large range of Deborah numbers. This thesis constitutes a comprehensive set of experimental measurements to which constitutive models and numerical simulations can be rigorously compared. The test fluid was thoroughly characterized in both shear and extension. Pressure drop measurements showed a large extra pressure drop that increases monotonically with Deborah number above the value observed for a similar Newtonian fluid at the same flow rates. The enhanced pressure drop was found to be qualitatively insensitive to changes in aspect ratio and lip curvature and was also determined to be independent of the onset of an elastic flow instability. The stress singularity at the re-entrant lip which is a major difficulty for numerical simulations of the flow of a viscoelastic fluid through a contraction-expansion can thus be removed without qualitatively affecting the flow. In fact, in Chapter 5 rounding the re-entrant corner was observed to have the same effect as reducing the Deborah number. A simple geometric scaling argument was shown to collapse the data from several lip curvatures onto a single master curve. This result also suggests that a numerical simulation need not be able to predict the elastic flow instability in order to observe an enhanced pressure drop. However, even after rounding the re-entrant lip, this enhancement in the pressure drop is not predicted by any existing steady-state or transient numerical computations with simple dumbbell models. The lack of agreement between experiments and numerical simulations must therefore be the result of inadequacies in the constitutive models.

In this thesis we have demonstrated that this extra pressure drop is in part the result of an additional dissipative contribution to the polymeric stress arising from a stress-conformation hysteresis in the strong non-homogeneous extensional flow near the contraction plane. In uniaxial elongational flows, the stress and polymer chain configurations evolve along different pathways during stretch than during relaxation. The result is a hysteresis loop and an energy loss for polymer solutions in these strong extensional flows. In Chapter 7, the strain rate profile imposed by a filament stretching rheometer was designed to reproduce the extensional flow along the centerline upstream of a 4:1:4 contraction-expansion at several Deborah numbers. The stress and average conformation of a polymer coil were measured simultaneously. The resulting measurements of stress-conformation hysteresis leads to the conclusion that the energy dissipated by a polymeric solution in extension is directly related to the additional pressure drop and drag coefficients observed for these same fluids in complex flows.

The importance of extensional rheology cannot be over emphasized. If one hopes to accurately model a polymer solution in complex flows, our experiments have demonstrated that it is absolutely essential

that the chosen constitutive model can quantitatively reproduce the stress and polymer conformation in transient extensional flows. With the current bead-spring constitutive models being used in simulations, this is not yet possible. Additional microstructural information is required to capture the non-equilibrium internal conformations and dynamics of a polymer coil unraveling in a strong flow. A systematic comparison of our experimental measurements with numerical simulations using constitutive models such as the Rallison dissipative stress model [Rallison 1997] or the adaptive lengthscale model of Ghosh *et al.* [2001] still needs to be performed. Each of these constitutive models can predict qualitatively, but not quantitatively, the stress-conformation hysteresis observed in strong extensional flows. These simulations will help determine how sensitive the pressure drop measurements are to the accuracy of the transient extensional rheology of the constitutive model.

Some additional measurements using the filament stretching rheometer could also yield significant physical insight into the flow of viscoelastic fluids in the axisymmetric contraction-expansion and other complex flows. For example, filament stretching measurements of the polystyrene solution for a series of centerline strain rate profiles upstream of the 2:1:2 and 8:1:8 axisymmetric contraction-expansion would make the data presented in this thesis more complete. A similar series of filament stretching experiments using the PIB/PB and the PAA/CS Boger fluids used in the contraction flow literature [Boger and Binnington 1994; McKinley *et al.* 1991; Nguyen and Boger 1979] would also be very interesting. To date, no one has attempted to measure the birefringence of these polymers in the filament stretching rheometer, not even in homogeneous transient uniaxial elongation. Measuring the energy dissipated for each of these three polymer solutions and then comparing them to each other and to the enhanced pressure drop measurements would be very insightful. The filament stretching rheometer can also be used to investigate the enhanced drag coefficient measured in other complex flows of viscoelastic fluids such as the flow past spheres and arrays of cylinders.

The kinematics of the viscoelastic flow field upstream and downstream of an axisymmetric abrupt contraction-expansion were measured through laser Doppler velocimetry, particle image velocimetry and streak images. The stability and flow transitions were characterized using these techniques in conjunction with pressure drop measurements across the contraction-expansions. A supercritical Hopf bifurcation was documented for all contraction ratios and re-entrant corner curvatures at a large critical Deborah number. At even higher Deborah numbers a non-linear helical jetting instability is observed for the 4:1:4 axisymmetric contraction-expansion. Using flow induced birefringence measurements, the influence of these instabilities was shown to persist very far downstream ($z/R_2 \approx 15$). The onset of this elastic instability was not connected in any way to the enhanced pressure drop measurements.

In Chapter 4, the effect of contraction ratio on the vortex growth dynamics was systematically investigated. For a given elastic fluid, as the contraction ratio is increased, the flow evolves from a lip vortex regime to the corner vortex flow regime, but the critical contraction ratio for this crossover in vortex evolution is strongly dependent on the properties of the test fluid. In this thesis, a new dimensionless group was formed by taking the ratio of the elastic normal stresses generated in steady shear to the elastic normal stresses generated in homogenous transient uniaxial elongation. The normal stress number, $\aleph$, rationalizes the dependence of the growth of elastic 'lip' and corner vortices on contraction ratio and test fluid. For a normal stress ratio less than $\aleph \leq 0.055$, the flow is considered to be extension dominated and an elastic corner vortex develops. For a normal stress ratio greater than $\aleph > 0.055$, the flow is shear dominated and an elastic 'lip' vortex develops. This scaling was found to be consistent not only for the PS/PS Boger fluid tested in this thesis, but for all the rheologically characterized test fluids used in contraction flow literature to date.

The axisymmetric flow induced birefringence upstream and downstream of the contraction-expansion was investigated in Chapter 6. These measurements provide detailed information about the local orientation and deformation of the polymer coil *in situ* and are an excellent source of comparison for validating numerical simulations and constitutive models. Flow induced birefringence measurements were demonstrated to be a very sensitive measurement technique for investigating flow stability of polymeric fluids capable of detecting instabilities not found using LDV or pressure drop measurements. The AFIB measurements are used to calculate the normal stress number for a polymer coil *in situ* for both the 2:1:2 and 4:1:4 axisymmetric contraction-expansion. The results are in excellent agreement with the normal stresses calculated from steady shear and transient extensional rheology.

To extend and complete this research, axisymmetric flow induced birefringence measurements are required for both the PIB/PB and the PAA/CS Boger fluids used in the contraction flow literature [Boger and Binnington 1994; McKinley *et al.* 1991; Nguyen and Boger 1979]. Such experiments could yield additional support that the concept of a normal stress ratio developed in this thesis is the proper dimensionless group to characterize *a priori* the vortex growth mechanisms upstream of a sudden contraction.

In the two flows of viscoelastic fluids investigated in this thesis, we have demonstrated that to understand the flow kinematics and stability it is necessary to characterize the flow in terms of at least two dimensionless parameters. These complex flows cannot be rationalized by the Deborah number alone. To understand the importance of non-isothermal flow effects on the stability of torsional flows of polymer solutions the Deborah number and the thermoelastic number were needed while to understand the flow transitions upstream of a axisymmetric contraction-expansion the Deborah number and normal stress ratio

were required. In both cases, the second dimensionless group is set by the material properties of the fluid and the flow geometry, but not by the flow strength.

Bibliography

1. Al-Mubaiyedh, U.A., R. Sureshkumar and B. Khomami. "Influence of energetics on the stability of viscoelastic Taylor-Couette flow", Phys. Fluids, **11** (1999) 3217-3226.

2. Al-Mubaiyedh, U.A., R. Sureshkumar and B. Khomami. "Energetic effects on the stability of viscoelastic Dean flow", J. Non-Newtonian Fluid Mech., **95** (2000) 277-293.

3. Al-Mubaiyedh, U.A., R. Sureshkumar and B. Khomami. "Linear stability of viscoelastic Taylor-Couette flow: Influence of fluid rheology and energetics", J. Rheol., **44** (2000) 1121-1138.

4. Anna, S.L., G.H. McKinley, D.A. Nguyen, T. Sridhar, S.J. Muller, J. Huang and D.F. James. "An inter-laboratory comparison of measurements from filament stretching rheometers using common test fluids", J. Rheol., **45** (2001) 83-114.

5. Anna, S.L., C.B. Rogers and G.H. McKinley. "On controlling the kinematics of a filament stretching rheometer using a real-time active control mechanism", J. Non-Newtonian Fluid Mech., **87** (1999) 307-335.

6. Arigo, M., "The effects of fluid rheology on the dynamics of isothermal and non-isothermal flows of viscoelastic fluids", Ph.D. Thesis, Harvard University, Cambridge, 1999.

7. Arigo, M.T. and G.H. McKinley. "An experimental investigation of negative wakes behind spheres settling in a shear-thinning viscoelastic fluid", Rheol. Acta, **37** (1998) 307-327.

8. Arigo, M.T., D. Rajagopalan, N. Shapley and G.H. McKinley. "The sedimentation of sphere through an elastic fluid .1. Steady motion", J. Non-Newtonian Fluid Mech., **60** (1995) 225-257.

9. Avagliano, A. and N. Phan-Thien. "Torsional flow: elastic instability in a finite domain", J. Fluid Mech., **312** (1996) 279-298.

10. Avagliano, A. and N. Phan-Thien. "Torsional flow stability of highly dilute polymer solutions", J. Non-Newtonian Fluid Mech., **84** (1999) 19-44.

11. Azzam, R.M.A. "Propagation of partially polarized light through anisotropic media with or without depolarization: A differential 4x4 matrix calculus", J. Opt. Soc. Am., **68** (1978) 1756-1767.

12. Batchelor, G.K. *An Introduction to Fluid Dynamics*, Cambridge Univ. Press, England, 1985.

13. Baumert, B.M. and S.J. Muller. "Flow regimes in model viscoelastic fluids in a circular Couette system with independently rotating cylinders", Phys. Fluids, **9** (1997) 566-586.

14. Becker, L.E. and G.H. McKinley. "The stability of viscoelastic creeping plane shear flows with viscous heating", J. Non-Newtonian Fluid Mech., **92** (2000) 109-133.

15. Beraudo, C., A. Fortin, T. Coupez, Y. Demay, B. Vergnes and J.F. Agassant. "A finite element method for computing the flow of multi-mode viscoelastic fluids: comparison with experiments", J. Non-Newtonian Fluid Mech., **75** (1998) 1-23.

16. Bernstein, B., K.A. Feigl and E.T. Olsen. "Steady flows of viscoelastic fluids in axisymmetric abrupt contraction geometry: A comparison of numberical results", J. Rheol., **38** (1994) 53-71.

17. Binding, D.M. and K. Walters. "On the use of flow through a contraction in estimating the extensional viscosity of mobile polymer solutions", J. Non-Newtonian Fluid Mech., **30** (1988) 233-250.

18. Bird, R.B., R.C. Armstrong and O. Hassager. *Dynamics of Polymeric Liquids: Volume 1 Fluid Mechanics*, John Wiley & Sons, New York, 1987.

19. Bird, R.B., C.F. Curtiss, R.C. Armstrong and O. Hassager. *Dynamics of Polymeric Liquids: Volume 2 Kinetic Theory*, John Wiley & Sons, New York, 1987.

20. Bird, R.B. and J.R. DeAguiar. "An encapsulated dumbell model for concentrated polymer solutions and melts I. Theoretical development and constitutive equation", J. Non-Newtonian Fluid Mech., **13** (1983) 149-160.

21. Bird, R.B. and J.M. Wiest. "Constitutive-equations for polymeric liquids", Annu. Rev. Fluid Mech., **27** (1995) 163-193.

22. Boger, D.V. "A highly elastic constant-viscosity fluid", J. Non-Newtonian Fluid Mech., **3** (1977/78) 87-91.

23. Boger, D.V. "Viscoelastic flows through contractions", Annual Review of Fluid Mechanics, **19** (1987) 157-182.

24. Boger, D.V. and R.J. Binnington. "Circular entry flows in fluid M1", J. Non-Newtonian Fluid Mech., **35** (1990) 339-360.

25. Boger, D.V. and R.J. Binnington. "Experimental removal of the re-entrant corner singularity in tubular entry flows", J. Rheol., **38** (1994) 333-349.

26. Boger, D.V., R. Gupta and R.I. Tanner. "The end correction for power-law fluids in the capillary rheometer", J. Non-Newtonian Fluid Mech., **4** (1978) 238-248.

27. Boger, D.V., D.U. Hur and R.J. Binnington. "Further observations of elastic effects in tubular entry flows", J. Non-Newtonian Fluid Mech., **20** (1986) 31-49.

28. Boger, D.V. and K. Walters. *Rheological Phenomena in Focus*, Elsevier, New York, 1993.

29. Brandrup, J. and E.H. Immergut. *Polymer Handbook*, John Wiley & Sons, New York, 1989.

30. Byars, J.A., R.J. Binnington and D.V. Boger. "Entry flow and constitutive modelling of fluid S1", J. Non-Newtonian Fluid Mech., **72** (1997) 219-235.

31. Byars, J.A., A. Oztekin, R.A. Brown and G.H. McKinley. "Spiral instabilities in the flow of highly elastic fluids between rotating parallel disks", J. Fluid Mech., **271** (1994) 173-218.

32. Cartalos, U. and J.M. Piau. "Creeping flow regimes of low concentration polymer solutions in thick solvents through an orifice die", J. Non-Newtonian Fluid Mech., **45** (1992) 231-285.

33. Cartalos, U. and J.M. Piau. "Pressure drop scaling laws and structural stress contributions for complex flows of flexible polymer solutions in thick solvents", J. Non-Newtonian Fluid Mech., **44** (1992) 55-83.

34. Caswell, B. "Report on the IXth International Workshop on Numerical Methods in Non-Newtonian Flows", J. Non-Newtonian Fluid Mech., **62** (1996) 99-110.

35. Chmielewski, C., K.L. Nichols and K. Jayaraman. "A comparison of the drag coefficients of spheres translating in corn-syrup-based and plybutene-based Boger fluids", J. Non-Newtonian Fluid Mech., **35** (1990) 37-49.

36. Chow, A.W. and G.G. Fuller. "Response of moderately concentrated xanthan gum solutions to time-dependent flows using 2-color flow birefringence", J. Rheol., **28** (1984) 23-43.

37. Coates, P.J., R.C. Armstrong and R.A. Brown. "Calculation of steady-state viscoelastic flow through axisymmetric contractions with the EEME formulation", J. Non-Newtonian Fluid Mech., **42** (1992) 141-188.

38. Cogswell, F.N. "Measuring the extensional viscosity of polymer melts", Polym. Eng. Sci., **12** (1972) 64-73.

39. Dagan, Z., S. Weinbaum and R. Pfeffer. "An infinite-series solution for the creeping motion through an orifice of finite length", J. Fluid Mech., **115** (1982) 505-523.

40. Denn, M.M. "Issues in Non-Newtonian Fluid Mechanics." in: J. L. Lumley, A. Acrivos, L. G. Leal, and S. Leibovich (Eds), Research Trends in Fluid Dynamics, AIP Press, New York, 1993.

41. Doyle, P.S., E.S.G. Shaqfeh, G.H. McKinley and S.H. Spiegelberg. "Relaxation of dilute polymer solutions following extensional flow", J. Non-Newtonian Fluid Mech., **76** (1998) 79-110.

42. Eisenbrand, G.D. and J.D. Goddard. "Birefringence and pressure drop for the orifice flow of a polymer solution", J. Non-Newtonian Fluid Mech., **11** (1982) 37-52.

43. Ferry, J.D. *Viscoelastic Properties of Polymers*, Wiley-Interscience, New York, 1980.

44. Flory, P. *Principles of Polymer Chemistry*, Cornell University Press, Ithaca, 1953.

45. Frattini, P.L. and G.G. Fuller. "A note on phase-modulated flow birefringence", J. Rheol., **28** (1984) 61-70.

46. Fuller, G.G. *Optical Rheometry of Complex Fluids*, Oxford University Press, New York, 1995.

47. Ghosh, I., G.H. McKinley, R.A. Brown and R.C. Armstrong. "Deficiencies of FENE dumbell models in describing the rapid stretching of dilute polymer solutions", J. Rheol., **45** (2001) In Press.

48. Gupta, M., C.A. Hieber and K.K. Wang. "Viscoelastic modelling of entrance flow using multimode Leonov model." International J. Numerical Methods in Fluids, **24** (1997) 493-517.

49. Gupta, R.K., D.A. Nguyen and T. Sridhar. "Extensional Viscosity of Dilute Polystyrene Solutions: Effect of Concentration and Molecular Weight", Phys. Fluids, **12** (2000) 1296-1318.

50. Happel, J. and H. Brenner. *Low Reynolds Number Hydrodynamics*, Prentice-Hall Inc., Englewood Cliffs, NJ, 1965.

51. Hassager, O. "Working group on numerical techniques, Fifth International Workshop on Numerical Methods in Non-Newtonian flows, Lake Arrowhead, USA", J. Non-Newtonian Fluid Mech., **29** (1988) 2-5.

52. Heslot, F., B. Castaing and A. Libchaber. "Transition to turbulence in helium gas", Phys. Rev. A, **36** (1987) 5870-5873.

53. Hinch, E.J. "Uncoiling a polymer molecule in a strong extensional flow", J. Non-Newtonian Fluid Mech., **54** (1994) 209-230.

54. Ho, T.C., M.M. Denn and B.E. Anshus. "Stability of low Reynolds number flow with viscous heating", Rheol. Acta, **16** (1977) 61-68.

55. Iooss, G. and D.D. Joseph. *Elementary Stability and Bifurcation Theory*, Springer, New York, 1980.

56. James, D.F. and G.M. Chandler. "Measurement of the extensional viscosity of M1 in a converging channel rheometer", J. Non-Newtonian Fluid Mech., **35** (1990) 445-458.

57. James, D.F. and J.H. Saringer. "Extensional flow of dilute polymer solutions", J. Fluid Mech., **97** (1980) 655-671.

58. Janeschitz-Kriegl, H. *Polymer Melt Rheology and Flow Birefringence*, Springer-Verlag, Berlin, 1983.

59. Keiller, R.A. "Entry-flow calculations for the Oldroyd-B and FENE equations", J. Non-Newtonian Fluid Mech., **46** (1993) 143-178.

60. Keiller, R.A., J.M. Rallison and J.G. Evans. "Sink flows of a suspension of rigid rods: the failure of a similarity solution", J. Non-Newtonian Fluid Mech., **42** (1992) 249-266.

61. Khomami, B. and L.D. Moreno. "Stability of viscoelastic flow around periodic arrays of cylinders", Rheol. Acta, **36** (1997) 367-383.

62. King, D.H. and D.F. James. "Analysis of the Rouse model in extensional flow. II. Stresses generated in sink flow by flexible macromolecules and by finitely extended macromolecules." J. Chem. Phys., **78** (1983) 4749-4754.

63. Kolte, M.I., H.K. Rasmussen and O. Hassager. "Transient filament stretching rheometry I: Numerical simulation", Rheol. Acta, **36** (1997) 285-302.

64. Kunisch, K. and X. Marduel. "Optimal control of non-isothermal viscoelastic fluid flow", J.Non-Newtonian Fluid Mech., **88** (2000) 261-301.

65. Larson, R.G. *Constitutive Equations for Polymer Melts and Solutions*, Butterworths, Boston, 1988.

66. Larson, R.G. "Instabilities in Viscoelastic Flows", Rheol. Acta, **31** (1992) 213-263.

67. Larson, R.G., S.J. Muller and E.S.G. Shaqfeh. "The effect of fluid rheology on the elastic Taylor-Couette instability", J. Non-Newtonian Fluid Mech., **51** (1994) 195-225.

68. Larson, R.G., E.S.G. Shaqfeh and S.J. Muller. "A purely elastic instability in Taylor-Couette flow", J. Fluid Mech., **218** (1990) 573-600.

69. Lawler, J.V., S. J. Muller, R. A. Brown and R.C. Armstrong. "Laser Doppler Velocimetry Measurements of Velocity Fields and Transitions in Viscoelastic Fluids", J. Non-Newtonian Fluid Mech., **20** (1986) 51-92.

70. Li, J.-M. and W.R. Burghardt. "Flow Birefringence in Axisymmetric Geometries", J. Rheol., **39** (1995) 743-766.

71. Li, J.-M., W.R. Burghardt, B. Yang and B. Khomami. "Flow birefringence and computational studies of a shear thinning polymer solution in axisymmetric stagnation flow", J. Non-Newtonian Fluid Mech., **74** (1998) 151-193.

72. Li, J.-M., W.R. Burghardt, B. Yang and B. Khomami. "Birefringence and computational studies of a polystyrene Boger fluid in axisymmetric stagnation flow." J. Non-Newtonian Fluid Mech., **91** (2000) 189-220.

73. Li, L. and R. Larson. "Excluded volume effects on the birefringence and stress of dilute polymer solutions in extensional flow", Rheol. Acta, **39** (2000) 419-427.

74. Li, L., R.G. Larson and T. Sridhar. "Brownian dynamics simulations of dilute polystyrene solutions", J. Rheol., **44** (2000) 291-322.

75. Lielens, G., P. Halin, I. Jaumain, R. Keunings and V. Legat. "New closure approximations for the

kinetic theory of finitely extensible dumbbells", J. Non-Newtonian Fluid Mech., **76** (1998) 249-279.

76. Liu, A., "Viscoelastic Flow of Polymer Solutions Around Arrays of Cylinders: Comparison of Experiment and Theory", Ph.D. Thesis, MIT Dept. Chemical Engineering, Cambridge, 1997.

77. MacDonald, M.J. and S.J. Muller. "Shear rheology of polymer solutions near the critical condition for elastic instability", Rheol. Acta, **36** (1997) 97-109.

78. Mackay, M.E. and D.V. Boger. "An explanation of the rheological properites of Boger fluids", J. Non-Newtonian Fluid Mech., **22** (1987) 235-243.

79. Mackay, M.E. and D.V. Boger. "Flow Visualisation in Rheometry." in: A. A. C. a. D. W. Clegg (Eds), Rheological Measurement, 1988.

80. Mackay, M.E., Y.L. Yeow and D.V. Boger. "Pressure-drop in pipe contractions - experimental-measurement or finite-element simulation", Chemical Eng. Research and Design, **66** (1988) 22-25.

81. Mackey, J.R., K.K. Das, S.L. Anna and G.H. McKinley. "A compact dual-crystal modulated birefringence-measurement system for microgravity applications", Measurement Sci. Tech., **10** (1999) 946-955.

82. Magda, J.J. and R.G. Larson. "A transition occurring in ideal elastic liquids during shear flow", J. Non-Newtonian Fluid Mech., **30** (1988) 1-19.

83. Magda, J.J., R.G. Larson and M.E. Mackay. "Deformation-dependent Hydrodynamics Interaction in Flows of Dilute Polymer Solutions", J. Chem. Phys., **89** (1988) 2504-2513.

84. Matta, J.E. and R.P. Tytus. "Liquid stretching using a falling cylinder", J. Non-Newtonian Fluid Mech., **35** (1990) 215-229.

85. McKinley, G.H., J.A. Byars, R.A. Brown and R.C. Armstrong. "Observations on the elastic instability in cone-and-plate and paralle-plate flows of polyisobutylene Boger fluid", J. Non-Newtonian Fluid Mech., **40** (1991) 201-229.

86. McKinley, G.H., A. Oztekin, J.A. Byars and R.A. Brown. "Self-similar spiral instabilities in elastic flows between a cone and a plate", J. Fluid Mech., **285** (1995) 123-164.

87. McKinley, G.H., P. Pakdel and A. Oztekin. "Rheological and geometric scaling of purely elastic flow instabilities", J. Non-Newtonian Fluid Mech., **67** (1996) 19-47.

88. McKinley, G.H., W.P. Raiford, R.A. Brown and R.C. Armstrong. "Nonlinear dynamics of viscoelastic flow in axisymmetric abrupt contractions", J. Fluid Mech., **223** (1991) 411-456.

89. McKinley, G.H. and T. Sridhar. "Filament stretching rheometry", Annu. Rev. Fluid Mech., (2002)

90. Mompean, G. and M. Deville. "Unsteady finite volume simulation of Odroyd-B fluid through a three-dimensional planar contraction", J. Non-Newtonian Fluid Mech., **72** (1997) 253-279.

91. Mongruel, A. and M. Cloitre. "Extensional flow of semidilute suspensions of rod-like particles through an orifice", Phys. Fluids, **7** (1995) 2546-2552.

92. Müller, A.J., J.A. Odell and A.A. Keller. "Elongational flow and rheology of monodisperse polymers in solution", J. Non-Newtonian Fluid Mech., **30** (1988) 99-118.

93. Nguyen, H. and D.V. Boger. "The Kinematics and Stability of Die Entry Flows", J. Non-Newtonian Fluid Mech., **5** (1979) 353-368.

94. Olagunju, D.O. "Effect of free surface and inertia on viscoelastic parallel plate flow", J. Rheol., **38**

(1994) 151-168.

95. Olagunju, D.O. "Elastic instabilities in cone-and-plate flow: Small gap theory", ZAMP, **46** (1995) 946-959.

96. Olagunju, D.O. "Hopf bifurcation in creeping cone-and-plate flow of a viscoelastic fluid", ZAMP, **48** (1997) 361-369.

97. Olagunju, D.O. "On short wave elastic instabilities in parallel plate flow", Proceedings of 1997 ASME Annual Meeting, (1997)

98. Olagunju, D.O. and L.P. Cook. "Secondary flows in cone and plate flow of an Oldroyd-B fluid", J. Non-Newtonian Fluid Mech., **46** (1993) 29-47.

99. Olagunju, D.O., P. Cook and G.H. McKinley. "Effect of viscous heating on stability of viscoelastic cone-and-plate flow: Axisymmetric case", (2001) In preparation.

100. Ooi, Y.W. and T. Sridhar. "Extensional Rheometry of Fluid S1", J. Non-Newtonian Fluid Mech., **52** (1994) 153-162.

101. Orr, N.V. and T. Sridhar. "Probing the dynamics of polymer solutions in extensional flow using step strain rate experiments", J. Non-Newtonian Fluid Mech., **82** (1999) 203-232.

102. Öttinger, H.C. "Generalized Zimm model for dilute polymer-solutions under theta-conditions", J. Chem. Phys., **86** (1987) 3731-3749.

103. Öztekin, A. and R.A. Brown. "Instability of a viscoelastic fluid between rotating parallel disks: analysis for the Oldroyd-B fluid", J. Fluid Mech., **255** (1993) 473-502.

104. Öztekin, A., R.A. Brown and G.H. McKinley. "Quantitative prediction of the viscoelastic instability in cone-and-plate flow of a Boger fluid using a multi-mode Giesekus model", J. Non-Newtonian Fluid Mech., **54** (1994) 351-377.

105. Pakdel, P. and G.H. McKinley. "Digital particle imaging velocimetry of viscoelastic fluids", AIChE J., **43** (1997) 289-302.

106. Perkins, T.T., D.E. Smith and S. Chu. "Direct Observation of Tube-like Motion of a Single Polymer Chain", Science, **264** (1994) 819-826.

107. Perkins, T.T., D.E. Smith and S. Chu. "Single Polymer Dynamics in an Elongational Flow", Science, **276** (1997) 2016-2021.

108. Petrie, C.J.S. and M.M. Denn. "Instabilites in Polymer Processing", AIChE J., **22** (1976) 209-236.

109. Phan-Thien, N. "Coaxial-disk flow of an Oldroyd-B fluid: Exact solution and stability", J. Non-Newtonian Fluid Mech., **13** (1983) 325-340.

110. Phan-Thien, N. "Cone-and-plate flow of the Oldroyd-B fluid is unstable", J. Non-Newtonian Fluid Mech., **17** (1985) 37-44.

111. Pope, D.P. and A.A. Keller. "Alignment of macromolecules in solution by elongational flow: a study of the effect of pure shear ina four-roll mill", Colloid Polym. Sci., **255** (1977) 633-643.

112. Pope, D.P. and A.A. Keller. "A study of chain extending effect of elongational flow in polymer solutions", Colloid Polym. Sci., **256** (1978) 751-756.

113. Purnode, B. and M.J. Crochet. "Flows of plymer solutions through contractions. Part 1: Flows of polyacrylamide solutions through planar contractions." J. Non-Newtonian Fluid Mech., **65** (1996)

269-289.

114. Quinzani, L.M., R.C. Armstrong and R.A. Brown. "Birefringence and laser-Doppler velocimetry (LDV) studies of viscoelastic flow through a planar contraction." J. Non-Newtonian Fluid Mech., **52** (1994) 1-36.

115. Quinzani, L.M., R.C. Armstrong and R.A. Brown. "Use of coupled birefringence and LDV studies of flow through a planar contraction to test constitutive equations for concentrated polymer solutions", J. Rheol., **39** (1995) 1201-28.

116. Rajagopalan, D., J.A. Byars, R.C. Armstrong, R.A. Brown, J.S. Lee and G.G. Fuller. "Comparison of numerical simulations and birefringence measurements in viscoelastic flow between eccentric rotating cylinders", J. Rheol., **36** (1992) 1349-1375.

117. Rallison, J.M. "Dissipative stresses in dilute polymer solutions", J. Non-Newtonian Fluid Mech., **68** (1997) 61-83.

118. Remmelgas, J., L.G. Leal, N.V. Orr and T. Sridhar. "Viscous and Elastic Stresses in Extensional Rheometry", J. Non-Newtonian Fluid Mech., **76** (1997) 111-135.

119. Renardy, Y. and M. Renardy. "A model equation for axisymmetric stability of small-gap parallel-plate flows." J. Non-Newtonian Fluid Mech., **77** (1998) 103-114.

120. Ryskin, G. "Calculation of the effect of polymer additive in a converging flow", J. Fluid Mech, **178** (1987) 423-440.

121. Sampson, R.A. Phil. Trans. Roy. Soc., **182** (1891) 449.

122. Shaqfeh, E.S.G. "Purely elastic instabilities in viscometric flows", Annu. Rev. Fluid Mech., **28** (1996) 129-185.

123. Solomon, M.J. and S.J. Muller. "Flow past a sphere in polystyrene-based Boger fluids: the effect on the drag coefficient of finite extensibility, solvent quality and polymer molecular weight." J. Non-Newtonian Fluid Mech., **62** (1996) 81-94.

124. Spiegelberg, S.H. and G.H. McKinley. "Stress relaxation and elastic decohesion of viscoelastic polymer solutions in extensional flow", J. Non-Newtonian Fluid Mech., **67** (1996) 49-76.

125. Sridhar, T. and R.K. Gupta. "Material properties of viscoelastic liquids in uniaxial extension", J. Rheol., **35** (1991) 363-377.

126. Sridhar, T., D.A. Nguyen and G.G. Fuller. "Birefringence and stress growth in uniaxial extension of polymer solutions", J. Non-Newtonian Fluid Mech., **90** (2000) 299-315.

127. Sridhar, T., V. Tirtaatmadja, D.A. Nguyen and R.K. Gupta. "Measurement of extensional viscosity of polymer solutions", J. Non-Newtonian Fluid Mech., **40** (1991) 271-280.

128. Stokes, J.R., "Swirling flow of viscoelastic fluids", Ph.D. Thesis, Melbourne, Parkville, Victoria, 1998.

129. Szabo, P. "Transient filament stretching rheometry I: Force balance analysis", Rheol. Acta, **36** (1997) 277-284.

130. Szabo, P., J.M. Rallison and E.J. Hinch. "Start-up of flow of a FENE-fluid through a 4:1:4 constriction in a tube", J. Non-Newtonian Fluid Mech., **72** (1997) 73-86.

131. Talbott, W.H., "Streaming birefringence in extensional flow of polymer solutions", Ph. D. Thesis,

University of Michigan, Ann Arbor, 1978.

132. Talbott, W.H. and J.D. Goddard. "Streaming birefringence in extensional flows of polymer solutions", Rheol. Acta, **18** (1979) 505-517.

133. Tirtaatmadja, V. and T. Sridhar. "A filament stretching device for measurement of extensional viscosity", J. Rheol., **37** (1993) 1133-1160.

134. Townsend, P. and K. Walters. "Expansion flows of non-Newtonian fluids", Chem. Eng. Sci., **49** (1994) 749-763.

135. Wales, J.L.S. and H. Janeschitz-Kriegel. "Effects of concentration and polydispersity on flow birefringence of polystyrene", Rheol. Acta, **7** (1968) 19-23.

136. Wheeler, E.K., P. Fischer and G.G. Fuller. "Time-Periodic Flow Induced Structures and Instabilities in a Viscoelastic Surfactant Solution", J. Non-Newtonian Fluid Mech., **75** (1998) 193-208.

137. White, S.A., A.D. Gotsis and D.G. Baird. "Review of the entry flow problem: experimental and numerical", J. Non-Newtonian Fluid Mech., **24** (1987) 121-160.

138. Winter, H.H. "Viscous Dissipation in Shear Flows of Molten Polymers", Adv. Heat Transfer, **13** (1977) 205-267.

139. Yang, B. and B. Khomami. "Simulations of sedimentation of a sphere in a viscoelastic fluid using molecular based constitutive models", J. Non-Newtonian Fluid Mech., **82** (1999) 429-452.

140. Yesilata, B., A. Oztekin and S. Neti. "Non-isothermal viscoelastic flow through an axisymmetric sudden contraction", J. Non-Newtonian Fluid Mech., **89** (2000) 133-164.

141. Yu, G., T.Q. Nguyen and H.-H. Kausch. "Birefringence of dilute PS solution in transient elongational flow", J. Polymer Science: Part B: Polymer Physics, **36** (1998) 1483-1500.

142. Yueh, C.-S. and C.-I. Weng. "Linear stability analysis of plane Couette flow with viscous heating", Phys. Fluids, **8** (1996) 1802-1813.

143. Zimm, B.H. "Dynamics of polymer molecules in dilute solution: viscoelasticity, flow birefringence and dielectric loss", J. Chem. Phys., **24** (1956) 269-278.